Thermally Driven Vacuum Micropumps

Guillermo Lopez Quesada

THÈSE

En vue de l'obtention du

DOCTORAT DE L'UNIVERSITÉ DE TOULOUSE

Délivré par l'Institut National des Sciences Appliquées de Toulouse

Cotutelle internationale : University of Thessaly

Présentée et soutenue par

Guillermo LÓPEZ QUESADA

Le 25 septembre 2019

Thermally Driven Vacuum Micropumps

Ecole doctorale : **MEGEP - Mécanique, Energétique, Génie civil, Procédés**

Spécialité : **Dynamique des fluides**

Unité de recherche :
ICA - Institut Clément Ader

Thèse dirigée par
Stéphane COLIN et Dimitris VALOUGEORGIS

Jury

M. Nikolaos ANDRITSOS, Examinateur
M. Jürgen BRANDNER, Rapporteur
M. Stéphane COLIN, Co-directeur de thèse
Mme Silvia GAASTRA-NEDEA, Examinatrice
M. Pierre PERRIER, Examinateur
M. Stefan STEFANOV, Rapporteur
M. Dimitris VALOUGEORGIS, Co-directeur de thèse

UNIVERSITY OF THESSALY

Department of Mechanical Engineering

Volos, Greece

and

UNIVERSITÉ DE TOULOUSE

Institut National des Sciences Appliquées de Toulouse

Toulouse, France

Thermally Driven Vacuum Micropumps

by

Guillermo López Quesada

A Dissertation for the Partial Fulfillment of the
Requirements for the Degree of
Doctor of Philosophy

September 2019

Certified by the members of the Dissertation Committee:

1st member	Prof. Dimitris Valougeorgis
(Co-supervisor)	University of Thessaly
2nd member	Prof. Stéphane Colin
(Co-supervisor)	Université de Toulouse, CNRS, INSA, ISAE-SUPAERO, Mines-Albi, UPS
3rd member	Prof. Jürgen Brandner
	Karlsruhe Institute of Technology
4th member	Prof. Stefan Stefanov
	Bulgarian Academy of Sciences
5th member	Prof. Nikolaos Andritsos
	University of Thessaly
6th member	Asst. Prof. Silvia Gaastra-Nedea
	Eindhoven University of Technology
7th member	Chargé de Recherche Dr. Pierre Perrier
	Université d'Aix-Marseille

Dedicated to my family.
The given, the chosen and the missing,
thanks.

Acknowledgements

First and foremost, I would like to express my deep and sincere gratitude to my supervisors, Stéphane Colin and Dimitris Valougeorgis, for their guidance and support during the whole project and their understanding and endless patience during the most difficult times. They are not just outstanding researchers, but also remarkable individuals with great values. I sincerely think that I could not have found better mentors for these three years.

I also want to thank to the whole microfluidics team at the Institut Clément Ader for their valuable help through the project. I am very grateful to Lucien, Christine, Marcos, Pascale and Ahmad not only for the scientific discussions and precious technical advice with my project, but also for showing me the work environment I would like to find in my future. I would also like to specially thank Nicolas Laurien and Stéphane Orieux for all the technical support and help in the laboratory. Additionally, to all my fellow colleagues in Toulouse (former and new), an international and endless list composed by people from France, Italy, India, China, Lebanon, Togo, Cameroon, Vietnam, Algeria, Tunisia and Morocco; thanks for all those necessary coffee breaks over both scientific and not-so scientific discussions.

I want to thank as well to all the team in the University of Thessaly for all their assistance, not only with the scientific stuff but also with all the γραφειοκρατία. Many thanks to Steryios, Makis, Zoe and Eleni. To the fellow colleagues that shared their time with me in Volos, Giorgos, Alex, Nikos and Ali; the experiences and moments that we have created are truly invaluable and without those coffee and lunch breaks my time in Greece would feel a bit empty.

I also want to express my gratitude to Martin Wuest and INFICON for hosting me during part of this project and showing me how a leading company in the vacuum technology industry works. Additionally, for all the technical support and training at Laboratoire d'Analyse et d'Architecture des Systemes regarding the microfabrication efforts, I am deeply grateful to Laurent Mazenq, Rémi Courson, Adrian Laborde, Samuel Charlot, Fabien Mesnilgrante and Andrea Nicollet for teaching me everything I have learnt about working in a clean room.

I would also like to thank the whole MIGRATE network and the European Commission, not only for this unique opportunity to develop a research career with a challenging project, but essentially for allowing me to meet, exchange and learn with the kind of Senior Scientist that one day I will hopefully become. I also want to thank the coordination of the project and the constant

administrative support provided by Martin Knapp and Verena Tomczyk. Moreover, I want to thank to each of the other Early Stage Researcher, Sofia, Natasa, Gustavo, Sulaiman, Varun, Martin, Ricardo, Daniel, Alberto, Vikash, Stavros, Danish, Moritz and Jojo; for all the scientific, cultural and life exchanges we have had during these last three years and that will hopefully continue in the future. Additionally, I want to thank all the fellow Ph.D. students related in some way with the network, but especially to Dominique and Irene, for the many moments together during the conferences, visits, and trips and the scientific discussions and mutual support shared over a beer.

I would like to deeply thank all the members of the committee for finding the time to review my dissertation and provide their valuable input. Dankeschön, благодаря ви много, ευχαριστώ πολύ, dank u wel, merci beaucoup, Professors Jürgen Brandner, Stefan Stefanov, Nikolaos Andritsos, Asssitant Professor Silvia Gaastra-Nedea and Dr. Pierre Perrier.

Finally, I am grateful to everyone that I have met in every step of the way. Every single experience and moment has taken me to this point after living in Toulouse, Volos and Vorarlberg and meeting researchers, engineers, martial artists, tänzer, independancers, dolfinnoulas, engendros and zombies. Not forgetting to thank the ones always waiting for my return, growing in number little by little, because wherever they are I know I will be welcome. And lastly to my family, because without them it is certain that I would not stand where I am, thank you.

This work has been funded by the European Union's Framework Programme for Research and Innovation Horizon 2020 (2014–2020) under the Marie Skłodowska-Curie (grant agreement number. 643095)

Thermally Driven Vacuum Micropumps

Guillermo López Quesada
National Institute of Applied Sciences (INSA) and University of Thessaly (UTH)
Supervisors: Prof. S. Colin and Prof. D. Valougeorgis
September 2019

The rapid development of the semiconductor industry has been followed, in the last decades, by huge progress in microfabrication processes, providing a large number of micro-electro-mechanical systems (MEMS). Some of these systems, such as lab-on-a-chip or micro total analysis systems for gas sensing, analyzing and separation, as well as for drug delivery, require an external pumping system to transfer the gas samples inside, outside and through the device. Additionally, radio frequency switches, accelerometers, gyroscopes, atomic clocks, electron beam optic systems, vacuum tubes, and other components that depend on electron or ion optics require a stable vacuum environment for proper operation. Since merely sealing these devices is not sufficient to guarantee long-term operation free of leakages and outgassing, miniaturized vacuum pumping components are needed to maintain proper functionality. Different processes and devices have been developed in the recent years for these MEMS, however, some of them are at the stage of laboratory research while the more established ones have only limited applications. The gas sampling process has been partially solved by applying vacuum encapsulated methods while for MEMS requiring high vacuum (< 0.1 Pa) or continuous pumping, different vacuum pumps based on various principles (membrane, diffusion, rotatory and sorption pumps) have been miniaturized.

The Knudsen pump, which is a device exploiting the thermal transpiration phenomenon, is able to generate a macroscopic gas flow by applying exclusively a tangential temperature gradient along a surface without any moving parts or external pressure gradient. The induced thermal transpiration flow is useful for technological purposes, provided that the flow is through microscale channels, since the phenomenon is intensified as the characteristic length of the

system is decreased. Since the Knudsen pump only requires a temperature gradient for its operation, its architecture is quite simple and it does not require any moving parts, which provides high reliability and avoids any maintenance and generation of particles due to friction. Its advanced compactness and working principle enables the device to be powered by wasted heat from other processes and allows for low power consumption. Furthermore, since the direction of the flow can be reversed by inverting the thermal gradient in the microchannels, the Knudsen pump provides significant benefits for sampling and separation devices. Consequently, the Knudsen pump is considered as a suitable candidate to address many of the issues existing in MEMS requiring any kind of gas pumping devices. Some specific geometrical and operational configurations have been investigated to optimize the efficiency of this thermally driven pump, however, when it comes to the particular point of fabricating a Knudsen pump, the progress in the field is limited mainly due to micro-fabrication difficulties and constraints linked to the control of local thermal gradients, with only a few working prototypes achieved. The classic architecture of the Knudsen pump consists of a series of wide channels (or reservoirs) connected by small pumping microchannels or a porous medium. In order to avoid large temperature gradients, and since the pumping effect generated by a single stage with a moderate temperature gradient is not adequately strong, a multistage system is commonly applied, with a periodic temperature variation in each stage. The thermal transpiration flow produced in the pumping microchannels or the porous medium is much larger than the counter one in the wide channels and therefore, a net pumping effect, which is expected to be increased with the number of stages, is obtained.

This work presents a computational and experimental investigation of the performance characteristics of different multi-stage Knudsen pumps including the quantitative comparison and optimization of various designs plus the fabrication and testing of some preliminary samples to characterize their performance and optimize efficiency and low energy consumption. The computational investigation has been performed with a code developed during the stay in the University of Thessaly (UTH, Volos, Greece) based on kinetic modeling via the infinite capillary theory, taking into account all foreseen manufacturing and operation constraints. The manufacturing of the prototypes has been done in collaboration with the Laboratoire d'Architecture et d'Analyse des Systèmes (LAAS, Toulouse, France) including the partial development of the manufacturing process for multi-layered devices with dry film (DF)

photoresist. Finally, the experimental work has been conducted in the microfluidics laboratory in the Institut Clément Ader (ICA, Toulouse, France).

The computational investigation has been focused on characterizing the performance of two Knudsen pump designs comprising different configurations of each of them to various target applications. The first design consisting on long tapered orthogonal (rectangular) ducts exploiting the diode effect has been investigated through a parametric study with four different configurations combining converging, diverging and uniform cross section ducts in various multi-stage assemblies. Additionally, the diode effect exhibited by the converging-diverging assembly submitted to thermal transpiration flow leads to interesting bi-directional flow and flow blocking capabilities, making the device work more as a gas diode than as a gas pump. Therefore, the critical operating pressure or blocking pressure at which a zero flow is obtained for the converging-diverging assembly is characterized and the potential use of this assembly as thermal driven diode is explored for flow control and gas mixture separation applications. The second Knudsen pump design consists of three different pump configurations targeting different applications based on the arrangement of their circular pumping channels. The first one targets applications such as micro-gas chromatography, where the needed mass flow rate is high while the corresponding pressure difference is small. This goal can be reached by arranging a large number of channels in parallel to increase the overall mass flow rate within just one stage. The second configuration targets applications such as vacuum maintenance in low-power devices where the needed pressure difference is high, while the corresponding mass flow rate is not so relevant. Hence, a large number of stages with just a single pumping channel are used. Finally, the third configuration is less specific and targets applications where both relatively high mass flow rates and pressure differences are needed. By combining the two previous configurations including a large number of pumping parallel channels per stage and a large number of stages, a wide range of applications can be explored.

The proposed manufacturing approach using the lamination of DF photoresist is based on a negative epoxy, which is a low-cost material that can be combined with standard photolithography procedures and multilevel laminating by rolling the DF layers with a specific pressure and temperature. Each new layer can then be stacked on the previous one without damaging the patterns of other layers, which leads to the creation of 3D structures and allows for fabricating multi-stage Knudsen pumps. This technique is characterized by its simplicity,

rapidness, good bonding (no leakage) and low thermal conductivity of involved materials (comparable to glass); but it requires certain standards and detailed procedures to achieve the desired resolution. This manufacturing process can be used for manufacturing the channels along the surface of the device, as well as through its thickness, allowing for complex designs. Following extensive efforts, certain guidelines have been provided to improve the standard procedures at LAAS in order to achieve the expected resolutions in multi-layered processes.

Regarding the experimental work, thermal transpiration flow experiments in a long glass tube have been performed as part of a broader ongoing project between ICA and UTH related to the estimation of the coefficients of the Cercignani-Lampis boundary condition model. Also, thermal transpiration experiments have been carried out on tapered channels fabricated using the investigated manufacturing process. Preliminary experimental results with the tapered channels suggest the existence of the diode effect between the converging and diverging directions of the flow in the tapered channel.

The present computational and modeling work providing design guidelines for two innovative multi-stage Knudsen pumps may pioneer further investigations of thermally driven gas diodes based on tapered channels. Furthermore, the proposed fabrication improvements and guidelines may be useful in the development of versatile, fast and low-cost manufacturing processes for microfluidic devices. In addition, the experimental results of thermal transpiration flows through glass tubes and tapered channels may also support further research in this field. Overall, it is hoped that the present work will prove to be useful to the scientific communities in rarefied gas dynamics, vacuum science and technology and gaseous microfluidics and more specifically in the development of gas pumps, sensors, separators and mixers.

Table of Contents

List of Tables

List of Figures

Nomenclature and acronyms

TPD	Thermomolecular pressure difference
BGK	Bhatnagar-Gross-Krook
CFD	Computational fluid dynamics
MEMS	Micro electro mechanical systems
UDF	User Defined Function
DVM	Discrete Velocity Method
CVD	Chemical Vapor Deposition
RIE	Reactive Ion Etching
DF	Dry Film
f	Velocity distribution function
f^M	Maxwellian distribution
f^0	Reference distribution function
g	Perturbed distribution function
φ, ψ	Reduced distribution function
δ_{Dirac}	Dirac function
n_d	Dimensionless number density
$\boldsymbol{u}$	Dimensionless velocity vector
$\boldsymbol{U}$	Velocity vector (m s^{-1})
$\boldsymbol{\xi}$	Molecular velocity vector (m s^{-1})
$\boldsymbol{\zeta}$	Dimensionless molecular velocity
N	Molecular number density (m^{-3})
τ	Dimensionless temperature
$\boldsymbol{r}$	Position vector (m)
t	Time (s)
σ	Collision cross section (m^2)
Ω	Solid angle of deflected molecules after a collision (rad)
m	Molecular mass (kg)

k_B	Boltzmann constant (J K^{-1})
$\boldsymbol{F}$	External force (N)
$Q(f, f')$	Collision integral
g_r	Relative velocity (m s^{-1})
P_{ij}	Stress tensor (Pa)
p_{ij}	Dimensionless stress tensor
X_P	Dimensionless pressure gradient
X_T	Dimensionless temperature gradient
$\boldsymbol{q}$	Dimensionless heat flux
$\boldsymbol{Q}$	Heat flux (W m^{-2})
H	H function
λ	Mean free path (m)
D_{mol}	Molecular diameter (m)
L_{mol}	Molecular spacing (m)
$\bar{\upsilon}$	Mean thermal velocity (m s^{-1})
ν	Collision frequency (s^{-1})
k_2	Constant from the collision model
μ	Dynamic viscosity (Pa s)
R_g	Gas constant (J kg^{-1} K^{-1})
ω	Viscosity exponent
$\boldsymbol{n}$	Vector normal to the boundary
W_D	Diffuse scattering kernel
W_S	Specular scattering kernel
W_{DS}	Maxwell scattering kernel (diffuse-specular)
$A_S(z)$	Local cross section area (m^2)
α_t	Tangential accommodation coefficient
L_C	Characteristic length of the system (m)

L	Length of the channel (m)
$H(z)$	Variable dimension of the tapered channel (m)
H_m	Mean value of the tapered dimension (m)
$H_{\max}$	Maximum value of the tapered dimension (m)
$H_{\min}$	Minimal value of the tapered dimension (m)
W	Constant dimension of the tapered channel (m)
α	Inclination ratio
T	Temperature (K)
P	Pressure (Pa)
P_{in}	Pressure at the inlet (Pa)
P_{out}	Pressure at the outlet (Pa)
T_C	Temperature at the cold side (K)
T_H	Temperature at the hot side (K)
ΔT	Difference of temperature (K)
ΔP	Pressure difference (Pa)
$\Delta P_{\max}$	Maximal pressure difference (Pa)
$\Delta P_{\max}^{peak}$	Peak of the maximal pressure difference (Pa)
$P*$	Critical pressure or blocking pressure (Pa)
$\dot{m}$	Mass flow rate (kg s^{-1})
$\dot{m}_{\max}$	Maximal mass flow rate (kg s^{-1})
n	Number of parallel pumping channels
d	Diameter of the pumping channels (m)
D	Diameter of the counter-flow channel (m)
R	Radius of a circular channel (m)
$\dot{m}_n$	Mass flow rate from the assembly of parallel pumping channels (kg s^{-1})
ΔP_n	Pressure difference from the assembly of parallel pumping channels (Pa)
υ_0	Most probable molecular velocity (m s^{-1})

δ	Gas rarefaction parameter
G_P	Dimensionless pressure driven flow rate
G_T	Dimensionless temperature driven flow rate
Kn	Knudsen number
N	Number of stages

Introduction

The work presented in this manuscript corresponds to the research carried out during three years as part of the MIGRATE International Training Network (ITN) fully funded by the European Union's Framework Programme for Research and Innovation Horizon 2020 (2014–2020) under the Marie Skłodowska-Curie (grant agreement number. 643095). The initial ambitious plan for this research project was to perform the computational and experimental investigation of the performance characteristics of different multi-stage Knudsen pumps including the quantitative comparison and optimization of various designs plus the fabrication and testing of some prototypes to characterize their performance and optimize efficiency and low energy consumption. However, while the computational investigation has been extensive, various unexpected issues emerged during the collaboration with the Laboratoire d'Architecture et d'Analyse des Systèmes (LAAS, Toulouse, France) for manufacturing the devices. Additionally, due to the limited time frame and the mobility of the project, although most of the difficulties in the manufacturing of the device have been addressed and the experimental workbench has been adapted for the continuation of the experimental work, there has not been enough time to test a prototype.

The first period of the project was spent at the Institut Clément Ader (ICA, Toulouse, France) where a bibliographic review about the thermal transpiration phenomenon and Knudsen pumps prototypes was performed. Also, during this first stay analysis of alternative designs and preliminary numerical assessment of the performance of Knudsen pump designs with a commercial Computational Fluid Dynamics (CFD) code was performed. Additionally, a first contact was established with the manufacturer LAAS and some geometric constraints coming from the manufacturing processes were outlined. Next, during the stay in the University of Thessaly (UTH, Volos, Greece), the main computational investigation was performed with a code developed based on kinetic modeling via the infinite capillary theory, taking into account all foreseen manufacturing and operation constraints. Following, during a secondment at INFICON AG (Balzers, Liechstenstein), a couple of new potential applications of the Knudsen pump for the vacuum industry were identified and experience related to vacuum technology,

sensors and techniques were acquired. Finally, during the last period of the project, again at ICA, both the fabrication of the sample prototypes and thermal transpiration flow experiments have been performed.

Originally the fabrication of the samples was supposed to be completed externally by LAAS before the last staying at ICA, so that once the last period commenced, only the experimental work would be left. However, several unexpected delays and external difficulties were encountered and the fabrication had to be postponed. Further discussion about these issues is detailed on the chapter dedicated to the manufacturing process. In any case, this manufacturing delay meant that the last staying at ICA of 9 months had to be dedicated both to the manufacturing and the experimental work. Consequently, the completion of part of the goals in the scope of the project, namely the fabrication and testing of several prototypes, has not been possible. Nevertheless, since the delay of the manufacturing has allowed for personal participation in the microfabrication processes and the associated training, the discovery and study of unexpected challenges and the further development of the manufacturing process have had substantial importance leading to a significant acquisition of know-how.

The present work has been divided into six chapters mainly associated with the different periods and tasks during the research project.

Chapter 1 introduces the thermal transpiration phenomenon and the working principle behind the Knudsen pump. A historical overview on the discovery of the thermal driven flows as well as the general development of the numerical and experimental efforts in the field has provided. Also, a brief review of the several Knudsen pump designs proposed as well as the prototypes completed and their applications has been performed.

Chapter 2 includes a review of the basic principles of kinetic theory and gas micro-flow modeling as well as the governing kinetic model equations and the associated boundary conditions. Additionally, the numerical methods implemented in the computational investigation carried out Chapter 3 are presented along with the methodology followed to study the pumping performance of the Knudsen pumps proposed.

Chapter 3 consists on the computational investigation of two Knudsen pump designs comprising different configurations of each of them to various target applications. The first design consisting on long tapered orthogonal ducts exploiting the diode effect has been studied following a parametric study with four different configurations combining converging, diverging

and uniform cross section ducts in various multi-stage assemblies. The diode effect in thermal transpiration flows consists on the different performance exhibit by the same geometry under different operating conditions, i.e. the thermal gradient and the operating pressure, allowing for a bi-directional flow and flow blocking capabilities. The critical operating pressure or blocking pressure at which the zero flow is obtained for the converging-diverging assembly has been characterized and the potential use of this assembly as thermal driven diode with control based on the temperature has been explored. The second Knudsen pump design consists of three different pump modules targeting different applications based on the arrangement of circular channels through the thickness of a low thermal conductivity material. The first module targets applications such as micro-gas chromatography, in which the required mass flow rate is high while the corresponding pressure difference is small. The second module targets applications such as vacuum maintenance in low-power devices in which the pressure difference required is high, while the corresponding mass flow rate is not so relevant. Finally, the third module is less specific and targets applications where both relatively high mass flow rates and pressure differences are needed. By combining the two previous modules the pump can be tailored to target specific performances.

Chapter 4 includes the manufacturing effort performed in collaboration with LAAS including an overview of the various issues related to the manufacturing processes that have been considered in the project. Then, a comprehensive description of the manufacturing process explored based on multi-level lamination of dry film photoresist layers is provided, presenting the significant challenges encountered and the improvements implemented in the manufacturing process.

Chapter 5 contains the experimental work carried out in the in the microfluidics laboratory at ICA and the modification of the existing experimental setup for future work. First thermal transpiration experiments on a glass tube were conducted for two gases (helium and nitrogen) with the goal of comparing the results with the Cercignani-Lampis model to extract the accommodation coefficients in collaboration with the University of Thessaly. The experimental test-bench has been adapted and two specific housing devices for the expected sample prototypes from the manufacturing have been completed. Also, some preliminary thermal transpiration tests on tapered channels (converging-diverging) have been performed.

Chapter 6 concludes the dissertation by providing a brief summary of the work performed in this research project as well as outlining the main results obtained. Also, perspectives for future works are suggested in order to further investigate some of the key points explored in this manuscript with several improvements proposed.

Chapter 1

Thermal transpiration flows and its applications

In this chapter the thermal transpiration phenomenon and the Knudsen pump are introduced by reviewing the main works published in the literature, starting by the more fundamental explanation of the physical phenomenon followed by the different pump configurations that have been proposed, the various prototypes fabricated and the potential applications of this technology. For years the thermal transpiration phenomenon has been extensively investigated, however, functional prototypes based on this phenomenon have been only recently achieved. Usually, the Knudsen pumps can be divided in two big groups: Knudsen pumps based on a porous media and Knudsen pumps based on micromachined channels. Since the porous media do not usually require a complex manufacturing process, most of the first prototypes were based on them. However, with the development of microfabrication techniques, micromachined Knudsen pumps with detailed geometry have started to develop.

1.1 Thermal transpiration flow

A thermal transpiration flow is a macroscopic gas flow generated exclusively by applying a tangential temperature gradient along a surface. A theoretical justification of this thermally driven flow generated, also known as thermal creep, has been provided by Sone [1], [2] and it is induced by momentum exchange during collisions between gas molecules and the surface. As shown in Figure 1.1, when there is a temperature gradient along a surface, a molecule from the higher-temperature side has a larger momentum than a molecule from the lower-temperature side. Thus, statistically, the surface gains momentum in the direction from higher to lower temperature due to gas-surface collisions, and the gas gains momentum in the opposite direction, from the lower to the higher temperature side. The intensity of the thermal transpiration phenomenon is typically stronger when the gas is under rarefied conditions, i.e. when the mean free path of the gas molecules is of the same order of magnitude or larger than the characteristic length of the sampling volume. This can usually be achieved by either reducing the characteristic length of the system or by reducing the pressure.

The phenomenon of a rarefied gas macroscopically displaced by a temperature inequality (a temperature gradient) was first described by Reynolds in 1879 [3]. During his experiments, he encountered that by applying a difference of temperature between two regions, which were separated by a porous plate, gas would pass through it (Figure 1.2). The gas, which had no initial difference of pressure and no initial difference on chemical constitution, by "transpirating" through the plate, was able to generate a pressure variation in both reservoirs. The porous plate configuration allowed Reynolds to obtain a high level of rarefaction of the gas even by imposing relatively high working pressure conditions in the two separated regions, due to the small pore size (characteristic length of the order of the mean free path of the gas molecules). The final difference of pressure obtained between two regions by only applying a temperature inequality was largely analyzed by Reynolds for different rarefaction conditions of the gas. Therefore, by both experimental and theoretical observations, Reynolds could enunciate several laws, which were derived as a direct consequence of the kinetic theory of gases [3]:

Law (i): when gas exists at equal pressure on either side of a porous plate across which the temperature varies, the gas will transpire through the plate from the colder to the hotter side, with velocities depending on the absolute temperature and chemical nature of the gas, the relation between the density of the gas and the fineness of the pores, the thinness of the plate and the difference of temperatures on the two sides of the plate.

Law (ii): in order to prevent transpiration through the plate, the pressure on the hotter side must be greater than the pressure on the colder side. This difference of pressure, at which the transpiration is zero, will depend on the same parameters as in law (i) and on the mean pressure of the gas, but not on the thickness of the plate.

Law (iii): the difference of pressure achieved in the case of law (ii), which depends on the rarefaction of the gas, reaches a maximum value somewhere in between the free molecular and hydrodynamic regimes.

Law (iv): in free molecular regime, the equilibrium state relation between pressure and temperature in the two regions is:

$$P_2 / P_1 = (T_2 / T_1)^{1/2} \qquad (0.1)$$

Maxwell, who was working on the physics of the gas-surface interaction, closely followed this investigation and developed a theoretical methodology by applying the kinetic theory of gases [4]. The model that Maxwell developed described the influence of the difference of

temperature on the velocity in the direction of the temperature gradient. From his theoretical approach, Maxwell showed the connection between the pressure variation along a capillary with the developed gas mass flow rate and the temperature gradient, but also that it was dependent on the rarefaction conditions of the gas, the gas-surface interaction and the gas itself.

Later, while Knudsen was performing an extensive research involving gas flows through small orifices, he found out that the results of the experiments were altered when imposing a temperature gradient along the setup. After investigating this particular phenomenon he concluded that it was possible to achieve a difference of pressure between two regions separated by a small orifice or a narrow tube by just imposing a temperature gradient between their extremities [5], [6]. He named this phenomenon thermomolecular pressure difference (TPD), unaware that the thermal transpiration phenomenon had been previously partly described by Reynolds and Maxwell. During his investigation Knudsen proved the validity of the laws already enunciated by Reynolds for the case of narrow tubes. Then, he stated that the expression provided by law (iv) was exclusively valid at the zero-flow final equilibrium stage of the experiment that followed a transitional stage of gas displacement. Additionally, he indicated that at sufficiently high pressures, when the number of mutual collision of molecules cannot be disregarded in comparison with the number of impacts with the wall, a counter flow of gas occurred along the axis of the tube at the final zero-flow stage, inducing the TPD to tend to zero at very high pressures. Furthermore, Knudsen's considerations led as well to the idea that if the temperature difference on the tube was maintained constant, the gas would continuously flow through the tube in the case where the pressures at both ends of it were maintained equal, suggesting the feasibility of a never stopping pump.

Following his experimental and theoretical researches, Knudsen proposed a semi-empirical model to calculate the TPD for hydrogen under any rarefaction condition in which the limiting values at the free molecular regime and the hydrodynamic regime fulfilled his statements. Next, another semi-empirical model was proposed by Weber and Schmidt [7] based on the previous formulation of Maxwell, but although it was meant to be applicable to different gases, Van Itterbeek and De Grande [8] proved that it was only suited for helium. Later, Los and Ferguson [9] extended Weber and Schmidt model from helium to argon and nitrogen and clearly showed the existence of a maximum of the TPD as a function of the gas rarefaction as enunciated by law (iii) of Reynolds. Also, Liang [10] performed additional experimental work and extended the

semi-empirical model of Weber to additional gases by adjusting a fitting parameter depending on the gas, resulting in a simplified formula compared to the original model proposed by Weber. Additionally, Liang proved that the semi-empirical model developed had lost part of its accuracy during the simplification of the kinetic theory models [11]. However, even though Liang provided a simple mathematical prove that the TPD has only one peak function of the gas rarefaction, his attempts to define at what particular rarefaction condition this maximum existed required a correction since his formulation did not include the viscosity of the gas, but depended only on empirical constants. Bennet and Tompkins [12] provided the corrections needed to Liang's semi-empirical formulation and proposed the consideration of potential parasite thermal transpiration effects inside the gauges used in the experimental setups, estimating even more than 10% error depending on the gas. Finally, Takaishi and Sensui improved the semi-empirical model proposed by Liang by extending it to a larger range of temperature differences and gases in addition to an extended range of gas rarefaction conditions [13].

In addition to the first experimental works and definition of semi-empirical models, during the first decade of the space race a vast amount of experimental data was obtained by the rarefied gas dynamics community. Podgurski and Davis [14] provided time reliable data by using the "absolute method" pressure measurements and showed how the pressure ratio developed due to thermal transpiration depended not only on the gas rarefaction, gas properties and the temperature difference, but also on the absolute temperatures. Edmonds and Hobson [15] examined thermal transpiration flows on different geometries using ultrahigh-vacuum techniques and proved that the pressure ratio developed tended to a constant value for the gas in the free molecular regime. Later, Watkins et al. [16] compared their results with the semi-empirical models and found a good qualitative agreement but a rather poor quantitative agreement, suggesting that a further investigation of the models should be realized.

The large amount of experimental data produced during the 1950s and 1960s provided good test cases for the recently developed kinetic models. Sone and Yamamoto [17] studied thermal transpiration and Poiseuille flows through a tube by linearizing the Bhatnagar-Gross-Krook (BGK) model equation and solving it using the small perturbation method. However, since the BGK model does not treat thermal problems accurately, Loyalka [18] propose to adjust the collision frequency. Next, Annis [19] realized that the complete diffuse reflection of the Maxwellian model was not appropriate to predict the thermal transpiration phenomenon at

arbitrary rarefaction conditions. Therefore, he extracted the accommodation coefficient from his experimental results by fitting Maxwell's model, and found good agreement with the results of Loyalka [20], who studied the thermal transpiration phenomenon numerically with arbitrary accommodation coefficients at the surface. Finally, Porodnov et al. [21] stated that it was very difficult to compare numerical and experimental results since the existing numerical solutions were obtained for small perturbations while the temperature difference applied to the systems was much larger. Hence, their experimental approach consisted in applying small temperature differences to a single capillary for a large number of different gases. In their work, they found that the maximum TPD value was in a precise range of the gas rarefaction conditions for all the studied gases, namely in between the transition and the slip flow regimes and they experimentally showed the influenced of the gas-surface interaction on the final pressure ratio developed by thermal transpiration flows.

In the recent years, additional analytical and numerical studies have been performed to develop more accurate solutions of particular geometries for different rarefaction conditions. A complete analytical solution based on the Navier-Stokes equations was derived by Méolans and Graur [22] for thermal transpiration flows in rectangular channels. Also, with the development of computational fluid dynamics (CFD) codes, it is easy to implement the boundary conditions associated to the slip velocity and the temperature jump in the Knudsen layer to take into account the macroscopic effect of local thermodynamic disequilibrium in the slip flow regime, using Navier-Stokes equations [23]. By using the kinetic Shakhov model, Sharipov provided the solution of both pressure driven and temperature driven flows for any gas rarefaction condition through a long tube [24] and a long rectangular channel [25]. Next, the solution of both flows was provided for long tubes of variable radius [26], long rectangular channels with variable cross sections [27] and a long pipe of elliptic cross section [28], triangular and trapezoidal channels [29]. Also, by applying the Direct Simulation Monte Carlo (DSMC) method introduced by Bird [30], thermal transpiration flows have been widely studied [31], [32] providing numerical results consistent with experimental studies. Finally, the thermal transpiration flow of gas mixtures has also been investigated [33], [34], following the growing interest for applications of gas mixers or separators [35].

1.2 Knudsen pump designs

The Knudsen pump, or thermally driven pump, is a motionless gas pump based on the thermal transpiration phenomenon. The first functional pump was developed by Knudsen [5] by connecting a set of capillaries in series in which a small hot point was maintained at higher temperature than the ambient temperature to develop a thermal gradient. The classic architecture of the Knudsen pump (Figure 1.3) consists of a series of wide channels (or reservoirs) connected by small pumping microchannels or by a porous medium, with alternative hot point at temperature T_h and cold points at temperature T_c. In order to avoid large temperature gradients, and since the pumping effect generated by a single stage with a moderate temperature gradient is not adequately strong for technological purposes, a multistage system is commonly applied with a periodic temperature variation in each stage. This choice may, however, depend upon the target application of the device. The thermal transpiration flow produced in the pumping microchannels or the porous medium is much larger than the counter-flow in the wide channels and therefore, a net pumping effect is obtained. In addition to the typical setup consisting of narrow and wide channels of constant cross section, alternative pump designs have been proposed. They include curved channels with constant and varying width [36]–[40], sinusoidal channels [40], channels with ratchet-type walls (saw-tooth patterns) [41], [42], piping elements arrayed in a matrix form [40], as well as tapered channels [43].

The numerical study of the thermal transpiration in curved channels (Figure 1.4.a) proved that an effective pump can be achieved by the larger pumping flow generated in the curved area compared to the counter-flow generated in the straight section of the channel. Then, by connecting a cascade of curved channels in a serpentine-like pattern, a significant compression ratio could be achieved, providing an increasing performance with larger curvatures. However, this design presents some practical difficulties regarding the thermal control of the hot and cold points required to be particularly closed to each other. The analysis of the curved channel with varying cross section (Figure 1.4.b) shows that the performance of the Knudsen pump is enhanced in terms of mass flow rate by the change in the geometry, while also partially solving the difficulties associated with the proximity of the hot and cold points by separating them and locating the channel in between them.

The numerical study of the sinusoidal channels (Figure 1.4.c) in comparison to the classic Knudsen pump design with rectangular straight channels showed that the mass flow rate

performance could be improved with a similar pressure gain, due to reductions in the tortuosity of the flow path and the optimization of the recirculation flows.

The matrix channels layout (Figure 1.4.d) generate the thermal transpiration flow by imposing hot and cold points in the corners of the columns in the central area. This design was found to provide mass flow rates comparable to the one of a classic Knudsen pump design, while the pressure gain was improved in spite of the significant recirculation caused by the open nature of the pump design. Additionally, this design theoretically showed the potential implementation of flow vectoring through the management of the temperature distribution on each element of the pump, but experimental validation is still required.

In the ratchet surfaces channel design (Figure 1.4.e) the thermal transpiration flow is generated not by a temperature gradient along a surface, but by two isothermal cold and hot walls. Consequently, one of the advantages of this particular design is the spatial separation of the typical hot and cold points from the other Kndusen pump designs, providing a relatively easier thermal management. In the numerical study, the pumping performance of the asymmetrical ratchet surfaces was provided along with some basic design guidelines. Additionally, this design could potentially regulate the mass flow rate generated by adjusting the misalignment between the hot and cold surfaces. However, this particular design was found very sensitive to small geometry changes, and since manufacturing of very regular saw-tooth like surfaces can be difficult, experimental confirmation of the viability of this design is still necessary.

Finally, the tapered channel design (Figure 1.4.f) is based on the diode effect provided by the inclination of the walls of the pumping channel, resulting in different pumping performances of the thermal transpiration flow in the converging and diverging directions depending on operating pressure. The numerical study showed that an effective pumping could be achieved and that the pressure gain of the tapered channels increased with the inclination ratio of the tapered walls while the mass flow rate got constrained. Therefore, a combination of converging and diverging channels was suggested for developing a Knudsen pump in which the wide channels, where the counter-flow occurs, could be replaced by converging or diverging channels depending on the diodicity (comparison of performance between the channels), allowing to accommodate more stages in the same area.

1.3 Knudsen pump prototypes and applications

The rapid development of the semiconductor industry has been followed, in the last decades, by huge progress in microfabrication processes, providing a large number of micro-electro-mechanical systems (MEMS). Some of these systems, such as lab-on-a-chip or micro total analysis systems for gas sensing, analyzing and separation, as well as for drug delivery, require an external pumping system to transfer the gas samples inside, outside and through the device. Additionally, radio frequency switches, accelerometers, gyroscopes, atomic clocks, electron beam optic systems, vacuum tubes, and other components that depend on electron or ion optics require a stable vacuum environment for proper operation. Since merely sealing these devices is not sufficient to guarantee long-term operation free of leakages and outgassing, miniaturized vacuum pumping components are needed to maintain proper functionality. Different processes and devices have been developed in the recent years for these MEMS. However, some of them are at the stage of laboratory research while the more established ones have only limited applications. The gas sampling process requires the injection of a gas sample inside the analysis system from the ambient which adds a complexity to these sensing devices that require vacuum environment for operating properly. This issue has been partially solved by applying vacuum encapsulated methods while for MEMS requiring high vacuum (< 0.1 Pa) or continuous pumping, different vacuum pumps based on various principles (membrane, diffusion, rotatory and sorption pumps) have been miniaturized.

Since the Knudsen pump only requires a temperature gradient for its operation, its architecture is quite simple and it does not require any moving parts, which provides high reliability and avoids any maintenance and generation of particles due to friction. Its advanced compactness and working principle enables the device to be powered by wasted heat from other processes and allows for low power consumption. Furthermore, since the direction of the flow can be reversed by inverting the thermal gradient in the microchannels, the Knudsen pump provides significant benefits for sampling and separation devices. Consequently, the Knudsen pump is considered as a suitable candidate to address many of the issues existing in MEMS requiring any kind of gas pumping devices.

Some specific geometrical and operational configurations have been investigated to optimize the efficiency of this thermally driven pump. However, when it comes to the particular point of fabricating a Knudsen pump, the progress in the field is limited mainly due to micro-

fabrication difficulties and constraints linked to the control of local thermal gradients, with only a few working prototypes achieved. There are two different kinds of architectures for manufacturing Knudsen pumps: either by using a porous media or by microfabrication of the channels. Typically, the Knudsen pumps based on a porous media are easier to fabricate and provide a higher mass flow rate but lower pressure gains than the ones provided by Knudsen pumps with micromachined channels. The tiny pore sizes provide the gas rarefaction conditions for thermal transpiration to generate an effective flow when the porous medium is subject to a temperature gradient, being able to work efficiently even at atmospheric pressures. Also, the porosity of the material offers a huge number of pores at each cross section acting as parallel channels, resulting in an elevated mass flow rate. However, since the geometry of the pores is unstructured, the equivalent length in which a temperature difference is applied is not so limited and therefore the pressure gain is reduced. With the development of various manufacturing techniques, Knudsen pumps based on micromachined channels instead of porous media started to be developed. These new pumps have more complex architecture and fabricating processes, but generally, they allow an easier comparison with numerical studies and better controlled performances due to their well-defined structure.

1.3.1 Knudsen pumps based on porous materials

Since the use of porous media does not require any particular microfabricating technique, most of the first prototypes of Knudsen pumps used them. Pham-Van-Diep et al. [44] built a Knudsen multi-stage compressor by stacking successive porous stages. Vargo et al. [45] used nanoporous materials with a low thermal conductivity delivering a Knudsen compressor that could operate in a wide range of rarefaction conditions. Next, the same research group proposed the use of nanoporous aerogels with pore sizes around 20 nm to develop an efficient Knudsen single-stage pump using helium at atmospheric pressure [46], and generating a pressure drop of around 15 kPa with an input power of 1.7 W. More recently, Young [47] reported a 15-stage Knudsen compressor using an aerogel membrane able to generate a pressure drop of around 16 kPa with by heating the device with a a radiant flux of 20.9 mW/cm^2 at atmospheric pressure. Later, mechanically machined aerogel membranes were experimentally investigated by Han and Muntz [48], [49] leading to an increased awareness of the recirculation flows and the counter thermal transpiration flows inside the device that reduce the performance of the Knudsen pump.

Gupta and Gianchandani built a single-stage Knudsen pump based on zeolite using clinoptilolite (Figure 1.5.a), demonstrating the viability of bulk nanoporous ceramics in the manufacturing of Knudsen compressors [50]. Afterwards, the same group developed a high-flow Knudsen pump (Figure 1.5.b) by using a nanoporous cellulose ester polymer membrane [51] and a 9-stage Knudsen pump with a clay-based microporous ceramic for a higher pressure gain [52]. The single-stage high-flow pump consisted on a membrane with a large porosity and a low thermal conductivity (0.2 W/m/K), generating an air flow of around 0.8×10^{-8} kg/s with a temperature variation of 30 K in the membrane delivered by an input power of 1.4 W. On the other hand, the 9-stage pump provided a pressure head up to 12 kPa with a difference of temperature of 55 K making possible the movement of water drops through a capillary at speeds around 1.2 mm/s. Additionally, the pump operated continuously for more than one year without any visible deterioration in its performance.

Finally, the implementation of thermoelectric materials by Pharas and McNamara [53] where the heating and cooling could be reversed, demonstrated the capability to generate bi-directional flows by coupling thermoelectric modules to a nanoporous material.

1.3.2 Knudsen pumps based on microfabricated channels

Initially, a 10-stage Knudsen pump consisting on an assembly of 18 glass tubes with inner diameter of 1.6 mm was constructed and investigated by Sugimoto and Sone [54]. This pump was able to reduce the pressure of a small reservoir of 8×10^{3} cm^3 to a half in 5 minutes when a temperature difference of 150 K was applied. However, the first Knudsen pump using the advancements in microfabrication was reported by McNamara and Gianchandani [55] by manufacturing a single-chip with a six-mask process using glass substrate on a silicon wafer. The Knudsen compressor built was able to operate at atmospheric pressure generating a pressure drop of around 54.7 kPa, with an input power of 80 mW, through a rectangular channel 10 μm wide and 0.1 μm deep. This concept was then extended by Gupta and Gianchandani [56] who fabricated a 48-stage Knudsen pump with integrated Pirani gauges by using a five-mask process on a single wafer (Figure 1.6.a). This pump was able to generate a pressure drop of around 95 kPa with an input power of 1.35 W for air at atmospheric pressure within a footprint of about 1.2 cm^2. The design was then further improved by the same research group [57] that developed a 162-stage Knudsen pump with a two-part architecture (Figure 1.6.b). The first 54 stages with 0.1

μm deep channels were designed for working at high pressures (from atmospheric pressure to about 7 kPa) while the following 108 stages with 1 μm deep channels were designed for further decreasing the pressure (from 7 kPa to 120 Pa) with an increased pumping speed due to the bigger size of the channels. Overall, the pump demonstrated the capability to decrease the pressure of a small chamber from atmospheric pressure to 120 Pa with 0.39 W of input power.

Finally, from the same research group, Qin et al. [58] reported a monolithic high-flow Knudsen pump using a four-mask lithographic process by constructing vertical channels in compact arrays for parallel pumping with Al_2O_3 channels 2 μm in depth (Figure 1.6.c). The highest mass flow rate of air produced by the pump was 4.2×10^{-6} kg/s with an input power of 37 W within a footprint of 3.2 cm^2. Furthermore, the pump was continuously operating for more than one year and a half with a gradual reduction in the performance of around 30% of the initial value. Most of the decline in the performance of the device occurred after the first year of operation and it is attributed to dust accumulation at the inlet where no filter was placed.

1.3.3 Knudsen pumps for vacuum generation

As mentioned before, a vacuum environment is required to avoid viscous damping and achieving high performance and stability in various devices including accelerometers, radio frequency switches, microresonators, and optical MEMS. The level of vacuum required is different for each device but ranges between a few kPa to below 1 Pa. Conventional rotary pumps coupled with turbo molecular pumps can be employed for generating a vacuum environment. However, these actuators have an elevated cost and cannot be implemented in handheld devices. On the other hand, some attempts have been made to develop microsystems keeping a constant inside vacuum level without using any pumping unit. Thus, some packaging solutions have been developed by either hermetically sealing the device with wafer bonding or by thin film encapsulation. Nevertheless, additional difficulties related to the high electrical resistance to outside connections to power the device, outgassing, leakages and high cost of packaging are generated.

A micropump for keeping the vacuum environment can then be a low-cost solution, in addition to be well-suited for miniaturization of the devices. A micropump based on a flexible diaphragm was proposed by Kim et al. [59], but the stress and fatigue during operation might cause the membrane breakage. Hence, the Knudsen pump can be a suitable candidate to address

the aforementioned issues since it is able to generate and maintain vacuum environments without any moving part and with low power consumption. Recently, Van Toan et al. [60] fabricated and tested a 96-stage Knudsen pump for generating vacuum environments by combining deep reactive ion etching, wet thermal oxidation and anodic bonding processes (Figure 1.7). The manufactured channels had a diameter of 0.2 μm and were able to decrease the pressure in a small chamber from atmospheric value to around 10 kPa with an applied temperature difference of only 25 K. This work, in the line of the previous 48-stage and the 162-stage Knudsen pumps, further proves the potential implementation of this technology for generating vacuum environments in MEMS since the device is easily scalable to any number of stages.

1.3.4 Knudsen pumps for power generation devices

Recently, power generation devices employing hydrocarbon fuels rather than electrochemical storage as the energy feedstock have been studied extensively due to the much higher energy densities that can deliver hydrocarbon fuels compared to the best available batteries. While many devices have been proposed, including internal combustion engines, gas turbines, thermoelectric modules and fuel cells, in order to obtain high energy density they typically require the use of air for the combustion reaction. Since air is usually taken and rejected at ambient pressure, actuators are required to pump the air through the device. This is problematic because most of the micropumps are extremely inefficient and may consume most of the electrical power generated. The Knudsen pump, however, can be used to address some of these issues since it can be powered by the wasted heat from the own combustion in the device.

Zeng et al. [61] thereby developed a self-sustained propane combustor by implementing a Knudsen pump based on porous media (Figure 1.8). The combustion reaction results in an increase of temperature allowing the Knudsen pump to transport the exhaust gases while at the same time introducing new fuel and air in the mixing and combustion chamber. Therefore the reaction would continue in a self-sustained manner by keeping a self-sustained temperature difference between the hot and cold sides of the membrane. The power density achieved was 40 mW/cm^2 with a fuel cell area of 0.95 cm^2 with a propane flow rate of 30 mL min^{-1} corresponding to a chemical enthalpy flux of 41.4 W, resulting in an overall efficiency of around 0.1%. This poor performance, far lower than the necessary one to compete with batteries, was attributed to a low temperature difference generated between the hot and cold sides of the membrane. It was

demonstrated, however, that the integration of Knudsen pumps on self-sustained combustors was feasible and it was suggested that a better thermal management of the device could greatly improve the performance.

1.3.5 Knudsen pumps for heat pumps

Air conditioning and refrigeration with heat pumps are among the most common electric applications for domestic and industrial use. Thus, lowering the electricity consumption of the heat pump can be very important for saving energy and reduce the emission of carbon dioxide. To tackle this problem, an adsorption heat pump was proposed, replacing the conventional electric compressor between the evaporator and the condenser by an actuator using adsorption to transfer the vapor. However, the chemical heat pump requires different switching mechanisms to regulate the vapor flow with the adsorption-desorption mechanism for operating properly. Hence, a Knudsen pump could address some of these issues providing a reliable operation with low power consumption without the need for any switches.

Through a series of works, Kugimoto et al. [62]–[64] implemented a Knudsen pump capable to perform the same work as a conventional compressor generating changes in the pressure and temperature in the evaporator and condenser of the heat pump. Then, the Knudsen heat pump comprised a condenser, an evaporator, a Knudsen pump and a capillary tube. The refrigerant vapor was transported from the evaporator to the condenser thanks to the Knudsen pump while the liquid refrigerant was returned from the condenser to the evaporator through the capillary tube. The architecture of the proposed Knudsen pump was based on a porous media with a single-stage. The experiments confirmed an effective heat transport from the evaporator to the condenser generating an output power of 3.09 W. Then, from their previously formulated model [63], it was estimated that a 30-stage Knudsen pump would be able to generate an output power of 1.27 kW and a temperature difference of 6 K, which would be enough to operate as a practical heat pump.

1.3.6 Knudsen pumps for gas chromatography

Several devices such as liquid phase microanalytical systems and vapor sampling elements for gas chromatographs and mass spectrometers require bi-directional flow for a proper operation. Normally, this is achieved by implementing various valves to enable the reversal of

the flow direction. However, the use of an intricate valve system increases the complexity, cost and failure rate of the devices. Since Knudsen pumps are able to reverse the flow direction by just changing the direction of the temperature gradient, they are considered as suitable candidates for devices requiring a bi-directional flow.

Following the investigation of Qin and Gianchandani [65], [66] on a fully microfabricated gas chromatograph, Cheng et al. [67] reported an improved Knudsen pump with bi-directional flow and enhanced thermal management integrating customized heat sinks to work more efficiently. The Knudsen pump structure consisted on a stack of mixed cellulose ester membranes contained between two glass dies with micromachined channels inside. At the same time, this glass dies were in contact with the heaters and thermoresistors. With an of the size of the device around 2.56 cm^2 and an input power of 2 W, the maximum measured mass flow rate was about 1.6×10^{-8} kg/s and the maximum blocking pressure around 880 Pa. It was demonstrated that by connecting the Knudsen pump to a micro gas chromatograph, a mass flow rate about 0.5×10^{-8} kg/s was achieved for separation, whereas for sampling, the performance would be slightly lower with mass flow rates of the order of 0.3×10^{-8} kg/s.

1.3.7 Knudsen pumps for gas separation

The investigation on how to reduce the energy cost of separation of gas mixtures has led to the development of various techniques. One of them, the membrane gas separation technique, has several advantages such as its simplicity, an operation close to ambient conditions, the continuous nature of the process and the absence of phase change requirement. Most of the studies performed on membrane separation are induced by molecular transport mechanisms due to a pressure gradient across the membrane. The species are then generally separated by the difference in the molecular velocities, smaller molecules usually diffusing faster than larger molecules (except in membranes with reversed selectivity). The separation capabilities of this method, however, are restricted by the selectivity of the membrane with high purity gases being difficult to obtain. Nevertheless, when a temperature gradient is applied in addition to the pressure difference, a new driving force on the gas molecules emerges. Therefore, by applying at the same time a pressure gradient and a temperature gradient across the porous membrane, heavier gas molecules could flow due to the pressure gradient while the lighter molecules flow in the other direction due to the thermal transpiration.

A series of works from Nakaye et al. [68], [69] have led to a novel gas separation device based on the superposition of both pressure driven and temperature driven flows (Figure 1.11). The authors first developed a Knudsen pump using a single mixed cellulose ester membrane of 9 cm^2 in which a variation of 15% of the mole fraction of helium in a helium-argon mixture was achieved with a 45 K temperature difference. Later, with a similar setup with an increased area of 27 cm^2, a variation of 6% of the mole fraction of helium for a helium-neon mixture was achieved when applying a temperature difference of 100 K across the membrane. Although the separation of gases was limited, the demonstration of the viability of the Knudsen pump as a tool for gas separation was proved.

1.4 Summary

An introduction to the thermal transpiration phenomenon has been provided along with a review of the main works reported in the subject including both experimental and numerical studies. This phenomenon and its application as a gas pump has been known for more than a century since the first studies of Reynolds [3], Maxwell [3], [4] and Knudsen [5], [6]. However, only in the last 20 years some functional prototypes adapted to real applications have been developed thanks to the development of microfabrication techniques.

The range of applications for thermally driven pumps (Knudsen pumps) is wide. They can be implemented for maintaining a vacuum environment on radio frequency switches, accelerometers, gyroscopes, atomic clocks, electron beam optic systems, vacuum tubes, and other components that depend on electron or ion optics as demonstrated in [56], [57], [60]. Also, they can be used as actuators for gas sampling devices such as gas chromatographs or mass spectrometers as shown in [65]–[67]. Additionally, prototypes for gas separation [68], [69], for developing self-sustained power generation devices [61] and for actuation of heat pumps have also been reported [62], [63], showing promising results.

Finally, alternative Knudsen pump designs based on different geometries such as curved channels of constant and varying cross section [36], [38]–[40], [70], sinusoidal channels [40], matrix channels [40], ratchet surfaces [41], [42] and tapered channels [43], have been numerically assessed, providing a window to further develop this technology and its applications. In particular, in the present work, two different designs of Knudsen pump with several configurations are investigated. The first one is based on a multi-stage cascade pump with

tapered orthogonal ducts while the second one is based on circular cross section channels across the thickness of a substrate, with the spatially separated heating and cooling zones provided by isothermal surfaces in a comparable way to that of the ratchet surfaces.

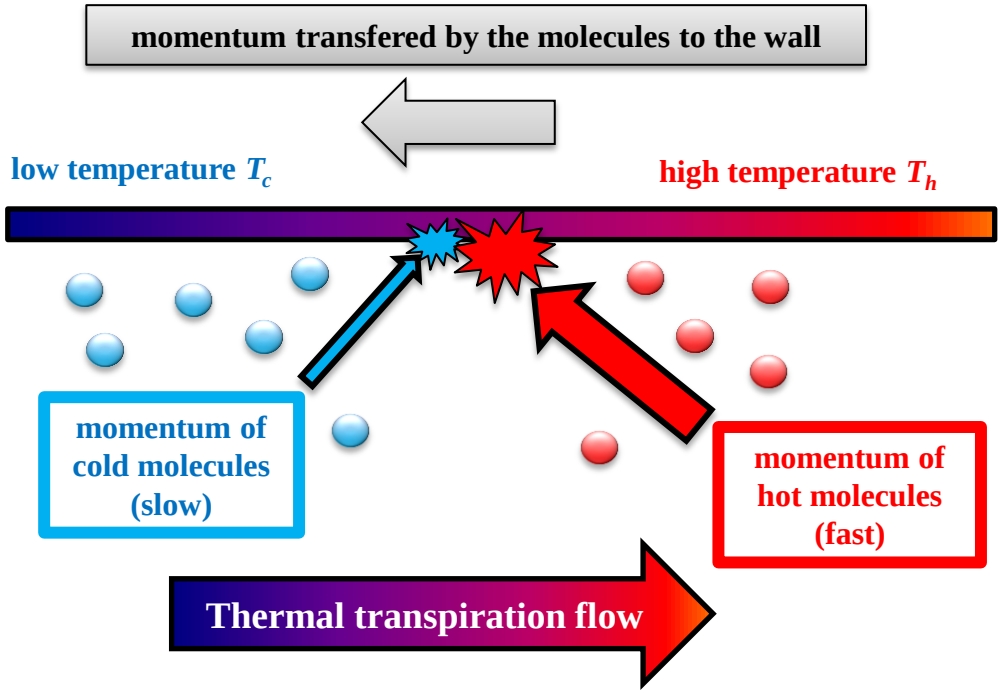

Figure 1.1: Physical mechanism of thermal transpiration.

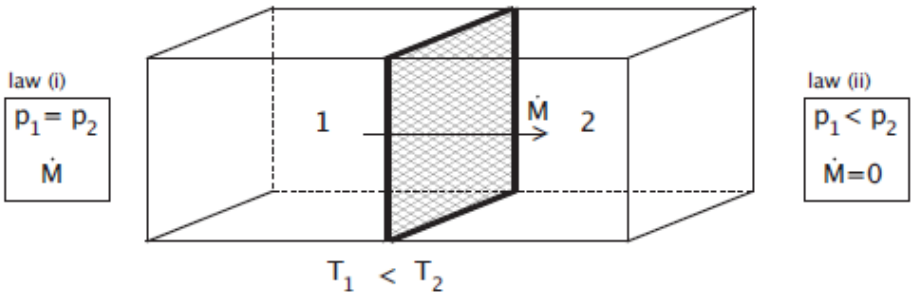

Figure 1.2: Scheme of the work carried out by Reynolds: difference of temperature applied to a porous medium separating two regions.

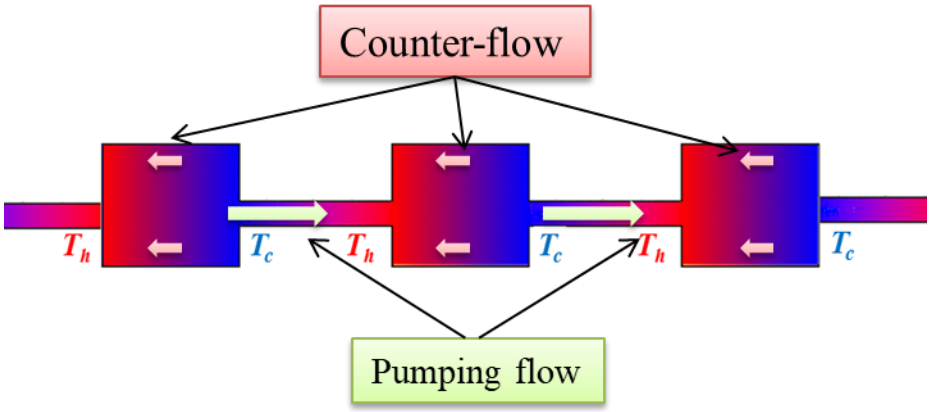

Figure 1.3: Representation of a typical Knudsen pump with straight channels. The small channels provide the pumping flow while the wide channels (reservoirs) generate some counter-flow.

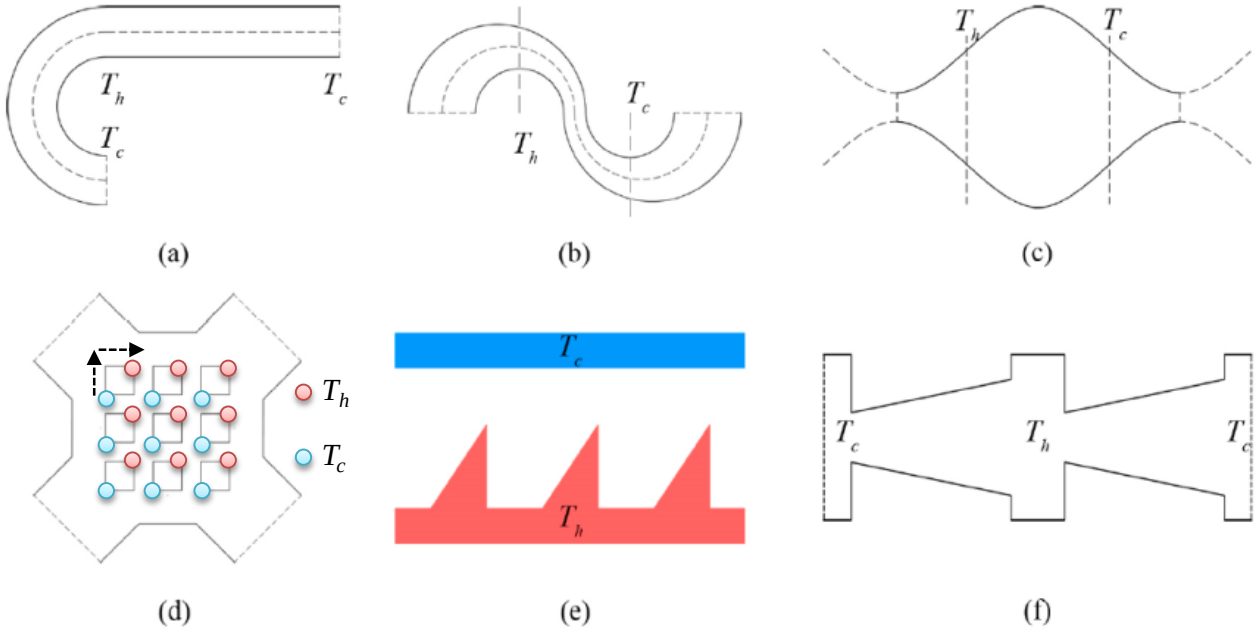

Figure 1.4: Different Knudsen pump structures (a) curved channel, (b) curved channel with different radius, (c) sinusoidal channel, (d) matrix channels, (e) ratchet channel, (f) tapered channel.

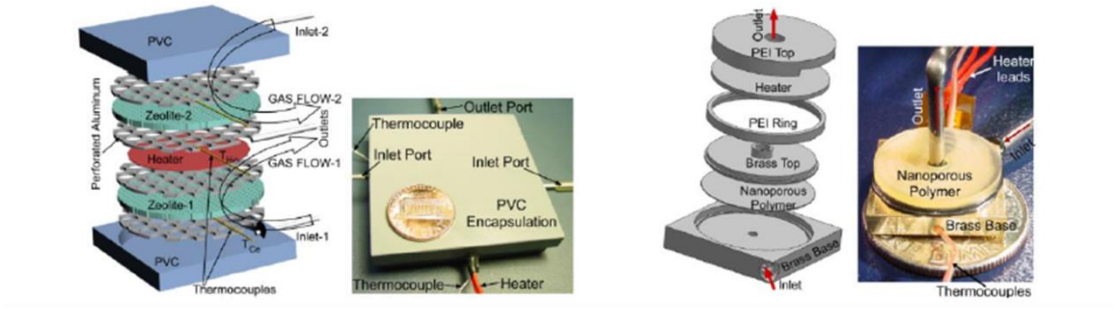

(a) (b)

Figure 1.5: Design and pictures of thermally driven pumps based on porous materials: (a) zeolite-based Knudsen pump [50], (b) nanoporous polymer membrane [52]

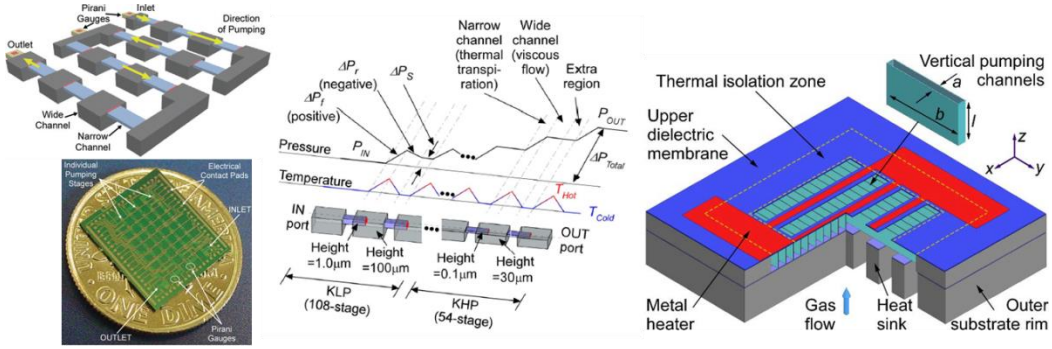

(a) (b) (c)

Figure 1.6: Various microfabricated thermal driven pumps: (a) schematic and picture of a 48-stage Knudsen pump [56]; (b) schematic of a 162-stage Knudsen pump [57] and (c) high flow Knudsen pump [51].

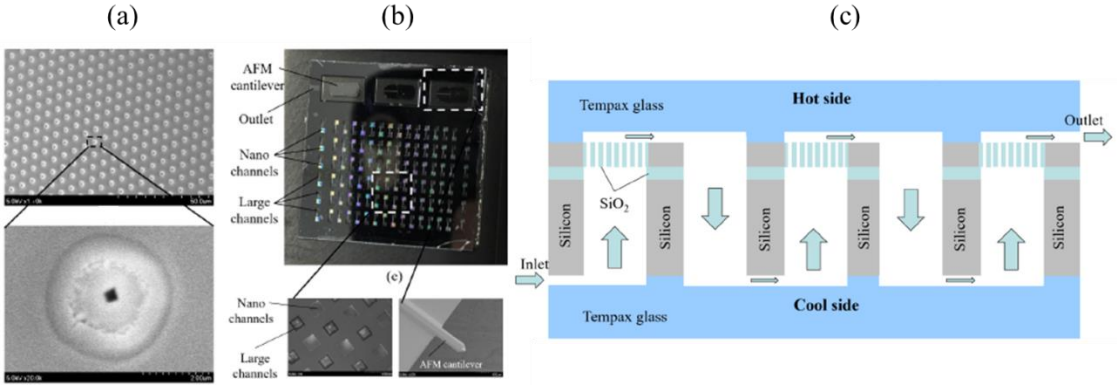

(a) (b) (c)

Figure 1.7: Knudsen pump for generating vacuum environments [60]**: (a) close-up image of the microfabricated channels, (b) picture of the whole assembly and (c) schematic of the architecture.**

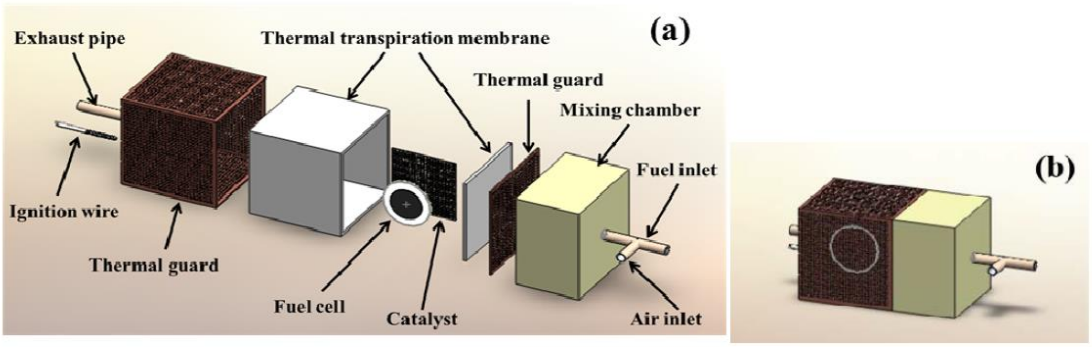

Figure 1.8: Schematic of a Knudsen pump for fuel cell feeding [61]: (a) exploded view and (b) assembled view.

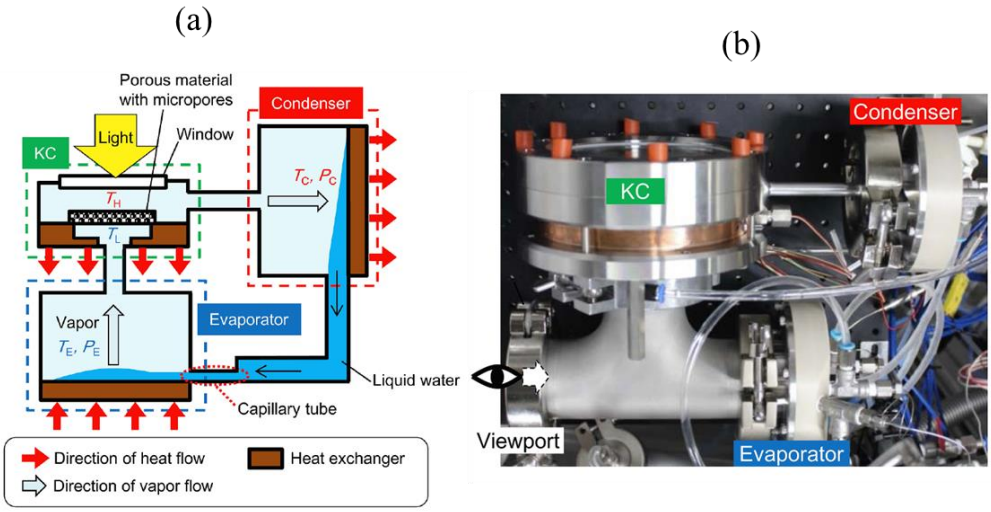

Figure 1.9: Prototype of Knudsen heat pump [64]**: (a) schematic view of the assembly and (b) picture of the experimental setup.**

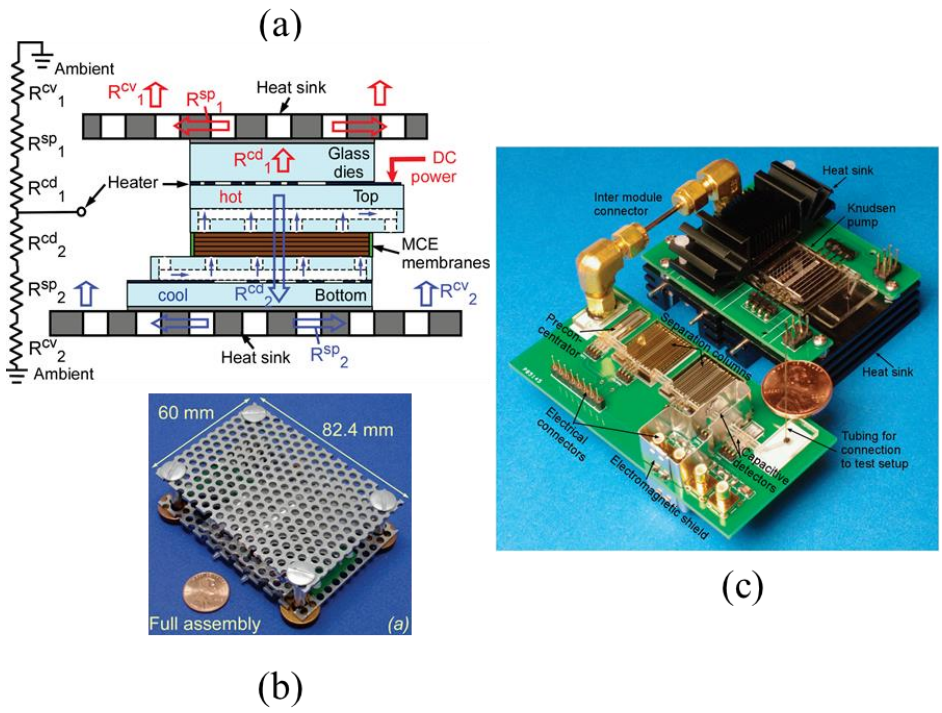

Figure 1.10: Knudsen pump implemented in a microfabricated gas chromatograph: (a) schematic of the Knudsen pump [67]**, (b) picture of the Knudsen pump with the customized heat sink** [67] **and (c) a fully micromachined gas chromatograph** [65]**.**

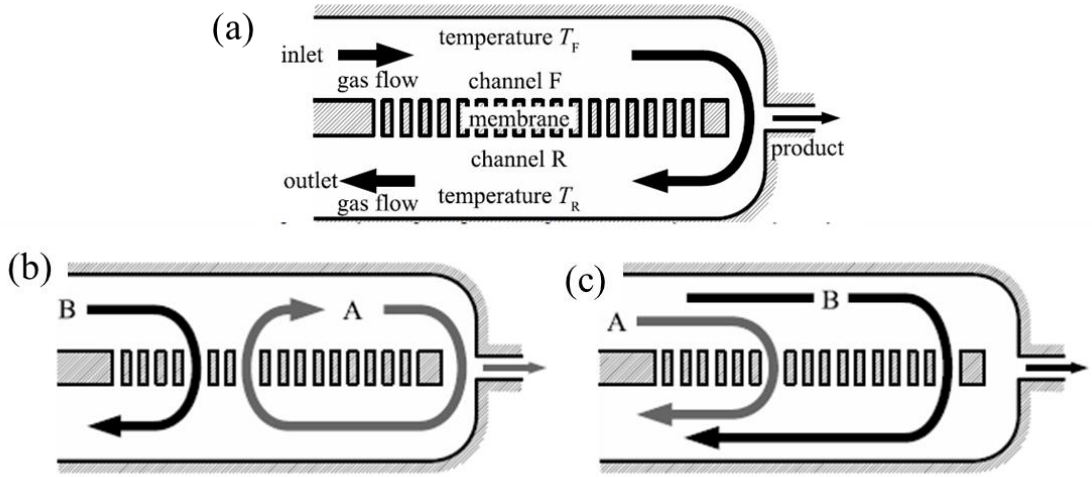

Figure 1.11: Knudsen pump for gas separation applications by combining a pressure and a thermal gradient across a membrane for A-lighter molecule and B-heavier molecule [69]**: (a) schematic of the gas separator, (b) $T_F>T_R$ recirculation due to thermal transpiration flow of the lighter molecule and (c) $T_F<T_R$ no existing recirculation.**

Chapter 2

Basics in kinetic theory and modeling

The numerical investigation of the Knudsen pumps studied in the present work aims to characterize the performance of different designs for a wide range of operating pressures. At the beginning of the project, a commercial CFD code (ANSYS Fluent) coupled with the necessary User-Defined Function (UDF) to take into account the slip velocity and the temperature jump boundary conditions was used. The application of the UDF was extended from 2D to 3D simple geometries; however, this method was only suitable for studying flows in the slip regime, forcing a limited range of pressures and/or geometries. Therefore, the method used for the computational investigation had to be extended to consider more rarefied regimes, so the use of the more fundamental kinetic theory was mandatory. In this chapter an introduction to the kinetic theory and modeling of gas microflows is provided. In particular, the linearized Shakhov model subject purely diffuse boundary conditions combined with the infinite capillary theory is presented, and will be used mainly in Chapter 3 to simulate the thermal transpiration flow of the proposed Knudsen pump designs. The methodology used for characterizing the Knudsen pump designs is introduced by clearly distinguishing three different flow scenarios: open system ($\dot{m} = \dot{m}_{\max}, \Delta P = 0$), closed system ($\dot{m} = 0, \Delta P = \Delta P_{\max}$) and general case in between ($\dot{m} \neq 0, \Delta P \neq 0$).

2.1 Kinetic theory of gases

The earliest notions of the kinetic theory were elaborated by the Greek philosophers Leucippus, Democritus and Epicurus (530 BC – 270 BC) who hypothesized that matter was composed by minuscule indivisible elements called atoms. They also introduced very complex ideas such as that between atoms lied empty space, that atoms are always in motion, and that atoms are of infinite number, size and shapes. Later, the Roman philosopher Lucretius (around 50 BC) tried to popularize this epicurean atomistic idea of macroscopic bodies composed by tiny and rapidly moving atoms bouncing off against each other. All these ancient ideas received very

little attention through history until similar ideas were proposed by the work developed by Bernoulli [71] on the description of fluids. In his work, he explained the pressure inside a vessel by considering it as the sum of forces exerted by the impact of the gas molecules on the walls of the vessel while the temperature is the kinetic energy of the moving molecules. Therefore, he defined for the first time macroscopic properties of a fluid by using a microscopic approach, originating the kinetic theory of gases.

After Bernoulli, other scientists contributed to develop this newly proposed theory. Herapath [72] developed the causes of heat, gravitation and other natural phenomena, Joule [73] calculated the velocity of molecules of hydrogen, Clausius [74] introduced the concept of mean free path of a molecule and Graham [75] experimentally demonstrated the passage of gas through solid graphite. Later, the fundamental formulation of the kinetic theory of gases would be provided by Maxwell and Boltzmann. First [76], Maxwell formulated the first-ever statistical law in physics, the velocity distribution function, describing the proportion of molecules having a certain velocity in a specific range. He also stated several ideas that would be later proven: e.g., the viscosity of a gas is independent of the density and molecules interact through potential forces [76]. He also developed the first conception of a gas-surface interaction model [77]. Afterwards, Boltzmann corrected, generalized and extended the concepts established by Maxwell's work and derived the transport equation for the distribution function [78].

The velocity distribution function $f\left(t,\boldsymbol{r},\boldsymbol{\xi}\right)$ introduced by Maxwell [76], indicates the probability of finding a molecule around the location $\boldsymbol{r}$, with velocity $\boldsymbol{\xi}$ at a particular time t, and it is provided by the following expression:

$$f^{M}\left(t,\boldsymbol{r},\boldsymbol{\xi}\right)=N\left(t,\boldsymbol{r}\right)\left[\frac{m}{2\pi k_{B}T\left(t,\boldsymbol{r}\right)}\right]^{3/2}\exp\left[-\frac{m\left(\boldsymbol{\xi}-\boldsymbol{U}\left(t,\boldsymbol{r}\right)\right)^{2}}{2k_{B}T\left(t,\boldsymbol{r}\right)}\right] \qquad (2.2)$$

where N, T and $\boldsymbol{U}$ are the local density, temperature and velocity vector, m is the molecular mass and k_B is the Boltzmann constant. Then, following Maxwell's work, Boltzmann extracted the evolution equation of the distribution function which can be derived either from the statistical analysis of the molecular motion or from the Liouville equation assuming that the gas is diluted and thus, only subjected to binary collision, that the volume occupied by the molecules is small compared to the studied volume and that the positions of the molecules in phase space are not

correlated (molecular chaos) [78]. This transport equation of the distribution function is commonly known as the Boltzmann equation and may be written as [79]

$$\frac{\partial f}{\partial t} + \boldsymbol{\xi} \cdot \frac{\partial f}{\partial \boldsymbol{x}} + \boldsymbol{F} \cdot \frac{\partial f}{\partial \boldsymbol{\xi}} = Q(f, f') \qquad (2.3)$$

The left hand side of Equation (2.2) describes the evolution of the velocity distribution function with time as the gas molecules move in space according to their molecular velocities and as they are accelerated due to an external force field with acceleration $\boldsymbol{F}$. The intermolecular collisions are considered in the right hand side term, and are provided by the collision integral

$$Q(f, f') = \int\int (f' f_*' - f f_*) g_r \sigma d\Omega d\boldsymbol{\xi}_* \qquad (2.4)$$

where $g_r = |\boldsymbol{\xi} - \boldsymbol{\xi}_*|$ is the relative velocity, σ is the collision cross section and Ω is the solid angle in which a molecule is deflected after the collision [79], [80]. The collision integral calculates the effect of collisions on the distribution of molecules with velocity $\boldsymbol{\xi}$, investigating possible collisions with molecules having all other velocities $\boldsymbol{\xi}_*$. It consists of a gain and a loss terms. The first term in the parenthesis corresponds to the gain part and refers to molecules that, after a collision, obtain a velocity $\boldsymbol{\xi}$. The second term in the parenthesis corresponds to the loss part and refers to molecules that had a velocity $\boldsymbol{\xi}$ and after a collision change their velocity. The collision cross section σ and the differential solid angle $d\Omega$ are provided by a molecular interaction potential or model [79]. Then, it should be noted that when the gas is in equilibrium, the three first terms of the left hand side of Equation (2.2) are neglected resulting in the velocity distribution function formulated by Maxwell. Therefore, the Maxwellian distribution is a particular solution of the Boltzmann equation for a gas in equilibrium.

Since the distribution function contains the information of the location and velocity of the molecules, all macroscopic quantities can be formulated as moments of the distribution function as follows:

- Number density: $N = \int f d\boldsymbol{\xi}$ (2.5)

- Velocity vector: $\boldsymbol{U} = \frac{1}{N} \int \boldsymbol{\xi} f d\boldsymbol{\xi}$ (2.6)

- Pressure: $P = \frac{m}{3}\int (\boldsymbol{\xi} - \boldsymbol{U})^2 \, f d\boldsymbol{\xi}$ (2.7)
- Stress tensor: $P_{ij} = m\int (\xi_i - U_i)(\xi_j - U_j) \, f d\boldsymbol{\xi}$ (2.8)
- Temperature: $T = \frac{m}{3k_B N}\int (\boldsymbol{\xi} - \boldsymbol{U})^2 \, f d\boldsymbol{\xi}$ (2.9)
- Heat flux vector: $\boldsymbol{Q} = \frac{m}{2}\int (\boldsymbol{\xi} - \boldsymbol{U})^2 (\boldsymbol{\xi} - \boldsymbol{U}) \, f d\boldsymbol{\xi}$ (2.10)

Additionally, Boltzmann also identified a fundamental quantity H and enunciated his H-Theorem, stating that the average value of the H function, defined as

$$H = \int f \log f d\boldsymbol{\xi} \qquad (2.11)$$

is a non-increasing function of time [78], [79]. The particular case in which $dH/dt = 0$ corresponds to the Maxwellian distribution with the gas in equilibrium. It is well known that this principle is directly related to the entropy increase and to the second law of thermodynamics. The inequality $dH/dt \leq 0$ shows the tendency of the gas to minimize the H function, that is to obtain the distribution with the highest number of microstates that correspond to the macroscopic state of the system and this distribution is the Maxwellian distribution. This fact shows an inherent irreversibility of macroscopic processes, although the interaction itself between molecules is time-reversible. Therefore, the H-Theorem is equivalent to the second law of thermodynamics, which states that the production of entropy cannot be negative. It is somehow more general, since the quantity H is defined for all systems, whereas the entropy is defined only at equilibrium. The H-Theorem however, has been proven only for dilute gases, whereas the second law applies to any system in equilibrium.

2.2 Collision models on dilute gas

As it has been mentioned before, two of the core premises of kinetic theory is that the gas is dilute and therefore the gas molecules only perform binary collision. The main characteristic lengths are presented in Figure 2.1. A gas can be considered as dilute when the molecular diameter D_{mol} is much smaller than the mean molecular spacing L_{mol}

$$\frac{D_{mol}}{L_{mol}} \ll 1 \qquad (2.12)$$

Additionally, the average distance that a gas molecule travels between successive intermolecular collisions is the mean free path λ and can be represented by the ratio of the mean thermal velocity $\bar{\upsilon}$ over the collision frequency ν

$$\lambda = \frac{\bar{\upsilon}}{\nu} \quad (2.13)$$

Then, under the hypothesis of dilute gas, binary collisions involving only two molecules are much more probable than collisions between multiple molecules at the same time. However, even if only binary elastic intermolecular collisions are considered, the momentum balance and energy conservation equations are not sufficient to yield the post-collision velocities. Consequently, a collision model is required to complete the modeling of molecular behavior and obtain the molecular diameter and collisional cross section to be able to calculate the dynamic viscosity, the collision frequency or the mean free path λ. In particular, the mean free path λ can be rewritten in terms of macroscopic quantities that are measurable and of a coefficient k_2 depending on the collision model:

$$\lambda = k_2 \frac{\mu \upsilon_0}{P} \qquad (2.14)$$

where μ is the dynamic viscosity at temperature T, P is the pressure and $\upsilon_0 = \sqrt{2R_g T}$ is the most probable molecular speed with R_g being the specific gas constant.

The more developed collision models are the hard sphere model, the variable hard sphere model [81] and the variable soft sphere model [82]. The hard sphere model is a simple model in which the collisional cross section is constant during the collision and the scattering probability is isotropic, resulting in a constant coefficient independent of the gas species. Then, the variable hard sphere model considers the molecule as a hard sphere with a collisional cross section variable with the relative velocity between the two colliding molecules, resulting in different coefficients depending on the gas species. Finally, the variable soft sphere model improves the variable hard sphere model by considering both the collisional cross section and the deflection angle dependent on the relative velocity between the colliding molecules. This last model is more complex and although it represents better the physics of the collision and provides more accurate results, it is computationally more expensive.

Therefore, during the present work, the variable hard sphere model has been applied, finding a compromise between accuracy and computational effort. Coefficient k_2 for calculating the mean free path λ and the dynamic viscosity are provided by the following expressions

$$k_2 = \frac{2(7-2\omega)(5-2\omega)}{15\sqrt{2\pi}} \qquad (2.15)$$

$$\mu = \mu_{ref}\left(\frac{T}{T_{ref}}\right)^{\omega} \qquad (2.16)$$

where the values of ω , μ_{ref} and T_{ref} are taken from the data provided by Bird [30] that depend on the gas species.

2.3 General modeling of gas microflows

In the computational investigation of gas flows, the macroscopic description provided by the Navier-Stokes-Fourier equations has proven to be a valid approach for most of the physical phenomena. However, there are a significant number of cases where the classical Newtonian mechanics and the assumptions of a continuous model are no longer valid and the more fundamental approach of the kinetic theory of gases is necessary. For example, the continuum approach requires that the sampling volume from which the local macroscopic properties are obtained from averaging the molecular properties is in thermodynamic equilibrium [30]. However, if the collision rate in the sampling volume is not high enough, this thermodynamic equilibrium cannot be reached. This situation is typically exhibited when the molecular mean free path λ becomes comparable with the characteristic length scale of the flow L_c .

The ratio between the mean free path and the characteristic length of the flow is known as the Knudsen number [5] and it describes the rarefaction conditions of the gas in a system, i.e. how far or close is the gas from reaching the local thermodynamic equilibrium:

$$Kn = \frac{\lambda}{L_c} \qquad (2.17)$$

Then, depending on the value of the Knudsen number, traditionally four different flow regimes can be distinguished as presented in Figure 2.2 [83], [84]:

- In the continuum –or hydrodynamic– regime ($Kn < 10^{-3}$), the gas can be considered as a continuum medium and rarefaction effects can be neglected, allowing the compressible Navier-Stokes-Fourier equations with classic no-slip boundary conditions to accurately model the flow.
- In the slip regime ($10^{-3} < Kn < 10^{-1}$), the intermolecular collision rate starts to decrease compared to the rate of collision between molecules and walls. Consequently, gas rarefaction effects start to manifest close to the solid boundaries and the Navier-Stokes-Fourier equations are still valid, but only if coupled with the appropriate velocity slip and temperature jump boundary conditions, to macroscopically take into account the effects of local thermodynamic disequilibrium.
- In the transition regime ($10^{-1} < Kn < 10$), the intermolecular collisions and the collisions of the molecules with the boundaries are of the same order of importance. Therefore, the effects of rarefaction are significant and the Navier-Stokes-Fourier equations are no longer valid. In this regime, however, some extended continuum models such as the R13 moments methods or the Burnett equation can be used, at least in the early transitional regime. For more rarefied gas flows, the resolution of the Boltzmann equation is required, usually provided by either kinetic modeling or by Direct Simulation Monte Carlo (DSMC) methods.
- In the free molecular regime ($Kn > 10$), molecules move freely between the walls and without experimenting intermolecular collisions and so, the Boltzmann equation is simplified without the collision term. Then, it can be solved by either analytical or numerical methods.

The limits of each flow regime are not rigid, so the values of the Knudsen number provided are just and indicative range. Alternatively, a quantity often used to characterize the rarefaction of a flow is the gas rarefaction parameter δ [85] that is inversely proportional to the Knudsen number and uses the concept of equivalent mean free path, which can be acquired from macroscopic measurable quantities. The gas rarefaction parameter is given by the following expression:

$$\delta = \frac{L_C P}{\mu \upsilon_0} \qquad (2.18)$$

and is related with the Knudsen number in the following way:

$$\delta = \frac{\sqrt{\pi}}{2Kn} \qquad (2.19)$$

Unlike continuum approaches, modeling based on kinetic theory is valid in the whole range of the Knudsen number. However, since kinetic modeling is computationally demanding compared to the continuum approaches, it is mainly used in the transition and free molecular regimes, as well as under non-equilibrium conditions, where the continuum methods fail. As already mentioned, during the beginning of this research project, part of the computational investigation was made using a commercial CFD code (ANSYS-Fluent) coupled with the appropriate velocity slip and temperature jump boundary conditions. However, since the aim of this work is to perform a comprehensive study of Knudsen pumps performances in the whole range of the Knudsen number, kinetic modeling is required to accomplish the proper parametric study of the various Knudsen pump designs proposed in the next chapters.

2.4 Kinetic models

Generally, the calculation of the Boltzmann equation is very challenging due to the five-fold collision integral, limiting considerably the capability to implement kinetic modeling for efficiently solving engineering problems. Therefore, various kinetic models have been proposed in which the complex collision integral is replaced by more simple relaxation models, finding a compromise between the accurate physics of the problem and the computational load to solve it. Typically, to qualify a kinetic model as acceptable, it should at least fulfill the main properties of the Boltzmann equation: it should satisfy the conservation of the collision invariants, fulfill the H-Theorem and provides correct transport coefficients.

One of the first proposed models was the BGK model for monoatomic gases [86], [87], in which the collision integral is replaced by the following expression

$$Q = \nu\left(f^{M} - f\right) \qquad (2.20)$$

where $\nu = P/\mu$ is the collision frequency, expressed as the ratio of the local pressure over the viscosity. It is the simplest kinetic model and it has been widely used due to its unexpected effectiveness. Therefore, the collision frequency is independent of the molecular velocity and the model assumes that after one collision the molecular velocities follow the local Maxwellian

distribution. Overall, the BGK model has provided results in very good agreement with the corresponding ones obtained by the Boltzmann equation in the whole range of δ [85]. However, it cannot provide correct expressions for the thermal conductivity and the viscosity at the same time, resulting in a Prandlt number equal to one for ideal monoatomic gases instead of the expected value of 2/3. Hence, the BGK model should not be used for problems with coupled hydrodynamics and heat transfer phenomena, such as thermal transpiration flows.

The Shakhov model [88], however, is a generalization of the BGK model and has proved to be a reliable approach for dealing with pressure and thermal driven flows. In this kinetic model the collision term is given by

$$Q = \nu\left\{ f^{M}\left[1+\frac{2\left(1-\mathrm{Pr}\right)}{5}\frac{m}{N\left(k_B T\right)^2}\boldsymbol{Q}\cdot\left(\boldsymbol{\xi}-\boldsymbol{U}\right)\left(\frac{m\left(\boldsymbol{\xi}-\boldsymbol{U}\right)^2}{2k_B T}-\frac{5}{2}\right)\right]-f\right\} \qquad (2.20)$$

The Prandlt number is now an input parameter and can be accordingly provided, retrieving the BGK model when $\mathrm{Pr}=1$. However, since the gain term is a polynomial function of the molecular velocities and not a purely exponential function, as in the BGK model, under certain conditions it can provide negative values of the distribution function, which is obviously unphysical. In addition, it has not been formally proven that it satisfies the H-Theorem. In spite of all of this, the Shakhov model has been demonstrated very consistent and accurate, providing physically justified results of the macroscopic quantities. Consequently, the Shakhov model has been applied during the computational investigation of the Knudsen pumps performances in this work, since it requires the solution of the coupled pressure and thermal driven flows generated by the thermal transpiration phenomenon.

2.5 Boundary conditions

The computational solution of the Boltzmann equation and the kinetic models requires the formulation of the associated boundary conditions, which in most cases are part of the solution. The goal of these boundary conditions is to correlate the distribution of molecules $\left(f^{-}\right)$ arriving to the wall with the distribution of molecules $\left(f^{+}\right)$ departing from the wall. Denoting as $\boldsymbol{n}$ the unit normal to the wall surface with direction towards the flow field, a general expression for the boundary conditions can be written as [80]

$$f^{+}(\boldsymbol{\xi}) = -\int_{\boldsymbol{\xi}'\cdot\boldsymbol{n}<0} \frac{\boldsymbol{\xi}'\cdot\boldsymbol{n}}{\boldsymbol{\xi}\cdot\boldsymbol{n}} W(\boldsymbol{\xi}'\to\boldsymbol{\xi})\, f^{-}(\boldsymbol{\xi}')\, d\boldsymbol{\xi}' \quad (2.21)$$

where $W(\boldsymbol{\xi}'\to\boldsymbol{\xi})$ is the scattering kernel, which represents the probability that a molecule arriving at the wall with a velocity $\boldsymbol{\xi}'$ departs from the wall with a velocity $\boldsymbol{\xi}$. The most commonly used boundary conditions are the ones provided by Maxwell, combining diffuse and specular reflections [89], [90]. In the diffuse (D) reflection, the gas molecules are assumed to depart from the wall following a Maxwellian distribution with the boundary temperature T_{BC} and velocity U_{BC} resulting in the following expression:

$$W_D(\boldsymbol{\xi}'\to\boldsymbol{\xi}) = \frac{1}{2\pi}\boldsymbol{\xi}\cdot\boldsymbol{n}\left(\frac{m}{k_B T_{BC}}\right)^2 \exp\left[-\frac{m(\boldsymbol{\xi}-\boldsymbol{U}_{BC})^2}{2k_B T_{BC}}\right] \quad (2.22)$$

Conversely, in the specular (S) reflection, only the velocity component normal to the boundary is changed during a collision, changing its sign while keeping its magnitude. Therefore, the specular scattering kernel is given by

$$W_S(\boldsymbol{\xi}'\to\boldsymbol{\xi}) = \delta_{Dirac}\left[\boldsymbol{\xi}'-\boldsymbol{\xi}+2(\boldsymbol{\xi}\cdot\boldsymbol{n})\boldsymbol{n}\right] \quad (2.23)$$

where δ_{Dirac} is the Dirac function. Then, combining the diffuse and specular scattering kernels the Maxwell (Figure 2.3) scattering kernel

$$W_{DS}(\boldsymbol{\xi}'\to\boldsymbol{\xi}) = \alpha_t W_D(\boldsymbol{\xi}'\to\boldsymbol{\xi}) + (1-\alpha_t) W_S(\boldsymbol{\xi}'\to\boldsymbol{\xi}) \quad (2.24)$$

is obtained, where α_t is the tangential momentum accommodation coefficient and represents the proportion of molecules undergoing diffuse reflection while $(1-\alpha_t)$ is the proportion of molecules experiencing specular reflection.

Since the Maxwell scattering kernel is independent of the magnitude and direction of the molecular velocity, other more complex scattering kernels have been proposed to better represent the interaction of the molecules with the wall. For instance, the Cercignani-Lampis scattering kernel [91] takes into account two accommodation coefficients, one for the tangential momentum and another one associated to the kinetic energy of the normal component of the molecular velocity. The Meolans-Dadzie scattering kernel [92] considers the anisotropic effects of the gas-wall interaction in three different momentum accommodation coefficients. Although the Maxwell diffuse-specular boundary condition is rather simple and does not contain as much

information of the interaction with the boundary as the posterior scattering kernels developed, it has been extensively used due to its reduced computational effort and the overall accuracy of the results obtained. Consequently, in the present work the Maxwell scattering kernel has been implemented in the solution of the kinetic model.

2.6 Linearization of kinetic models

Linear kinetic theory can be applied in the cases where the driving force is relatively small. For example in the case of a flow driven by a moving wall or due to a temperature difference, this small parameter can be the ratio of the wall velocity over the most probable molecular velocity $\varepsilon = U_W / \upsilon_0$ or the ratio of the small temperature difference over the characteristic temperature $\varepsilon = \Delta T / T_0$, respectively. Also, the dimensionless molecular velocity is defined as $\boldsymbol{\zeta} = \boldsymbol{\xi} / \upsilon_0$ .The formulation of the kinetic equations is independent of the driving force and the small parameter ε , which is only used in the dimensionalization process.

An expansion of the distribution function f around a reference value f^0 using $f = f^0(1+\varepsilon g)$ is performed. Introducing this expansion the kinetic equation for the perturbed distribution function g is obtained and it may be written as [25], [85], [93], [94]

$$\zeta_x \frac{\partial g}{\partial x} + \zeta_y \frac{\partial g}{\partial y} = \delta\left[g^{eq} - g \right] \quad (2.25)$$

where the equilibrium distributions for the BGK and Shakhov models are as follows:

BGK:

$$g^{eq} = \rho + 2\boldsymbol{\zeta} \cdot \boldsymbol{u} + \tau\left(\boldsymbol{\zeta}^2 - \frac{3}{2} \right) \quad (2.26)$$

Shakhov:

$$g^{eq} = \rho + 2\boldsymbol{\zeta} \cdot \boldsymbol{u} + \tau\left(\boldsymbol{\zeta}^2 - \frac{3}{2} \right) + \frac{4}{15}\boldsymbol{\zeta} \cdot \boldsymbol{q}\left(\boldsymbol{\zeta}^2 - \frac{5}{2} \right) \quad (2.27)$$

Upon applying the projection procedure, Equation2.25 results to the following system of equations:

$$\zeta_x \frac{\partial \varphi}{\partial x} + \zeta_y \frac{\partial \varphi}{\partial y} = \delta\left[\varphi^{eq} - \varphi \right] \quad (2.28)$$

$$\zeta_x \frac{\partial \psi}{\partial x} + \zeta_y \frac{\partial \psi}{\partial y} = \delta\left[\psi^{eq} - \psi\right] \qquad (2.29)$$

The equilibrium distributions for the BGK and Shakhov models are:

BGK:

$$\varphi^{eq} = n_d + 2\boldsymbol{\zeta}\cdot\boldsymbol{u} + \tau\left(\boldsymbol{\zeta}^2 - 1\right), \psi^{eq} = \frac{\tau}{2} \quad (2.30)$$

Shakhov:

$$\varphi^{eq} = n_d + 2\boldsymbol{\zeta}\cdot\boldsymbol{u} + \tau\left(\boldsymbol{\zeta}^2 - 1\right) + \frac{4}{15}\boldsymbol{\zeta}\cdot\boldsymbol{q}\left(\boldsymbol{\zeta}^2 - 2\right), \psi^{eq} = \frac{\tau}{2} + \frac{2}{15}\boldsymbol{\zeta}\cdot\boldsymbol{q} \qquad (2.31)$$

The reduced distribution functions are defined as

$$\varphi = \frac{1}{\sqrt{\pi}} \int_{-\infty}^{+\infty} g e^{-\zeta^2} d\boldsymbol{\zeta} \qquad (2.32)$$

$$\psi = \frac{1}{\sqrt{\pi}} \int_{-\infty}^{+\infty} \left(\boldsymbol{\zeta}^2 - \frac{1}{2}\right) g e^{-\zeta^2} d\boldsymbol{\zeta} \quad (2.33)$$

The macroscopic quantities in terms of the reduced distribution functions are given by the following expressions:

Number density:

$$n_d = \frac{N - N_0}{\varepsilon N_0} = \frac{1}{\pi} \int \varphi e^{-\zeta^2} d\boldsymbol{\zeta} \qquad (2.34)$$

Velocity vector:

$$\boldsymbol{u}_i = \frac{U_i}{\varepsilon \upsilon_0} = \frac{1}{\pi} \int \boldsymbol{\zeta}_i \varphi e^{-\zeta^2} d\boldsymbol{\zeta} \qquad (2.35)$$

Temperature:

$$\tau = \frac{T - T_0}{\varepsilon T_0} = \frac{2}{3\pi} \int \left[\left(\boldsymbol{\zeta}^2 - 1\right)\varphi + \psi\right] e^{-\zeta^2} d\boldsymbol{\zeta} \qquad (2.36)$$

Stress tensor:

$$p_{i,j} = \frac{P_{i,j}}{2\varepsilon P_0} = \frac{1}{\pi} \int \boldsymbol{\zeta}_i \boldsymbol{\zeta}_j \varphi e^{-\zeta^2} d\boldsymbol{\zeta}, i \neq j \quad (2.37)$$

Heat flux vector:

$$q_i = \frac{Q_i}{\varepsilon P_0 \upsilon_0} = \frac{1}{\pi} \int \boldsymbol{\zeta}_i \left[\left(\boldsymbol{\zeta}^2 - 2\right)\varphi - \psi\right] e^{-\zeta^2} d\boldsymbol{\zeta} \qquad (2.38)$$

Pressure perturbation:

$$p = \frac{P - P_0}{\varepsilon P_0} = n_d + \tau \qquad (2.39)$$

Then the diffuse-specular boundary conditions are formulated as follows

$$\varphi^+ = (1-\alpha_t)\left[\varphi^-\left(\boldsymbol{\zeta} - 2\left(\boldsymbol{n}\cdot\boldsymbol{\zeta}\right)\cdot\boldsymbol{n}\right)\right] + \alpha_t\left[n_{BC} + 2\boldsymbol{\zeta}\cdot\boldsymbol{u}_{BC} + \tau_{BC}\left(\boldsymbol{\zeta}^2 - 1\right)\right] \qquad (2.40)$$

$$\psi^+ = (1-\alpha_t)\left[\psi^-\left(\boldsymbol{\zeta} - 2\left(\boldsymbol{n}\cdot\boldsymbol{\zeta}\right)\cdot\boldsymbol{n}\right)\right] + \alpha_t\left(\tau_{BC}/2\right) \qquad (2.41)$$

With $u_{BC} = U_{BC}/\left(\varepsilon\upsilon_0\right)$, $\tau_{BC} = \left(T_{BC} - T_0\right)/\left(\varepsilon T_0\right)$ and n_{BC} being the quantity used to satisfy the impermeability condition

$$n_{BC} = -\frac{\int_{\boldsymbol{n}\cdot\boldsymbol{\zeta}<0}(\boldsymbol{n}\cdot\boldsymbol{\zeta})\varphi^- e^{-\zeta^2}d\boldsymbol{\zeta} + \alpha_t\int_{\boldsymbol{n}\cdot\boldsymbol{\zeta}>0}(\boldsymbol{n}\cdot\boldsymbol{\zeta})\left[2\boldsymbol{\zeta}\cdot\boldsymbol{u}_{BC} + \tau_{BC}\left(\zeta^2-1\right)\right]e^{-\zeta^2}d\boldsymbol{\zeta} + (1-\alpha_t)\int_{\boldsymbol{n}\cdot\boldsymbol{\zeta}>0}(\boldsymbol{n}\cdot\boldsymbol{\zeta})\left[\varphi^-\left(\boldsymbol{\zeta} - 2(\boldsymbol{n}\cdot\boldsymbol{\zeta})\cdot\boldsymbol{n}\right)\right]e^{-\zeta^2}d\boldsymbol{\zeta}}{\alpha_t\int_{\boldsymbol{n}\cdot\boldsymbol{\zeta}>0}(\boldsymbol{n}\cdot\boldsymbol{\zeta})e^{-\zeta^2}d\boldsymbol{\zeta}} \qquad (2.42)$$

The accommodation coefficient $\alpha_t \in [0,1]$ denotes the percentage of particles undergoing purely diffuse emission, with $\alpha_t = 0$ representing a purely specular boundary condition while $\alpha_t = 1$ characterizes a purely diffuse boundary condition.

2.7 Numerical methods

To solve the Boltzmann equation and the kinetic models, several numerical methods have been developed through the years. The Discrete Velocity Method (DVM) is one of the most reliable and commonly employed deterministic methodologies for solving the kinetic equations, and it has been implemented in the computational investigation of the present work [95].

According to this method, the continuous molecular velocity space is discretized and a set of discrete molecular velocities is generated. Then, the macroscopic quantities calculated from the moments of the distribution function are computed by numerical integration of the distribution function at the set of discrete velocity points considered. By applying the DVM, the kinetic integro-differential equations are reduced to a system with one differential equation for each of the discrete molecular velocities generated. These ordinary differential equations can be calculated using finite element or finite volume approaches, leading to a linear algebraic system, which can be solved using conventional methods.

Additionally, to further reduce the computational time, the infinite capillary theory can be applied to fully developed flows when channels are sufficiently long [85]. This approach can be

implemented when the length of the channels is much larger than its hydraulic diameter, so that the inlet and outlet effects of the flow can be neglected. Then, a fully developed flow can be considered in which the pressure at each given cross section is constant and the velocity profile only changes in the radial direction.

The kinetic coefficients have been calculated using the linear Shakhov model subject to pure diffuse boundary conditions, for a broad range of gas rarefaction conditions and for the different geometries studied in this work, namely rectangular cross sections with variable aspect ratio and constant circular cross sections.

2.8 Fully developed linear Shakhov model

Applying the infinite capillary theory to the linearized Shakhov kinetic model equation when a flow is fully developed in the z-direction results to the following expressions [26], [28], [85]:

- Pressure driven flow:

$$\zeta_x \frac{\partial \varphi_P}{\partial x} + \zeta_y \frac{\partial \varphi_P}{\partial y} = \delta\left[u_{z,P} + \frac{2}{15} q_{z,P}\left(\zeta^2 - 1\right) - \varphi_P \right] - \frac{1}{2} \qquad (2.43)$$

$$\zeta_x \frac{\partial \psi_P}{\partial x} + \zeta_y \frac{\partial \psi_P}{\partial y} = \delta\left[\frac{3}{2} u_{z,P} + \frac{1}{5} q_{z,P}\zeta^2 - \psi_P \right] - \frac{3}{4} \qquad (2.44)$$

- Temperature driven flow:

$$\zeta_x \frac{\partial \varphi_T}{\partial x} + \zeta_y \frac{\partial \varphi_T}{\partial y} = \delta\left[u_{z,T} + \frac{2}{15} q_{z,T}\left(\zeta^2 - 1\right) - \varphi_T \right] - \frac{1}{2}\left(\zeta^2 - 1\right) \qquad (2.45)$$

$$\zeta_x \frac{\partial \psi_T}{\partial x} + \zeta_y \frac{\partial \psi_T}{\partial y} = \delta\left[\frac{3}{2} u_{z,T} + \frac{1}{5} q_{z,T}\zeta^2 - \psi_T \right] - \frac{3}{4}\zeta^2 \qquad (2.46)$$

with the velocity and the heat flux given by

$$u_{z,P} = \frac{U_{z,P}}{X_P \upsilon_0} = \int \varphi_P e^{-\zeta^2} d\zeta ; u_{z,T} = \frac{U_{z,T}}{X_T \upsilon_0} = \int \varphi_T e^{-\zeta^2} d\zeta \qquad (2.47)$$

$$q_{z,P} = \frac{Q_{z,P}}{X_P \upsilon_0 P_0} = \int \left[\left(\zeta^2 - \frac{5}{2} \right) \varphi_P + \psi_P \right] e^{-\zeta^2} d\zeta ; q_{z,T} = \frac{Q_{z,T}}{X_T \upsilon_0 P_0} = \int \left[\left(\zeta^2 - \frac{5}{2} \right) \varphi_T + \psi_T \right] e^{-\zeta^2} d\zeta \qquad (2.48)$$

where U_z and Q_z are the dimensional velocity and heat flux, respectively, and the dimensionless gradients X_P and X_T are defined as $X_P = \frac{L_C}{P_0}\frac{dP}{dz}$ and $X_T = \frac{L_C}{T_0}\frac{dT}{dz}$. Finally the dimensionless flow rates, also known as kinetic coefficients, can be calculated as

$$G_P = -2\int_{-1/2}^{1/2} u_{z,P}\,dz \qquad (2.49)$$

$$G_T = 2\int_{-1/2}^{1/2} u_{z,T}\,dz \qquad (2.50)$$

2.9 Modeling of thermal transpiration flow in Knudsen pumps

In general, an imposed thermal gradient along the walls of a channel of length L connecting two reservoirs at temperatures T_C and T_H, with $T_C < T_H$, results in a thermal driven flow from the cold reservoir towards the hot reservoir. Then, if the system remains open with equal pressures at the inlet and the outlet of the channel ($P_{in} = P_{out}$), a constant mass flow rate $\dot{m}$ due to the thermal transpiration flow will develop. On the other hand, if the system is closed, the thermal transpiration flow along the walls of the channel will increase the pressure in the hot reservoir resulting on a pressure driven flow in the opposite direction (from the hot reservoir to the cold reservoir), until the net mass flow rate in the channel is zero and a constant pressure difference between the inlet and outlet of the channel $\Delta P = P_{out} - P_{in}$ is reached. These two cases, open system and closed system, can be considered as the two limiting flow scenarios. In the open system, the mass flow rate is maximal ($\dot{m} = \dot{m}_{\max}$) when the pressures in the inlet and the outlet are equal ($\Delta P = 0$). In the closed system, the maximal pressure difference ($\Delta P = \Delta P_{\max}$) or TPD studied by Knudsen is achieved when the thermal driven flow and the associated opposite pressure driven flow are equal and the net mass flow rate in the channel is zero ($\dot{m} = 0$). In between these two limiting cases, a general flow configuration characterizing the working regime of the Knudsen pump can be considered, where both the mass flow rate and the pressure difference generated are different from zero ($\Delta P \neq 0, \dot{m} \neq 0$).

The fully developed rarefied gas flow in a channel driven by pressure and temperature gradients has been significantly studied based on linearized kinetic model equations [85]. Due to

linearity, the pressure and temperature driven flows can be solved separately to deduce the corresponding kinetic coefficients in terms of gas rarefaction parameter and cross section geometry. Then, the solution of the combined thermal transpiration flow with the associated pressure driven one may be obtained by linear superposition of the two flows. Accordingly, based on the mass conservation principle, the net mass flow rate may be obtained by combining the dimensionless flow rates providing that the channel geometry and the inlet and outlet conditions are known [25], [27]–[29], [43], [85], [94] as shown in Figure 2.4. It results to the following ordinary differential equation in circular channels

$$\frac{dP}{dz} = -\frac{\upsilon(z)}{A_S(z)L_C(z)G_P(\delta,z)}\dot{m} + \frac{G_T(\delta,z)}{G_P(\delta,z)}\frac{P(z)}{T(z)}\frac{dT}{dz} \quad (2.51)$$

where, $z \in [0, L]$, $\upsilon(z) = \sqrt{2R_g T(z)}$, is the most probable velocity along the channel length, $P(z)$ and $T(z)$ are the pressure and temperature distributions along the channel, while dP/dz and dT/dz denote the corresponding local gradients. Also, $A_S(z)$ is the local cross section area and $L_C(z)$ is the local characteristic length of the system. Finally, $G_P(\delta,z)$ and $G_T(\delta,z)$ are the kinetic coefficients, also known as the dimensionless flow rates [28], [34], [85], [96], for the pressure and temperature driven flows, depending on the local gas rarefaction parameter

$$\delta(z) = \frac{P(z)L_C(z)}{\mu(z)\upsilon(z)} \quad (2.52)$$

and the local geometry of the channel, with $\mu(z)$ denoting the local dynamic viscosity and $L_C(z)$ the local characteristic length of the system.

Equation (2.51) is valid at any cross section $z \in [0, L]$ and the mass flow rate $\dot{m}$ is constant. Once the geometry and the temperature distribution are defined, Equation (2.51) can be solved providing two out of the three quantities, namely the pressure at the inlet $P(0) = P_{in}$, the pressure at the outlet $P(L) = P_{out}$ or the mass flow rate $\dot{m}$. Therefore, when simulating an open system, the pressures at the inlet and the outlet are known and equal ($P_{in} = P_{out}$) and the mass flow rate $\dot{m}$ can be calculated using a shooting approach. Following this method, an initial value for the mass flow rate is specified and then Equation (2.51) is integrated with the initial condition $P(0) = P_{in}$

along the length of the channel $z \in [0, L]$, using Euler's method or a higher order integration scheme. For each node and at each integration step, the values of G_P and G_T are accordingly updated with the local values of all the variables at each cross section. Then, the computed pressure $P(L)$ at the end of the channel is compared to the known value P_{out} and the mass flow rate is accordingly adjusted depending on the difference between the computed $P(L)$ and the specified P_{out}. After that, Equation (2.51) is solved again using the adjusted mass flow rate and repeating this procedure upon convergence of the computed pressure at the end of the channel and the specified outlet pressure ($P(L) = P_{out}$). Conversely, when the mass flow rate $\dot{m}$ with either P_{in} or P_{out} are provided, Equation (2.51) is trivially integrated to find the pressure distribution $P(z)$, including the unknown pressure from either the inlet or the outlet of the channel. This situation refers then to either the closed system, when the mass flow rate is zero ($\dot{m} = 0$) and the maximum difference of pressure $\Delta P_{\max}$ can be calculated for a specified pressure at the inlet P_{in}, or the general case where both the mass flow rate and the generated pressure difference are different from zero ($\Delta P \neq 0, \dot{m} \neq 0$).

The representative metric performances for pumps are typically the net mass flow rate $\dot{m}$, and the pressure head ΔP (the pressure difference generated between the inlet and the outlet of the pump). Combining these two, the characteristic performance curves of the pump are provided, in which the different possible working regimes can be calculated. Consequently, with the three different flow scenarios described and summarized in Figure 2.5, the computational investigation in the present work aims to fully characterize different Knudsen pump designs. Flow scenario A (open system) will provide the maximal mass flow rate calculated as a function of the specified operating inlet pressure $\dot{m}_{\max}(P_{in})$, while flow scenario B (closed system) will provide the maximal pressure difference $\Delta P_{\max}(P_{in})$. Then, flow scenario C (general case) will provide the mass flow rate $\dot{m}$ in terms of the pressure difference ΔP (characteristic curves) for specific operating pressures.

2.10 Summary

An introduction to the kinetic theory of gases and modeling of gas microflows along with the description of the methods used in the computational investigation performed in the present work have been provided. A kinetic code based on the linear Shakhov model subject to pure diffuse boundary conditions combined with the infinite capillary theory has been developed. Also, the methodology to be used to perform a parametric study of the different Knudsen pump designs has been introduced, distinguishing three different flow configurations and allowing for a full characterization of the pump. The two limiting cases open system ($\dot{m} = \dot{m}_{\max}, \Delta P = 0$) and closed system ($\dot{m} = 0, \Delta P = \Delta P_{\max}$) yield the maximum mass flow rate and the maximum pressure difference generated respectively, while the general flow case ($\dot{m} \neq 0, \Delta P \neq 0$) provides the characteristic curves ΔP vs $\dot{m}$ of the pump.

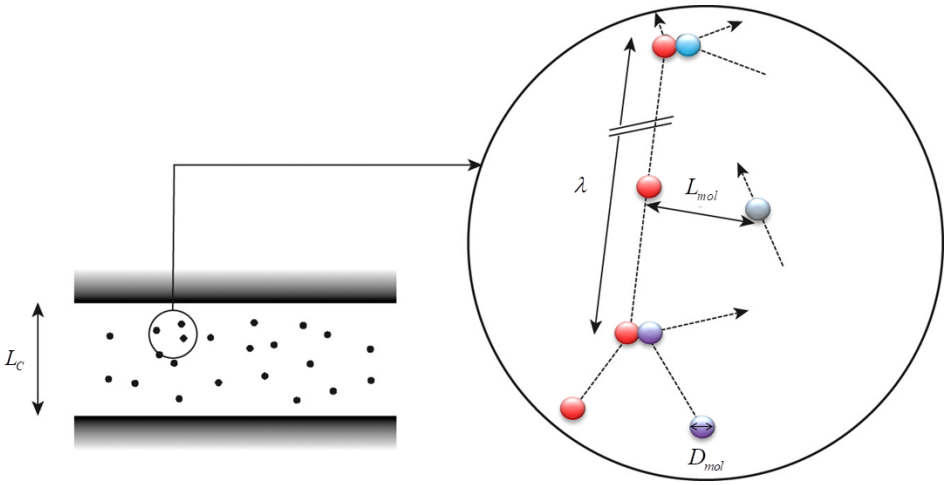

Figure 2.1: Main characteristic lengths taken into account at the molecular level [83]

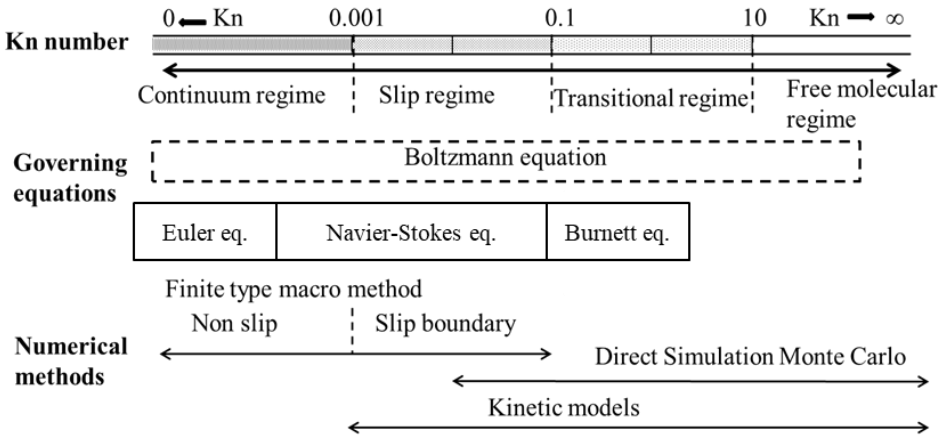

Figure 2.2: Gas flow regimes and associated methods used to solve them.

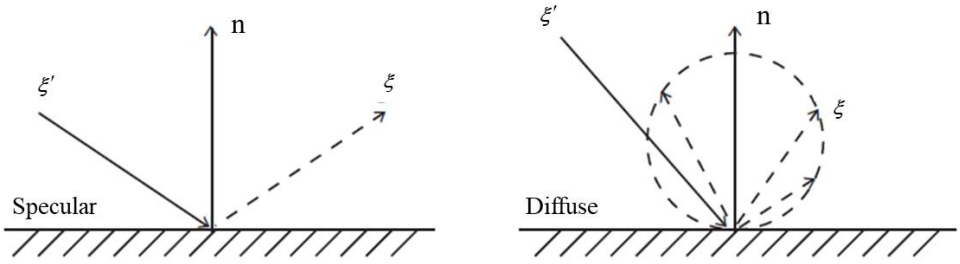

Figure 2.3: Velocities before and after gas-surface interaction with (left) specular boundary condition and (right) diffuse boundary condition.

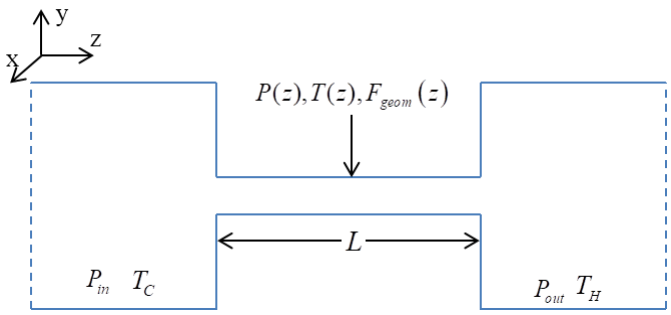

Figure 2.4: Scheme of a channel connecting two reservoirs at different temperatures and the main parameters in the calculation of the flow. The dashed line represents the boundary that will be open or closed depending on the different flow configurations.

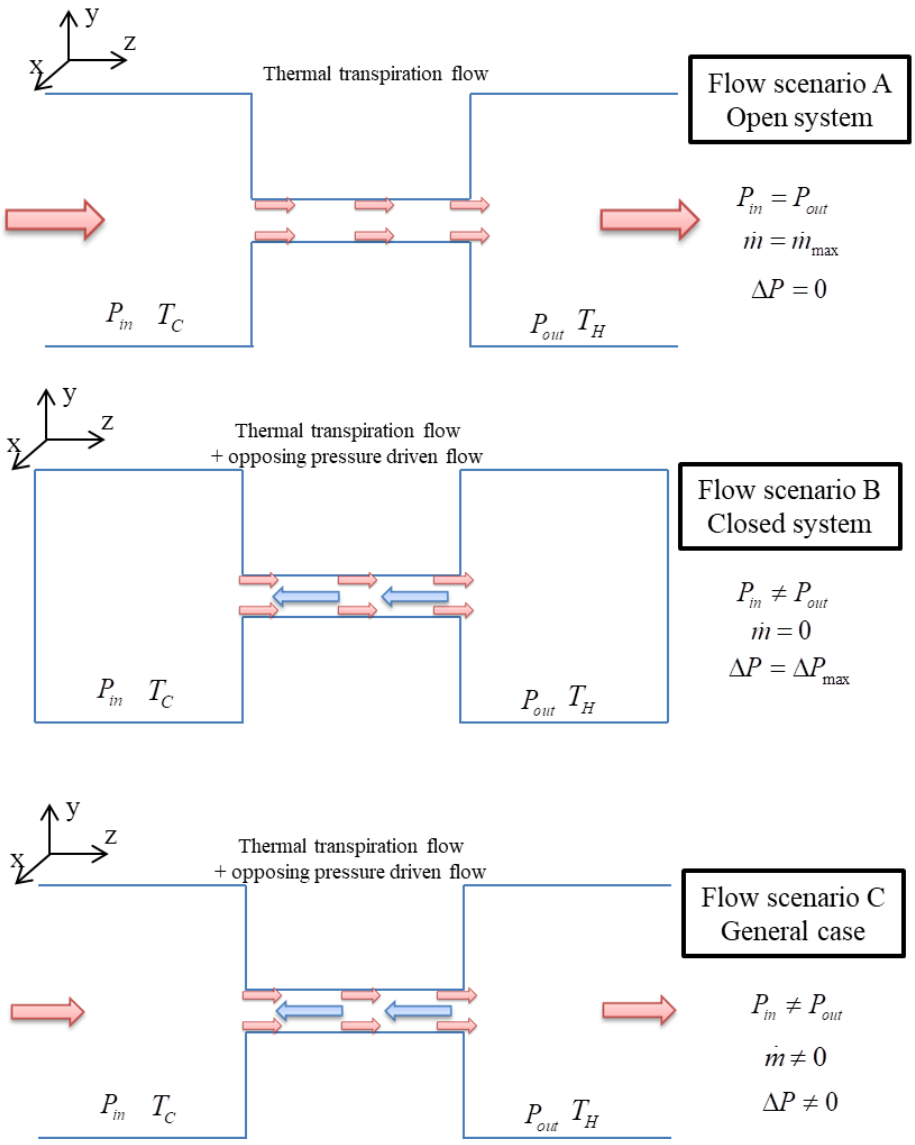

Figure 2.5: Different flow scenarios and the associated boundary conditions.

Chapter 3

Numerical study of Knudsen pumps and diodes

In this chapter a detailed parametric study of the pumping performance of two different Knudsen pump designs taking into account manufacturing and operational constraints has been performed in order to provide basic design guidelines for prototype designs.

The first design, consisting of long tapered rectangular ducts exploiting the diode effect, has been assessed following a parametric study with four different assemblies combining converging, diverging and uniform cross section ducts in various multi-stage assemblies. Additionally, the assembly combining converging and diverging ducts is further study not only regarding its pumping performance, but also its potential use as a thermal driven diode. This thermal driven diode can block the flow in one or the other direction depending on the operating pressure. Therefore, the critical operating pressure or the so-called blocking pressure corresponding to this zero flow state for the converging-diverging assembly has been characterized and the potential use of this assembly as a thermal driven diode for gas separation or gas actuator based on the temperature has been explored.

The second design consists of three different pump configurations targeting different applications based on the arrangement of circular microchannels through the thickness of the substrate connecting top and bottom reservoirs with different temperatures. This way, the cold and hot regions are spatially separated, in contrast with the typical manufacturing of the pump with the microchannels along the substrate. The first configuration targets applications such as micro-gas chromatography, where the needed mass flow rate is high while the corresponding pressure difference is small. This goal can be reached by arranging a large number of channels in parallel to increase the overall mass flow rate within just one stage. The second configuration targets applications such as vacuum maintenance in low-power devices where the needed pressure difference is high, while the corresponding mass flow rate is not so relevant. Hence, a large number of stages with just a single pumping channel are used. Finally, the third configuration is more flexible and targets applications where both relatively high mass flow rates

and pressure differences are needed. By combining the two previous configurations i.e., by including a large number of pumping parallel channels per stage and a large number of stages, a wide range of applications can be explored.

3.1 Fundamental architecture of a Knudsen pump

As it has been already reviewed in Chapter 1, the first functional Knudsen pump prototypes emerged along with the development of manufacturing technologies. Most of the first prototypes have been based on porous media with an imposed thermal gradient. However, the advancements in the microfabrication techniques allowed more accurate and intricate geometries and a decrease of the size of the devices, leading to various prototype designs. Nonetheless, most of the realized designs have been based on the classic Knudsen pump design involving a small channel with a temperature gradient connecting two reservoirs. Since the maximum temperature difference employed is limited by what the materials can withstand or what can be supplied to the device, and the performance provided by just one pumping channel is usually not sufficient for technological applications, a multi-stage system is generally required. In such a system, a cascade of stages is able to provide adequate pumping features.

In general, each stage of a multi-stage Knudsen pump comprises a pumping sub-stage and a counter flow sub-stage (Figure 3.1). The pumping sub-stage usually consists of a small channel subject to a thermal gradient, developing a thermal driven flow along the wall due to thermal transpiration. Inevitably, in order to limit the temperature in the device, a bigger channel or reservoir in which the temperature is decreased is necessary. The resulting inverse thermal gradient generates in this counter-flow sub-stage a flow in the opposite direction. To reduce this undesirable opposing thermal transpiration flow, the counter-flow sub-stage requires a large characteristic length, resulting in bigger channels or reservoirs.

Manufacturing this kind of micromachined pumps in which a large contrast of dimensions between the pumping and counter-flow sub-stages is required, along with the thermal management of local hot and cold points very close to each other, remains challenging even with the recent advancements in microfabrication techniques. Therefore, different preliminary Knudsen pump designs have been proposed in the literature to address some of these issues [23], [39], [40], [42], [43], [97], but most of the completed prototypes have still been based on a classic architecture with big reservoirs connected by constant cross section microchannels or

porous media [50], [52], [53], [55]–[57]. The designs proposed in this chapter attempt to address some of the issues inherent to the fundamental operation of the Knudsen pumps as well as to adapt the design for diverse applications and explore new potential functions.

3.2 Knudsen pumps and diodes based on rectangular tapered channels

The first proposed design is based on a previous computational investigation for temperature driven flows between single converging and diverging rectangular channels and the associated diode effect [43], [98], [99]. It has been numerically shown that depending on the direction of the temperature gradient applied in the converging or diverging direction, the pumping performance is different. Thus, an effective flow can be achieved by connecting successive tapered channels with the same geometry without the need of big reservoirs. Consequently, the original concept of this design is to substitute the usual big reservoirs and constant cross section channels by tapered channels. Then, by connecting in sequence tapered channels with opposing thermal gradients, one of the flow directions (either diverging or converging) provides a stronger performance, resulting to one of them acting as pumping channel and the following as counter-flow channel as presented in Figure 3.2. This way, the use of big reservoirs may be avoided, leading to easier manufacturing and reduced footprint.

Moreover, the numerical studies on the diode effect [43] have indicated that in addition to pumping, depending on the operating pressure range, additional effects such as bi-directional pumping or flow blocking may be observed without the need of changing the temperature gradients in the device. Based on the above, the study performed for single tapered plates [43] is extended to computationally investigate thermal transpiration pumping in multi-stage assemblies consisting of series of converging, diverging and constant cross sections rectangular ducts through a detailed parametric study following the methodology introduced in Chapter 2.

To perform a comprehensive study, the characteristics of thermal transpiration flows through single channels with converging, diverging and constant cross sections are first presented (Sections 3.2.2 and 3.2.3). The resulting effects on one single-stage pumping unit and to multi-stage assemblies is then analyzed (Section 3.2.4). Finally, a more focused investigation is provided for the converging-diverging assembly working as a thermal driven diode and its flow

blocking and bi-directional pumping capabilities to demonstrate their potential application as gas mixture separators or gas actuators in microfluidic devices (Section 3.2.5).

3.2.1 Pump geometry and characterization parameters

In all multi-stage pump designs considered in this section, the key elements are long channel with constant or variable rectangular cross sections, which are accordingly combined to obtain certain pump performance characteristics. Actually, the methodology described in Chapter 2 for simulating a temperature-driven flow in a single channel may be extended, in a straightforward manner, to obtain the overall properties of the pump assembly.

The geometry of the considered channel with variable rectangular cross-section (tapered rectangular channel) is given by its length L and its cross section defined by a variable height $H(z)$, $0 \le z \le L$, and a constant width W. The height $H(z)$, as well as the duct aspect ratio $H(z)/W$, vary linearly along the duct in the $z-$direction with $H(z) < W$ so that $H(z)$ is considered as the characteristic length of the channel. The mean heigth $H_m = \left(H(0) + H(L)\right)/2$ is taken as the reference dimension to make the comparison of different configurations. The duct inclination parameter α is always defined, independently of the duct geometry, as the ratio of the largest over the smallest heigth $\alpha = H_{\max} / H_{\min}$. Therefore, the inclination ratios for the converging and diverging ducts are $\alpha = H(0)/H(L)$ and $\alpha = H(L)/H(0)$ respectively, while the case of $\alpha = 1$ corresponds to a constant cross section duct. This definition of α facilitates the direct comparison between pump setups consisting of converging and diverging ducts with the same inclination ratio.

The two ends of the tapered rectangular channel, at $z = 0$ and $z = L$, are maintained at different temperatures, namely $T(0) = T_C$ and $T(L) = T_H$, with $T(0) < T(L)$, while it is assumed that the temperature along all four duct walls varies linearly between these two limiting values as $T(z) = T(0) + \left[T(L) - T(0)\right] z / L$. Hence, the constant temperature gradient along the duct is given by $dT/dz = \left[T(L) - T(0)\right]/L$. As it has been already explained in previous chapters, due to the externally imposed and maintained temperature gradient, a thermal transpiration flow is generated in the $z-$direction and the gas travels from the cold towards the

hot region along the channel walls. Then, due to the increased pressure at the hot end of the channel, a pressure driven flow in the opposite direction is generated from the hot towards the cold region of the duct in the center part of the duct. By taking $H_m << L$ the flow can be considered as locally fully developed and the inlet and outlet effects are ignored, while the pressure (and density) remains constant in each duct cross section and varies only in the flow direction, i.e. $P = P(z),\ z \in [0, L]$.

This flow is then investigated by computing the net mass flow rate $\dot{m}$ and the pressure distribution $P(z)$ along the duct in terms of duct geometry parameters L, W, $H(z)$, temperatures $T(0)$, $T(L)$ at the two ends of the duct and corresponding pressures $P(0)$, $P(L)$. Based on the well-known methodology already described in Chapter 2 [26], [27], [43], [85], [94], both the pressure distribution $P(z)$ and the mass flow rate $\dot{m}$ may be obtained by solving Equation (2.25), which in our case results to the following first-order ordinary differential equation:

$$\frac{dP}{dz} = -\frac{\upsilon(z)}{WH^2(z)G_P(\delta, H/W)}\dot{m} + \frac{G_T(\delta, H/W)}{G_P(\delta, H/W)}\frac{P(z)}{T(z)}\frac{dT}{dz}. \qquad (3.1)$$

This equation is valid at any cross section of the channel $z \in [0, L]$. The geometry of the channel, temperature $T(z)$ and its gradient dT/dz and the most probable molecular velocity $\upsilon(z)$ are known. In addition, kinetic coefficients G_P and G_T have been obtained by solving the classical fully developed rarefied gas flow through a rectangular channel for the local gas rarefaction parameter $\delta(z)$ and the local duct aspect ratio $H(z)/W$,. The values of the kinetic coefficients, based on the linearized Shakhov model subject to purely diffuse boundary conditions, are provided in Appendix A. This methodology presented for a single channel may be directly applied to the whole multi-stage assembly provided that the gas, the geometry, the temperature variation along the channels and the end pressures are all specified.

To facilitate the presentation of the results, the corresponding abbreviated names of the converging, diverging (in the direction of the temperature gradient) and uniform cross-section channels are “con”, “div” and “uni”. As shown in Figure 3.3, each stage of a multi-stage pump consists of the combination of a) uni - uni, b) div – uni, c) con – uni and d) con – div rectangular

channels. The first rectangular duct (the pumping channel) ,submitted to a positive thermal gradient, increases the pressure of the system in *z*-direction, while the second rectangular duct (the counter-flow channel), with a negative thermal gradient, reduces the pressure of the system. As expected, providing that the pressure difference developed by the pumping channel is larger than the opposed pressure difference developed by the counter-flow channel, a net flow is achieved in z-direction. On the contrary, if the opposing pressure difference of the counter-flow channel is larger than the one from the pumping channel, the flow is reversed. In the case that the pressure differences provided by the pumping channel and the counter-flow channel are equal to each other, the flow is blocked and the net flow rate in the device is zero. This specific behavior is a particularity of the tapered channel design associated to the diode effect. Normally, in the classic Knudsen pump design this would never happen since the characteristic length of the counter-flow sub-stage (wide channel or big reservoir) is much larger than the characteristic length of the pumping channel. However, due to the diode effect, this behavior of hindering the pumping flow may be present in tapered channels and may be used in developing new potential applications where the flow blocking characteristic could be exploited. The "uni – uni" assembly represents the classical Knudsen pump configuration, while the other three assemblies are new proposed designs. As shown in the next section, with the "con – uni" and "div – uni" designs a balanced performance between $\dot{m}$ and ΔP may be obtained, while with the "con – div" design, exploiting the diode effect, flow blocking and bi-directional pumping may be observed.

The length of each stage is $2L$ and by adding in series a number of single stages, four corresponding multistage pump designs, with abbreviated names "con – div", "con – uni", "div – uni" and "uni – uni" are formed. The total length of the pump is then $2NL$, where N is the number of stages. The temperature variation is periodic along *z* with a period equal to $2L$. The lowest and highest temperature points are denoted (as illustrated in Figure 3.3 in the case of a uni – uni pump) by T_C and T_H respectively and they are located at $z = 2iL$ and $z = (2i+1)L$, with $i = 0,1,...,N-1$. Then, solving Equation 3.1 along $z \in [0; 2NL]$, yields the mass flow rate $\dot{m}$ and the pressure distribution $P(z)$ along the whole multi-stage pump. The computed mass flow rate $\dot{m}$ with the associated pressure difference $\Delta P = P_{out} - P_{in} = P(2NL) - P(0)$ between the inlet and the outlet of the pump fully characterizes the pump performance.

As noted in the introduction the final objective is the fabrication of functional Knudsen pumps, however, during the course of the present work the investigation of the converging-diverging assembly operating a thermal driven diode suggests very interesting applications for gas mixture separation and gas actuators.More details about the manufacturing process and progress are presented in Chapter 4. , It is important to note that the present computational investigation is taking into account most of the envisioned manufacturing constraints. There have been many technical discussions with the manufacturer, the Laboratoire d'Architecture et d'Analyse des Systèmes (LAAS), in Toulouse, France, and most of the design parameters had been specified.. The manufacturing process considered is based on the deposition of dry film photoresist layers. Due to the particular fabrication process detailed in Chapter 4, the constant distance W between the parallel walls of the channels corresponds to the thickness of the photoresist film, and the following dimensions have been preliminary considered: $L = 200\,\mu\text{m}$, $W = 100\,\mu\text{m}$ and $H_m = 10\,\mu\text{m}$. In addition, due to manufacturing constraints, the minimum attainable size is expected to be $H_{\min} = 1.5\,\mu\text{m}$, while the inclination ratio may vary as $1 \le \alpha \le 10$. The configuration with $\alpha = 7$ will be used, as the representative one, to show the results when the influence of the inclination ratio is not relevant, remaining within the manufacturing limitations.

It is noted that $H_m << L$ is fulfilling the assumption of fully developed flow. In addition, since $H(z) < W$, the dimension $H(z)$ is the most characteristic length of the problem and it plays a significant role on the thermal transpiration flow and the diode effect.. Furthermore, the temperature at the cold spots will be fixed to $T_C = 300\,\text{K}$, while the temperature at the hot spots should be around $T_H \sim 400\,\text{K}$. These temperatures are on line with the temperature gradients already successfully applied for generating thermally driven flows through glass tubes [100]. Finally, the operating pressures at the inlet may vary as $P_{in} = 1 - 10^2\,\text{kPa}$ and the gas will be a noble monatomic gas, i.e. argon unless specified. The above data result in rarefied gas flows covering regimes from the transitional up to the slip regimes ($\delta = 0.1 - 2\times10^2$).

In the next sections, a detailed computational investigation is performed for all pump configurations in a wide range of the variable geometric and flow parameters in order to develop comprehensive guidelines concerning the expected performance characteristics of the multistage pumps. Additionally the blocking pressure of the “con – div” assembly is investigated in order to

demonstrate its flow blocking capabilities and its potential implementation as a thermal driven diode. The analysis will follow the methodology presented in Chapter 2 featuring the three flow scenarios, i.e. A (open system), B (closed system) and C (general case), in order to yield the maximal mass flow rate and pressure difference as well as the characteristic performance curves of the pump.

- In Section 3.2.2, the two limiting cases are presented for thermal transpiration flows through single channels with converging, diverging and constant cross sections channels.
- In Section 3.2.3, the characteristic performance curves of single-stage pumps are evaluated along with the pressure distribution developed in the channels.
- In Section 3.2.4, the "con – div", "con – uni", "div – uni" and "uni – uni" multistage assemblies are fully analyzed in terms of the number stages.
- Finally, in Section 3.2.5, the last part of the investigation of this tapered-pump design is focused on the "con – div" assembly with regard to the flow blocking and bi-directional pumping, to potentially develop thermally driven tapered diodes.

3.2.2 Pumping performance of single channels

The long rectangular channels investigated here have fixed length $L = 200\,\mu\text{m}$, width $W = 100\,\mu\text{m}$ and mean height $H_m = 10\,\mu\text{m}$ with various values of the inclination parameter $\alpha = [1, 3, 5, 7, 10]$. The corresponding minimum and maximum heights are tabulated in Table 1. The mean height is always kept the same to perform the comparison of the various ducts ("con", "div" and "uni") on the same basis (i.e. with the same average characteristic length). The cold and hot temperatures considered are $T(0) = T_C = 300\,\text{K}$ and $T(L) = T_H = 400\,\text{K}$ respectively. As commented previously, in many cases when results are qualitatively similar for different inclination parameters the representative value $\alpha = 7$ will be detailed. Also, since the main aim of using this pump design with tapered channels is to avoid the need of big reservoirs in order to further miniaturized each stage, when the one-stage (or the multi-stage assemblies of following sections) "uni-uni", "con-uni" or "div-uni" are studied, the counter-flow channel of each stage (the second duct of the stage) will be a uniform cross section duct with $H = 17.5$ μm. This value

corresponds to the maximal height $H_{\max}$ of the ducts with $\alpha = 7$. Thus, no additional footprint compared to the associated converging and diverging ducts with $\alpha = 7$ is required.

For these single rectangular ducts with converging, diverging and uniform cross section channels, the maximum mass flow rate $\dot{m}_{\max}$ corresponding to flow scenario A (open system with $\Delta P = 0$) is plotted in Figure 3.4 in terms of the inlet operating pressure $P(0) = P_{in} = P(L) = P_{out}$. The pressure range is $P_{in} = 1 - 10^2$ kPa with a resulting mass flow rate $\dot{m}_{\max}$ in the order of 10^{-11} kg/s and in all cases the mass flow rate is increasing with the operating pressure until close to the slip regime is reached. Then, as the operating pressure increases and the flow approaches the hydrodynamic regime, the mass flow rate tends to a constant value. It is clearly seen that the inclination parameter has a significant effect and more specifically, as α is decreased the mass flow rate is increased, and the uniform cross section duct ($\alpha = 1$) has a larger flow rate than the tapered ducts. This is due to the narrowing in the inlet and the outlet of the diverging and converging ducts respectively, although the mean height $H_m = 10\,\mu$m (and consequently the total volume of the channel) is the same in all cases and equal to the height (respectively the volume) of the uniform cross section duct. Comparing tapered ducts with the same inclination parameter α, it is observed that the mass flow rate in the diverging duct is always larger than in the converging one, which indicates the presence of the diode effect.

For the same single rectangular ducts, assuming now that the ends are closed, which corresponds to flow scenario B (closed system with $\dot{m} = 0$), the maximum pressure difference $\Delta P_{\max}$ is plotted in Figure 3.5 in terms of operating pressure $P(0) = P_{in}$. The pressure range is again $P_{in} = 1 - 10^2$ kPa with a resulting maximal pressure difference $\Delta P_{\max} = 20 - 200$ Pa. As the operating pressure is increased, in all cases, a non-monotonic behavior is observed: initially $\Delta P_{\max}$ increases and reaches a peak value $\Delta P_{\max}^{peak}$ and then it decreases. The inclination parameter has again a significant effect but now, as α is decreased the pressure difference is also decreased, and the uniform cross section duct ($\alpha = 1$) develops a smaller pressure difference than the tapered ducts. Thus, the narrowing of the tapered ducts helps to the development of higher pressure differences compared to the case of uniform cross sections ones with the same mean height. The largest values of the maximum pressure difference, $\Delta P_{\max}^{peak}$, are observed for

slightly higher values of P_{in} as α is increased. This peak is, however, always in the range of $P_{in} = 5-10$ kPa, corresponding to values of the gas rarefaction parameter $\delta \approx 4-6$, i.e., in the transition regime. This behavior has also been observed and reported in experimental studies, and the peak is exhibited at these values of δ independently of the working gas, the channel characteristic length, and the temperature difference [101].

The diode effect can be clearly observed by comparing the maximum pressure difference curves between diverging and converging ducts with the same α. It is seen that when P_{in} is below a critical value P^* (marked by the red dots in Figure 3.5), the maximum pressure difference $\Delta P_{\max}$ of the diverging duct is larger, while when P_{in} is above this critical value, the situation is reversed and $\Delta P_{\max}$ is larger for the converging duct. The critical pressure P^* in which the two corresponding curves are crossing each other is observed for $P_{in} = 7-15$ kPa, depending on α. These crossing points are also observed between the maximum pressure difference curves of tapered ducts with different α at other reference pressures. Then, by accordingly combining diverging and converging ducts at suitable operation pressures, it is possible to either have bi-directional flow or block the flow by creating positive, negative or zero pressure differences depending on this critical or blocking pressure P^*. This particular blocking pressure is further analyzed in Section 3.2.5 when the investigation is focused on the "con-div" assembly.

3.2.3 Pumping performance of one-stage pumps

The pumping channels for the one-stage pump possess the same geometry as before, i.e. a fixed length $L = 200\,\mu$m, width $W = 100\,\mu$m and mean height $H_m = 10\,\mu$m, but they will be only consider for inclination parameter $\alpha = 7$. It has already been shown how increasing the inclination parameter improves the pressure difference and reduces the mass flow rate. This behavior of the pumping performance remains qualitatively the same for different inclination parameters. Also, the main aim of using this kind of pump with tapered channels is to avoid the need of big reservoirs in order to further miniaturize each stage. Therefore, when the one-stage pumps (or the multi-stage assemblies in the following section) "uni-uni", "con-uni" or "div-uni" are studied, the counter-flow channel of each stage (the second duct of the stage) is a uniform

cross section duct with $H = 17.5$ μm corresponding to the maximal tapered dimension $H_{\max}$ of the ducts with $\alpha = 7$ as already explained before.

After the description of the limiting cases through single rectangular tapered ducts, the pumping effect in one-stage pumps is assessed by considering the pressure distribution along the channel when the system is closed (flow scenario B, $\Delta P = \Delta P_{\max}$) and the characteristic curves (flow scenario C) of the following four modules: "con-div", "con-uni", "div-uni" and "uni-uni". The "con-div" assembly consists of a converging duct followed by a diverging duct, both with $H_m = 10$ μm, while the other three assemblies are formed by a converging, diverging or uniform cross section duct with $H_m = 10$ μm followed by a bigger uniform cross section duct (the counter-flow channel) with $H = 17.5$ μm.

In Figure 3.6 the pressure distribution along the channel of a single-stage pump is shown for the four different "con-div", "con-uni", "div-uni" and "uni-uni" configurations, when the system is closed (Flow scenario B, $\dot{m} = 0, \Delta P = \Delta P_{\max}$). These results are presented for $P_{in} = [1, 8, 50]$ kPa, representing low, medium (approximately where the largest maximum value $\Delta P_{\max}^{peak}$ is achieved) and high operating pressures respectively. It can be observed how the pressure is increased in the pumping channel while the pressure is decreased in the counter-flow channel, due to the counter thermal creep flow. However, depending on the geometry of the channel, the way the pressure distribution increases or decreases varies. In the uniform cross section ducts ("uni") the variation of pressure along the channel follows a quasi linear trend, while for the tapered ducts ("con", "div") the pressure distribution displays a varying curvature depending on the operating pressure P_{in}. This curvature on the pressure distribution of the tapered ducts is clearly due to the varying geometry $H(z)/W$ and the associated rarefaction parameter $\delta(z)$ along the duct, and the converging and diverging ducts display opposing curvatures.

Regarding the pumping performances (difference of pressure between the inlet and the outlet), in the "uni-uni", "con-uni" and "div-uni" configurations, the pressure difference provided by the pumping channel is larger than the opposing one from the counter-flow channel for any operating pressure, resulting in a positive $\Delta P_{\max}$ and demonstrating the pumping capabilities of the designs. However, for the "con-div" assembly, depending on the operating pressure P_{in}, the system may operate below or over P^* (critical operating pressure in which pressure differences

generated by the converging and diverging ducts are equal). When operating at $P_{in} > P*$ (see case $P_{in} = 50$ kPa), since the pressure difference provided by the converging duct (pumping channel) is larger than the one provided by the diverging duct (counter-flow channel), an effective pumping is achieved and the pressure in the outlet of the one-stage pump is higher than in the inlet. On the contrary, when operating at $P_{in} < P*$ (see case $P_{in} = 1{,}8$ kPa) the diverging duct (counter-flow channel) provides a larger pressures difference than the converging duct (pumping channel), resulting in a pressure at the outlet lower than the pressure at the inlet, demonstrating the possibility to generate a reversed flow.

The characteristic curves (ΔP in terms of $\dot{m}$, flow scenario C) showing the intermediate operating scenarios between the two limiting cases for one-stage pumps are presented in Figure 3.7, for the four "con-uni", "div-uni", "uni-uni" and "con-div" assemblies. As expected, in all cases the characteristic performance curves exhibit a decrease of the absolute value of the pressure difference as the absolute value of the mass flow rate is increased. Furthermore, the performance curves display a linear trend, since with only one stage the output pressure is very close to the inlet pressure, which results in a limited variation of δ and the associated G_P and G_T for the different intermediate operating scenarios. However, as more of stages are added the behavior is nonlinear and it will be clearly demonstrated in the multi-stage assemblies. Regarding the performance of each assembly, the "uni-uni" one has the lowest slope and produces the largest values of $\dot{m}$ from all four assemblies. For $P_{in} = 1$ kPa, since the diverging duct outperforms the converging duct when $P_{in} < P*$, the values of ΔP are larger for the "div-uni" assembly than for the "con-uni" one. For $P_{in} = 8$ kPa, the operating pressure is very close to $P*$ and therefore, the $\Delta P_{\max}$ for the "div-uni" and "con-uni" assemblies are almost the same, but slightly larger in the "div-uni" assembly. When $P_{in} = 50$ kPa, the converging duct outperforms the diverging one in terms of pressure difference, and consequently the "con-uni" assembly develops slightly larger ΔP for most of the intermediate operating scenarios. Finally, the diode effect can be clearly observed for the "con-div" assembly where ΔP can display positive values (when $P_{in} > P*$) or negative values (when $P_{in} < P*$). In fact, for $P_{in} = 8$ kPa the operating pressure is very close to the critical value $P*$ and for that reason the characteristic curve is

almost reduced to a point at the origin of coordinates, and no mass flow rate nor pressure difference would be developed at $P_{in} = P*$.

3.2.4 Pumping performance of multi-stage assemblies

Following the study of the performance of single ducts and one-stage pumps, the pump characteristics of multi-stage assemblies are investigated first for the "con-uni", "div-uni" and "uni-uni" assemblies followed by the "con-div" assembly due to its particular diode effect. Again, since results of each assembly are qualitatively similar for different values of α, the representative value of the inclination parameter $\alpha = 7$ will be used to present the results. Also, as commented in the previous section, $H_m = 17.5\mu m$ will be the size of the constant cross section counter-flow duct in the "con-uni", "div-uni" and "uni-uni" assemblies. Additionally, two different "uni-uni" assemblies will now be considered, keeping the same counter-flow channel with $H_m = 17.5\mu m$ but with different pumping channels. Then, "uni-uni" (10 μm) assembly will keep the same geometry as in the previous section with $H_m = 10\mu m$ for the pumping channel and $H_m = 17.5\mu m$ for the counter-flow channel. The new "uni-uni" (2.5 μm) assembly will consist of a uniform cross section pumping channel with $H_m = 2.5\mu m$ followed by the counter-flow channel with $H_m = 17.5\mu m$. It is interesting to consider this new "uni-uni" (2.5 μm) assembly since the size of its pumping channel is equal to the smallest tapered dimension $H_{\min}$ of the reference tapered channels with $\alpha = 7$. Due to its reduced characteristic length, this newly introduced module will obviously outperform any of the other assemblies in terms of $\Delta P_{\max}$, but the corresponding $\dot{m}_{\max}$ will be accordingly reduced due to the smaller size of the pumping channel.

In Figure 3.8, $\Delta P_{\max}$ is presented in terms of the number of stages $N = [1-1000]$ for the "uni-uni" (10 μm), "div-uni", "con-uni" and "uni-uni" (2.5 μm) assemblies. It can be observed that $\Delta P_{\max}$ increases with the number of stages in a similar trend for the four assemblies but with different mean slopes. When P_{in} is higher than the value at which $\Delta P_{\max}^{peak}$ appears, every single duct operates in the region where $\Delta P_{\max}$ decreases when P_{in} increases (Figure 3.5). Thus, each time a stage is added, the contribution to the overall $\Delta P_{\max}$ of the assembly is slightly reduced

compared to the previous one, since the inlet pressure of each new stage is increased. On the other hand, when P_{in} is lower than the value at which $\Delta P_{\max}^{peak}$ appears, the assembly operates in the increasing region of $\Delta P_{\max}$, with every added stage contributing with a larger pressure difference compared to the previous stage until the pressure of the system reaches the value $P_{in} = 8-10$ kPa at which the $\Delta P_{\max}^{peak}$ occurs. Consequently, it can be observed in the detail from Figure 3.8 for $P_{in} = 1$ kPa how the maximum pressure difference $\Delta P_{\max}$ for a low number of stages $N < 200$ increases more rapidly with each additional stage, until the pressure of the system reaches the value at which $\Delta P_{\max}^{peak}$ appears. Then, $\Delta P_{\max}$ keeps increasing but at a slower pace that gradually decreases as the number of stages increases. For $P_{in} = 8$ kPa and $P_{in} = 50$ kPa, the system starts operating already around the maximum value $\Delta P_{\max}^{peak}$ or over it respectively, displaying a similar trend to the one for $P_{in} = 1$ kPa when $N > 200$.

Regarding the different configurations, as it was expected, the "uni-uni" (2.5 μm) assembly provides the greatest pumping performance for every operating pressure P_{in}, due to the smaller characteristic length of the pumping channel, while the "con-uni" and "div-uni" assemblies have a similar performance with the "con-uni" assembly reaching slightly higher output pressures for a high number of stages. More specifically, only when operating at $P_{in} = 1$ kPa with $N < 500$ and $P_{in} = 8$ kPa with $N < 100$ the "div-uni" assembly provides a higher $\Delta P_{\max}$ than the "con-uni" assembly (observable in the red details of Figure 3.8). This is due to operation of the system below the critical value $P*$ at which the diverging duct performs better than the converging one in terms of $\Delta P_{\max}$. Then, as the pressure in the system is increased either because of a higher initial operating pressure P_{in} or because of an increasing number of stages, the pressure in the system surpasses the value $P*$ and therefore the "con-uni" assembly provides a higher $\Delta P_{\max}$. Finally, the "uni-uni" (10 μm) assembly provides the lowest $\Delta P_{\max}$ as it was expected. Overall, it can be observed that for multi-stage pumps with a number of stages $N > 100$, the maximal pressure difference generated is very significant, of the same order as the operating pressure in the inlet, or even several times higher.

Now, $\dot{m}_{\max}$ is presented in Figure 3.9, in the same way as the pressure difference, in terms of the number of stages $N=[1-1000]$ for the four "uni-uni" (10 μm), "div-uni", "con-uni" and "uni-uni" (2.5 μm) assemblies. It can be clearly observed how $\dot{m}_{\max}$ is increased with the operating pressure P_{in} and it is kept constant as the number of stages is increased for each of the assemblies. This is due to the fact that all stages for each different assembly have the same geometry and the same inlet and outlet pressures since the operating scenario A corresponds to a pump with the same pressure at both ends of the multi-stage assembly. At the operating pressure $P_{in}=1$ kPa, the range is $\dot{m}_{\max}=5\times10^{-13}-2.1\times10^{-12}$ kg/s, while for $P_{in}=8$ kPa and $P_{in}=50$ kPa the range is $\dot{m}_{\max}=4\times10^{-12}-1.5\times10^{-11}$ kg/s and $\dot{m}_{\max}=1\times10^{-11}-2.5\times10^{-11}$ kg/s, respectively. As expected, for every operating pressure the "uni-uni" (2.5 μm) and the "uni-uni" (10 μm) modules provide the lowest and highest $\dot{m}_{\max}$, respectively, while the tapered modules provide mass flow rates within between the two limiting ones. Comparing the mass flow rates of the "div-uni" and "con-uni" assemblies it is seen that the former one provides a larger $\dot{m}_{\max}$ with respect to the latter one

Moving onto the analysis of the intermediate operating conditions (flow scenario C) with $\dot{m}<\dot{m}_{\max}$ coupled with an associated $\Delta P<\Delta P_{\max}$, Figure 3.10 shows the characteristic performance curves ΔP in terms of $\dot{m}$ for an increasing number of stages $N=[100,200,500,1000]$. Results are shown now only for two representative operating pressures $P_{in}=1$ kPa and $P_{in}=50$ kPa (left and right respectively) for the "uni-uni" (10 μm), "div-uni" and "uni-uni" (2.5 μm) assemblies. The "con-uni" assembly is overlooked because it provides qualitative and quantitative results very similar to the "div-uni" assembly with just slightly larger pressure difference ΔP and smaller mass flow rate $\dot{m}$. As expected, in all cases the characteristic performance curves exhibit a decrease in ΔP as $\dot{m}$ is increased. Since $\Delta P_{\max}$ is increased with the number of stages, while $\dot{m}_{\max}$ is constant independently of the number of stages (see the discussion in Figure 3.8 and Figure 3.9), the mean slope of the characteristic curves is increased with the number of stages. For a specified mass flow rate, the developed pressure difference is increased as the number of stages is increased; similarly, for a specified pressure difference, the produced mass flow rate is increased with the number of stages.

Furthermore, it is seen that the performance curves for $N = 100$ are still close to linear as it had been shown before for the one-stage pumps except for the "uni-uni" (2.5 μm) assembly at $P_{in} = 1$ kPa. This is justified since the output pressure is still relatively close to the inlet one, and the terms in Equation (3.1) are just slightly altered for the intermediate operating scenarios. There is the exception of the "uni-uni" (2.5 μm) assembly at $P_{in} = 1$ kPa where the pressure difference developed is high enough to display a non-linear behavior. Then, as N is increased, the outlet pressure is also increased, resulting in a more significant variation of G_P and G_T along the pump stages. This results in the performance curves exhibiting a non-linear behavior as the terms in Equation (3.1) develop larger variations. This behavior starts to appear from $N = 200$ and becomes more evident as N is further increased. Moreover, another interesting remark can be done in the case of low values of P_{in} and high values of *N*: the pressure difference ΔP decreases very slowly as the mass flow rate increases and then, when the mass flow rate approaches its maximal value $\dot{m}_{\max}$, the pressure difference abruptly decreases. This strongly non-linear behavior, clearly shown for $P_{in} = 1$ kPa due to the higher variation of ΔP, is beneficial for assemblies operating at low inlet pressures, where the relative variation of ΔP for most of the intermediate scenarios is larger than for higher inlet pressures.

Having a look to both Figure 3.8 and Figure 3.9, it is evident that the assemblies with tapered ducts provide a performance in between the "uni-uni" (2.5 μm) and "uni-uni" (10 μm) as it is expected. Depending on the operating pressure, ΔP is increased about 1.5-2 times when passing from the "uni-uni" (10 μm) to the "div-uni" assembly, $\dot{m}$ is reduced between 30%-40%. Then, with the reduction of H_m when passing from the "div-uni" assembly to the "uni-uni" (10 um), ΔP is increased about 2-7 times, depending on the operating pressure while $\dot{m}$ is reduced between 60%-75%. Consequently, although the tapered assemblies provide a smaller ΔP than assemblies with a smaller pumping channel, they can be implemented for applications requiring moderate pressure differences and mass flow rates. However, the most interesting characteristic of this design is not its pumping performance, but its capacity to block the flow and generate a functional diode effect.

Next, focusing on the "con-div" assembly where the diode effect can change the behavior and the pumping direction depends on the operating pressure, first the quantities $\Delta P_{\max}$ and $\dot{m}_{\max}$ in

terms of the number of stages are presented in Figure 3.11, followed by the characteristic curves displaying the intermediate operating scenarios in Figure 3.12. As discussed before (Figure 3.5), when the operating pressure is below the blocking pressure $P*$, the diverging duct outperforms the converging duct in terms of ΔP and thus, the pumping direction of the "con-div" assembly will be reversed. On the other hand, when the operating pressure is over the blocking pressure $P*$, the converging duct outperforms the diverging duct and the pumping direction is the expected one.

This change in the net flow direction is clearly observed in Figure 3.10 where $\Delta P_{\max}$ and $\dot{m}_{\max}$ are shown in terms of the number of stages $N = [1-2000]$ for $P_{in} = [1, 8, 20, 50]$ kPa. Concerning $\Delta P_{\max}$ (see Figure 3.11-left), for operating pressures $P_{in} = 20$ kPa and $P_{in} = 50$ kPa larger than the blocking pressure $P*$, $\Delta P_{\max}$ developed by the assembly is positive since the converging duct outperforms the diverging duct.. On the other hand, for the operating pressures $P_{in} = 1$ kPa and $P_{in} = 8$ kPa, lower than the blocking pressure $P*$, $\Delta P_{\max}$ is negative, resulting in a lower pressure at the "outlet" of the pump (in fact, since the flow is reversed, the outlet becomes the inlet and vice versa) than at the "inlet". Logically, the absolute pressure at the end of the pump cannot go below zero and for that reason, as the number of stages is increased, $\Delta P_{\max}$ tends asymptotically to the value of the operating pressure at the "inlet" of the module.

Regarding $\dot{m}_{\max}$ (see Figure 3.11-right), in the same way as in Figure 3.10, and since the geometry of each stage is the same and the inlet and outlet pressures are equal, $\dot{m}_{\max}$ is kept same with the number of stages and it varies only with each operating pressure P_{in}. However, whereas for the previous assemblies $\dot{m}_{\max}$ is increased monotonically with P_{in}, now, when $P_{in} < P*$ the flow is reversed and $\dot{m}_{\max} < 0$ while when $P_{in} > P*$ the flow follows in the usual pumping direction and $\dot{m}_{\max} > 0$. Also, when $\dot{m}_{\max}$ is positive, it seems to increase monotonically with the operating pressure but when $\dot{m}_{\max}$ the absolute value is slightly reduced. Nevertheless, in the next section a more detailed description of the evolution of both $\Delta P_{\max}$ and $\dot{m}_{\max}$ depending on the operating pressure and the blocking pressure $P*$ is provided.

In Figure 3.12, the characteristic performance curves displaying the intermediate operating scenarios for the "con-div" module with different numbers of stages

$N=[100,500,1000,1500,2000]$ are presented for $P_{in}=[1,8,20,50]$ kPa. At $P_{in}=20$ kPa and $P_{in}=50$ kPa, the operating pressure is larger than the blocking pressure $P*$ and thus, the curves resemble the performance curves from the previous assemblies at large inlet pressure (see Figure 3.11-right). However, at $P_{in}=1$ kPa or $P_{in}=8$ kPa, the operating pressure is below the blocking pressure $P*$ and both ΔP and $\dot{m}$ are negative, implying a reversed flow. Now, since the absolute value of $|\Delta P_{\max}|$ cannot surpass the inlet pressure (otherwise the absolute pressure at one end of the pump would be below zero), as the number of stages is increased the performance curves get closer and become almost identical as it can be observed for $P_{in}=1$ kPa and $N=[1500,2000]$. For $P_{in}=8$ kPa this behavior will be also observed for a number of stages larger than 2000 ($N>2000$) since the limiting value $|\Delta P_{\max}|=P_{in}$ is almost reached for $N=2000$. Also, for $P_{in}=1$ kPa, the performance curves are again quasi-linear because the relative variation of the inlet and outlet pressure and the associated G_P along the pump stages is limited, while for $P_{in}=8$ kPa, the non-linear behavior can be observed for $N=[1500,2000]$ due to higher variations of the pressure difference generated from one stage to the other.

Finally, it is important to note that in a "con-div" multi-stage assembly, the blocking pressure $P*$ at which the zero flow is achieved is the same as for a one-stage. However, increasing the number of stages results in a larger ΔP and the associated $\dot{m}$ for all the intermediate operating scenarios when the operating pressure is different from its value at this particular blocking pressure ($P_{in}\neq P*$). Meaning that as more stages are added the blocking pressure is the same, but the performance of the pump will be increased. The overall performance of the "con-div" multi-stage assembly, compared to the previous assemblies, is limited. Nevertheless, the blocking pressure along with the bi-directional pumping developed can be potentially exploited as a thermal driven diode in microfluidic devices requiring certain degree of flow control or for gas mixture separation.

3.2.5 Tapered thermal driven diodes

Here, a more in depth analysis of the diode effect and the blocking pressure $P*$ is presented for a one-stage "con-div" assembly. As commented before, adding more stages to the "con-div"

assembly does not change the value of the blocking pressure P^*, but will instead improve the performance of the bi-directional pumping. The evolution of $\Delta P_{\max}$ and $\dot{m}_{\max}$ (see Figure 3.13) in terms of inlet pressure will be first presented for different values of inclination parameter α to clearly identify the values of the blocking pressure P^*. Then, a parametric study of the effect of different geometrical and operating constraints on the blocking pressure value is presented in Figure 3.14, in order to provide some basic design guidelines for this fluidic diode.

In Figure 3.13, maximum mass flow rates $\dot{m}_{\max}$ (top) and pressure differences $\Delta P_{\max}$ (bottom) are shown for operating pressures $P_{in} = [1-100]$ kPa for "con-div" assemblies with the same $H_m = 10$ μm, but with varying inclination parameter $\alpha = [3,5,7,10]$. The red dots along the x-axis are the points where the curves cross the x-axis representing the value of the blocking pressure P^*, where both $\Delta P_{\max} = 0$ and $\dot{m}_{\max} = 0$. These red dots correspond to the ones shown in Figure 3.5, where the performances of the converging and diverging ducts cross each other. At $P_{in} = 1$ kPa ($P_{in} < P^*$), the values of $\Delta P_{\max}$ for all α. As the inlet pressure is increased, the values of $\Delta P_{\max}$ are decreased until they reach a minimum value before they start increasing up to zero (red points, where $P_{in} = P^*$). This can be understood by looking at Figure 3.5 where, as the operating pressure P_{in} is increased, the pressure difference generated by the converging and diverging ducts increase with the diverging duct outperforming the converging one, with the gap between the performances of the diverging and converging ducts expanding, until the diverging duct pressure difference reaches its peak value $\Delta P_{\max}^{peak}$. Then, the pressure difference of the diverging duct decreases while the converging performance keeps increasing until it reaches its own $\Delta P_{\max}^{peak}$. Consequently, at some inlet pressure $P_{in} = P^*$ the pressure differences generated by the converging and diverging ducts are equal.

For $P_{in} > P^*$, the values of $\Delta P_{\max}$ for the con-div assembly shown in Figure 3.13 are positive and keep increasing with P_{in} in a non-monotonic trend. More specifically, they reach various local peaks depending on the inclination parameter α. It is noted again that the shape of these curves and the local peaks are formed due to the gap between the single converging and diverging duct performances (difference in $\Delta P_{\max}$) shown in Figure 3.5. Similarly, at $P_{in} = 1$ kPa

($P_{in} < P^*$) the values of $\dot{m}_{\max}$ are negative and further decrease as P_{in} increases until reaching a minimal value before increasing towards zero ($P_{in} = P^*$).Then, $\dot{m}_{\max}$ becomes and remains positive and in general, it keeps increasing. It is also seen that in the pressure regions where the local peaks of $\Delta P_{\max}$ are displayed, the slope of $\dot{m}_{\max}$ is decreased. In general, a higher inclination parameter α provides higher absolute values of $\Delta P_{\max}$ both above and below P^*, whereas for $\dot{m}_{\max}$ the behavior is the opposite one. However, for $\alpha = 5$, there are some operating pressures at which $\dot{m}_{\max}$ slightly surpasses the value obtained for $\alpha = 3$.

Having analyzed the evolution of $\Delta P_{\max}$ and $\dot{m}_{\max}$ in terms of operating pressure where the blocking pressure P^* can be clearly identified, the focus will now be on calculating the value of P^* to investigate the design of potential fluidic diodes by changing geometrical and operational parameters.

As it has been demonstrated, with different values of α, different blocking pressures P^* can be achieved. In fact, as it was mentioned, in a one-stage "con-div" assembly where the first channel (pumping channel) is a fixed converging duct, different blocking pressures P^* can be obtained by varying the inclination parameter of the diverging duct (counter-flow channel). Therefore, the blocking pressure P^* has been calculated for a one-stage "con-div" assembly with the first converging duct fixed with $\alpha_{con} = 7$ whereas the following diverging duct has a variation of the inclination parameter $\alpha_{div} = [1.5 - 8.5]$. The results are plotted in Figure 3.14 for various geometrical and operating conditions. Considering a base case with $H_m = 10$ μm, $W = 100$ μm, $\Delta T = 100$ K and argon as the working gas (noted with the red dotted curves in Figure 3.14), the influence of these geometrical (H_m, W) and operational (ΔT, working gas) parameters is assessed. It is expected that the blocking pressure P^* will be increased with the increase of the inclination parameter α_{div} of the diverging duct since the crossing point of the ΔP will occur at higher inlet pressures. In addition, the slope of this curve is expected to change since the performance of the fixed converging duct and the varying diverging ducts in terms of ΔP display similar shapes, which however are shifted to each other (Figure 3.5).

Firstly, in Figure 3.14.a, the blocking pressure P^* is calculated for a varying inclination parameter α_{div} of the diverging duct from the "con-div" assembly for different values of the

mean tapered dimension H_m μm of both the converging and diverging ducts of the assembly. It can be observed that the shape of the curves for all values of H_m is very similar but their position is shifted with an increasing P^* as H_m is reduced. This behavior was expected since the tapered dimension $H(z)$ is the characteristic length of the duct and by reducing it the effect of the thermal transpiration is increased accordingly. Therefore, the overall ΔP performances of the fixed converging and varying diverging ducts are both increased in a very similar way. They have the same slope, but shifted towards higher operating pressures to keep the peak values $\Delta P_{\max}^{peak}$ at the same $\delta = 4-6$. Hence, the values and range of P^* are increased even though the relative shapes of the curves is kept, providing then a similar shape of P^* for all values of H_m here considered. As the tapered dimension is reduced and the curves of the blocking pressure are shifted up, the pressure ranges of the blocking pressure with the increasing α_{div} goes from $P^* = 0.2-5.6$ kPa for $H_m = 40$ μm to $P^* = 1.5-42.7$ kPa for $H_m = 5$ μm, keeping the same shape but amplifying the range of possible blocking pressures of the diode.

In Figure 3.14.b, the blocking pressure P^* is calculated for a varying inclination parameter α_{div} of the diverging duct of the "con-div" assembly with $W = [10, 50, 100, 1000]$ μm. This dimension W is the constant distance between the parallel walls of the tapered ducts. It is clearly observed that for large values of W the difference between the curves of the calculated blocking pressure P^* is almost negligible. This is expected since thermal transpiration generating the diode effect is driven by the characteristic length $H(z)$. Therefore, when W is large compared to $H(z)$, its influence on the performances of the fixed converging and varying diverging ducts and the associated blocking pressure is almost negligible. However, when W is of the order of H_m, the performances of the fixed converging duct and the varying diverging duct are changed. Depending on the inclination parameter α of the ducts, W can be larger or smaller than $H(z)$ at different points along the duct, resulting in small modifications in the shape of the ΔP performance curves. Hence, it is observed that for $W = 10$ μm there is a difference in the shape of the curve.

In Figure 3.14.c, the blocking pressure is calculated for a varying inclination parameter α_{div} of the "con-div" assembly, for $\Delta T = [50,100,150,200]$ K and a constant temperature $T_C = 300$ K of the cold side. It is evident that when ΔT is increased, the developed pressure difference ΔP of both the fixed converging duct and the varying diverging duct are increased, reaching larger values of $\Delta P_{\max}^{peak}$. This is achieved without moving to higher operating pressures and therefore, the slope of the ΔP performance curves is pronouncedly changed when ΔT is increased, resulting to a significant variation of the blocking pressure $P*$. It is interesting to note that as ΔT is decreased the computed blocking pressure when $\alpha_{div} < \alpha_{con}$ is decreased while when $\alpha_{div} > \alpha_{con}$ the behavior is changed and the blocking pressure is increased. In the specific case of $\alpha_{div} = \alpha_{con}$, the values of the blocking pressure are approximately the same for different ΔT. Consequently, the largest variation of the blocking pressure $P* = 0.3 - 89.2$ kPa is observed at $\Delta T = 50$ K and the smaller variation $P* = 3.1 - 17.8$ kPa at $\Delta T = 200$ K.. Unlike H_m and W which are fixed once the "con-div" module is manufactured, ΔT is an operating parameter that can be easily modified by just controlling the power input provided to the assembly, allowing the adjustment of the blocking pressure for a given "con-div" module geometry. Thus, it is important to note that when $\alpha_{div} = \alpha_{con}$, the variation of $P*$ with ΔT is very small, providing a more stable blocking pressure, whereas as the values of α_{div} differ more from α_{con}, the range of blocking pressures with ΔT is bigger but more sensitive to any changes in temperature. Then, depending on the target application, either more stable diodes with narrow pressure range or less stable diodes with wide pressure range could potentially be implemented.

Finally, in Figure 3.14.d the blocking pressure is calculated for a varying inclination parameter of the diverging duct α_{div} for different working gases (He, Ne, Ar and Xe). Similarly to Hm, when the molecular weight of the working gas is decreased, the pressure difference ΔP for both the fixed converging duct and the varying diverging duct are increased in a very similar way, having the same slope, while shifted towards higher operating pressures to keep the peak values.. Therefore, the values and range of $P*$ are increased for lighter gases but the relative shape of the curves is kept for the four different working gases and covers different ranges ($P* = 2.1 - 57.3$ kPa for He, $P* = 1.5 - 40.6$ kPa for Ne, $P* = 0.8 - 21.4$ kPa for Ar and $P* = 0.4 - 11.3$ kPa for Xe). Consequently, the present results clearly indicate that the blocking

pressure phenomenon may be implemented in the design of gas separators or gas controllers in microfluidic devices since depending on the gas molecular mass the blocking pressure occurs at different distinctive values and ranges.

3.2.6 Concluding remarks on the tapered channel design

An extensive computational study of multi-stage Knudsen pumps consisting of long rectangular tapered ducts taking into account manufacturing and operational constraints has been completed. Also, one particular assembly combining converging and diverging ducts has been investigated regarding its flow blocking capabilities as a thermal driven fluidic diode. The analysis has been performed by accordingly integrating the dimensionless flow rates, obtained by linear kinetic modeling into a simple algorithm based on the mass conservation principle. The analysis of single converging, diverging and uniform cross section ducts with the same mean tapered dimension H_m, clearly shows that as the inclination parameter α is increased, the maximal generated pressure difference $\Delta P_{\max}$ is increased while the maximal mass flowrate $\dot{m}_{\max}$ is decreased. Also, the diverging duct provides always larger $\dot{m}_{\max}$ than the converging one, while depending on the operating pressure the pressure difference $\Delta P_{\max}$ of the diverging duct is larger than that of the converging duct when $P_{in} < P^*$, and vice versa when $P_{in} > P^*$.. Whenever the operating pressure is equal to this critical pressure P^*, the performance of both diverging and converging ducts are equal. Then, by accordingly combining diverging and converging ducts at suitable operation pressures, it is possible to either control a bi-directional flow or block the flow by creating positive, negative or zero pressure differences. This existence of a critical or blocking pressure P^* clearly demonstrates a diode effect and the potential application of tapered ducts associations as thermally driven diodes.

Continuing with analysis of multi-stage pumps, the limiting cases $\left(\Delta P = \Delta P_{\max}, \dot{m} = 0\right)$ and $\left(\dot{m} = \dot{m}_{\max}, \Delta P = 0\right)$ have been investigated along with all the intermediate operating scenarios for the “uni-uni”, “con-uni”, “div-uni” and “con-div” assemblies in terms of number of stages. A positive pumping effect is always achieved for the “uni-uni”, “div-uni” and “con-uni” assemblies, whereas for the “con-div” assembly, due to the diode effect, the pumping flow is reversed when $P_{in} < P^*$. The “con-uni” and “div-uni” assemblies behave in a similar way (with

just slight deviations depending on whether $P_{in} > P*$ or $P_{in} < P*$), always delivering a performance in terms of ΔP about 1.5-2 times larger than the equivalent "uni-uni" (10 μm) assembly (pumping channel with the same H_m) but with a reduction of 30%-40% of the mass flow rate, depending on the operating pressure. On the other hand, when comparing with "uni-uni" (2.5 μm) in which the pumping channel is smaller (i.e. pumping channel with a constant $H_{\min}$ of the tapered channels), ΔP is reduced 2-7 times depending on the operating pressure, while $\dot{m}$ is increased by 60%-75%. Consequently, although the tapered assemblies "con-uni" and "div-uni" provide a smaller $\dot{m}$ than assemblies with a smaller pumping uniform cross section channel as the "uni-uni" (2.5 μm) assembly, the mass flow rate generated is higher, and so, they can potentially be implemented for applications requiring moderate pressure differences and mass flow rates.

Regarding the "con-div" assembly, they deliver the worst pumping performance when compared to the other assemblies. However, the diode effect and the existence of a blocking pressure with the capability to develop a bi-directional pumping without inverting the temperature gradients can be of interest for designing thermally driven diodes. Therefore, a parametric study of a "con-div" module with a fixed converging duct $(\alpha_{con} = 7)$ has been performed to assess the blocking pressure $P*$ in terms of the inclination parameter of the diverging duct $\alpha_{div} = [1.5 - 8.5]$, by modifying the mean tapered dimension H_m, the constant distance between the parallel walls of the duct W, the difference of temperature ΔT and the working gas. The blocking pressure $P*$ increases monotonically with the inclination parameter α_{div}. The variation of H_m does not modify the shape of the blocking pressure curves but amplifies its range of variation as H_m is decreased. The variation of W only has a slight influence on the shape of the blocking pressure curve when $W \approx H_m$. When ΔT is increased, the range of the blocking pressure is reduced. In addition, when $\alpha_{div} = \alpha_{con}$, the variation of $P*$ with ΔT is significantly smaller, resulting in a more stable diode; On the other hand, when α_{div} is far from α_{con}, the range of the blocking pressure variation with ΔT grows, allowing for the adjustment of the blocking pressure in a wider extent. Finally, modifying the working gases results in different values and ranges of the blocking pressure, typically increased for lighter

gases, demonstrating the potential use of this thermally driven diode as a gas separator or gas controller in microfluidic devices.

3.3 Modular Knudsen pump design for target applications

The design proposed is based on the fabrication of circular channels through the thickness of a layer of low thermal conductivity bulk material. The schematic and principle is similar to the classic Knudsen pump design, but with the innovation in manufacturing techniques, instead of building the channels along the surface of the substrate, now the microchannel is fabricated by drilling through the thickness of the substrate material. In most of the available Knudsen pumps, based on micromachined channels, the channels are fabricated along the surface, arranging the geometry of the pumping and of the counter-flow channels in the same plane [56], [57]. In the present setup the pumping channels are made across the thickness of the material, being able to arrange more channels or stages per unit area. Additionally, by spatially separating the hot and cold regions, the problems associated with local heating and cooling are significantly reduced since only uniform hot and cold temperatures on the top and bottom sides are required.

Similar setups have been recently explored with the manufacturing of high flow Knudsen pumps [58] based on an array of micromachined parallel channels and for gas chromatography analyzers [67] that combined micromachined channels with a porous media inside. In both cases a good mass flow rate has been achieved but with a limited pressure head due to the absence of a multi-stage system. For particular applications such as for the gas microchromatographer [65], [67] the overall performances achieved are adequate, while for various other applications larger pressure heads are required. Then, it is reasonable to consider an architecture based on a similar structure, combining however multiple stages to improve the overall pumping performance and expanding the range of potential applications of these Knudsen pumps.

Here, an innovative Knudsen pump design combining arrays of parallel channels in a multi-stage cascade system for targeting different performances is proposed. Specific guidelines for three Knudsen pump configurations centered on this architecture depending upon the target application are provided, based on a numerical investigation according to the methodology presented in Chapter 2 and of the previous section. This kind of architecture could be fabricated by various manufacturing process such as drilling of the substrate, 3D printing or deposition of dry film photoresist layers. More details about the manufacturing process are given in Chapter 4.

3.3.1 Pump geometry and characterization parameters

Based on the architecture mentioned above, three alternative configurations can be outlined regarding the performance characteristics for target applications, named below as modules A, B and C. The first one (module A) targets applications such as micro-gas chromatography [66], where the needed mass flow rate is high while the corresponding pressure difference is small. This goal can be reached by designing a large number of channels in parallel to increase the overall mass flow rate. As there is no need to generate a strong pressure difference, this configuration does not require multiple stages. The second configuration (module B) targets applications such as vacuum maintenance in low-power consuming devices, where the needed pressure difference is high [56], [57], while the corresponding mass flow rate is not important.. It requires a large number of stages to increase the pressure difference, which is limited for each stage by the available temperature difference. In order to increase compactness and decrease power consumption, each stage is made of a single channel, as a small mass flow rate is acceptable. The third configuration (module C) is more general oriented and targets applications, where both relatively high mass flow rates and pressure differences are needed. This is achieved by combining the two previous designs of modules A and B, resulting in multi-stage systems with multiple parallel channels in each pumping sub-stage. Since the performance of this design is less constrained and can be tailored for targeting particular applications, it is expected to be used in various MEMS.

Therefore, the three pump configurations, shown in Figure 3.15, can be ~~more~~ specifically defined in the following way:

- Module A consists of an array of multiple parallel pumping channels in one single pumping stage to achieve high mass flow rate ($\dot{m}$) performance. The layout area is $a \times a$ with n parallel pumping channels of diameter d and length L.
- Module B consists of a multistage system where each stage is formed by one single pumping microchannel followed by one counter-flow channel (where the reduced counter thermal transpiration flow will appear) to achieve high pressure difference (ΔP) performance. The layout area is $(W \times W) + (b \times b)$. The diameter of the pumping and counter-flow channels are d and D, respectively, and the length of both channels is L.

- Module C combines the two previous designs, consisting on a multistage system with each stage formed by an array of n parallel pumping microchannels, followed by one counter-flow channel where the reduced counter thermal transpiration flow will appear. This design aims to provide high ΔP and $\dot{m}$ performances, due to the multi-stage cascade system and to the multiple pumping microchannels per stage, respectively. The layout area is $(W \times W) + (c \times c)$. The diameter of the pumping and counter-flow channels are d and D, respectively, while the length of all channels is L.

Simulations of pumps A, B, and C have been performed via kinetic modeling, and the performance characteristics are here analyzed, in terms of the parameters affecting the flow. The flow configurations in the three proposed pump designs are modeled in order to obtain the expected performance in each case. Therefore, the thermal transpiration flow through circular channels has been modeled based on the infinite capillary theory by considering that the length of the channels is much longer than the radius. However, in cases where the fully developed assumptions are not met (i.e., in the counter-flow with channels of diameter D), the end effect correction is accordingly introduced [102], [103]. The correction is introduced only in the pressure, and not in the corresponding temperature-driven flow, since the mass flow rate in the former one is about one order of magnitude larger than in the latter.

Consider the fully developed thermal transpiration flow and the associated pressure driven flow of a monatomic variable hard sphere molecule through a circular channel with length L and radius R (with $R << L$) that connects two reservoirs maintained at different temperatures T_C and T_H, with $T_C < T_H$. Then, equation (2.25) can be rewritten as

$$\frac{dP}{dz} = -\frac{\dot{m}\upsilon_0(z)}{\pi R^3 G_P(\delta)} + \frac{G_T(\delta)}{G_P(\delta)} \frac{P(z)}{T(z)} \frac{dT}{dz}, \tag{3.2}$$

subject to the given pressures $P(0)$ and $P(L)$ at the channel inlet and outlet, respectively, while $z \in [0, L]$ is the coordinate along which the flow is directed, $\upsilon_0(z)$ is the local most probable molecular speed, $T(z)$ is the imposed linear temperature distribution along the channel wall and $P(z)$ is the unknown pressure distribution. Additionally, $G_P(\delta)$ and $G_T(\delta)$ are the dimensionless flow rates, also known as kinetic coefficients, for the pressure- and temperature-

driven flows respectively, depending on the local gas rarefaction parameter $\delta(z)$. The kinetic coefficients $G_P(\delta)$ and $G_T(\delta)$ are retrieved from a kinetic database, which has been developed based on the linearized Shakhov model subject to pure diffuse boundary conditions in the range $\delta \in [0,50]$. Additionally, when $\delta > 50$, the analytical slip solution is used. More details on the calculation of the kinetic database can be found in Appendix A. Equation (3.2) refers to a single channel but may be applied in a straightforward manner to modules A, B, and C; therefore, it is solved for the three flow scenarios (open system, closed system or general case) depending on the module investigated.

The performance characteristics of the three proposed pump designs are computationally investigated, taking into account manufacturing and operational constraints after several discussions with the manufacturer (LAAS). Proper thermal management is of major importance. Previous experimental works on thermal transpiration flows through capillaries [101], [104], supplemented by recent typical heat transfer simulations in film layers, clearly indicate that it is possible to provide temperature differences $\Delta T = T_H - T_C$ on the order of 100 K within a channel of length $L = 300\,\mu\text{m}$ by integrating active heating and cooling. In addition, microchannels with diameters ranging from 100 down to 5 μm are expected to be attained with $L = 300\,\mu\text{m}$. This length corresponds to the thickness of each layer and is kept small in order to minimize the pump volume. In a later stage, smaller diameters may be fabricated by further reducing the channel length, i.e., the film layer thickness.

Based on the above, simulations for pump modules A, B, and C consisting of pumping channels and counter-flow channels with diameters $d = 50, 20, 10, 5\,\mu\text{m}$ and $D = 100\,\mu\text{m}$, respectively, always keeping the length $L = 300\,\mu\text{m}$, have been performed. Similarly to previous sections, the temperature difference is set to $\Delta T = 100\,\text{K}$, maintaining the cold and hot temperatures at $T_C = 300\,\text{K}$ and $T_H = 400\,\text{K}$, respectively, while the gas species considered is argon.

Furthermore, taking into account the space needed between the channels from the fabrication point of view, it can be estimated that the minimum total square area allowing an array of at most $n = 400$ pumping channels is $200 \times 200\,\mu\text{m}^2$. A schematic view of the corresponding layouts to be examined is shown in Figure 3.16. As the pumping channel diameter

is reduced, the number n of parallel pumping channels in the layout is increased, keeping the same area ratio between the flow and the layout cross section areas. In this way, the comparison of the performance characteristics of the different layouts always involves the same cross section flow area. Additional details of the layout geometry are provided in Table 3.2.

The computational investigation includes the performance of pump modules A, B, and C and is presented in the following sections, in terms of the inlet pressure $P_{in} \in \left[0.1-10^5\right]$ kPa, the diameter d of the pumping channels and the number N of stages.

3.3.2 Pump module A: multiple parallel pumping channels

Pump module A consists of a single pumping stage with n parallel microchannels, mainly targeting high mass flow rates $\dot{m}$ and small pressure differences ΔP. It is obvious that, as the channel diameter is reduced, the mass flow rate in a single channel, is also reduced. This mass flow rate loss is partly compensated ~~for~~, since as the diameter is decreased more channels are packed in parallel, keeping the same cross section area. The total mass flow rate will be equal to that of a single channel multiplied by the number n of parallel channels. On the contrary, the total pressure difference will be equal to that of each channel and increases as the channel diameter decreases. Therefore, first, a comparison is performed between the performances of a single-stage pumping for the different layout geometries by varying the pumping channel diameter and the number of channels, while preserving the same total surface, as shown in Figure 3.16 and Table 3.2.

The investigation is performed by computing the total maximal mass flow rate $\dot{m}_n$ through the n parallel channels corresponding to zero pressure difference (open system) as well as the maximal pressure difference ΔP_n corresponding to zero net mass flow rate (closed system). For $n = 4, 25, 100,$ and 400, $\dot{m}_n$ and ΔP_n are compared with the reference values $\dot{m}_1$ and ΔP_1 respectively, corresponding to the case of a single channel, $n = 1$. The channel diameters associated with $n = 1, 4, 25, 100,$ and 400 are $d = 100, 50, 20, 10,$ and 5 μm, respectively. The ratios $\dot{m}_1 / \dot{m}_n$ and $\Delta P_n / \Delta P_1$ are computed to estimate the mass flow rate decrease and the pressure difference increase when the number of channels is increased and their diameter is decreased. The results are presented in Figure 3.17 as a function of the inlet pressure P_{in}.

As expected, as the diameter is decreased and the number of pumping channels is increased, both $\dot{m}_1 / \dot{m}_n$ and $\Delta P_n / \Delta P_1$ are monotonically increased, meaning that the total flow rate through the parallel channels decreases and the pressure difference increases. In terms of the inlet pressure, it is seen that at a low inlet pressure the ratios of the total mass flow rates $\dot{m}_1 / \dot{m}_n$ are larger than the corresponding ratios of pressure differences $\Delta P_n / \Delta P_1$, while at moderate and high inlet pressures, the situation is reversed and the ratios $\dot{m}_1 / \dot{m}_n$ become smaller than the corresponding $\Delta P_n / \Delta P_1$. This behavior clearly implies that, in the pumping channels, the relative pressure difference increase compared to the corresponding total mass flow rate decrease is less significant in highly rarefied conditions, while in less rarefied conditions closer to the slip and hydrodynamic limit, it becomes more significant. Furthermore, the solid red circles indicate the inlet pressure values where the two ratios are equal. Then, at the left side of these points, the ratios of the mass flow rates $\dot{m}_1 / \dot{m}_n$ are larger than the corresponding ratios of pressure differences $\Delta P_n / \Delta P_1$, while at the right side $\Delta P_n / \Delta P_1$ are larger than $\dot{m}_1 / \dot{m}_n$. For $P_{in} \geq 5\,\text{kPa}$, whatever the number n of parallel microchannels, the relative variation in pressure difference is much more significant than the relative variation in the total mass flow rate through the combined parallel channels.

To have a clear view of the performance characteristics of the single-stage module A in absolute quantities (not in relative ones, as previously), the maximal pressure difference $\Delta P_{\max}$ and the maximal mass flow rate through a single channel $\dot{m}_{\max}$ are plotted in Figures 3.18 and 3.19 respectively, for channels with $d = 5, 10, 20\,\mu\text{m}$, as a function of the inlet pressure P_{in}. In all cases, as the inlet pressure is increased, the pressure difference is initially rapidly increased, reaching its peak value, and then is slowly decreased. The peak values $\Delta P_{\max}^{peak}$ occur, depending upon the diameter d, at about $P_{in} = 4 - 10\,\text{kPa}$, corresponding to values of the gas rarefaction parameter $\delta = 4 - 6$, i.e., in the transition regime. This behavior has also been observed and reported in experimental studies and is independent of the working gas, the channel characteristic length and the temperature difference [100], [105]. Depending on the inlet pressure, the generated maximal pressure difference $\Delta P_{\max}$ varies from 10 to 420 Pa and, as expected, the obtained pressure difference is increased as the diameter is reduced with the maximal

$\Delta P_{\max} = 420, 200, 100\,\text{Pa}$ for $d = 5, 10, 20\,\mu\text{m}$, respectively. Regarding the maximal mass flow rate $\dot{m}_{\max}$, it is rapidly increased as the inlet pressure is initially increased and then it keeps increasing at a much slower pace until it becomes constant in the hydrodynamic regime. For $P_{in} \geq 20\,\text{kPa}$, $\dot{m}_{\max}$ is almost stabilized and reaches values of about 0.5×10^{-12}, 2.1×10^{-12} and $8.5\times10^{-12}\,\text{kg/s}$ for $d = 5, 10, 20\,\mu\text{m}$, respectively. Multiplying these values with the corresponding number of pumping channels, $n = 400, 100, 25$, results in mass flow rates higher than $10^{-10}\,\text{kg/s}$. These results, properly scaled, are in good agreement with the corresponding ones in [58], where a design similar to pump module A was realized for developing a high flow pump.

Overall, it may be stated that, for the pump module A, it is preferable to have a larger channel diameter to increase the total mass flow rate rather than a large number of parallel microchannels with smaller diameters. However, since reducing the channels diameter results in huge gains of ΔP with only small reductions of $\dot{m}_n$, as shown in Figure 3.17, depending on the application, it might be advisable to reduce the diameter to boost the pressure difference, while only slightly reducing the overall mass flow rate. Finally, it is preferable to operate the pump with moderate and high inlet pressures ($P_{in} > 5\,\text{kPa}$), where the mass flow rate starts to stabilize at large values.

3.3.3 Pump module B: multi-stage pumping with single pumping and counter-flow channels

Module B is a multistage system, where each stage consists of one single pumping channel with $d = 50, 20, 10, 5\,\mu\text{m}$, followed by one counter-flow channel with $D = 100\,\mu\text{m}$, targeting high pressure differences and small mass flow rates (as there is only one microchannel per stage).

The maximal pressure difference corresponding to zero net mass flow rate (closed system) at various inlet pressures $P_{in} = 1, 5, 10, 20, 50, 100\,\text{kPa}$ are provided in Figure 3.20 versus the number of stages with $N \leq 1000$ (left) and $N \leq 100$ (right). The considered pumping channel and counter-flow channel at each stage have diameters $d = 10\,\mu\text{m}$ and $D = 100\,\mu\text{m}$, respectively. As seen in Figure 3.20 (left), the maximal pressure difference, $\Delta P_{\max}$, increases with the number of stages in a qualitatively similar manner for all inlet pressures, except for the lowest inlet pressure

$P_{in}=1\,\text{kPa}$ and $N\le 100$. It is also seen that for a small number of stages the pressure difference is rapidly increased and then it keeps increasing, but at a slower pace that gradually decreases as the number of stages increases. This is due to the fact that, for all the inlet pressures shown, except $P_{in}=1\,\text{kPa}$, the pumps, independently of N, always operate in the decreasing region of $\Delta P_{\max}$ in terms of P_{in} (see Figure 3.18). In all these cases, each time a stage is added its contribution to the overall $\Delta P_{\max}$ is slightly reduced compared to the previous one, because the inlet pressure of the stage is increased. Therefore, the rate at which $\Delta P_{\max}$ is increased is slowly reduced with increasing number of stages. In the specific case of $P_{in}=1\,\text{kPa}$ the pump starts to operate in the increasing region of $\Delta P_{\max}$ in terms of P_{in} (see Figure 3.18). Consequently, starting at $P_{in}=1\,\text{kPa}$, every added stage, compared to the previous one, contributes with a larger $\Delta P_{\max}$ until the pressure of $P_{in}=5\,\text{kPa}$, corresponding approximately to the peak value of the pressure difference $\Delta P_{\max}^{peak}$, is reached. Thus, a more detailed view for $N\le 100$ is shown in Figure 3.20 (right). It is clearly seen that the pressure difference with respect to the number of stages for $P_{in}=1\,\text{kPa}$ is qualitatively different compared to all other P_{in} values and is increased more rapidly. Of course, once a sufficient number of stages has been added and the inlet pressure for the next stage becomes higher than $P_{in}=5\,\text{kPa}$, then the pump operates in the decreasing region of $\Delta P_{\max}$ in terms of P_{in} and it behaves qualitatively similar to all others. Overall, it is observed that for a multistage pump with $N\ge 100$ the pressure difference generated is very significant and may be of the same order as the inlet pressure or even several times higher, when $P_{in}\le 20\,\text{kPa}$. It is noted that the present results are in excellent qualitative agreement with the corresponding ones reported in [70]. Furthermore, running the present code for some of the geometrical and operational parameters in [70], it has been found that the deviation in the numerical results is small (about 10%) and is due to the corresponding deviation between the kinetic coefficients obtained by the ellipsoidal-statistical used in that work and the Shakhov model implemented here.

Although pump module B targets high ΔP and the mass flow rate is not of major importance, it is interesting to observe its variation versus the number N of stages. In Figure 3.21, the maximal mass flow rate corresponding to zero pressure difference (open system, flow

scenario A) is shown for the same parameters as in Figure 3.20. The mass flow rate is of the order of 10^{-12} or 10^{-13} kg/s and it is low since only one pumping channel is considered per stage. As expected, $\dot{m}_{\max}$ is decreased as P_{in} is decreased, but more importantly, $\dot{m}_{\max}$ is kept constant as the number of stages is increased due to the fact that all stages have the same geometry and the same inlet and outlet pressures. It may be stated that for Knudsen pumps based on the architecture of module B, it is desirable to add as many stages as possible and to operate the pump in low and moderate P_{in}, since $\Delta P_{\max}$ grows with N, while the $\dot{m}_{\max}$ remains constant. The corresponding results for other pumping channel diameters have a similar qualitative behavior.

The evolution of the pressure inside a system vacuumed with pump module B connected at its inlet, while the outlet is at the atmospheric pressure ($P_{out} = 100$ kPa), is analyzed in Figure 3.22, showing the influence of the number of stages and of the pumping channels diameter $d = 5, 10, 20$ μm, with the diameter of the counter-flow channel being always $D = 100$ μm. Three pressure drop regions can clearly be identified: at high pressures (green region), the pressure is reduced very slowly; at intermediate pressures (red region), the pressure is rapidly reduced; and finally, at low pressures (blue region), the pressure keeps reducing at a slower pace. This behavior can be understood by observing the corresponding results in Figure 3.18, where the pressure difference is very small at high inlet pressures, then becomes quite large at intermediate inlet pressures, where the maximal pressure difference is reported (red symbols in Figure 3.22) and, finally, becomes small again at low inlet pressures. These regions of Figure 3.18 correspond to the green, red, and blue regions in Figure 3.22. As expected, the required number of stages to reach the final low inlet pressure is increased by increasing the diameter of the pumping channels. These plots confirm that the optimal operating pressure range of the pump modules B presented is, as pointed above, in the red zone (Figure 3.22), i.e., at moderate and low inlet pressures corresponding to values of the gas rarefaction parameter close to $\delta = 4 - 6$ where $\Delta P_{\max}^{peak}$ is found (Figure 3.18).

3.3.4 Pump module C: multi-stage pumping with multiple parallel pumping channels and a single counter-flow channel

Module C is a multistage system, where each stage consists of n parallel pumping channels, followed by one counter-flow channel, targeting both high pressure differences and mass flow

rates. The total pressure difference is obtained by adding the pressure difference of each stage (shown in Figure 3.20), while the total mass flow rate $\dot{m}_n$ is calculated by multiplying the mass flow rate of a single microchannel multistage system (shown in Figure 3.21) times the number n of parallel microchannels.

The performance curves of pump module C, showing the variation of pressure difference ΔP versus the total mass flow rate $\dot{m}_n$ (general case, flow scenario C), are plotted in terms of the number of stages N in Figure 3.23 for $N = 1, 5, 10, 20$ and in Figure 3.24 for $N = 40, 100, 200, 500, 1000$, with inlet pressures $P_{in} = 1, 5, 20, 100$ kPa. They are presented in different figures for clarity purposes, since going from $N = 1$ up to $N = 1000$ the pressure difference is increased about two orders of magnitude. The pumping channels and counter-flow channel at each stage have diameters $d = 10\,\mu$m and $D = 100\,\mu$m, respectively, while the corresponding characteristic curves for other pumping channel diameters have a similar qualitative behavior. As expected, in all ~~the~~ cases the characteristic performance curves exhibit a pressure difference decrease as the mass flow rate is increased. Since the maximal pressure difference is increased with the number of stages, while the maximal mass flow rate is constant independently of the number of stages (see the discussion in Figure 3.20 and Figure 3.21), the mean slope of the characteristic curves is increased with the number of stages. For a specified mass flow rate, the developed pressure difference is increased as the number of stages is increased; similarly, for a specified pressure difference, the produced mass flow rate is increased with the number of stages. The largest pressure differences are observed at $P_{in} = 1$ kPa and $P_{in} = 5$ kPa for $N \geq 100$ and $N < 100$, respectively, as shown in Figure 3.20. On the contrary, as expected, the mass flow rates are monotonically increased with P_{in}, with a gain of a factor of 5 when the inlet pressure is increased by a factor of 100. Furthermore, it is seen that the performance curves in Figure 3.23 are close to linear. This is justified, since in pumps with a small number of stages, the output pressure is relatively close to the inlet pressure and the corresponding variation of δ and the associated $G_P(\delta)$ and $G_T(\delta)$ along the stages of the pump is small, resulting in almost constant terms in Equation (3.2). However, as N is increased, the outlet pressure is also increased, resulting in a more significant variation of the kinetic coefficients along the pump stages and therefore, the performance curves exhibit a nonlinear

behavior, as the terms in Equation (3.2) develop a larger variation. This behavior starts to appear from $N = 20$ in Figure 3.23 and becomes more evident as N is further increased in Figure 3.24. Another interesting issue is that, as P_{in} is decreased and N is increased, the pressure difference ΔP decreases very slowly as the mass flow rate increases and then, when the mass flow rate approaches its maximal value, the pressure difference rapidly decreases. This behavior, clearly shown in Figure 3.24, with $P_{in} = 1\,\text{kPa}$, is beneficial for pumps operating at low inlet pressures.

In order to maximize the performance of pump module C, it is preferable to operate at low and moderate inlet pressures in the wide range of $P_{in} \in [1-20]\,\text{kPa}$, with as many parallel pumping channels per stage and number of stages as possible, to take advantage of the flattening of the performance curves but not too close to the maximal mass flow to avoid the abrupt decrease of the pressure difference. Then, depending on the application, a larger number of pumping channels or number of stages can be favored in order to achieve targeted performances.

3.3.5 Concluding remarks on the Knudsen pump design targeted towards different performances.

The structure architecture of three thermally-driven micropump designs targeting specific applications have been proposed and the associated performances have been examined. The three pump configurations include single-stage pumping through many parallel pumping channels targeting high mass flow rates (module A), multi-stage pumping with each stage composed of a single pumping channel and a counter-flow channel targeting high pressure differences (module B) and a combination of the former two configurations targeting both high mass flow rates and pressure differences (module C). Modeling is based on kinetic theory via the infinite capillary approach following the methodology described in Chapter 2.

The proposed design is adaptive to specific applications and the thermal management of the pumps is significantly improved because of the involved low thermal conductivity materials and the separation of the hot and cold areas in two different surfaces. The computational investigation has taken into account all foreseen manufacturing and operational constraints, and the optimum performance conditions as a function of the inlet pressure and pump geometry (number of parallel pumping channels per stage and number of stages) have been identified. Micropumps based on the architecture of modules A and B operate more efficiently at inlet

pressures higher than 5 kPa and lower than 20 kPa, respectively. In addition, it is advisable to manufacture pump module A with as many parallel pumping channels as possible and pump B with as many stages as possible. Pump C should be built with both a high number of parallel pumping channels per stage and a high number of stages, although the purpose of the design is to tailor these two quantities for each particular application. Furthermore, their optimum operation range is found to be at inlet pressures between 1 kPa and 20 kPa and a working regime not too close to the limiting maximal mass flow rate.

Based on this particular architecture, the manufacturing of various pump modules have been started. However, due to several unexpected issues, the manufacturing of a prototype have been delayed and not experimental work has been realized. However, the experimental setup has been prepared for future thermal transpiration tests in the samples. More details about all the arising issues are discussed in Chapters 4 and 5.

3.4 Summary

The computational investigation of two different Knudsen pump designs based on different multi-stage configurations has been performed taking into account manufacturing and operational constraints. The analysis has been performed by accordingly integrating the dimensionless flow rates, obtained by linear kinetic modeling into a simple algorithm based on the mass conservation principle.

The first design investigated consists of long tapered rectangular channels exploiting the diode effect. This diode effect produces different performances of the thermal transpiration flow depending on the direction of the flow in the tapered channel. This design aims to build a Knudsen pump without big reservoirs by using instead the difference in performance of the direction of the flow. Four different assemblies combining converging, diverging and uniform cross sections rectangular channels have been evaluated. The pumping performance has been evaluated and the characteristic curves have been obtained for multi-stage pumps up to one thousand stages. Additionally, a particular focus has been made on the converging-diverging assembly in which the diode effect is capable of blocking the flow at certain operating pressure. This critical operating pressure or blocking pressure corresponds to the zero net flow state for the converging-diverging assembly. This way, instead of a Knudsen pump module, a thermal driven diode is developed, opening up a wide range of potential applications in the microfluidic field.

The potential use of this assembly as a thermal driven diode for gas mixture separation or gas actuator based on the temperature has been explored.

The second design investigated consists of three different pump modules targeting different applications based on the arrangement of circular microchannels drilled across the thickness of a substrate connecting top and bottom reservoirs with different temperatures. The main advantage of this design is the separation of the hot and cold side allowing for an easier temperature control to obtain a higher temperature difference. But also, that it is a compact design allowing for either a large number of parallel channels per unit area to increase the mass flow rate, a large number of stages per unit area to increase the pressure difference or the combination of both to find a compromise in performace between the two. This way, the Knudsen pump can be tailored to meet specific applications by arranging a particular number of parallel channels and stages.

Table 3.1: Geometry of single rectangular ducts with $L = 200\,\mu m$, $W = 15\,\mu m$, $H_m = 10\,\mu m$ and various inclination parameters α .

α	1	5	7	10
H_{min} (μm)	10	3,33	2,5	1,82
H_{max} (μm)	10	16,67	17,5	18,2

Table 3.2: Layout data in terms of diameter, number of microchannels, and elementary square area.

Total layout area *a* × *a* (μm × μm)	**Microchannel diameter *d* (μm)**	**Number *n* of parallel microchannels**
200 × 200	50	4
200 × 200	20	25
200 × 200	10	100
200 × 200	5	400

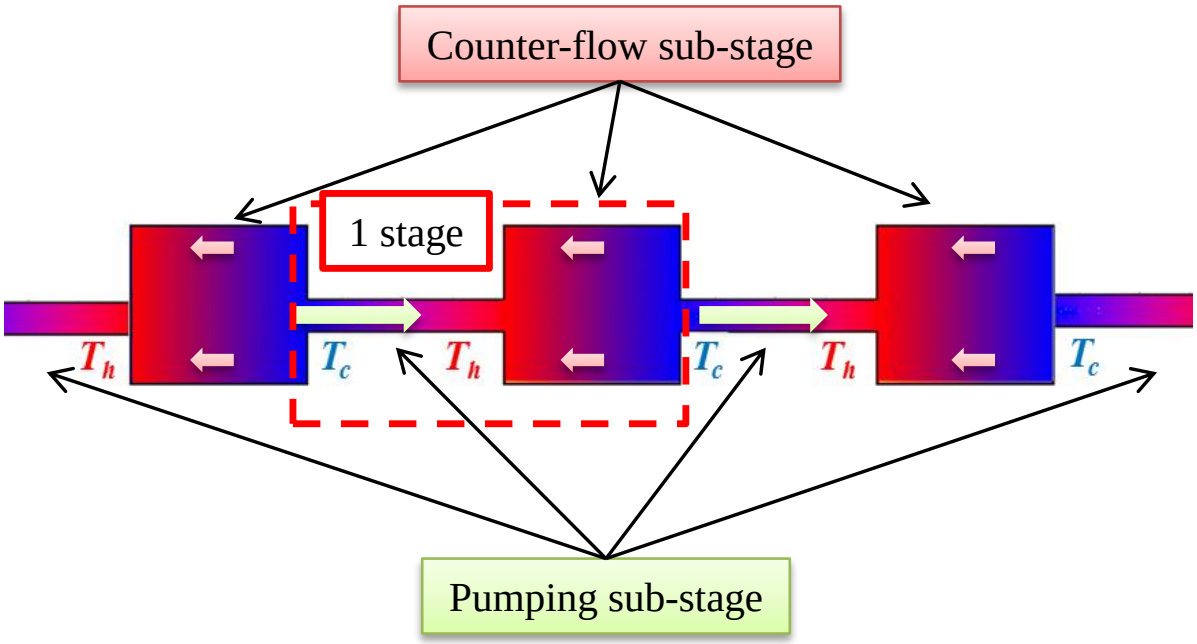

Figure 3.1: Scheme of a classic multi-stage Knudsen pump displaying the pumping sub-stage and the counter-flow sub-stage and the associated thermal transpiration flows.

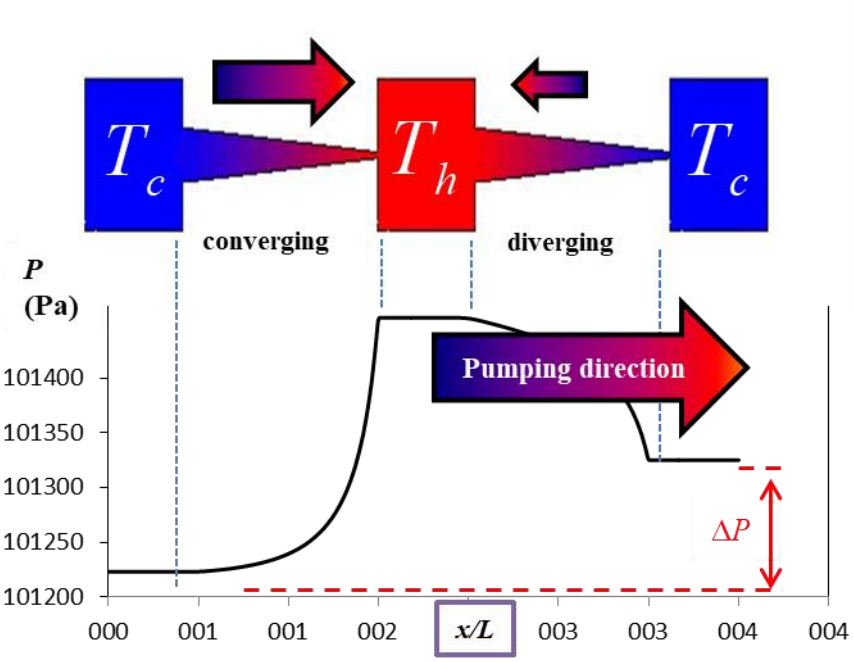

Figure 3.2: Scheme of Knudsen pump based on the diode effect in tapered channels. The converging duct is the pumping channels while the diverging duct is the counter-flow channel. Due to the difference in performance a net flow is achieved.

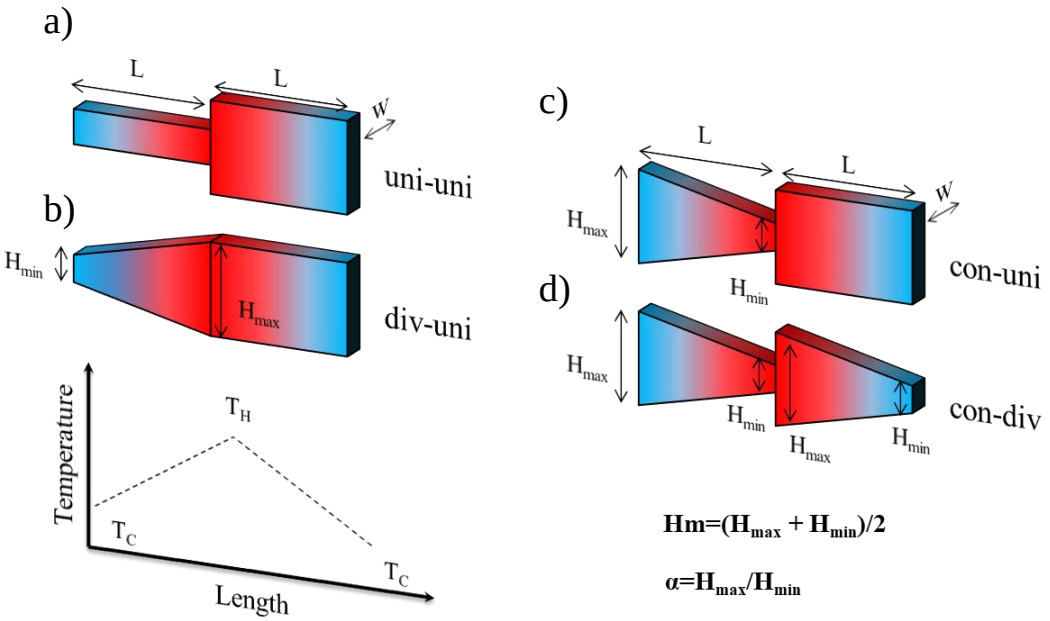

Figure 3.3: Schematic view of the four investigated multistage pump assemblies: a) uniform – uniform ("uni – uni"), b) diverging – uniform ("div – uni"), c) converging – uniform ("con – uni") and d) converging – diverging ("con – div") cross sections.

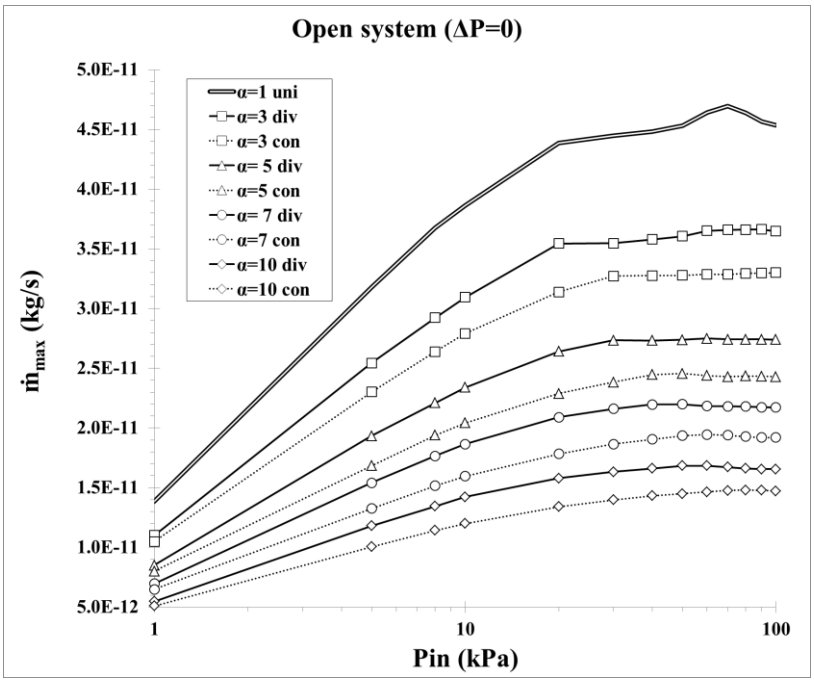

Figure 3.4: Maximal mass flow rate $\dot{m}_{max}$ in terms of the operating pressure P_{in} for thermal transpiration flow with $\Delta P = 0$ (flow scenario A), through orthogonal ducts of converging (con), diverging (div) and uniform (uni) cross sections with inclination parameters $\alpha = [1,3,5,7,10]$ ($L = 200\,\mu m$, $W = 100\,\mu m$, $Hm = 10\,\mu m$).

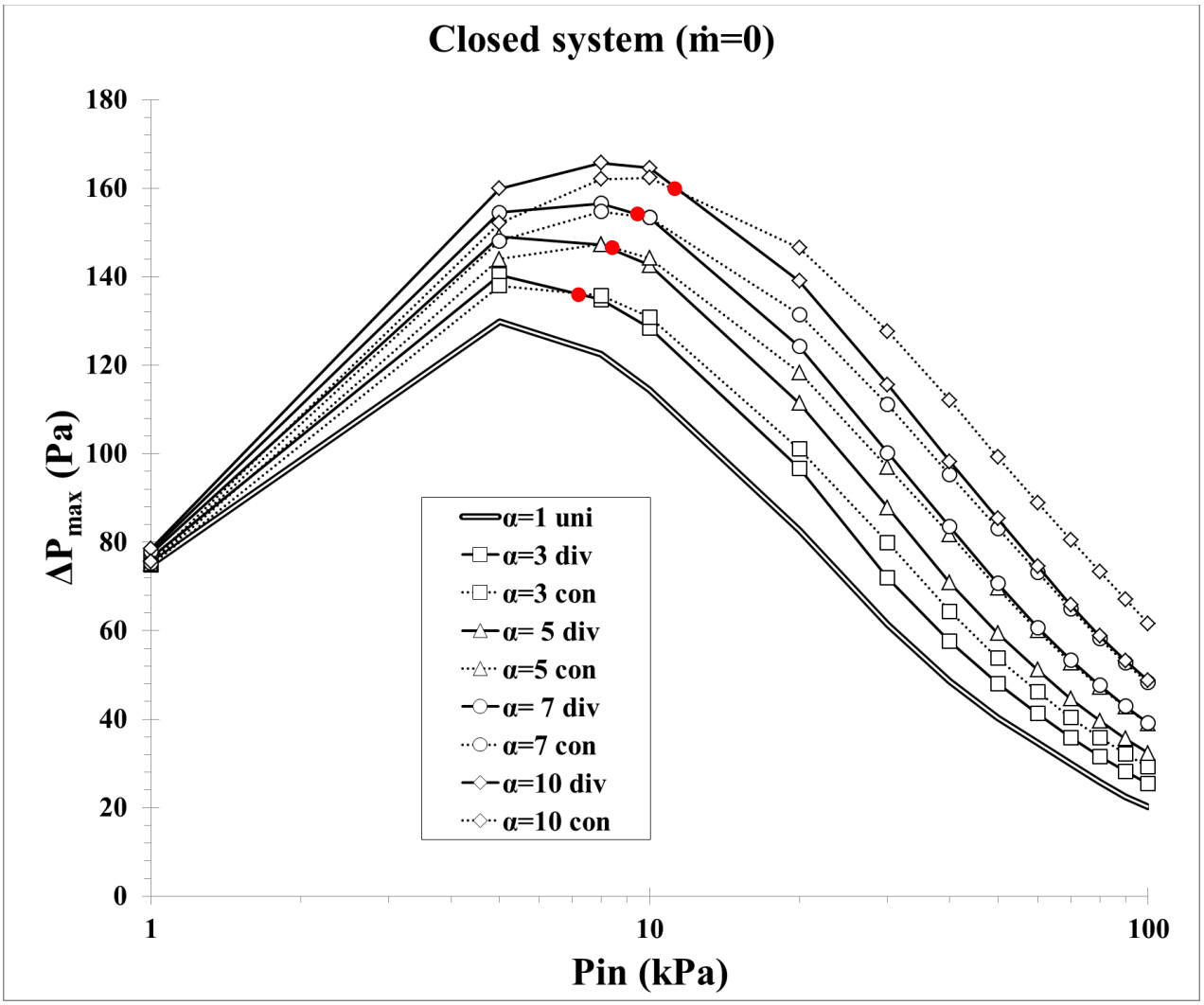

Figure 3.5: Maximal pressure difference ΔP_{max} in terms of the operating pressure P_{in} for thermal creep flow with $\dot{m}=0$ (flow scenario B), through orthogonal ducts of converging (con), diverging (div) and uniform (uni) cross sections with inclination parameters $\alpha=[1,3,5,7,10]$ ($L=200\,\mu m$, $W=100\,\mu m$, $Hm=10\,\mu m$). The red dots represent the critical pressure (blocking pressure) P^* at which the performance of the converging and diverging channels of same α are equal.

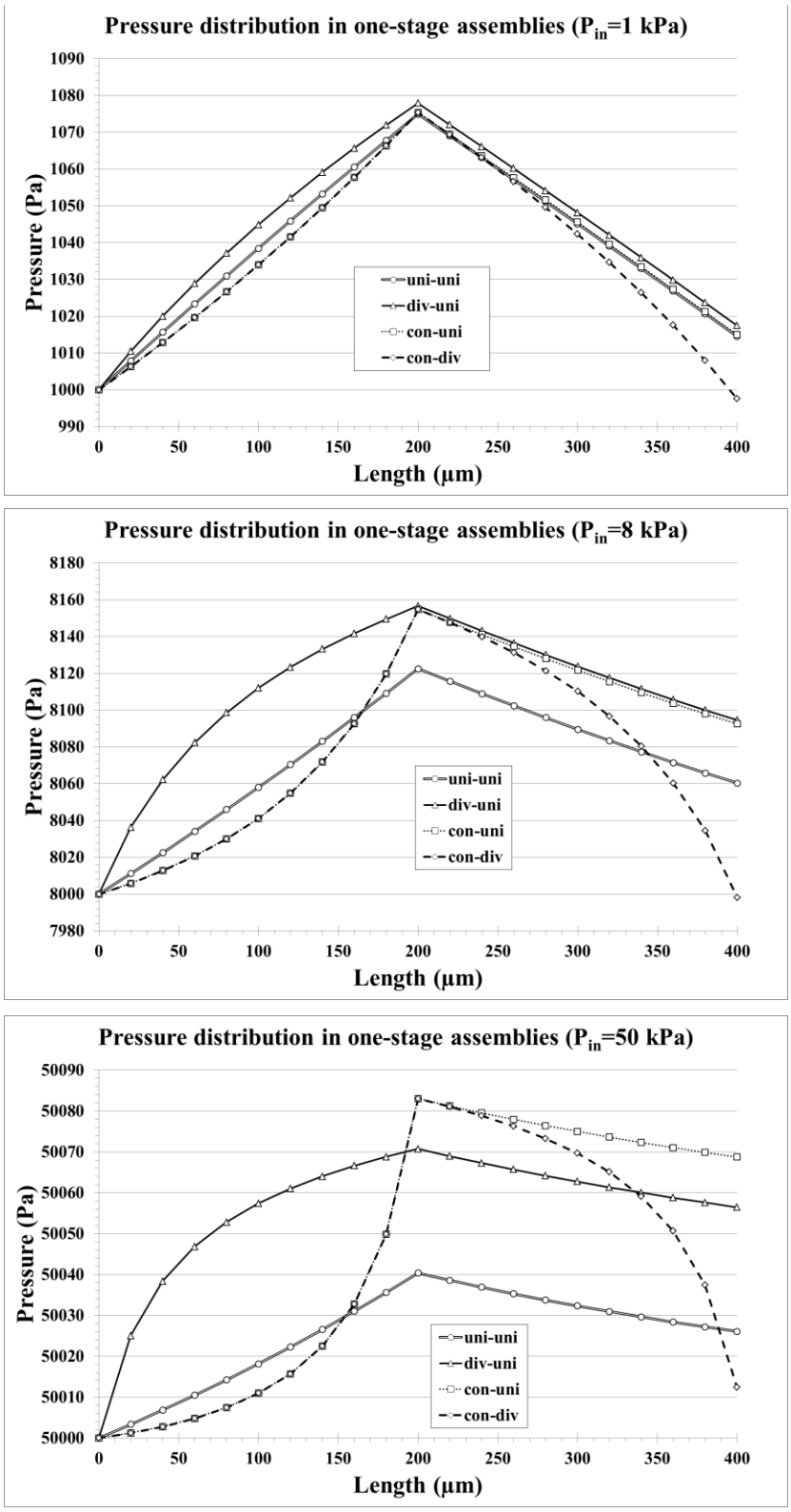

Figure 3.6: Pressure distribution along the channels of one-stage assemblies at three different operating pressures $P_{in} = [1, 8, 50]$ kPa when the system is closed (flow scenario B).

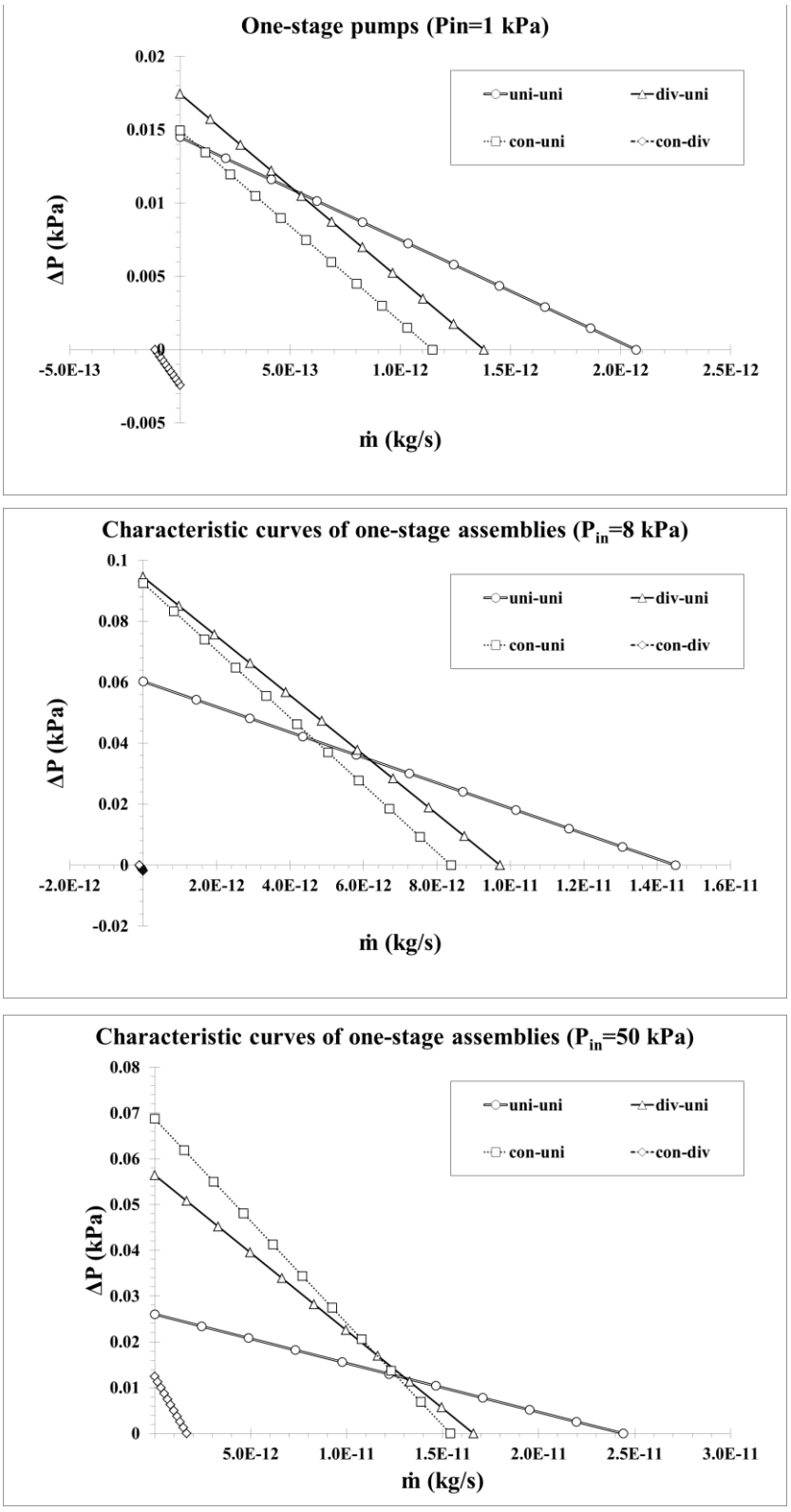

Figure 3.7: Characteristic curves of one-stage assemblies at three different operating pressures $P_{in} = [1, 8, 50]$ kPa (flow scenario C).

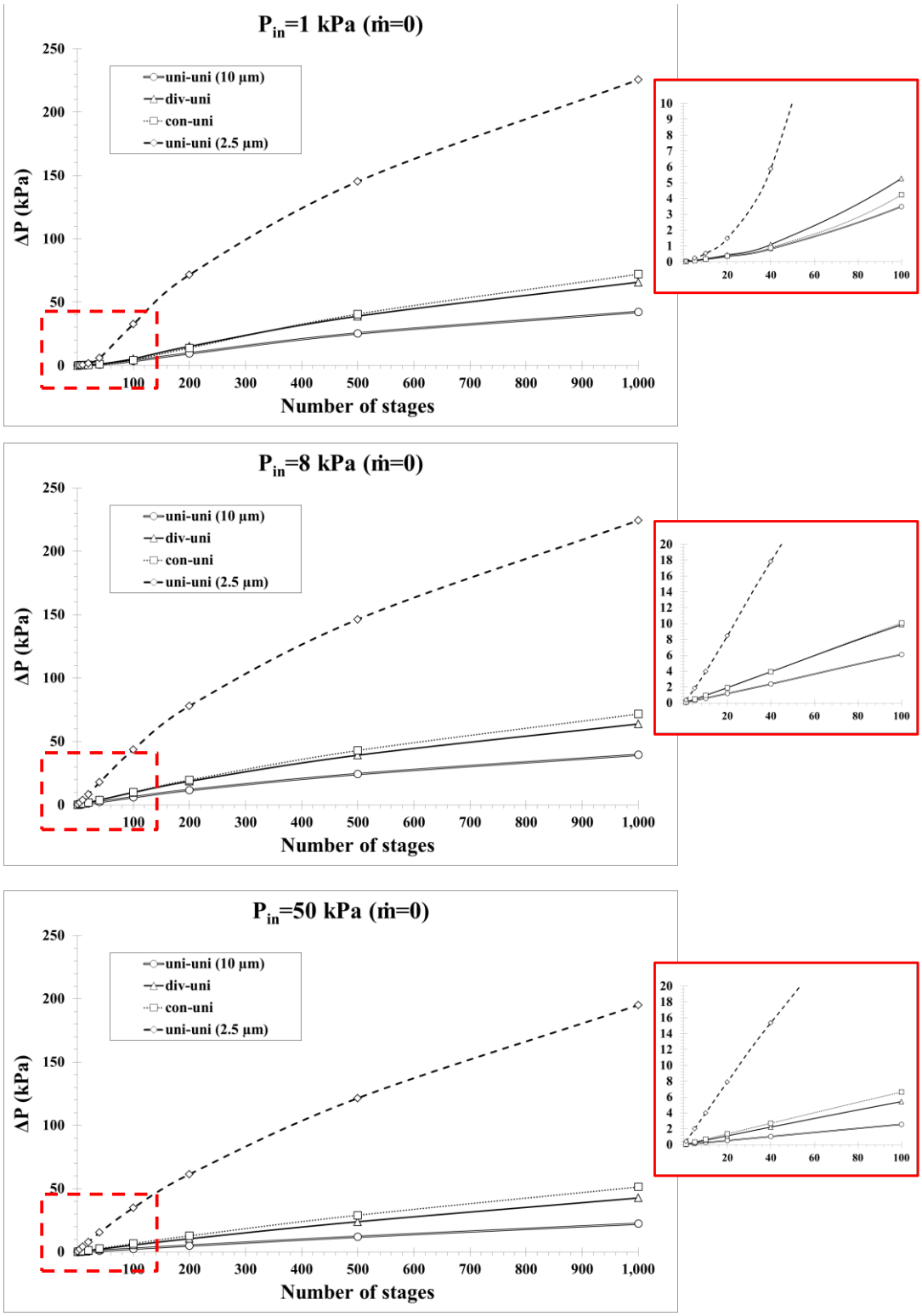

Figure 3.8: Maximal pressure difference ΔP_{max} (flow scenario B) for an increasing number of stages $N = [1-1000]$ at three operating pressures $P_{in} = [1, 8, 50]$ kPa of the four assemblies considered: "uni-uni" (10 µm), "con-uni", "div-uni" and "uni-uni" (2.5 µm). The detail view in red shows the performance of the first 100 stages.

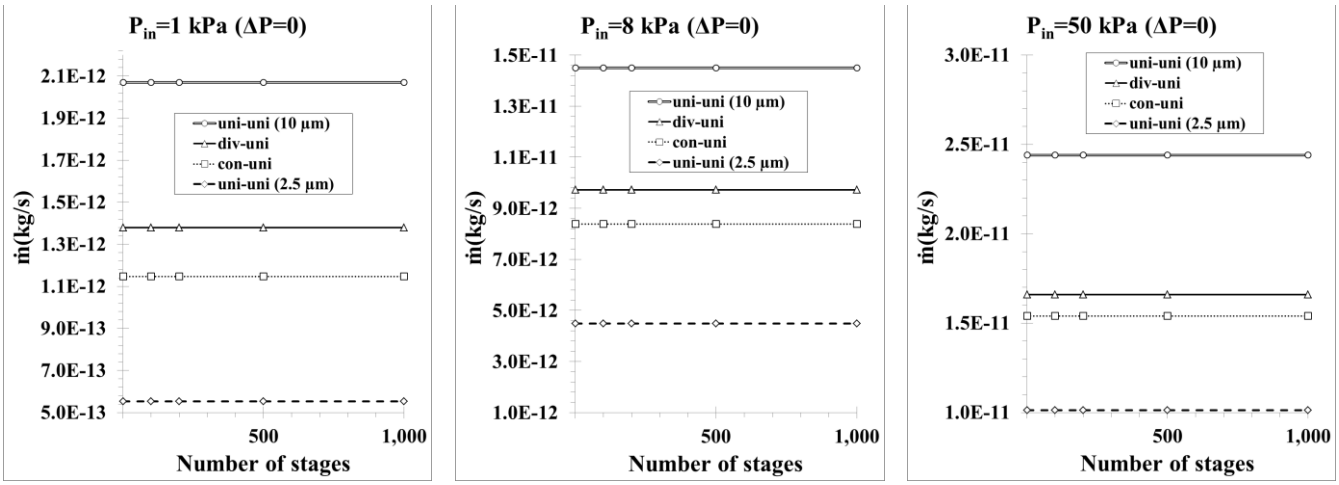

Figure 3.9: Maximal mass flow rate $\dot{m}_{\max}$ (flow scenario A) for an increasing number of stages $N = [1-1000]$ at three operating pressures $P_{in} = [1, 8, 50]$ kPa of the four assemblies considered: "uni-uni" (10 µm), "con-uni", "div-uni" and "uni-uni" (2.5 µm).

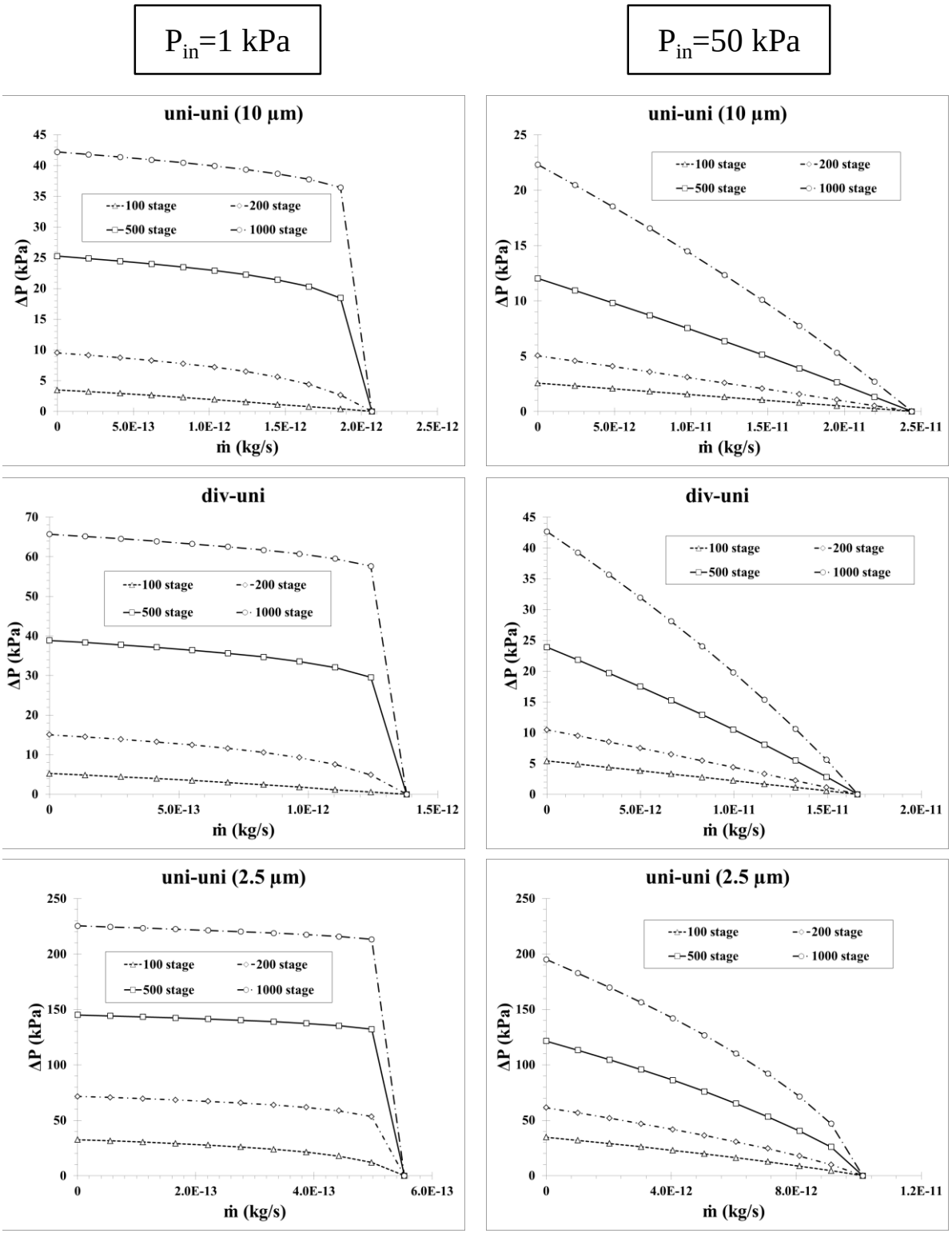

Figure 3.10: Characteristic performance curves (flow scenario C) at operating pressures $P_{in} = 1$ kPa (left) and $P_{in} = 50$ kPa (right) for a different number of stages $N = [100, 200, 500, 1000]$ of three different assemblies: "uni-uni" (10 µm), "div-uni" and "uni-uni" (2.5 µm).

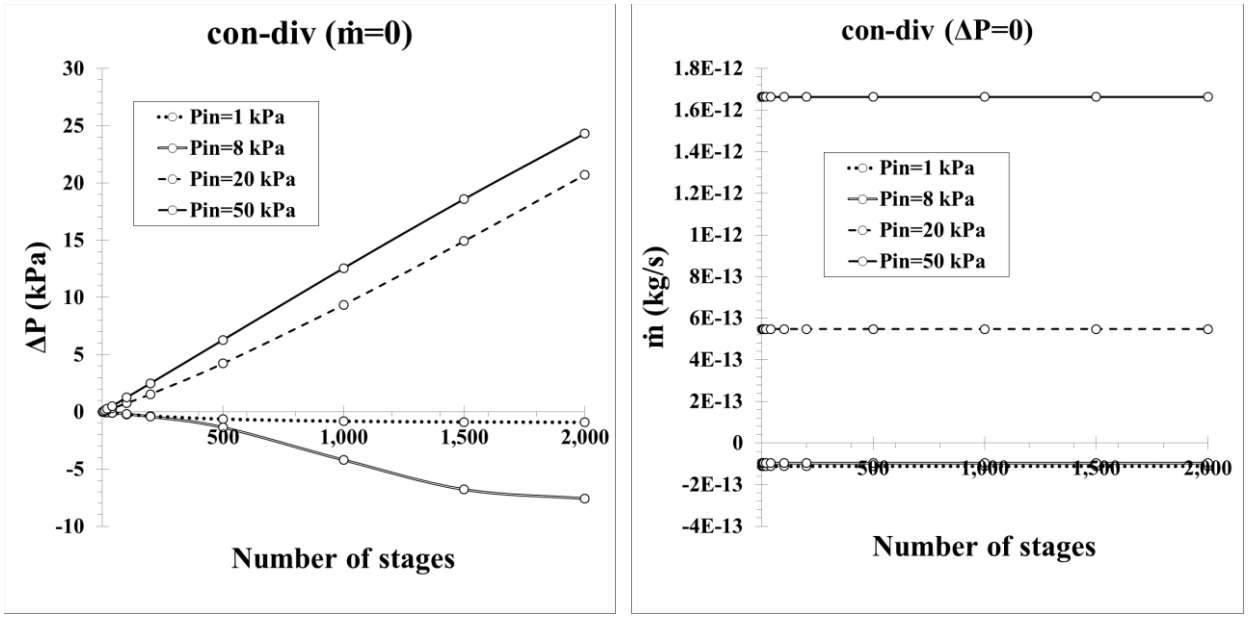

Figure 3.11: Maximal pressure difference $\Delta P_{\max}$ (left) and maximal mass flow rate $\dot{m}_{\max}$ (right) in terms of the number of stages $N = [1-2000]$ at four operating pressures $P_{in} = [1, 8, 20, 50]$ kPa for the "con-div" assembly.

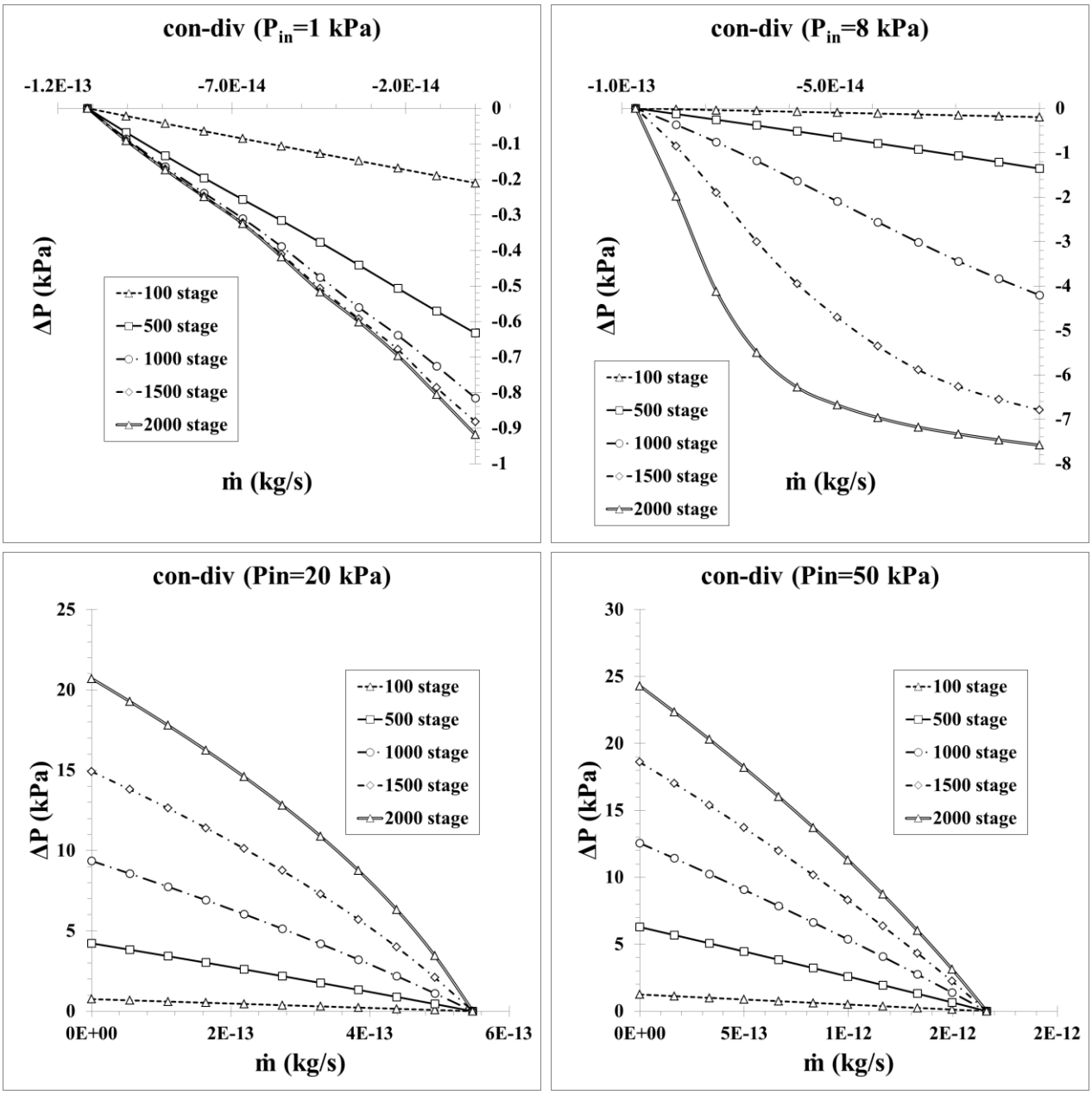

Figure 3.12: Characteristic performance curves (flow scenario C) of the "con-div" assembly at four different operating pressures $P_{in} = [1, 8, 20, 50]$ kPa for a different number of stages $N = [100, 500, 1000, 1500, 2000]$.

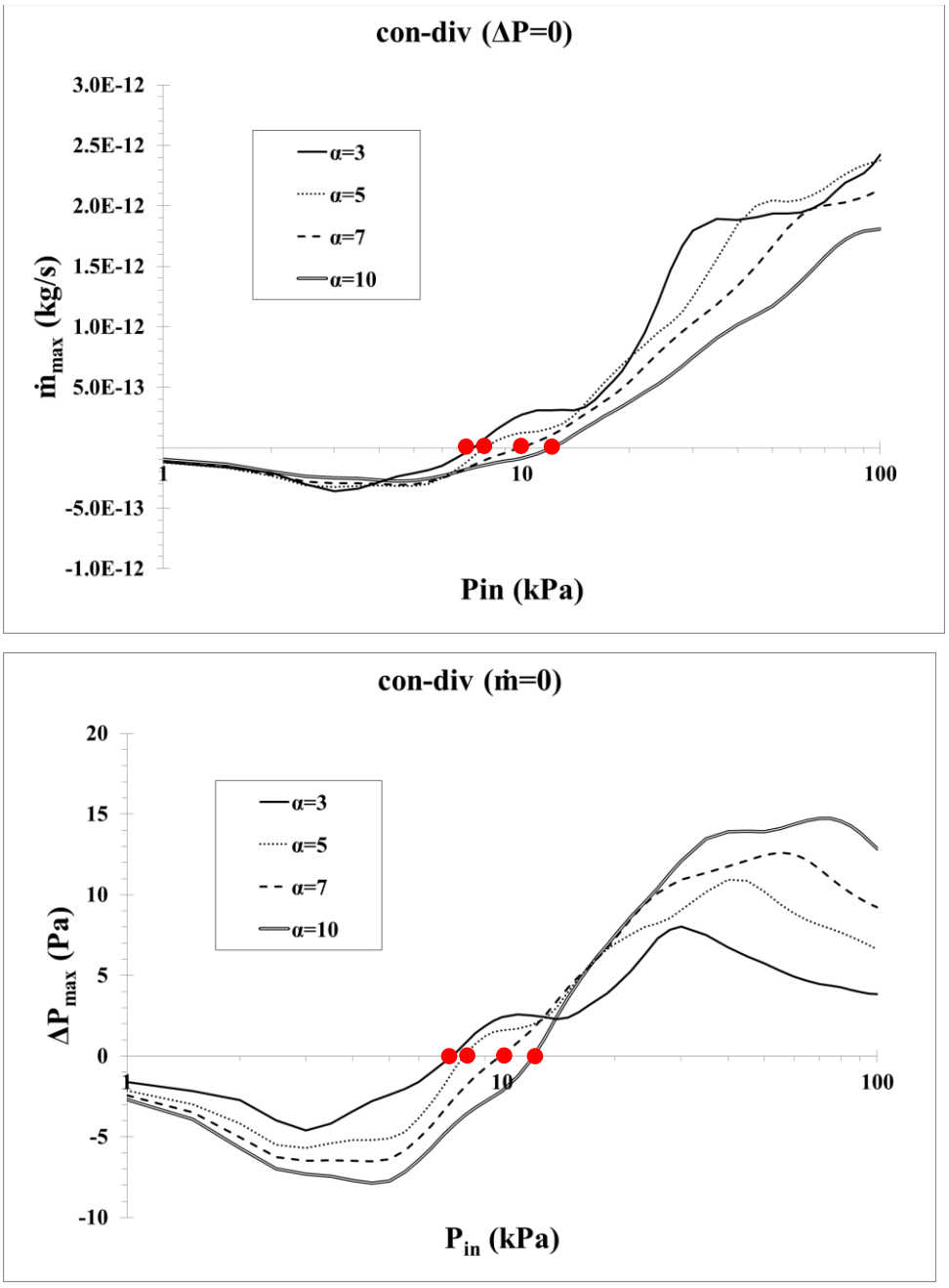

Figure 3.13: Maximal mass flow rate $\dot{m}_{max}$ (top) and maximal pressure difference ΔP_{max} (bottom) in terms of the operating pressure $P_{in} = [1-100]$ kPa for a one-stage "con-div" module with a varying inclination parameter $\alpha = [3,5,7,10]$. The red dots represent the values at which the blocking pressure $P*$ is achieved ($\dot{m} = 0$, $\Delta P = 0$).

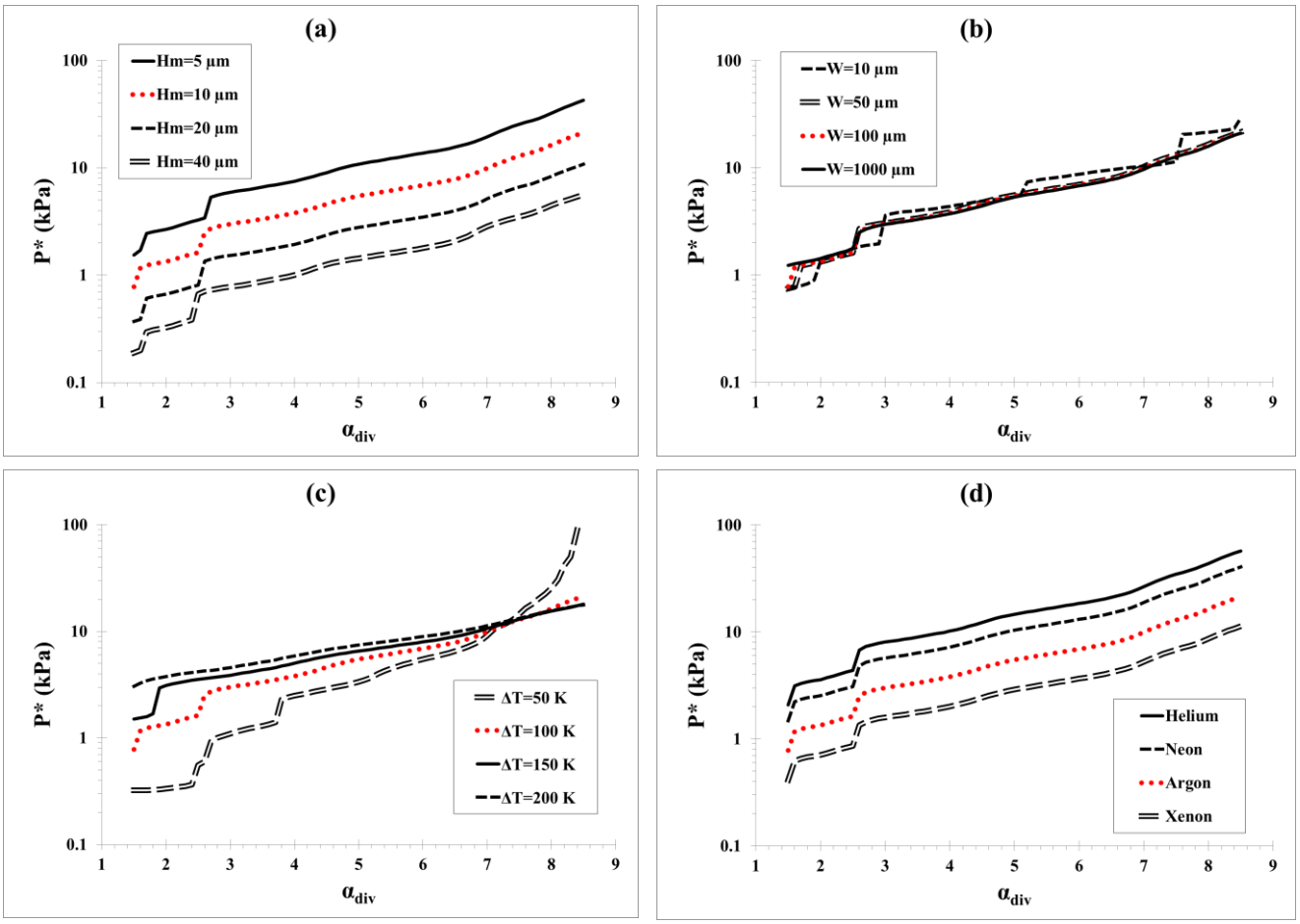

Figure 3.14: Blocking pressure $P*$ for one-stage "con-div" modules with a fixed converging duct ($\alpha_{con} = 7$) and a varying diverging duct ($\alpha_{div} = [1.5 - 8.5]$) for different (a) tapered dimensions Hm, (b) constant depth of the duct W, (c) difference of temperature ΔT and (d) working gas.

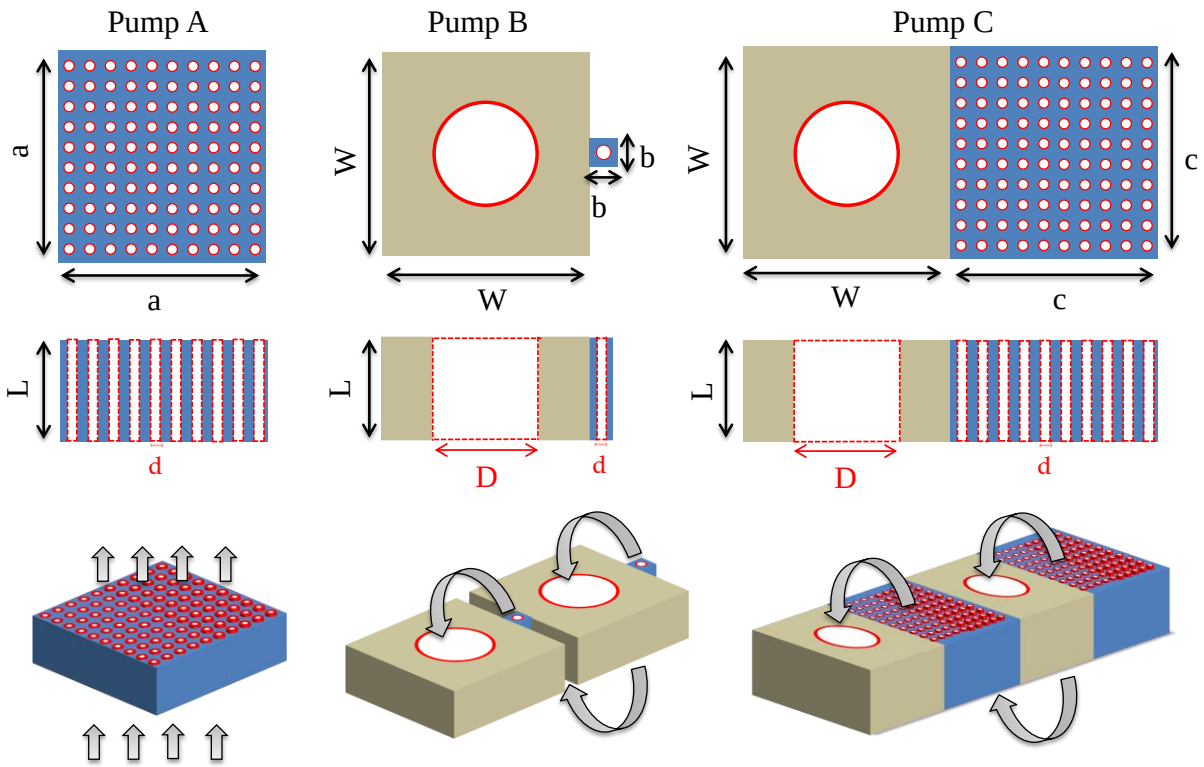

Figure 3.15: Representative view of single-stage pump module A, and of two consecutives stages of multi-stage pump modules B and C. Gray arrows denote the pumping flow direction, the hot and cold regions being at the top and the bottom of each stage, respectively.

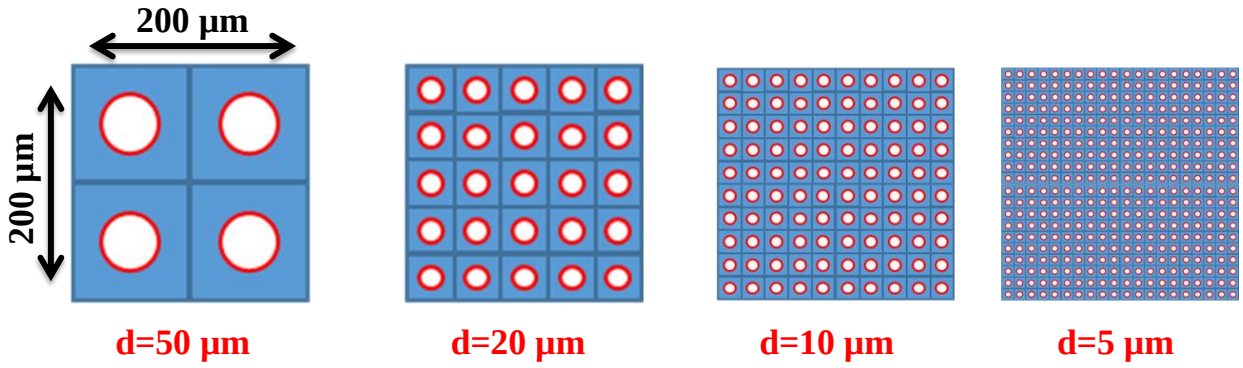

Figure 3.16: View of layouts with increasing the number *n* of microchannels and decreasing the channel diameter *d*, keeping the same ratio between the channels and the overall cross sections.

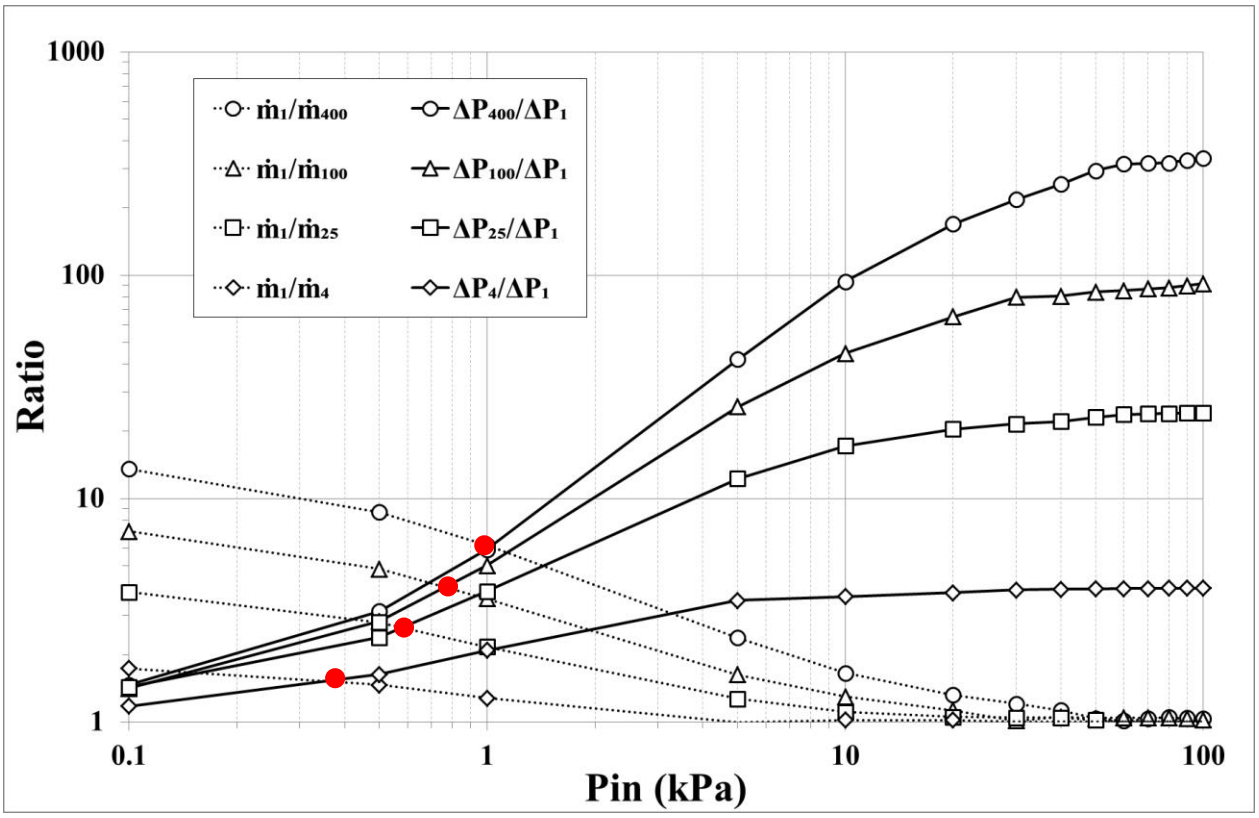

Figure 3.17: Ratios of total maximum mass flow rates $\dot{m}_1 / \dot{m}_n$ and associated maximum pressure differences $\Delta P_n / \Delta P_1$ for various one-stage layouts (numbers of microchannels $n = 4, 25, 100, 400$ and corresponding diameters $d = 50, 20, 10, 5$ µm) compared to the reference layout ($n = 1$, $d = 100$ µm).

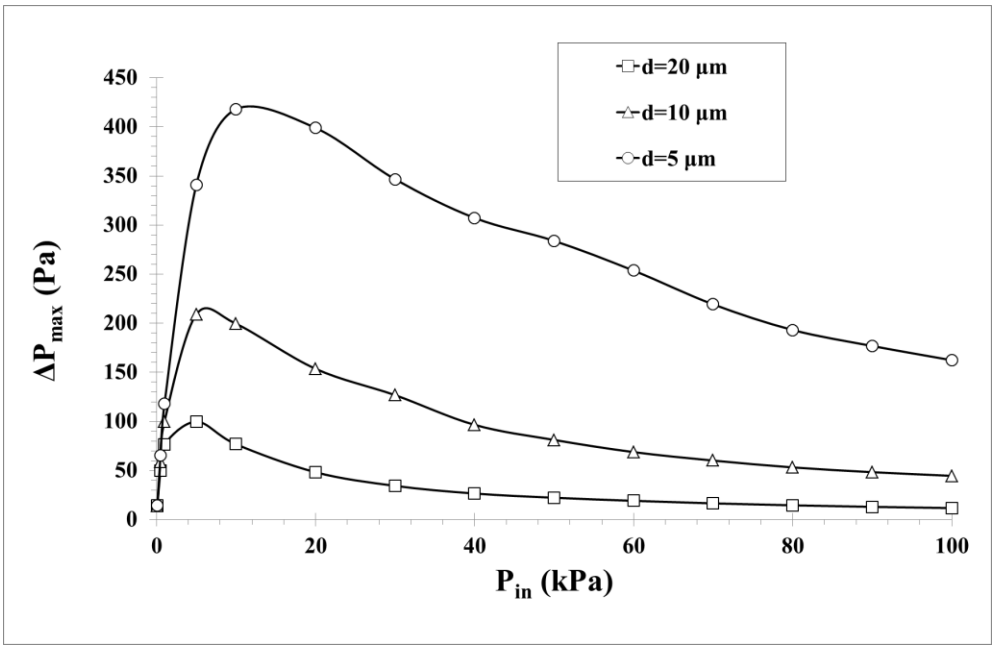

Figure 3.18: Maximal pressure difference versus inlet pressure (flow scenario B) for the one-stage pump module A with $d = 5, 10, 20$ µm. The rarefaction parameter is ranging from 0.03 to 130, and it increases with the inlet pressure and the diameter, providing the maximum pressure difference at $\delta = 4 - 6$, in the transition regime.

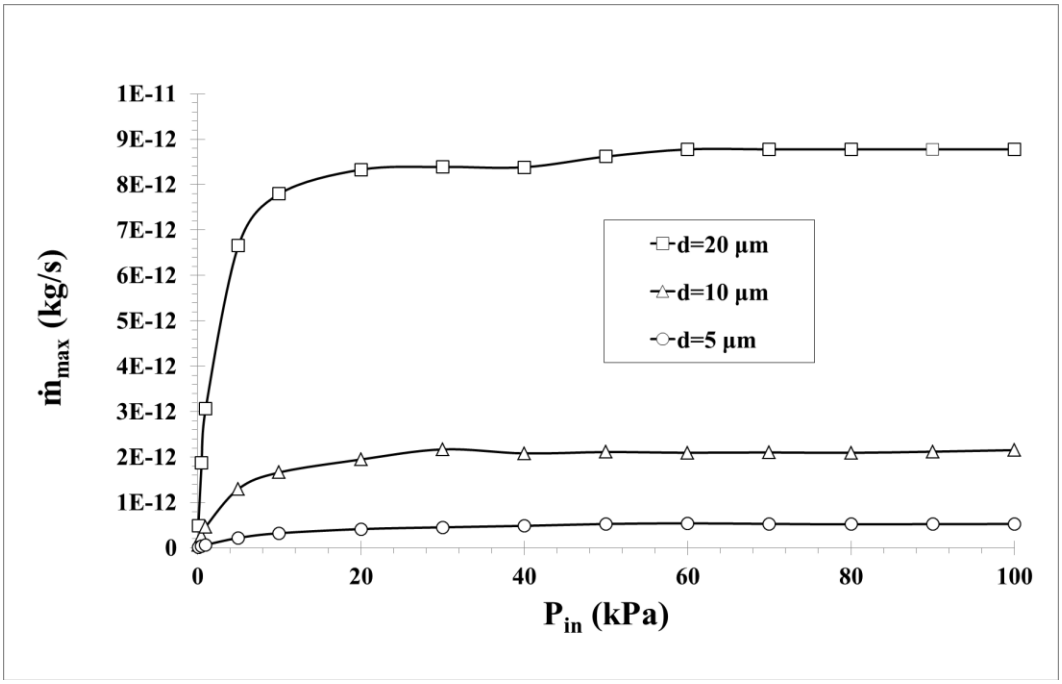

Figure 3.19: Maximal mass flow rate versus inlet pressure (flow scenario A) for the one-stage pump module A with $d = 5, 10, 20$ µm given for a single channel. The rarefaction parameter is ranging from 0.03 to 130, and it increases with the inlet pressure and the diameter, providing the maximum pressure difference at $\delta = 3 - 4$, in the transition regime.

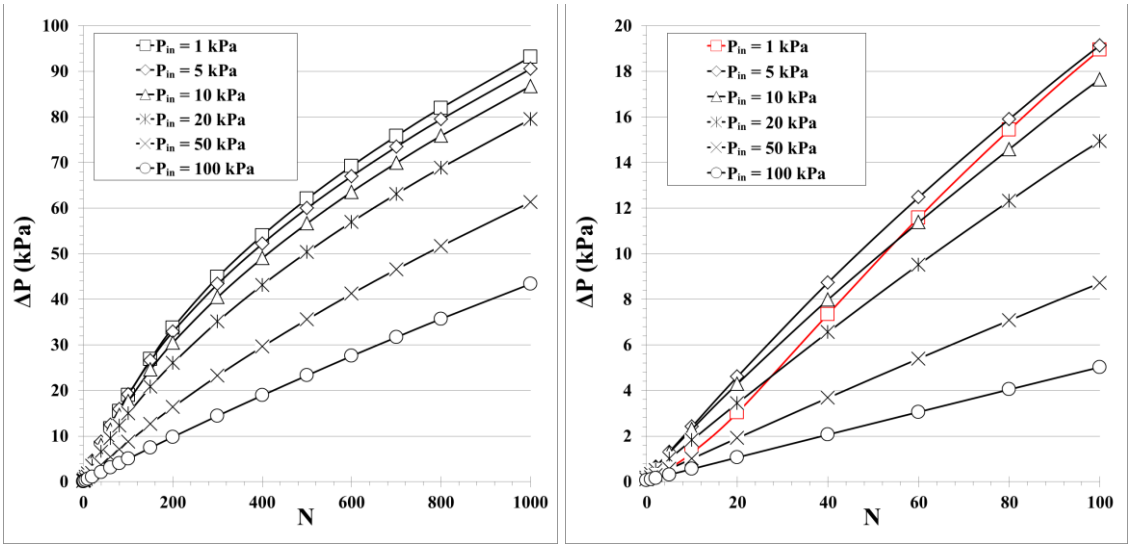

Figure 3.20: Maximal pressure difference (flow scenario B) of pump module B with single pumping and counter-flow channels of diameters $d = 10\,\mu m$ and $D = 100\,\mu m$, respectively, in each stage, at various inlet pressures, versus the number of stages with (left) $N \le 1000$ and (right) $N \le 100$. The range of the rarefaction parameter in the narrow channel is (left) $\delta \approx 0.6 - 56$ and (right) $\delta \approx 0.6 - 12$ for $P_{in} = 1$ kPa, and (left) $\delta \approx 60 - 86$ and (right) $\delta \approx 60 - 62$ for $P_{in} = 100$ kPa. Always, δ increases with the inlet pressure and the number of stages.

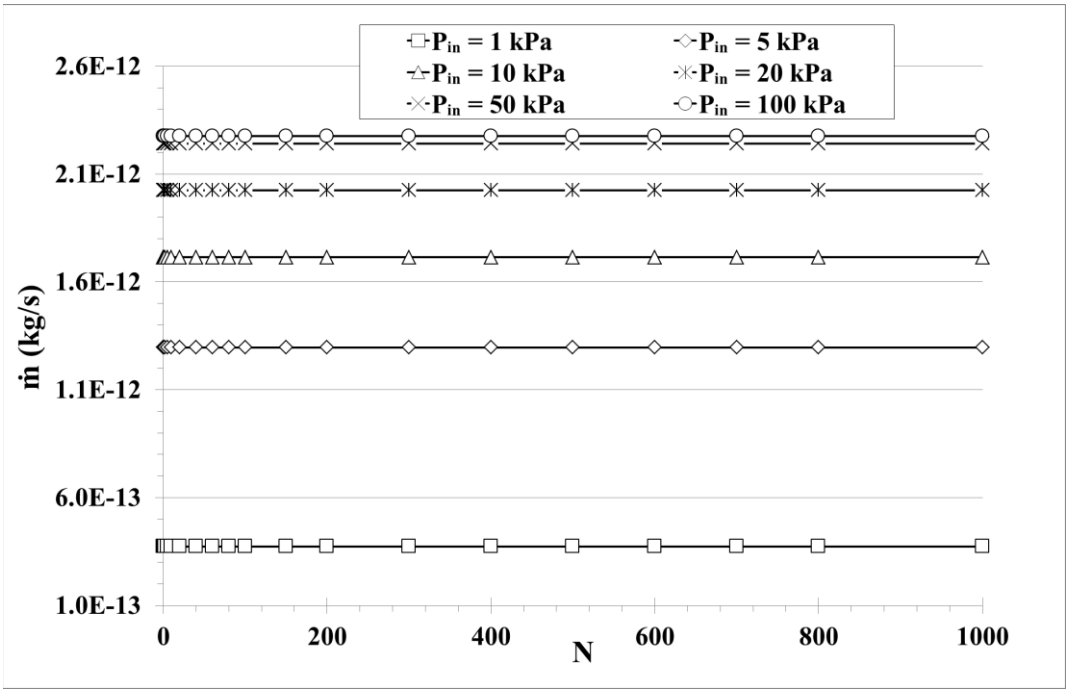

Figure 3.21: Maximal mass flow rate (flow scenario A) of pump module B with single pumping and counter-flow channels of diameters $d = 10\,\mu m$ and $D = 100\,\mu m$, respectively, in each stage, at various inlet pressures, versus the number of stages.

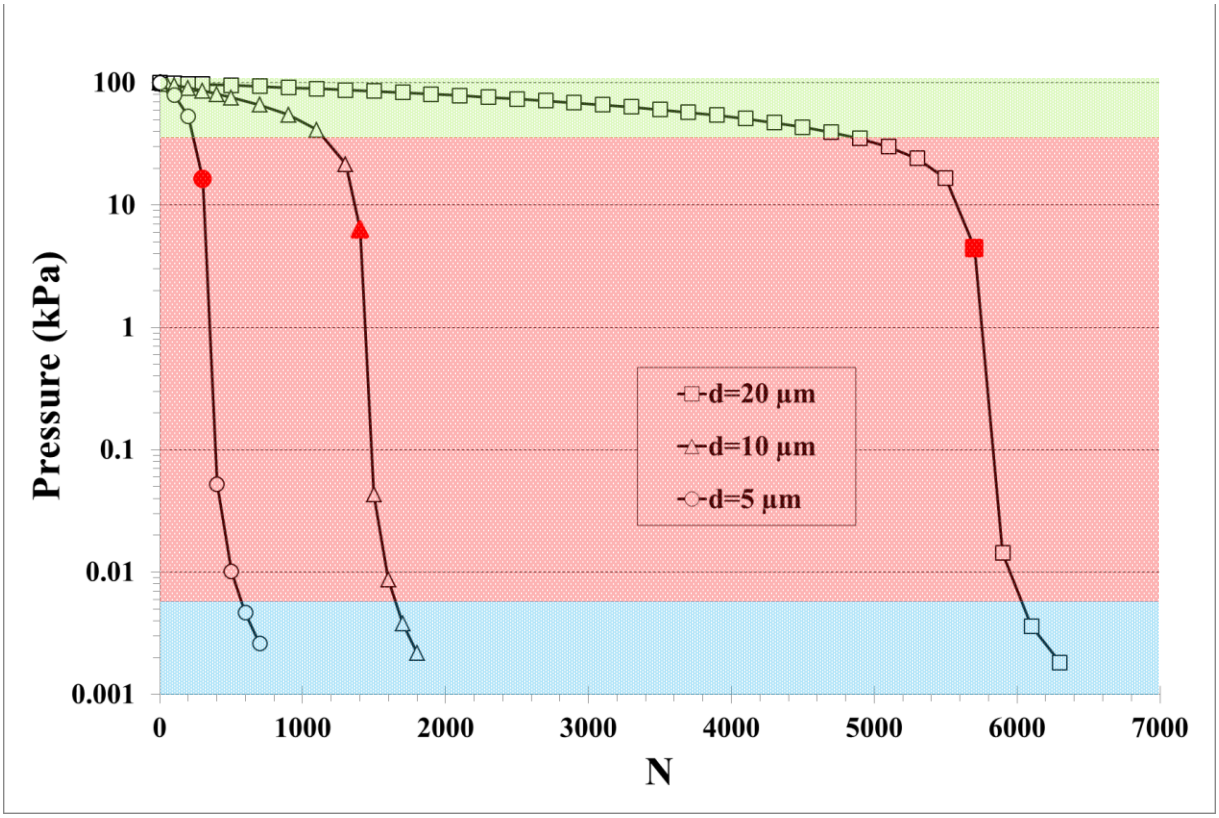

Figure 3.22: Inlet pressure evolution of a system connected to pump module B as a function of its number of stages, considering pumping diameter channels $d = 5,10,20$ µm and a constant outlet pressure kPa (red solid symbols represent the pressure and stage number, where the maximum slope is approximately observed, corresponding to the peak values of Figure 3.17).

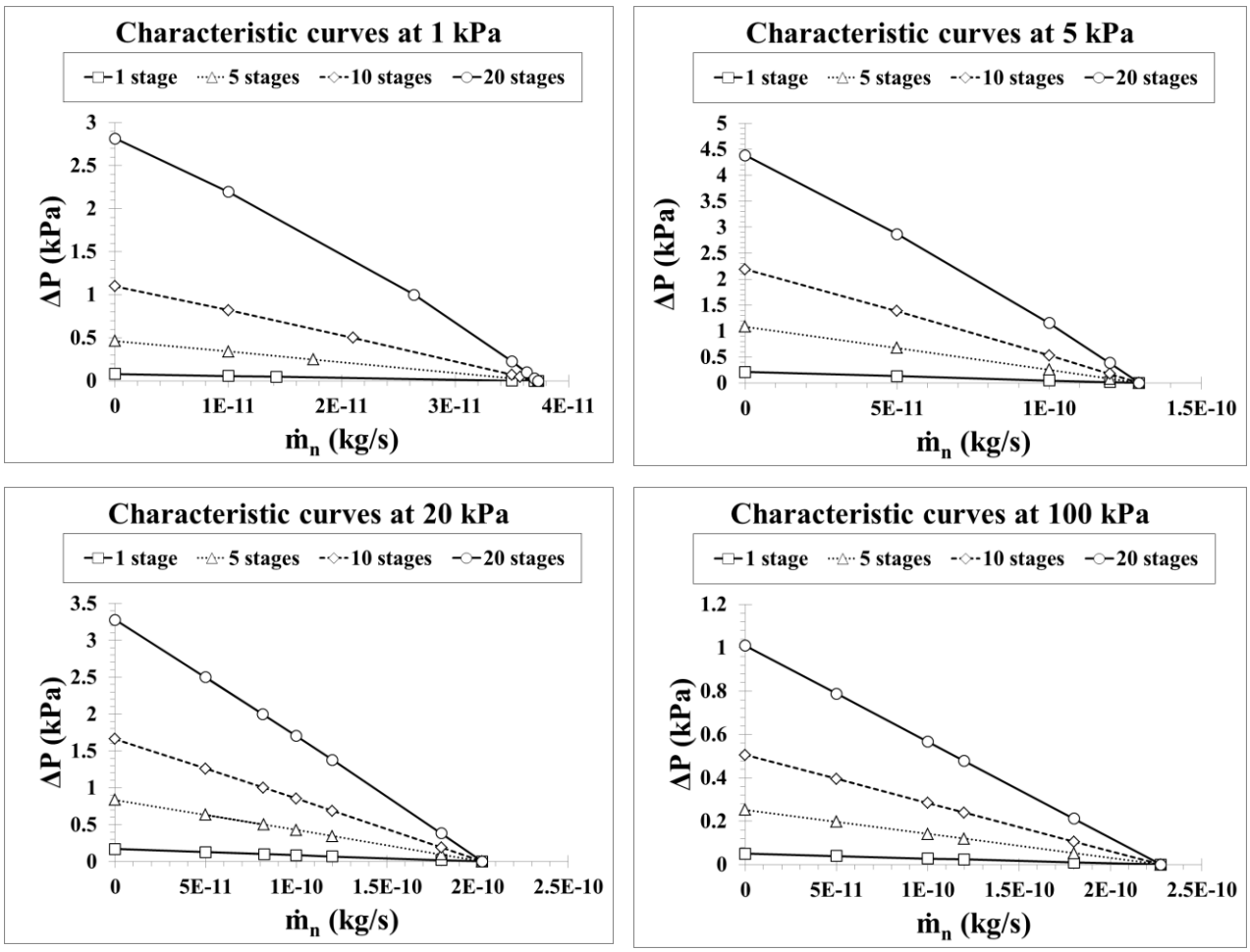

Figure 3.23: Performance characteristic curves (flow scenario C) of a Knudsen pump, based on pump module C, for a number of stages with inlet pressures kPa when pumping channels diameter µm and counter-flow channel diameter $D = 100$ µm.

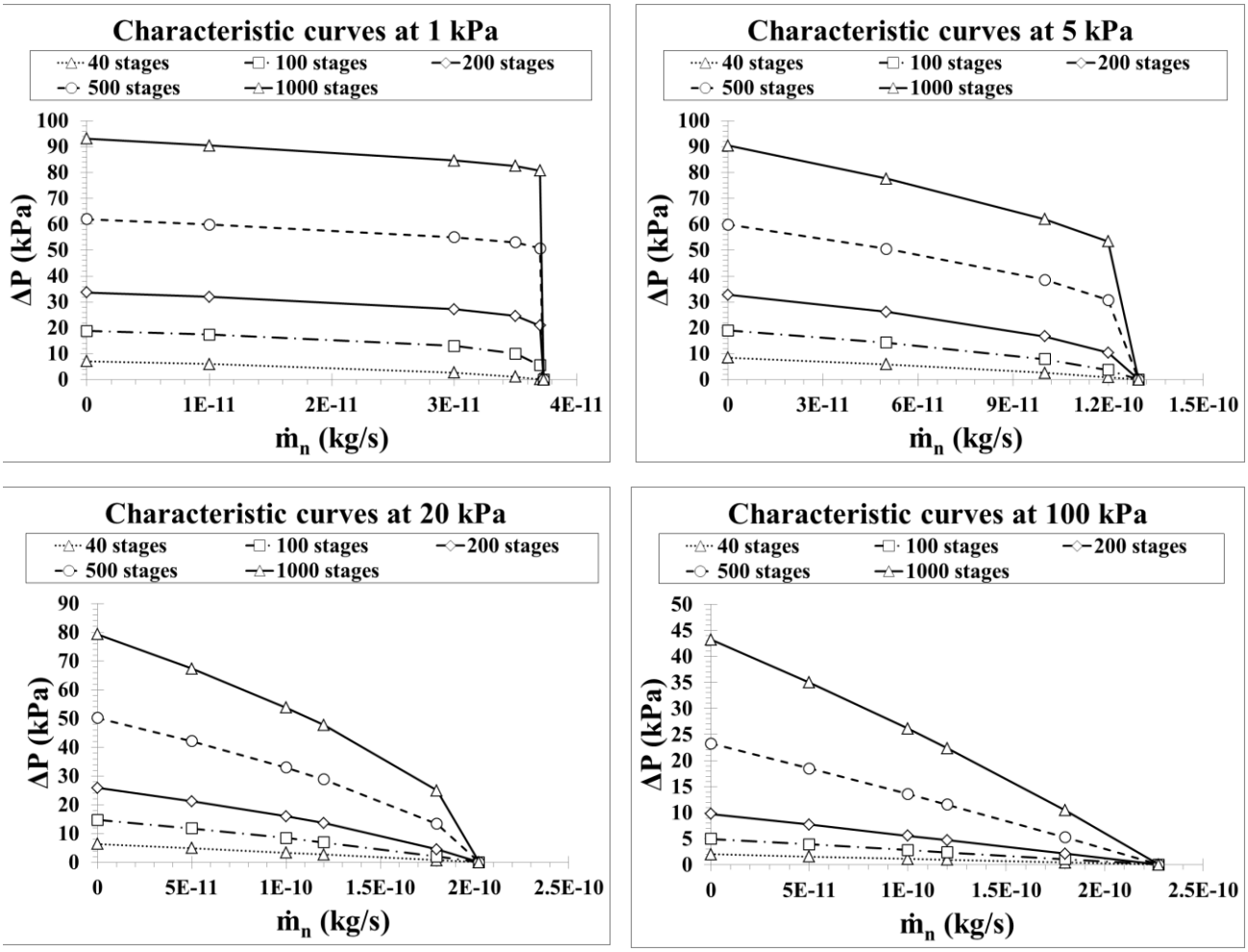

Figure 3.24: Performance characteristic curves (flow scenario C) of a Knudsen pump, based on pump module C, for a number of stages $N = 40,100,200,500,1000$ with inlet pressures $P_{in} = 1,5,20,100$ kPa when pumping channels diameter $d = 10$ μm and counter-flow channel diameter $D = 100$ μm.

Chapter 4

Manufacturing of the proposed Knudsen pump designs

The manufacturing of MEMS and microfluidic devices has been greatly benefited by the rapid development of the microfabrication techniques for the semi-conductor industry. Among the various manufacturing processes developed for MEMS, one usual technique involves the deposition of material layers followed by a patterning with photolithography and etching to produce the intended shapes, allowing for sub-μm resolution. Knudsen pump performance is strongly dependent on the characteristic length of the system and it is significantly enhanced as the characteristic length is decreased. Additionally, although the classical silicon substrate is widely used in MEMS fabrication, materials with low thermal conductivity (such as glass) are here preferred, to control higher temperature gradients and lower the energy consumption of the device. This chapter introduces the manufacturing processes developed in collaboration with LAAS for the manufacturing of the Knudsen pump prototypes presented in Chapter 3.

Initially it has been attempted to manufacture preliminary samples of tapered channels based on etching of a glass substrate. However, when implementing this particular process, several technical difficulties (e.g. equipment in LAAS out of service for long time) have been faced. Following the etching of the samples a fusion bonding process of the glass substrate with a sealing glass wafer that includes the inlet and outlet ports is required. This particular bonding process for glass to glass interface is challenging compared to the typical anodic bonding used for silicon. Several attempts have been made to accomplish the fusion bonding of the samples, but the process failed, resulting to unusable samples. Consequently, this fabrication process has been abandoned.

Next, a different manufacturing process, based on the lamination of dry film (DF) photoresist layers, has been proposed by LAAS. This more advanced approach is characterized by its simplicity, rapidness, good bonding and low thermal conductivity of involved materials (comparable to glass), but it requires certain standards and detailed procedures to achieve the

desired resolution. This manufacturing process can be used for manufacturing the channels along the surface of the device, as well as through its thickness, allowing both designs presented in Chapter 3 to be fabricated with the same technique. Following extensive efforts, certain guidelines have been provided to improve the standard procedures at LAAS in order to achieve the expected resolutions in multi-layered processes. The manufacturing of the tapered channel samples for the first design in Chapter 3, has been accomplished and preliminary experimental work, as described in Chapter 5, has been performed. However, the completion of a fully functional Knudsen pump based on the second design in Chapter 3 has not been feasible due to difficulties that will be further analyzed in this chapter. Nevertheless, it is strongly believed that taking advantage of the improvements of the manufacturing process performed and the new guidelines provided; a prototype should be completed soon in the short future.

4.1 Introduction to typical manufacturing processes for MEMS

MEMS fabrication methods can be classified into two general categories: subtractive techniques and additive techniques. Subtractive techniques involve the removal of part of the substrate, with two main processes: wet etching and dry etching. On the other hand, additive techniques physically add distinct layers of material on top of a substrate, and the two main processes are physical vapor deposition and chemical vapor deposition. Standard macro-scale manufacturing techniques such as casting, injection or milling are effective for generating three dimensional shapes, but they are limited for small scale applications. On the other hand, MEMS fabrication methods typically use processes involving the addition or subtraction of two dimensional layers on a substrate (traditionally silicon or glass) based on photolithography. As a result, the three dimensional structure of MEMS is due to patterning and interaction of two dimensional layers [84], [106].

The photolithography process (Figure 4.1) consists on transferring a particular pattern from an optical mask onto the surface of a substrate, usually a photoresist, by exposing it to ultraviolet (UV) light. The irradiation causes a chemical reaction on the photoresist material that either makes it more or less soluble to certain solvents corresponding to positive and negative photoresist respectively. The solvent used for developing the pattern in the substrate, as well as the particular wavelength required for the activation of the photosensitive reaction, depend on each particular photoresist material [106].

Wet etching consists in the removal of material through the immersion of the substrate in a bath of chemical solution. The etching process can be either isotropic or anisotropic depending on the solution of the bath. Isotropic etching processes remove the material of the substrate at a similar rate in all the directions, while the anisotropic etching processes remove the material faster in a preferred particular direction. The isotropic etching process is normally limited by the geometry of the structure to be etched, with an etching rate reduced in specific areas such as in deep and narrow channels where diffusion limiting factors can even stop the etching reaction. This effect is normally solved by agitating the solution. On the other hand, anisotropic etching processes are faster and since etching is performed in a specific direction, they usually generate better controlled profiles [84].

Dry etching is a plasma-based method able to remove material from a substrate by using suitably reactive gases, usually at high temperatures. The most common process is reactive ion etching (RIE), which generates plasma under vacuum by applying a strong radio frequency electromagnetic field to induce the chemical reaction. However, similar to the isotropic wet etching, achieving high aspect ratio structures is challenging. To produce higher aspect ratio structures, deep reactive ion etching (DRIE) can be used. In this process, a step of etching with a high density plasma (RIE) is alternated with the deposition of a protective polymer layer to keep a particular etching direction [107].

Physical vapor deposition (PVD) consists of vaporizing a solid purified material followed by condensation over a substrate, in order to generate a functional thin film. The deposited material is physically transferred to the substrate without any chemical reaction. The most common methods to generate the physically deposited layer are thermal evaporation and sputtering [84].

Chemical vapor deposition (CVD), on the other hand, is a process in which a substrate is exposed to certain volatile precursors that, after chemically reacting with the surface of the substrate, will generate a thin film of the wanted material. This process generates surface with higher roughness than the PVD process but a wider selection of materials can be deposited [84].

The lift-off process (Figure 4.2) is a method for generating structures of a target material over the surface of a substrate, by using a patterned sacrificial layer. This technique combines the standard photolithographic process to generate an inverse pattern on the sacrificial photoresist material with the deposition of the desired material (typically a metallic thin film produced by

PVD) over the whole surface of the substrate, covering both the areas with photoresist (inverse pattern) and without photoresist (desired pattern). Then, the sacrificial photoresist layer is removed (stripping step) leaving only the desired pattern of the target material. This process is often used for metallization of the substrate, used for example to fabricate heating elements in MEMS [108].

4.2 Discussion on the different manufacturing process for the proposed Knudsen pump designs

As reviewed in Chapter 1, most of the early prototypes of Knudsen pumps have been fabricated with porous media. This was mainly due to the difficulty of fabricating microchannels of a sufficient small size to make the thermal transpiration phenomenon significant. Then, with the development of the microfabrication techniques for the manufacturing, the first Knudsen pump prototypes with fabricated microchannels were developed. The manufacturing processes used for these prototypes have been adapted from the fabrication of other MEMS, involving typical processes such as CVD, RIE and lift-off for metallization patterns [57], [58], [60].

The two designs proposed in Chapter 3 have a fundamental difference in the architecture requiring different manufacturing processes: the tapered channels are built along the surface of the wafer (XY plane) while the circular channels are drilled across the whole thickness of the bulk material (Z direction), as presented in Figure 4.3. The tapered channel cannot go across the thickness of the material, due to the nature of the photolithographic process, where each layer uniformly etches the pattern on the substrate. In fact, the etched pattern is not completely straight and presents some inclination, but this distortion of the shape in Z-direction is usually unintended and very difficult to control. Then, achieving converging or diverging channels in the Z-direction is a very challenging process, except in a <100> oriented silicon wafer with a chemical wet etching (but in this case, the angle is imposed by the crystalline structure of Si, and its value is fixed to 54,7° and cannot be modified). In addition, the length of such channels is limited by the thickness of the substrate layer, i.e. no more than a few hundreds of microns.

4.2.1 Unsuccessful attempt of tapered channels fabrication based on plasma etching of glass

At the beginning of the collaboration with LAAS, only the tapered channel design was considered, with a preliminary mean tapered dimension $H_m = 10$ µm in the XY plane. The first manufacturing process suggested by LAAS was based on the typical etching of a silicon wafer in which the minimum dimension achievable in the XY plane would be around 0.7 µm, with an expected maximum aspect ratio between the inlet and the outlet of the channel ($\alpha = H_{\max} / H_{\min}$) around 10. If the contrast of dimensions should be higher than that, the etching speed could vary along the channel, leading to a non-constant depth in the Z-direction. This unintended non-constant depth, as it has been mentioned before, is quite difficult to control. But if the phenomenon is properly controlled, fabrication of tapered channels with a proper design is potentially possible. With channels minimal heigth 0.7 µm and aspect ratio around 10, the expected etched depth would be 20-50 µm. If the average size in the XY plane is increased, the depth of etching can be higher. Then, if the required depth is larger, a similar process etching the whole thickness of a 400 µm Si wafer is also possible. In this case, the wafer can be sandwiched between two glass wafers, with a uniform and well controlled channel depth equal to the thickness of the wafer (400 µm), but the minimum dimension in the XY plane would be at least 20 µm. However, although this two processes are appealing in terms of minimum achievable size, they need the use of Si, which has a high thermal conductivity and require some additional complex thermal insulating process to generate a high temperature difference. Therefore, it is preferable the use of low thermal conductivity materials.

The next approach in the manufacturing of the tapered channels was based on glass due to its low thermal conductivity, of the order of $1\,\mathrm{W\,m^{-1}K^{-1}}$. Most of the typical processes for Si manufacturing can be adapted for glass with some limitations. LAAS proposed a plasma etching process (RIE) for glass that would be able to achieve a relative good resolution in the XY plane (around 10 µm or even smaller). With regard to the etching depth however, there are more limitations compared to Si. It has been estimated that an average depth of 15 µm or even larger would be possible. Since this is not a process normally performed, to confirm these expectations, some tests should be run at LAAS. Also, the process of fusion bonding glass wafers is challenging and has been only recently developed and implemented at LAAS.

In contrast to the well-established process of deep silicon etching, plasma etching of glass suffers from limitations related to the chemical composition of the material and the formation of non-volatile compounds during the plasma etching process. Plasma etching of several types of glass based material has been reported using various fluor-based chemistries. However, they are characterized by low etching rates (less than 1 μm min^{-1}), thick mask layers required, rough surface generated and a difficulty to generate deep structures [107], [109].

The design of the mask for the manufacturing is shown in Figure 4.4 and the detailed geometrical parameters are provided in Table 1. The layout of 12 different samples of 2×2 cm^2 is presented in Figure 4.4 with two different channels in each sample with a distance of 1.6 mm between the inlet and outlet (minimum distance to connect the sample to the experimental setup). There are 4 distinctive designs: a) single long channels, b) single short channels, c) one-stage long channels and d) one-stage short channels. In each of the samples, one of the channels is tapered while the other is of uniform cross section. Also, samples of designs a) and b) are duplicated to account for possible defects during manufacturing. As it is noted in Table 1, the four designs have been proposed with an average dimension H_m of 50 μm and 100 μm, while the lengths of the long channels and short channels are 7 mm and 1 mm, respectively. The converging and diverging directions of the tapered channels will depend on the direction of the temperature gradient.

The fabrication begun and some preliminary tests were done to check the resolution in terms of minimum achievable size and depth. After a first attempt, the resolution was good and a depth of etching around 20 μm was accomplished. However, the bonding process was not successful and further technical developments were required. Nevertheless, the mask for manufacturing the first tapered channel samples was prepared and the photolithographic steps required before the plasma etching were performed but unfortunately, the equipment for plasma etching was unavailable for some months. This was going to be followed by a planned closure of the cleanroom at LAAS for several months to replace the air circulation and acclimatization systems, resulting on a long delay in the fabrication of the first basic samples, and another laboratory had to be contacted to complete the tapered samples. FEMTO-ST, in Besançon, was able to take on the request and the samples prepared at LAAS were sent to them to perform the glass etching process. At FEMTO-ST the etching of glass was completed showing good profiles (Figure 4.5)

with a depth of etching around 20 µm quite regular over the whole etched surface and a slight deviation angle of the walls from Z-direction of around 5.7º.

The bonding process proposed by FEMTO-ST consisted in fusion bonding of the etched glass wafer with the sealing wafer by pressing them together with a force of 3.5 kN applied for 2 h at 550 ºC. While the feasibility tests of the glass-glass bonding technique was carried out at FEMTO-ST, a similar fusion bonding process had been finally developed at LAAS. This process, involves first the making of the inlet and outlet holes by abrasive blasting of the top sealing wafer, followed by meticulous cleaning polishing and cleaning of the surface to have a very uniform surface to promote adhesion and bonding. This preparation of the wafer included a piranha bath (solution of sulfuric acid, H_2SO_4, and hydrogen peroxide, $H_2O_{2)}$, cleaning with O_2 plasma at and ultrasonic and megasonic cleaning. Once the two wafers are ready, the bonding is performed in a EVG501 bonder equipment in which the two wafers are aligned and put in contact. Then, the temperature gradually increases until 500 ºC and the wafers are pressed against each other for 2 h with a force of 3.5 kN while keeping the temperature. Next, the temperature gradually decreases to the room temperature again for 2 h while the pressing force is maintained.

The first attempt to bond the two wafers was unsuccessful and the process was repeated. However, it was unsuccessful again, and the parameters were changed by increasing the time of the process up to 8 h, the maximum temperature up to 600 ºC and the pressing force between the wafers up to 5 kN. Unfortunately, after several attempts the samples shattered, resulting in completely unusable samples. It became evident that an alternative manufacturing process should be realized.

4.2.2 Discussion about the laser drilling and 3D printing techniques

After investigating other manufacturing techniques such as laser drilling of glass which are able to manufacture channels through the whole thickness of the surface with very small sizes, a new design has been proposed. In this design presented in Section 3.3, the channels of the Knudsen pump have their axis in the Z-direction and are then etched through the whole thickness of the substrate, instead of along its surface (XY plane), as shown in Figure 4.3. Two main advantages result from this design. The first one is the separation of the hot and cold sides, allowing an easier temperature control and the possibility to generate a higher temperature

difference. The second advantage is that the design is more compact and has the capacity of including a large number of parallel channels to increase the mass flow rate (see Section 3.3).

With laser drilling, dimensions down to 10 µm can easily be achieved with a length of the channel equal to the thickness of the glass wafer. This technique theoretically allows a minimum size equal to the diameter of the laser point. However, the usual aspect ratio achieved is around 5, and the drilling of the entire thickness of a typical glass wafer (500 µm) should require rather larger dimensions of the channels cross-sections [107]. Also, this technology is still expensive and to manufacture a large number of small holes as planned for an optimal design would be unreasonable. Moreover, the challenging issue of the glass bonding would be even more complex since the middle glass wafer should be bonded to two other wafers to encapsulate the channels and create a multi-stage system.

To circumvent this problem regarding the bonding, another possible solution of fabrication is based on 3D printing technologies, with a Knudsen pump made out directly in one block. High resolution stereolithography was identified as a potential manufacturing technique with a DILASE 3D equipment. Following this manufacturing process, the device is generated below a thin substrate plate (usually glass) fixed below the Z-moving stage of the 3D printer as shown in Figure 4.6. Then, a first layer of liquid photo-polymer is placed in contact with the upper substrate plate and the regions of this layer to be polymerized are insulated by the laser beam. Once this layer is completed, the Z-moving stage moves up and the next layer is treated following the same process. These steps are repeated successively to complete the device [110].

The thickness of each layer depends on the desired resolution, typically with a 1:1 ratio. For example, to fabricate channels 20 µm in diameter, a typical layer thickness of 20 µm can be used, requiring 10 layers in order to reach channel lengths of 200 µm. This stepped process can generate small problems of alignments between layers, leading to little defaults along the channels. Also, when the Z-moving stage moves up after a layer is finished (polymerization completed), a liquid photo–polymer residue remains in the parts of the previous layers which are not insulated by the laser beam, and should be removed at the end, using a solvent. Additionally, the diameter of the laser beam is 5 µm and cannot be replaced in the equipment. As a consequence, large solid parts within the device are expensive, as they require being insulated by a high number of laser passages, each passage being 5 µm wide. The cost of the final device is a direct function of the required insulation time.

The issue regarding the removal of the remaining liquid polymer with a solvent (propanol) is not trivial. Since the intended device has only one inlet and one outlet, the solvent shall pass through all the stages in series this may be not possible due to the small sizes of the channel and the associated capillary forces. Another the main issue is linked to the fact that the channels connecting the bottom and top reservoirs are suspended in the middle of the device. When the structure of this middle layer is polymerized by the laser insulation, some of the liquid photo-polymer still remains in the cavity (the reservoirs that connects the pumping channels and the counter-flow channels of the Knudsen pump) from the previous layer. Unfortunately, the depth of field of the laser is 100 µm and cannot be changed. This means that when the structure of the middle layer that has to be polymerized is insulated, the cavity placed above it is also partly insulated, and part of the remaining photo-polymer will be polymerized. The only way to avoid this issue is to use a different equipment with a reduced depth of field, but this would lead to a much longer time of fabrication and a non-reasonable cost.

Finally, an alternative manufacturing process was proposed by LAAS. It is based on the lamination of successive dry film (DF) photoresist layers to fabricate multi-layered devices. This particular process had been developed in-house for the prototyping of microfluidic devices in a fast and cost-effective way, while it could also be adapted for batch production [111], [112]. Additionally, with this process both the tapered design samples and the new modular prototype could be manufactured.

4.3 Microfabrication based on the lamination of DF-1000 layers

The proposed DF photoresist (commercialized by EMS) approach is based on a negative epoxy, which is a low-cost material that can be combined with standard photolithography procedures and multilevel laminating by rolling the DF layers with a specific pressure and temperature. Each new layer can then be stacked on the previous one without damaging the patterns of other layers, which leads to the creation of 3D structures, and allows fabricating Knudsen pumps with flows both in the XY-plane (tapered channel design) and the-Z direction (modular design). A scheme of the manufacturing process with 4 layers of DF is shown in Figure 4.7, representing the different steps in the fabrication of the modular Knudsen pump. The fabrication for the tapered channel designs requires only 2 layers (one for the tapered channels in the XY plane and one for the inlet and outlet), simplifying the overall process. The fabrication

process can be summarized as follows: (i) the DF photoresist layer (uncrosslinked DF) is laminated onto a planar substrate (glass or silicon wafer); (ii) following standard photolithography procedures, the DF layer is exposed to UV light and baked to polymerize the photoresist (crosslinked DF); (iii) the DF layer is developed (reticulated DF) in a bath of solvent (cyclohexanone) that removes the material of the non-exposed areas during the photolithography process (the DF layer is a negative photoresist). This process is repeated for each of the successive layers, enabling the production of different patterns. The alignment of each layer has been reported with a deviation of less than 1 µm [111]–[113]. Thus, since the typical thicknesses of the commercialized DF layers are 5, 25, 50 and 100 µm, different layers can be stacked for a specific pattern, to increase and adjust the thickness of that particular pattern (i.e., the length of the channels) in the device. The minimum dimension that can be obtained with this process depends on the thickness on the DF layer to process. It has been demonstrated that a ratio of 1:5 to 1:7 between the dimension in the XY plane and the thickness of the DF was possible [111]. Channels of 10 µm diameter could then be etched within a layer of 50 µm, while structures with a minimal diameter of about 20 µm should be achievable with a layer of 100 µm.

Concerning the substrate in which DF photoresists are laminated, this process can use both silicon and glass with generally good adhesion. In the case of the tapered channel sample, since the heating and cooling systems are in the same plane (bottom part of the substrate), glass is preferred due to its lower thermal conductivity. This will help in keeping a higher temperature gradient along the channel and reducing the power consumption by reducing the heat flux in the surface of the substrate. On the other hand, for the modular design the cold and hot sides are completely apart, so that a good heat flux along the two separate surfaces is preferred. Hence, a silicon substrate is preferred to keep a more constant and uniform temperature in the along the same plane.

4.3.1 Design and fabrication of the modular Knudsen pump

For the new modular design, 4 masks are required to pattern each of the 4 layers: a first layer for the bottom reservoirs, a second layer for the pumping and counter-flow channels, a third layer for the top reservoirs and a fourth layer to seal the device and include an inlet and outlet. Six different pump designs are fabricated in each wafer, with different arrangement of the parallel channels and stages.

An overview of the masks designs is provided in Figure 4.8 with details of the 6 samples showing the first layer (bottom) in orange and the third layer (top) in green as well as the pumping and counter flow channels connecting them (dark areas). The details of each sample are summarized in Table 2. Samples A and B have a similar configuration with 900 parallel pumping channels per stage with 50 and 20 number of stages respectively. Sample C has a reduced number of parallel channels per stage in order to arrange a larger number of stages in the same surface. This way, sample C has 330 stages with 100 parallel pumping channels in each stage. Conversely, sample D makes use of the surface to include 4500 parallel pumping channels per stage and only 20 stages. Finally, samples E and F are consisting of a large number of parallel pumping channels but a very small number of stages. In fact, sample E consists of 48,000 parallel pumping channels to enhance the mass flow rate at the cost of a reduced pressure difference, with no counter-flow stage involved (only half a stage) and sample F follows the same architecture but includes 4 stages with 9600 parallel pumping channels per stage.

The diameter of the pumping channels is 10 µm, while the characteristic length of the counter-flow channels goes from the 100 µm to 300 µm, depending on the sample. It is noted that the counter-flow channel does not have a circular but a rectangle shape. This is made in order to have a more compact design, being able to arrange more pumping channels and more stages in the given surface. The arrangement of the channels in the samples E and F is around pillars with a cross shape that helps holding the middle layer. Sample D, however, has a large number of channels but the access and exit of the channels is through a long passage (300 µm) contained in between walls very close together (20 µm); so capillary effects in detriment of the flow are expected in the more enclosed areas further from the entrance/exit of the passage.

The manufacturing of the first and third layers containing the reservoirs (bottom and top) with minimum dimensions of 20 µm could be achieved with DF layers of 100 µm. Then, for the second layer with the pumping channels of 10 µm diameter, a DF layer of 50 µm should be able to achieve the required resolution.

This process was first used to fabricate some tapered channel samples using the mask design previously described. The manufacturing process proved to be quite fast and straightforward. Following the standard procedures at LAAS, within a couple of days, two samples with two layers each were prepared (see Figure 4.9) with tapered channels fabricated in a 100 µm DF layer while the sealing layer with the inlet and outlet was 25 µm thick. This clearly demonstrates

the potential of this technique for rapid manufacturing in comparison with the long process on glass etching. An additional sample with the tapered channels fabricated in a 200 µm DF layer (100 µm + 100 µm) with a sealing layer of 100 µm has been also completed achieving a good resolution even for the increased thickness. However, when trying to manufacture the modular prototype, it was discovered that the standard procedures developed at LAAS were not properly adapted for a multi-layered device and certain improvements are required.

4.3.2 Standard process at LAAS

The parameters of the standard process developed at LAAS depend on the thickness of the DF layers. This is evident since the photolithographic process to polymerize the DF and etch the patterns strongly depends on the thickness of the material different exposure doses, the baking times and the development baths. A detailed description of the whole process is provided below, while the main parameters of the standard process sheets at LAAS for each DF thickness are summarized in Table 3.

- Preparation of the wafer: before the first layer of DF is laminated onto the substrate, the wafer must be completely cleaned and an adhesion promoter is spin-coated to ensure a complete adhesion of the first layer. The cleaning of the wafer can be done either with a O_2 plasma process for 5 min at 800 W or with a piranha bath for 2 min followed by a dehydration of 15 min to ensure the complete evaporation of any liquid residue. Then, 2 mL of adhesion promoter is spin-coated at 4000 rpm for 30 s.
- Lamination: the equipment used for this step is a Shipley 3024. For the first layer the pressure of the rolls should be 2.5 bar at a roll speed of 0.5 m min^{-1} and a temperature of 100 ºC. For successive layers, in order to avoid the collapsing over the previous patterned levels and reduce the stress from the lamination step, a recommended pressure of 2 bar, a roll speed of 1 m min^{-1} and a temperature of 65 ºC are suggested in the literature [111].
- Exposure: the photolithography process has been performed with a Suss MicroTec mask aligner MA6 Gen4 at I-line irradiation (365 nm). The exposure dose depends on the DF layer thickness, as detailed in Table 3, and ranges from 160 mJ cm^{-2} for 5 µm layers to 500 mJ cm^{-2} for 100 µm layers.

- Post-exposure baking (PEB): the baking is done at 100 ºC on a standard hotplate (Electronic Micro Systems Ltd Model 1000-1). The times provided by the standard process developed at LAAS are detailed in Table 3 and depend on the thickness of the DF layer, ranging from 3 to 10 min for the 5 and 100 µm layers respectively.
- Development: the DF is developed in a bath of cyclohexanone and rinsed with isopropanol to clean the solvent. The number of baths and time of each bath is provided as well in Table 3. Following the development, a visual control is performed to ensure that the development step has been completed and there is no residue of the etched material. Additional development is done if required.
- Preparation for next layer: before doing the lamination of the next layer, a plasma activation of the surface of the DF is required. This O_2 plasma process is performed for 2 min at 200 W to activate the interface and ensure the adhesion of the next laminated DF layer. If the plasma activation is too strong (too high energy) the surface of the DF is "burnt" and sealed, reducing the adhesion with the next layer.

This process can be repeated as many times as required for building multi-layered devices such as the modular Knudsen pump.

4.4 Manufacturing of the modular Knudsen pump prototype

As mentioned before, following the standard process developed at LAAS has not led to good results in the fabrication of the second layer, namely the layer with the pumping and counter-flow channels. Regarding the first layer, even with a thickness of 100 or 200 µm (by laminating two layers of 100 µm one after the other) a good resolution has been achieved, with profiles well defined and only slight deviations from the intended dimensions. Some typical examples of first layer are shown in Figure 4.10 for thicknesses of 100 and 200 µm.

The reason of producing a 200 µm layer was to further avoid the collapsing of the following layers over the large spaces left in the first layer. Obviously, with the increase in the thickness of the layer, a larger exposure dose and baking times are required along with a longer development. To obtain a unique 200 µm layer, two 100 µm layers are laminated in immediate succession. The exposure energy density applied is 800 mJ cm^{-2} followed by a PEB at 100 ºC for 10 min. Even though it was expected that the PEB time should be made longer than the one for 100 µm layers

due to the larger thickness, the first attempt for the 200 µm layer with these operating parameters provided very good results. On the other hand, the development takes a longer time than in the case of a 100 µm layer, since the amount of material to etch is doubled. It requires at least 4 baths in the solvent for 3 min followed by 2 additional baths for 2 min, after visually checking that there is still some residue at the bottom of the sample.

For the second layer, the standard process was applied to DF layers of 50 µm following the exposure dose, baking time and development as given in the process sheet (Table 3). However, even though the first layer was good, in the second layer the pumping channels with a diameter of 10 µm were not generated and even the large counter-flow channels were not fully open. Several tries were made following the same process, but none of them was successful in achieving the pumping channels going through the entire thickness of the 50 µm layer. The most probable cause was an excessive polymerization of the second layer due to an over exposure during the photolithography process. Since the DF photoresist is a negative photoresist, the areas that are exposed to UV light start the polymerization reaction which is intensified and completed during the baking. If some of the areas that are not supposed to be polymerized (i.e. the channels of the second layer) receive some UV exposure, they will start the polymerization reaction and it will be difficult to etch the desired pattern. Therefore, the exposure dose and the baking time need to be reduced in order to limit polymerization of the DF around the 10 µm channel so that during the development, the solvent is able to etch the material. However, it is important to note that if the dose is too low, the amount of light reaching the bottom part of the second layer might not be sufficient to properly polymerize the interface between the second layer and the first one, causing major defects and the detachment of the second layer.

Following this idea, an extensive effort in improving the manufacturing process was made, and it has been summarized in Tables 4, 5 and 6, corresponding to the manufacturing of the second layer performed with DF-1050 (50 µm), DF-1005 (5 µm) and DF-1025 (25 µm) respectively. In these tables the main parameters of the manufacturing processes performed are provided for each wafer and each layer, including the exposure dose (PHOTO) and the PEB time (always at 100 ºC). Additional information is provided about the outcome of the lamination (LAMI), the resolution (RESOL) for each layer and the alignment (ALIGN) between layers. Finally, it is indicated if the pumping channels of 10 µm and the counter-flow channels are developed or not, or at least are partially formed.

The lamination is a completely manual process and thus prone to some faults, and it is usually more challenging after the first layer. Usually the lamination was good (OK), but sometimes the lamination was bad only in very specific areas of the wafer (≈OK) while other times it was bad over all the samples (bad). If the lamination is not good, problems around the interface of the layers are encountered and the 10 µm channels have difficulties to form due to the proximity to the walls of the first layer and the faulty interface. However, even if the lamination is not very good, the sample can be used to check a different exposure dose and PEB time to try to find the most suitable parameters. Regarding the resolution and the alignment, they can be checked from the alignment marks of in each sample. An example of good and bad alignments is shown in Figure 4.11 Additionally, every layer includes a small pattern to check the resolution achieved during the process. Some examples showing a good or a bad resolution are presented in Figure 4.12.

The manufacturing attempts are further discussed in Section 4.4.1, Section 4.4.2 and Section 4.4.3 corresponding to a second layer with a thickness of 50 µm, 5 µm and 25 µm respectively The discussion is mainly focused on the resolution of the second layer and how to achieve pumping channels with diameters of 10 µm Nevertheless, even if the second layer was not good, the fabrication of the third layer was attempted in some occasions. In most of the cases in which the third layer was processed, a relatively good resolution was achieved, and the pattern was correctly transferred to the substrate, evidencing that the problem is only related to the second layer. Some representative images of a sample with three layers are presented in Figure 4.13, showing a good alignment and resolution of the third layer even though the second layer has not developed the pumping channels and even the counter channels display some defects.

4.4.1 Manufacturing of the second layer with DF-1050 (50 µm)

In order to limit the polymerization of the DF in the area of the channels, the exposure dose and the PEB time have been reduced. Since the 50 µm layers should be able to achieve the intended resolution of 10 µm, the process was focused in this DF thickness. It is important to note that the original intended diameter of the pumping channels was 10 µm because that resolution had been previously achieved [111], [112]. However, if the channels are over polymerized and the diameters are smaller than 10 µm, it would even be beneficial for the pumping performance in terms of the pressure difference produced. Hence, even if the channels

are not 10 µm in diameter, as long as they connect the bottom and top reservoirs (first and third layers) they samples would be usable. The polymerization of the DF is a coupled non-linear effect between the exposure dose and the PEB. For this reason, it is usually difficult to quantify the influence of each of the parameters, and a long and extensive study is required to evaluate the polymerization of a substrate. Unfortunately, for this particular material this kind study has not yet been reported.

A description of the manufacturing process and results for a second layer of DF 50 µm is presented in Table 4 and summarized below:

- SIP3229: a first attempt to solve reduce the polymerization around the channels was made by decreasing the PEB time from 6 to 5 min (Figure 4.14). Unfortunately, the results were similar to the ones with the standard process, with the 10 µm channels not being developed. In fact, even the big counter-flow channels (rectangles with 100 µm width) have problems to be developed properly, displaying a dark area which is the material too polymerized to be dissolved during the development.
- SIP3226: for the next sample the exposure was reduced from 240 mJ cm^{-2} to 200 mJ cm^{-2} and the PEB time from 6 to 5 min (Figure 4.15). The counter-flow channels started to develop in a better way, only showing some imperfections in particular areas. Still, the pumping channels were not even started to be developed.
- SIP3225: further reducing the exposure dose to 150 mJ cm^{-2} while keeping the PEB time at 4 min (Figure 4.16) produced better results both for the counter-flow channels and the 10 µm channels. However, the 10 µm channels were still only developing for a few µm, and not through the whole thickness of the layer.
- SIP3228: the exposure dose was further reduced to 120 mJ cm^{-2} (i.e. 50% of the standard process) while keeping a baking time of 5 min. However, with such a low dose, the interface between the second layer and the first layer was not properly polymerized and during the development step, most of the DF was removed or damaged (Figure 4.17).
- SIP3465: the exposure dose was set again at 150 mJ cm^{-2} and the PEB time slightly reduced to 3.5 min (Figure 4.18). Similarly to the case of SIP3225, the 10

µm channels started to be etched but they are not completely developed across the entire thickness of the 50 µm layer, even though the resolution mark shows a rather good profile.

- SIP3467: finally an additional wafer with an exposure dose of 135 mJ cm^{-2} and a PEB time of 3.5 min was prepared. Surprisingly, even though the exposure dose was reduced, the resolution was worse than for SIP3465 and the 10 µm channels were still not completely developed.

4.4.2 Manufacturing of the second layer with DF-1005 (5 µm)

During these attempts to develop the process for the 50 µm DF layer, the process was also performed on thinner DF layers to check the feasibility of the process and try to find a comprehensible solution. Obviously the process on the DF layer of 5 µm should be easily accomplished. Since the DF layer is only 5 µm thick, it is very delicate and it can be often ripped apart just after the lamination or the development steps in particular locations where there is a higher stress concentration (i.e. at the edges of the first layer walls. Therefore, it is not recommend to use a DF layer of 5 µm when it is not the first layer. The different attempts using a second layer of 5 µm thickness are detailed in Table 5 and summarized below:

- SIP3439: first, the standard process was followed applying an exposure dose of 160 mJ cm^{-2} and a PEB of 3 min expecting to get easily achieve the 10 µm channels due to the reduced thickness of the second layer. Surprisingly, although the counter-flow channels were properly formed, the pumping channels were not developed at all, still denoting an over exposure also for thinner layers.
- SIP3232: the exposure dose was reduced to 80 mJ cm^{-2} (50% of the standard process) and the baking time was kept at 3 min. The 10 µm channels were clearly formed but due to the low exposure dose, the interface between the first and second layer was not properly polymerized, resulting in the detachment of the second layer in some areas of wafer in a similar way as presented in Figure 4.17.
- SIP3385: finally, with an exposure dose of 100 mJ cm^{-2} and a PEB time of 2.5 min the sample was successfully completed (Figure 4.19) with the targeted resolution achieved. The interface of the DF 5 µm layer was now properly

polymerized and the 10 µm channels were completely formed. However, as previously mentioned, the DF of 5 µm is not suitable for any intermediate layer since it is very fragile and can be easily ripped apart as shown in the figure.

4.4.3 Manufacturing of the second layer with DF-1025 (25 µm)

After proving that the process was indeed achievable for the 5 µm DF layer and while different attempts were made for the DF 50 µm, the process was also tested for DF layers of 25 µm (Table 6).

- SIP3392: the exposure dose and the baking time were substantially adjusted in the first try, applying an exposure dose of 140 mJ cm^{-2} and a PEB time of 4 min. The 25 µm DF layer was clearly over polymerized, with the 10 µm channels not starting to develop and even showing some defects on the counter-flow channels similarly.
- SIP3440: another attempt with an exposure dose of 120 mJ cm^{-2} while keeping the PEB time on 4 min was made. This time the 10 µm channels started to develop, but the etching was no complete across the thickness, still indicating over polymerization of the channels from the bottom side of the layer.

4.4.4 Physical mechanism proposed to explain the manufacturing difficulties encountered

The problems encountered in the process look deeper and more fundamental than it was originally assumed and so, a possible explanation has been drafted. Due to the refraction of the light in the second layer and the reflection on the walls of the first layer and the silicon substrate, the light reaches areas that were not supposed to be exposed. A schematic view of the proposed physical mechanism is presented in Figure 4.20. When light crosses the second DF layer, there is always some refraction that can be enlarged due to the deformation of the second layer over the cavities of the first layer. Then, not only because of the refraction inside the DF layer, but also because of the reflected deviated light on the walls of the first layer and the silicon bottom wafer, the area that should not be exposed can receive light from the bottom side of the second layer. With this irradiation from the bottom part, the channel starts to polymerize even when the dose is

very low. For this reason, in many cases the 10 µm channels start to form in the top part, but the solvent is not able to etch the entire channel because the bottom part has been polymerized. This explanation seems reasonable but it is difficult to accurately confirm this proposed mechanism.

One of the solutions to tackle this issue has been to decrease the exposure dose and the baking time to reduce the polymerization of the DF layer as it has been described before. An extensive study of the polymerization rate is still missing for this material and it would be a fundamental work to improve the manufacturing process, not only of this modular Knudsen pump prototype, but for any microfluidic device conceived with this technique. Unfortunately, due to the limited time at the final period of this research project, this evaluation was not possible, but at least some preliminary guidelines have been provided, such as the threshold exposure dose to adequately polymerize the interface of the DF layers of 5, 25 and 50 µm. Another way of improving the resolution of the second layer could be to reduce the thickness of the first layer. That way, even if the light is refracted and reflected, since the depth of the cavity would be lower, the light would have less space to travel towards the center of the cavity where the bottom part of the channel is placed. Finally, without any doubt, the best solution to rapidly accomplish a functioning device would be to change the dimensions of the design just by making increasing the size of the pumping channels.

4.4.5 Manufacturing results with a new mask for the first layer

A preliminary method to check if the main reason for the polymerization of the bottom part of the 10 µm channels is due to the reflection on the walls was tested. A new mask was designed with an increased distance between the walls of the first layer. In addition, since the main goal is to determine if the distance between the walls and the channels is the significant factor in the mechanism, a variety of distances has been included in the new mask.

The new mask design for the first layer is shown in Figure 4.21 and it is compared with the previous layer. Also, additional structures have been added in the form of pillars to better hold the DF of the second layer and reduce the deformation over big cavities. Since only the first layer has been modified, some of the channels of the second layer are over these new wall structures of the first layer. However, this is not an issue since the focus is on the generation of the rest of the channels developing across the whole thickness of the DF layer.

The details of the manufacturing attempts with the new mask for the first layer are detailed in Table 4.7. With the experience acquired from the previous attempts, the first couple of samples were made with a second layer of DF-1050 (50 µm), an exposure dose of 150 mJ cm^{-2} and PEB of 4 min (SIP1048) and PEB of 3.5 min (SIP1049). Unfortunately the quality of the sample was not good due to some defects during lamination, and the results obtained were worse than with the original mask for the first layer.

The last two samples have been manufactured with a first layer of 50 instead of 100 µm, in order to reduce the refraction-reflection problem encountered. Also, the second layer was now DF-1025 (25 µm) instead of DF-1050 (50 µm). For both the 50 and 5 µm layers, the threshold dose to polymerize the interface between layers had been tested and it was around 50 % of the standard process, but for the 25 µm this had not been checked yet. Therefore, an exposure dose of 100 mJ cm^{-2} (50 % of standard process) and a PEB time of 3 min were applied (SIP3652). As expected, this dose was too low to polymerize properly the interface between the DF 25 µm layer and the first layer, resulting in the detachment of the second layer in a similar way as shown in Figure 4.17. The last attempt (SIP3651) was performed with an exposure dose of 120 mJ cm^{-2} and a PEB time of 3.5 min (Figure 4.22). The resolution achieved for the second layer was finally good, even though the alignment was not the best. Finally, the pumping channels were completely developed and traversing through the entire 25 µm layer as it can be better observed in the SEM image (scanning electron microscopy) in Figure 4.23.

This final result was encouraging with good profiles developed for the pumping channels accomplishing the targeted resolution. Consequently, it is expected that a prototype will be completed following this work with the guidelines provided.

Still, there are many issues to solve, such as evaluating the polymerization of the DF layers, the behavior of the light within the cavity and the influence of the distance between walls. Additionally, several things can be improved in the design, such as the addition of more support columns in the first layer to reduce the deformation of the DF layer or the addition of heaters inside the device with a metallization process using the lift-off method. Finally, it is still unclear if the last successful result is due to the reduction of the thickness in the first layer, the use of appropriate parameters for the exposure and PEB, or a combination of both. Further investigation should follow the efforts presented in this chapter to better address the issues encountered.

4.5 Summary

An extensive investigation of several manufacturing processes to fabricate the designs proposed in Chapter 3 has been performed. The main criteria for selecting the manufacturing process have been the implementation of low thermal conductivity materials for the Knudsen pump and channel characteristic sizes of around 10 µm to generate a good and efficient pumping. The first considered manufacturing approach was deep RIE of glass to realize preliminary samples of the tapered channel design. However, following the etching of the samples, the fusion bonding process between the glass wafers was unsuccessful.

Other manufacturing processes were explored, such as laser drilling of glass or stereolithography with 3D printing equipment, but none of them was well suited for the modular Knudsen pump design. A manufacturing process based on the lamination of DF layers to generate multi-level devices was then investigated. This process is fast and cheap, and a priori free of leakage with a good bonding between layers. The process is quite simple and consists of lamination of a DF photoresist over a planar substrate followed by a standard lithographic process, exposing of the DF layer, baking at 100 ºC and finally developing in a bath of cyclohexanone. Following this process, the tapered channel designs can be manufactured using two DF layers: one for the channels and one for sealing with inlet and outlet holes included. On the other hand, the modular pump design requires at least 4 layers: the first one for the bottom reservoirs, the second one for the pumping and counter-flow channels, the third one for the top reservoirs and the fourth one for sealing the device with inlet and outlet holes included.

Using this method, a couple of samples with tapered channels were completed with a good resolution and aspect ratios up to 20. This first result was very encouraging; however, when trying to fabricate the modular Knudsen pump design several issues were encountered. First of all, the standard process developed at LAAS was not able to achieve the expected resolution in a multi-layered device. In the case of the modular Knudsen pump, the second layer which contains the pumping and counter-flow channels is critical. Using the standard process, the pumping channels were not developed. Even the counter-flow channels, which are much bigger, were not properly generated. This was very likely due to an excessive polymerization of the layer, making impossible to develop small channels through the entire thickness of the layer.

An extensive effort to solve this issue and accomplish a functional device has been made. An explanation of the mechanism based on the refraction and reflection of the light inside the

cavities of previous layers causing the over polymerization of the base of the pumping channels has been proposed, and several guidelines to improve the entire manufacturing process have been provided. In particular, it has been determined that for DF layers of 5, 25 and 50 µm the threshold exposure doses at which the layer cannot fully polymerize the interface with the previous layer are 80, 100 and 120 mJ cm^{-2}, respectively. Interestingly this dose corresponds to 50 % of the one recommended in the standard process, suggesting a large overexposure in the first manufacturing attempts. An attempt to verify the proposed mechanism and the influence of the distance between the walls and the channels of the second layer has been performed with fabrication of a new mask for the first layer. However, the two wafers done with a DF layer of 50 µm with this new mask do not clarify the situation, due to a faulty lamination. Then, the last sample (SIP3651) finally showed good results regarding the second layer, clearly displaying fully formed channels of 10 µm across the entire thickness of the 25 µm DF layer when an exposure dose of 120 mJ cm^{-2} and a PEB time of 3.5 min were applied. This result is encouraging and suggests that a fully completed device can be completed with this adjusted process.

Still, there are many ways to further improve the process, such as an in-depth evaluation of DF layers polymerization to check the realistic achievable resolution in multi-layered devices, with a clear understanding of the behavior of light within the cavity and its link with the distance between walls.

Table 4.1: Detailed description of the different channels from the tapered channel design mask

		Type	**Number of samples**	***L* (mm)**	***α***
a)	Single long channels H_m = 50 µm	straight	2	7	1
		tapered	2		10
	Single long channels H_m = 100 µm	straight	2		1
		tapered	2		10
b)	Single short channels H_m = 50 µm	straight	2	1	1
		tapered	2		10
	Single short channels H_m = 100 µm	straight	2		1
		tapered	2		10
c)	One-stage long channels H_m = 50 µm	straight	1	7	1
		tapered			10
	One-stage long channels H_m = 100 µm	straight	1		1
		tapered			10
d)	One-stage short channels H_m = 50 µm	straight	1	1	1
		tapered			10
	One-stage short channels H_m = 100 µm	straight	1		1
		tapered			10

Table 4.2: Detailed description of the different modular Knudsen pump samples to be fabricated

	number *n* of parallel pumping channels	**number *N* of stages**	**Diameter of the pumping channels (µm)**	**Characteristic length of the counter-flow channels (µm)**
A	900	50	10	100
B	900	20		
C	100	330		130
D	4500	20		100
E	48000	0		-
F	9600	4		300

Table 4.3: Summary of the parameters provided in the standard process sheet developed at LAAS for the manufacturing with DF layers.

	Thickness (µm)	**Exposure (mJ/cm^2)**	**PEB (min)**	**Development**
DF-1100	100	500	10	3 x 3 min
DF-1050	50	240	6	4 min + 3 min
DF-1025	25	200	5	2 x 4 min
DF-1005	5	160	3	1 x 3 min

Table 4.4: Summary of the manufacturing process with a second DF layer of 50 µm.

WAFER	MASK	DF (µm)	LAMI	PHOTO (mJ/cm^2)	PEB (min)	RESOL	ALIGN	Channel 10 um	counter-flow channel
SIP3307	1	100	OK	500	10	OK	OK	no	bad
	2	50	OK	240	6	bad			
SIP3308	1	100	OK	500	10	OK	≈OK	no	bad
	2	50	bad	240	6	≈OK			
SIP3229	1	100	OK	500	10	OK	≈OK	no	bad
	2	50	bad	240	5	≈OK			
SIP3226	1	100	OK	500	10	OK	OK	no	≈OK
	2	50	≈OK	200	5	≈OK			
	3	100	OK	500	10	OK			
SIP3225	1	100	OK	500	10	OK	OK	start	≈OK
	2	50	OK	150	4	≈OK			
	3	100	OK	500	10	OK			
SIP3228	1	200	OK	800	10	OK	Interface between layers not polymerized		
	2	50	OK	120	4	-			
SIP3465	1	100	OK	500	10	OK	OK	start	OK
	2	50	OK	150	3.5	≈OK			
SIP3467	1	100	OK	500	10	OK	≈OK	start	OK
	2	50	OK	135	3.5	≈OK			

Table 4.5: Summary of the manufacturing process with a second DF layer of 5 µm.

WAFER	MASK	DF (µm)	LAMI	PHOTO (mJ/cm^2)	PEB (min)	RESOL	ALIGN	Channel 10 um	counter-flow channel
SIP3439	1	100	OK	500	10	OK	OK	no	OK
	2	5	≈OK	160	3	bad			
SIP3232	1	100	OK	500	10	OK	Interface between layers not polymerized		
	2	5	≈OK	80	3	-			
SIP3385	1	100	OK	500	10	OK	OK	OK	≈OK
	2	50	bad	240	5	≈OK			
	3	50	OK	135	3.5	≈OK			

Table 4.6: Summary of the manufacturing process with a second DF layer of 25 µm.

WAFER	MASK	DF (µm)	LAMI	PHOTO (mJ/cm^2)	PEB (min)	RESOL	ALIGN	Channel 10 um	counter-flow channel
SIP3392	1	100	OK	500	10	OK	≈bad	no	≈OK
	2	25	OK	140	4	≈bad			
	3	100	OK	500	10	≈bad			
SIP3440	1	100	OK	500	10	≈OK	OK	start	OK
	2	25	OK	120	4	bad			

Table 4.7: Summary of the manufacturing process with the new mask for the first DF layer.

WAFER	MASK	DF (µm)	LAMI	PHOTO (mJ/cm^2)	PEB (min)	RESOL	ALIGN	Channel 10 um	counter-flow channel
SIP1049	1 (new)	100	OK	500	10	OK	bad	no, start	OK
	2	50	≈OK	150	3.5	bad			
SIP1048	1 (new)	100	OK	500	10	OK	OK	no	OK
	2	50	≈OK	150	4	bad			
SIP3651	1 (new)	50	OK	180	5	OK	bad	≈OK	OK
	2	25	OK	120	3.5	OK			
SIP3652	1 (new)	50	OK	180	5	OK	Interface between layers not polymerized		
	2	25	OK	100	3	-			

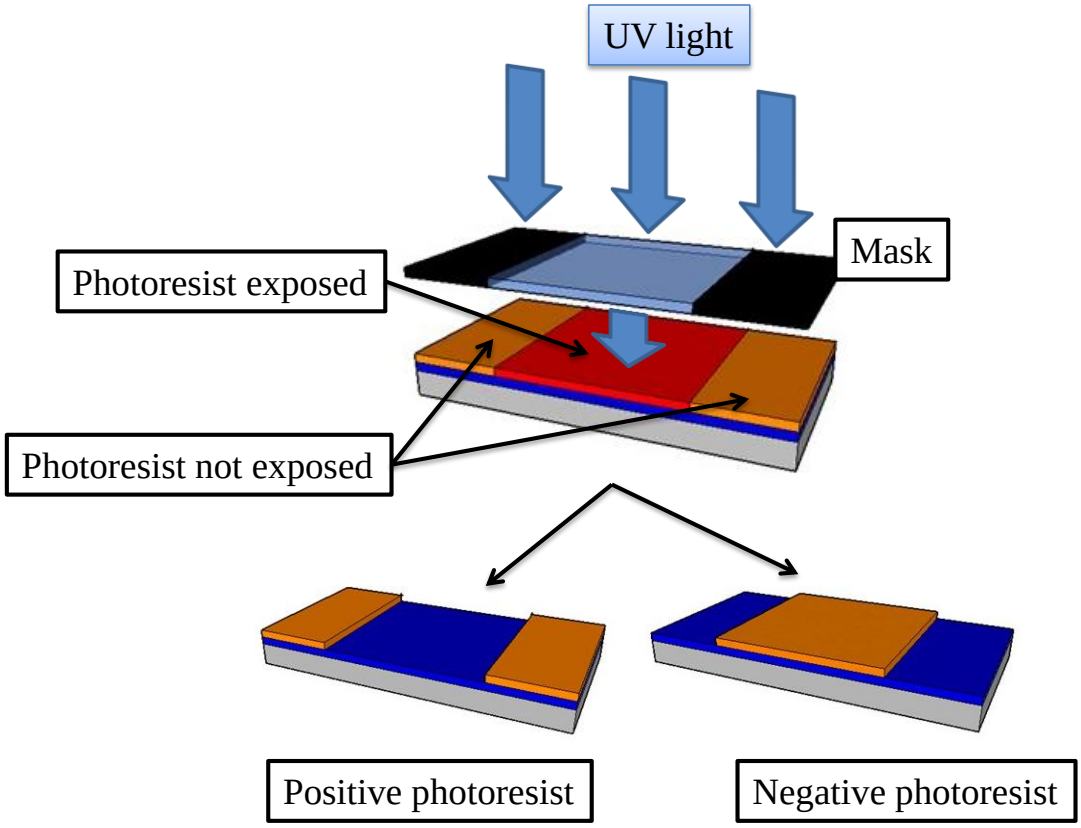

Figure 4.1: Scheme of a photolithographic process.

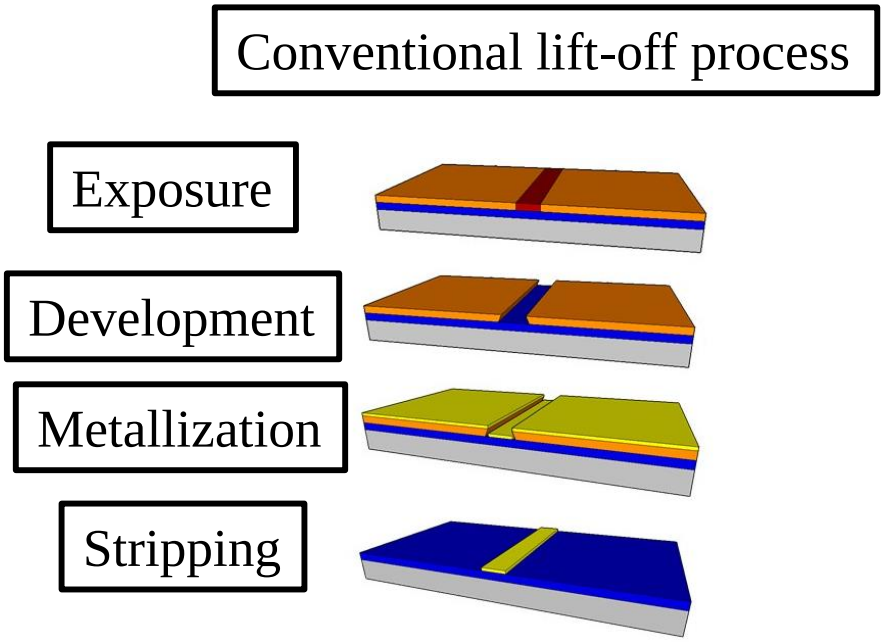

Figure 4.2: Scheme of a metallization process with the lift-off technique.

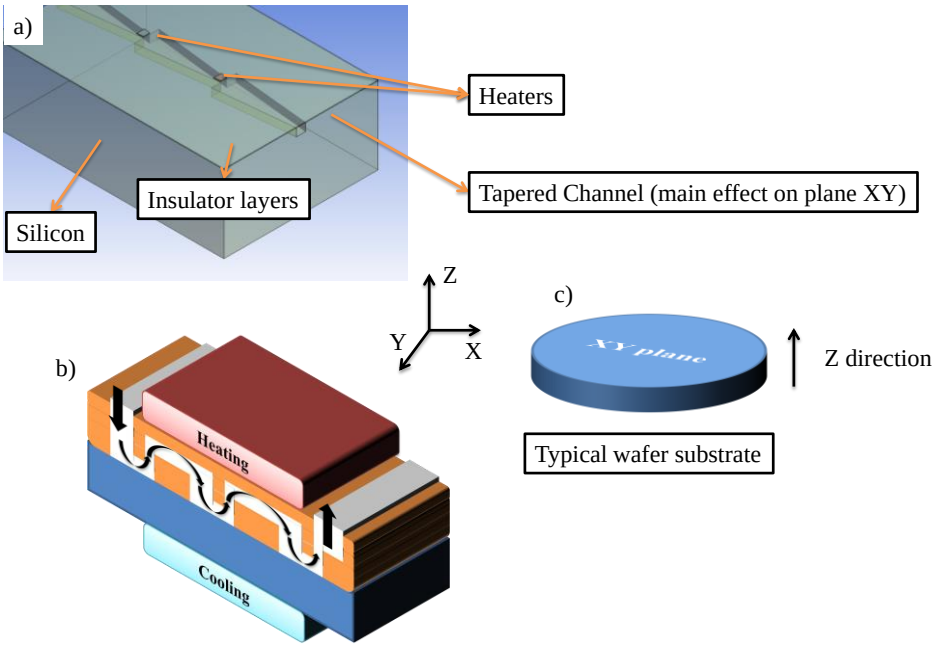

Figure 4.3: First conceptual sketch of a) a tapered channel assembly and b) the modular Knudsen pump. The representation of the orientation of the wafer and the definition of the system of coordinates is provided in c).

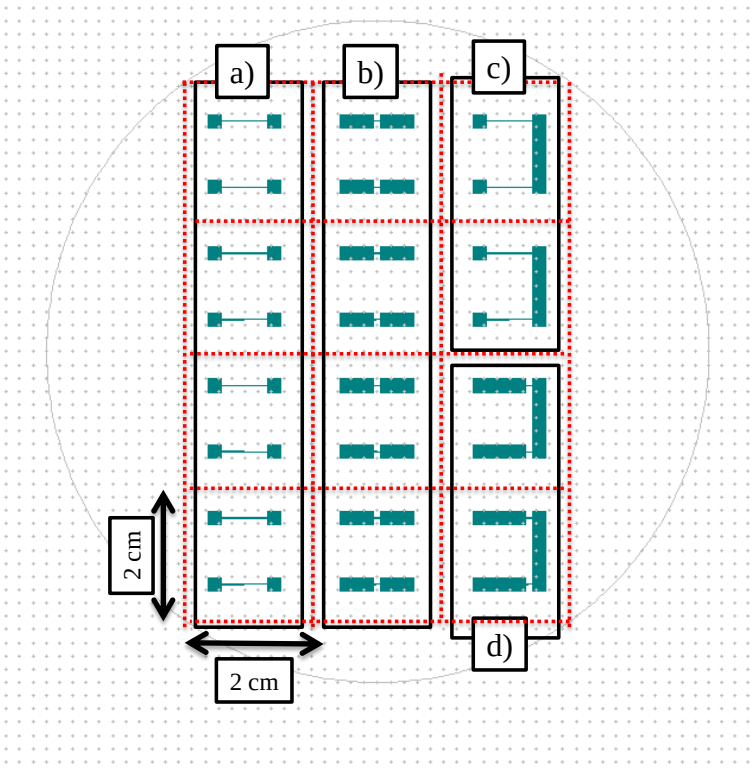

Figure 4.4: Mask design for the fabrication of preliminary tapered channels and uniform cross section channels to perform thermal transpiration experiments.

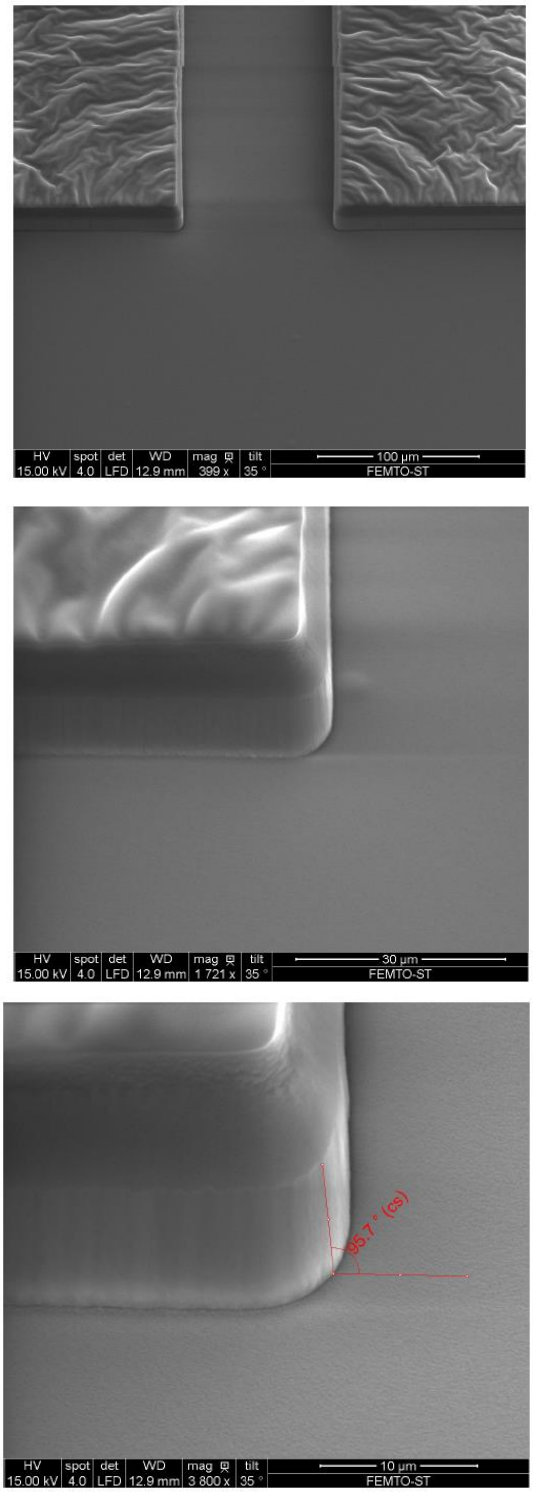

Figure 4.5: SEM images of details of the tapered channel samples provided by FEMTO-ST.

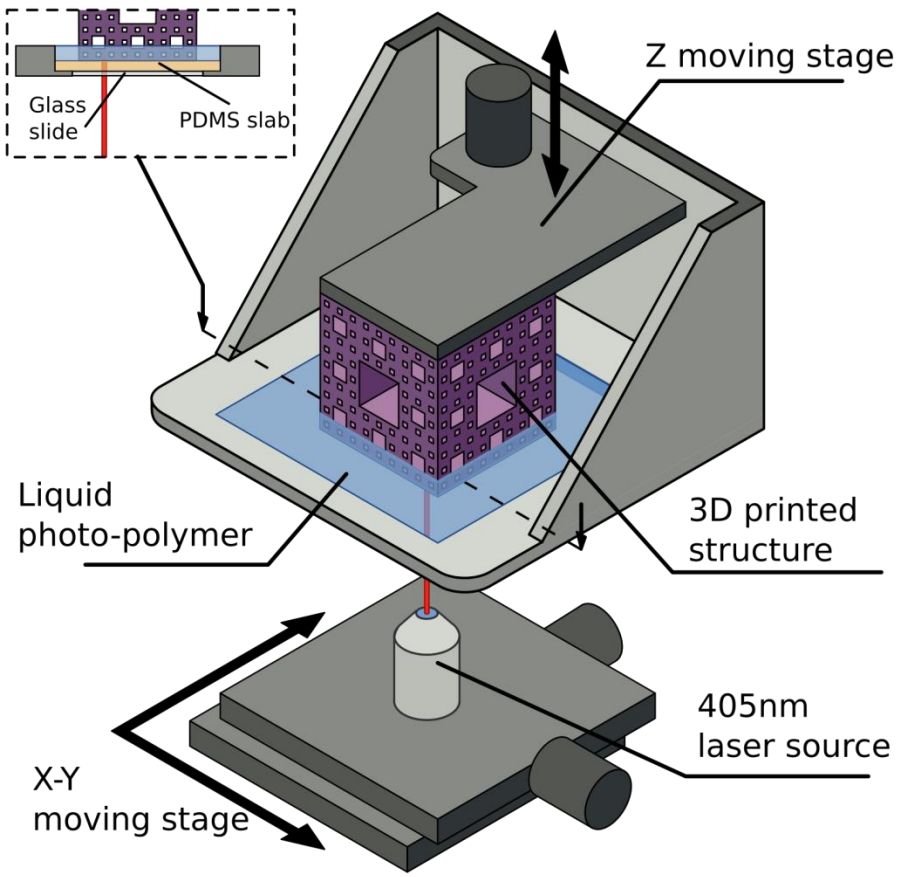

Figure 4.6: Overview of the 3D printing device showing the laser moving in the XY plane and the Z moving stage that moves up after each layer is completed.

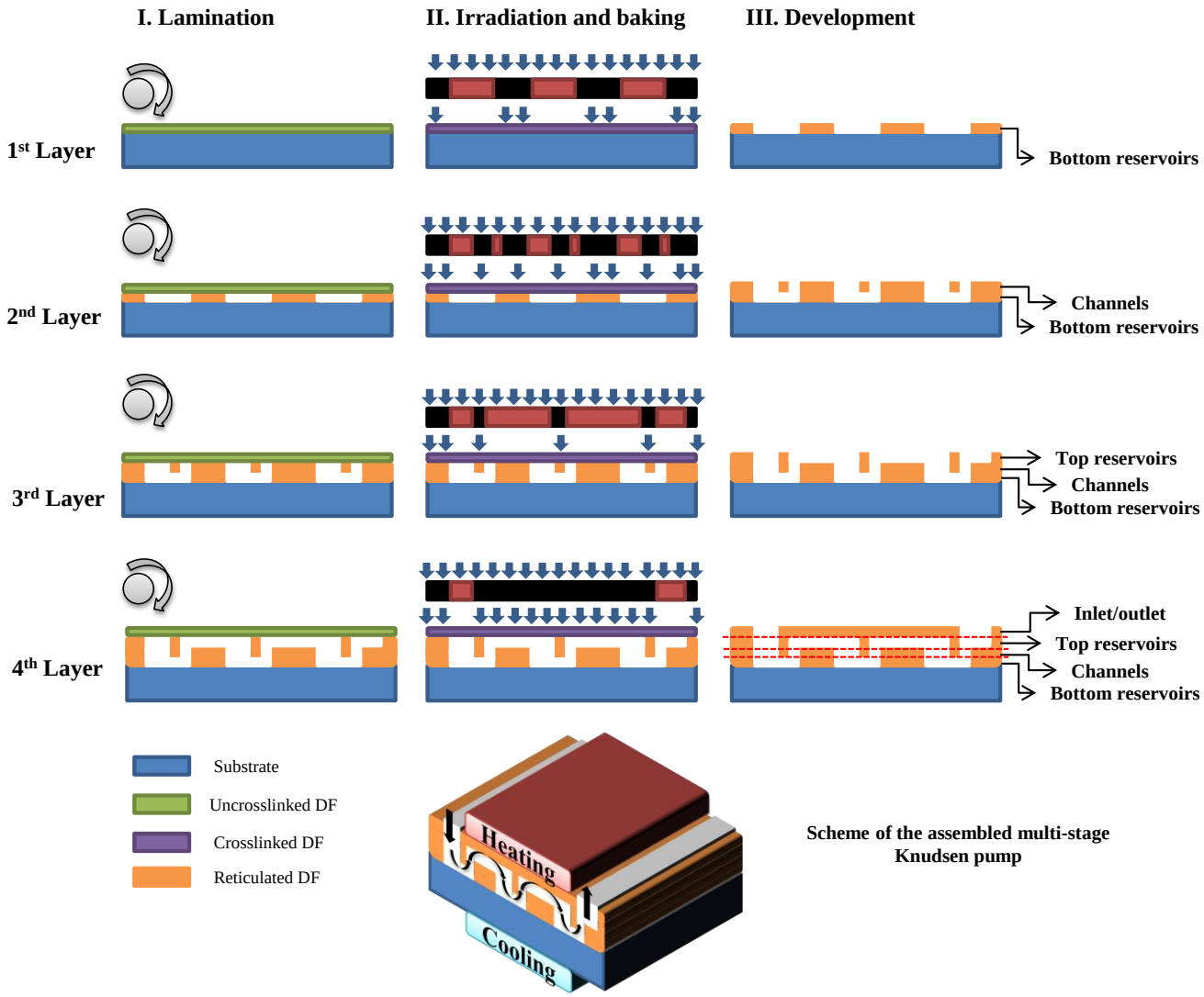

Figure 4.7: Description of the manufacturing process based on the lamination of DF layers for the fabrication of a modular Knudsen pump: (i) the DF photoresist layer (uncrosslinked DF) is laminated onto a planar substrate (glass or silicon wafer); (ii) the DF layer is exposed to UV light and baked to polymerize the photoresist (crosslinked DF); (iii) the DF layer is developed (reticulated DF) in a bath of solvent (cyclohexanone) that removes the material of the non-exposed areas during the photolithography process (the DF layer is a negative photoresist).

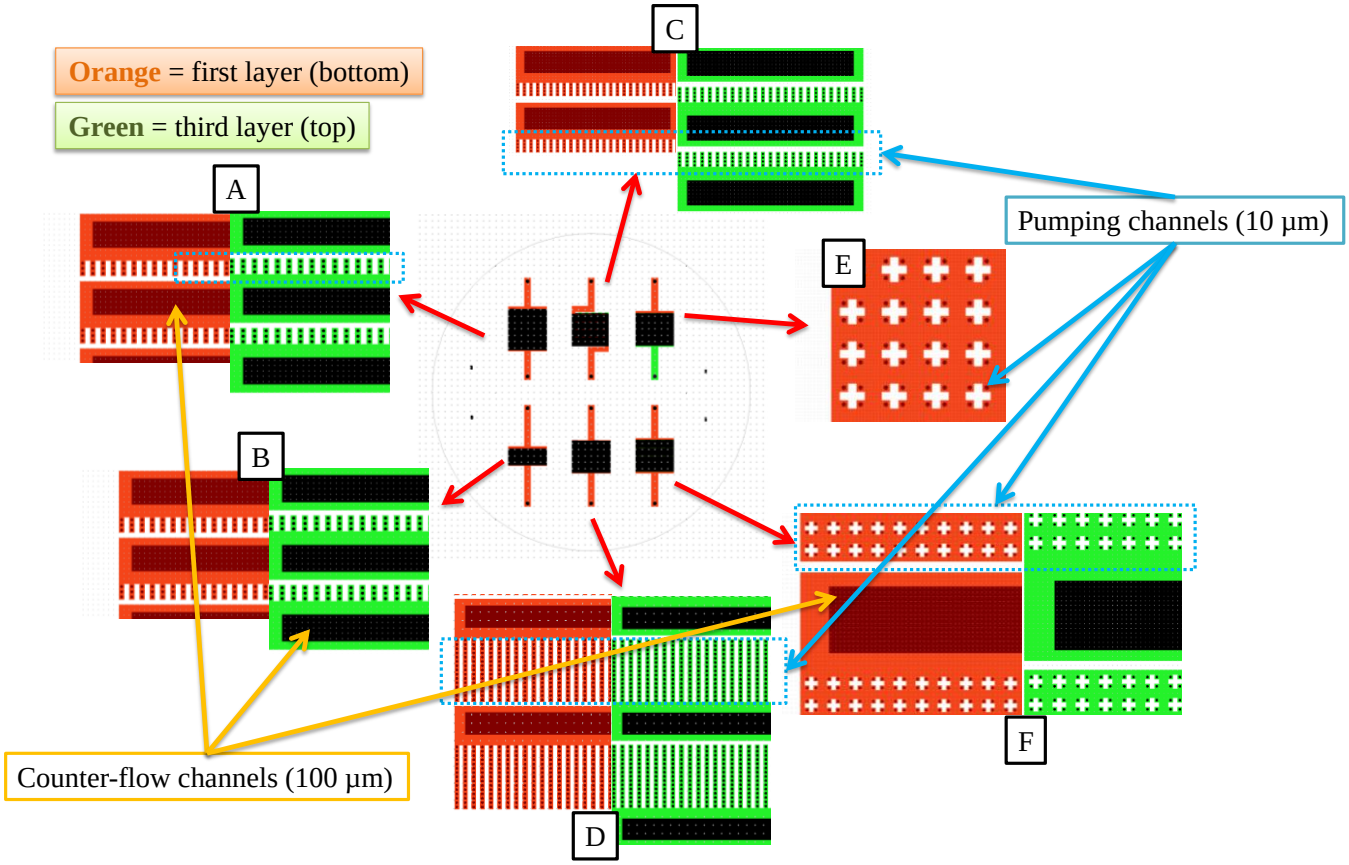

Figure 4.8: Design of the masks for the modular Knudsen pump design. Since the photoresist is negative, the areas not exposed (coloured areas) will be etched. The dark areas inside the orange and green patterns correspond to the pumping channels (small circles) and counter-flow channels (big rectangles) of the second layer. Samples A and B have a similar configuration with 900 parallel pumping channels per stage with 50 and 20 number of stages respectively. Sample C has 330 stages with 100 parallel pumping channels in each stage. Sample D has 4500 parallel pumping channels per stage arranged in long passages of 20x300 µm^2 and only 20 stages. Sample E consists of 48,000 parallel pumping channels to enhance the mass flow rate at the cost of a reduced pressure difference, with no counter-flow stage involved (only half a stage). Sample F follows a similar architecture but includes 4 stages with 9600 parallel pumping channels per stage.

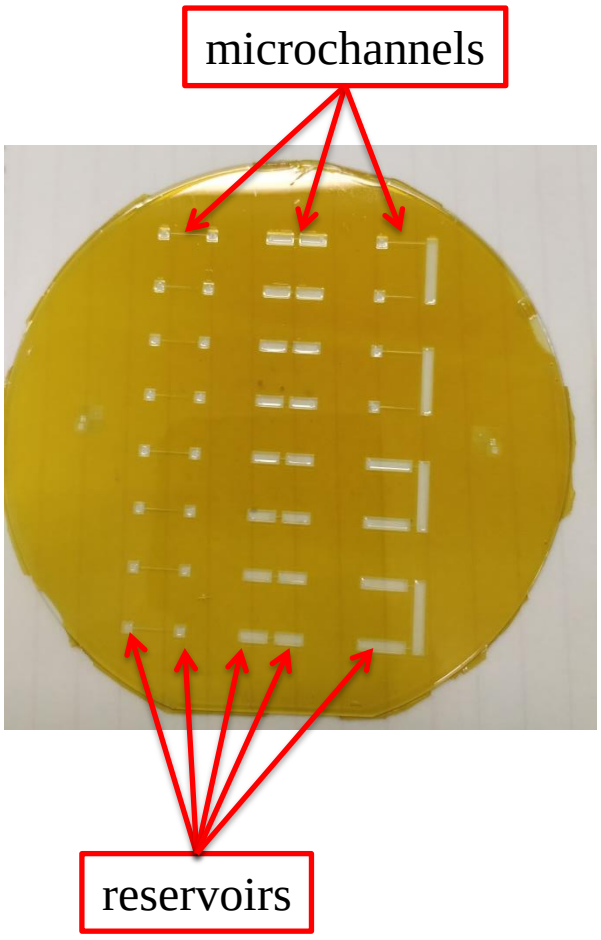

Figure 4.9: Fabricated tapered channel samples with the DF microfabrication process consisting of 16 single channels (first and second columns) and 4 one-stage samples (third column). The bigger visible structures are the inlet and outlet reservoirs at the extremities of the tapered channels.

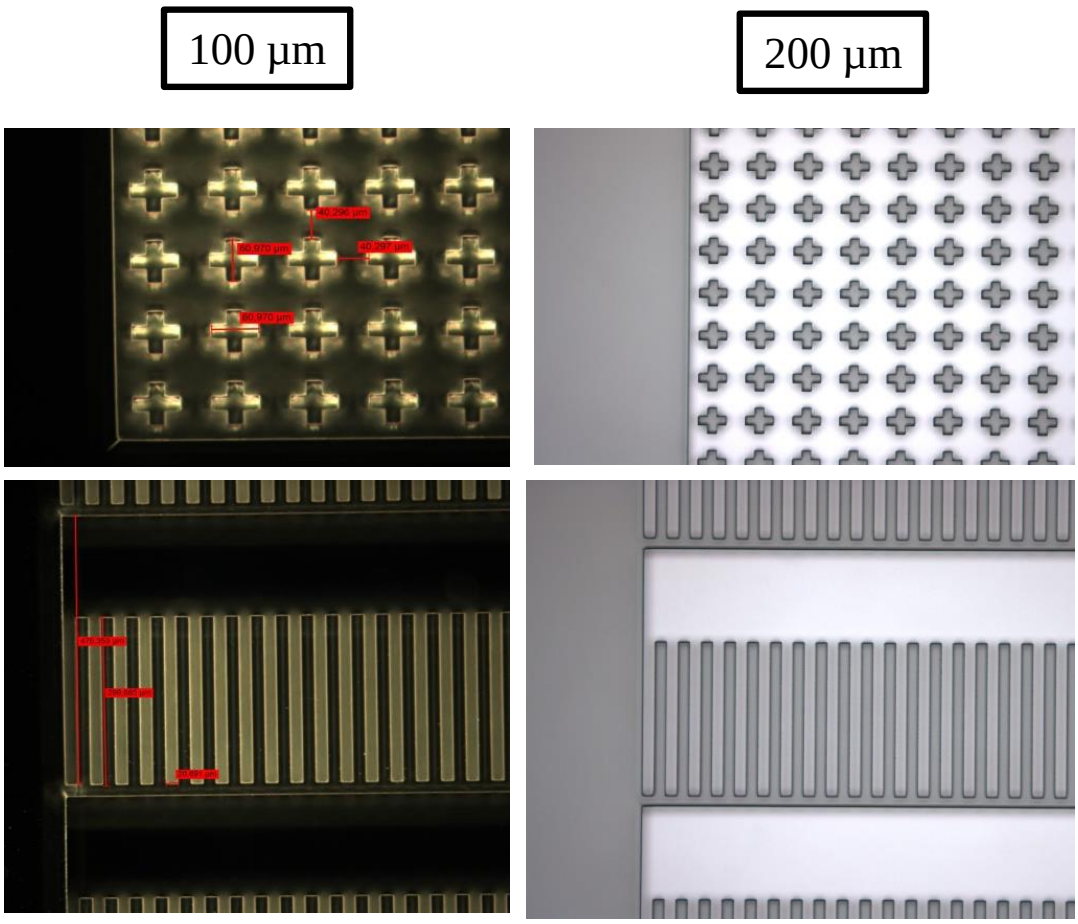

Figure 4.10: Optical microscope images of the first layer for a thickness of 100 µm (left) and 200 µm (right) showing the good resolution achieved (20 µm). The top images show an area of sample E with the crosses of the first layer having a thickness of the wall of 20.3 µm for the 100 µm layer and 20.6 µm for the 200 µm layer. The images on the bottom show an area of sample D with a thickness of the walls of 20.1 µm for the 100 µm layer and 20.8 µm for the 200 µm layer.

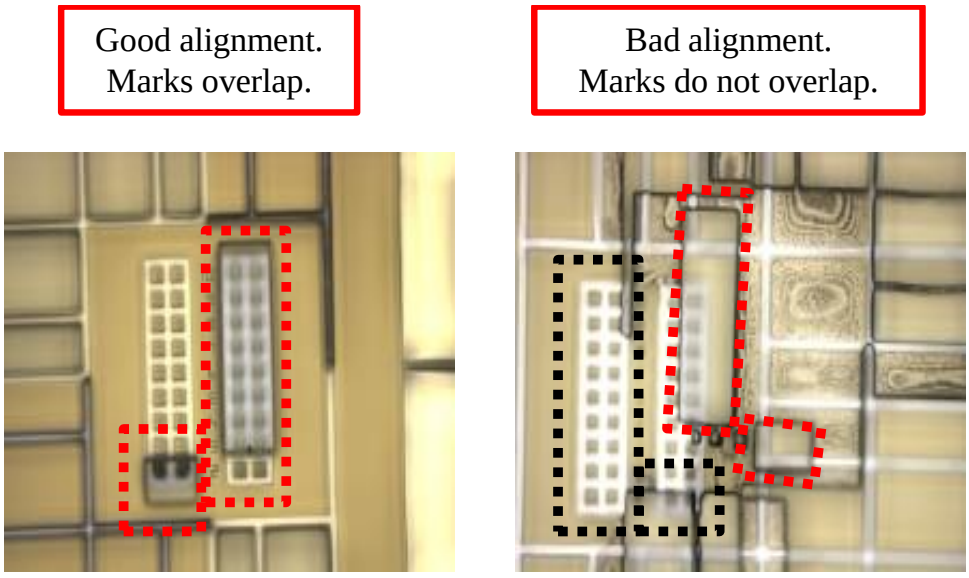

Figure 4.11: Optical microscope image depicting a good alignment (left) and a bad alignment (right) obtained between the first and second layers. The alignment marks should overlap perfectly with each other. For each layer that is added over the first one, one of the rectangles decreases 1 µm while the other increases 1 µm, allowing for up to 1 µm alignment accuracy.

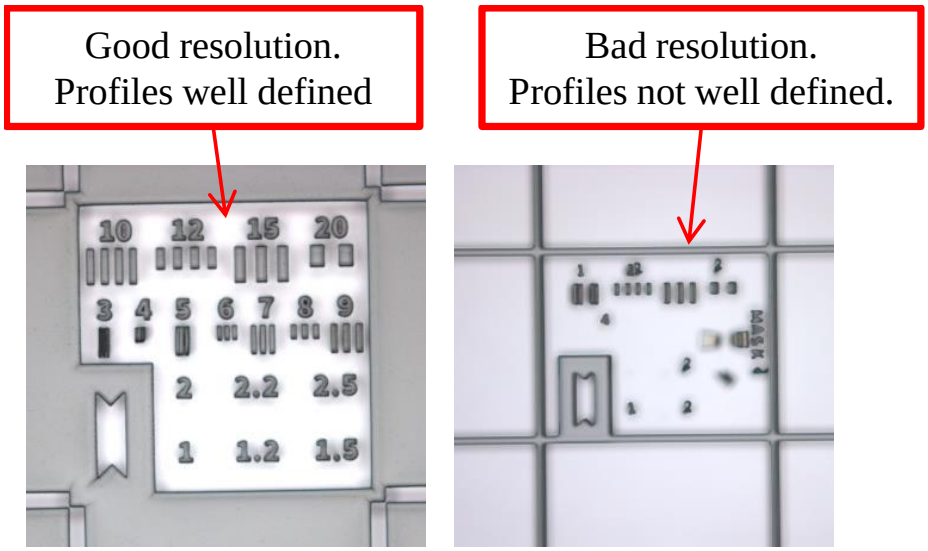

Figure 4.12: Optical microscope image depicting a good resolution (left) and a bad resolution (right) of the wafers. The resolution marks consists of a pattern with bars from 1 to 20 µm in thickness, which are used to check the overall resolution in the wafer. On the left a resolution of about 6 µm has been achieved. On the right a resolution between 12 and 15 µm might be achievable.

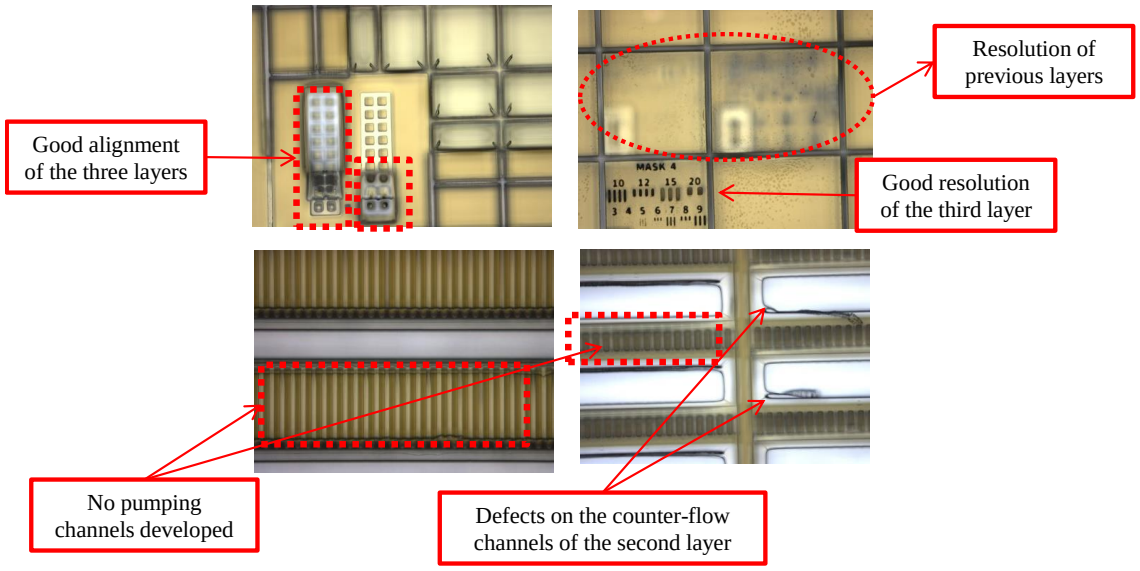

Figure 4.13: Optical microscope images of a sample after processing the third layer displaying a good alignment and resolution for that layer. The second layer did not develop properly the pumping channels and even the counter-flow channels present some defects.

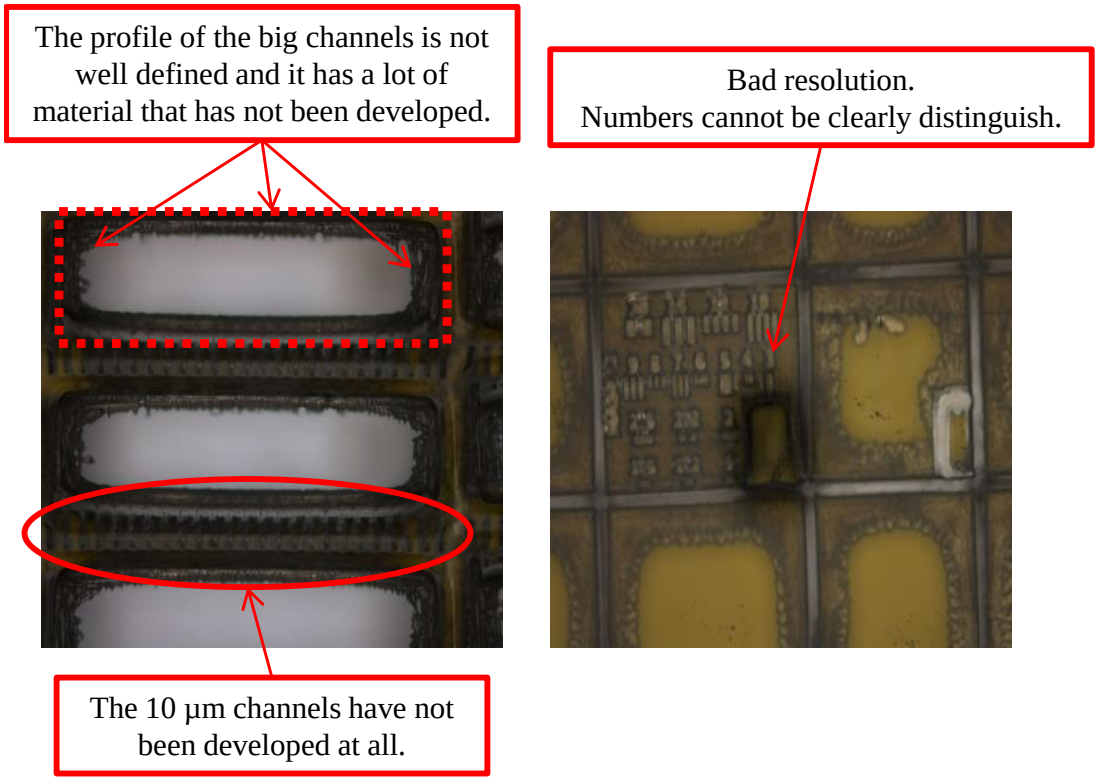

Figure 4.14: Optical microscope images of SIP3229 wafer showing a bad resolution and an over polymerization of both the pumping channels and counter-flow channels. On the left an area of sample C is shown. On the right the resolution mark is presented. (240 mJ cm-2 and PEB of 5 min)

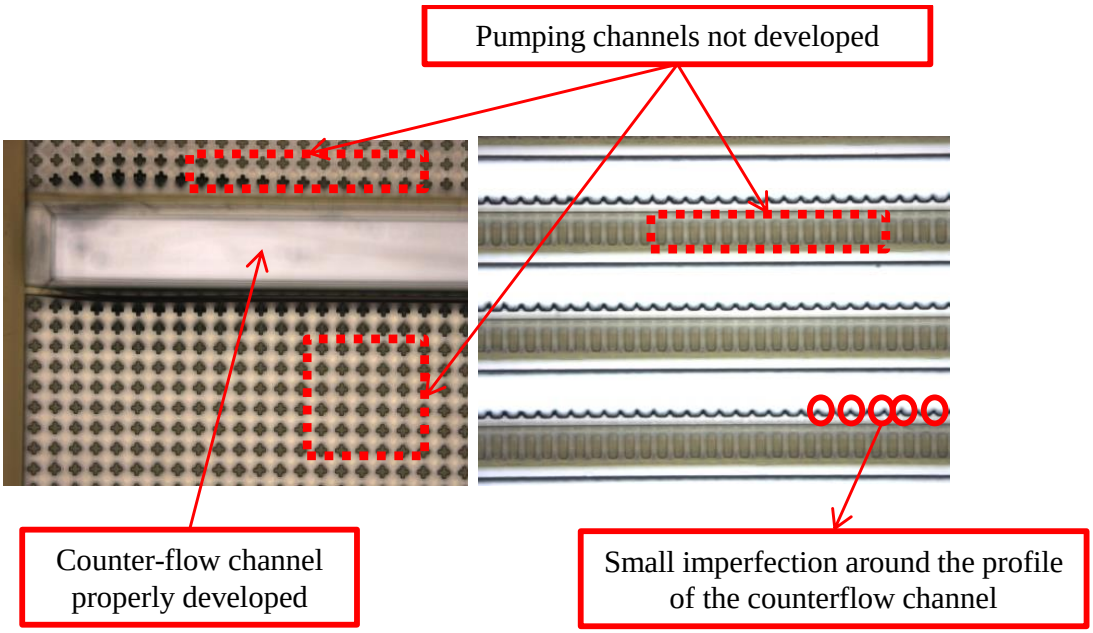

Figure 4.15: Optical microscope images of SIP3226 wafer presenting an over polymerization of the pumping channels (not developing) but a clean profile of the counter-flow channels with only some minor defects. On the left an area of sample F is shown while on the right an area of sample A is presented. (200 mJ cm^{-2} and PEB of 5 min)

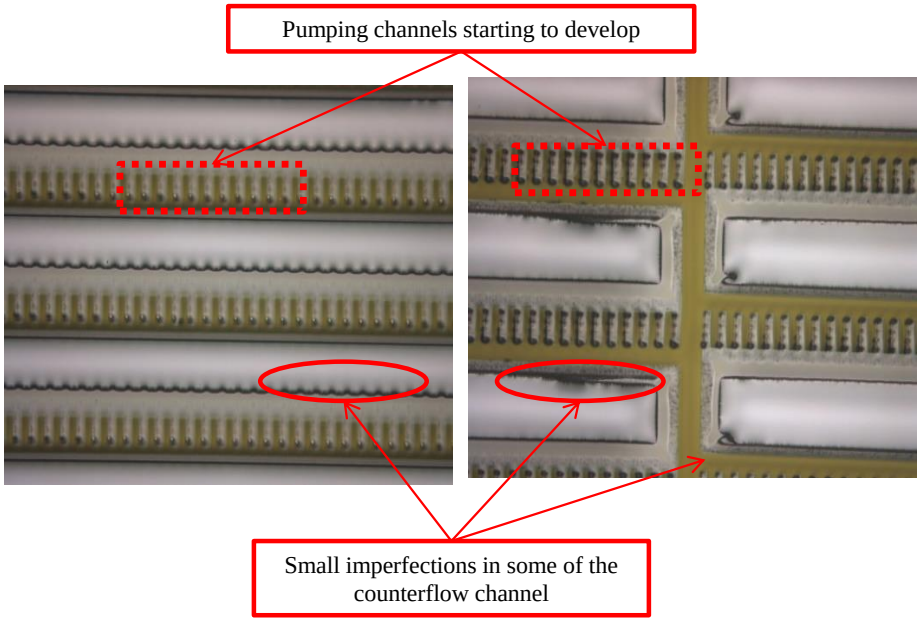

Figure 4.16: Optical microscope images of SIP3225 wafer with pumping channels starting to develop. The counter-flow channels still present some minor defects. A representative area of samples B and C are shown on left and right respectively. (150 mJ cm^{-2} and PEB of 4 min)

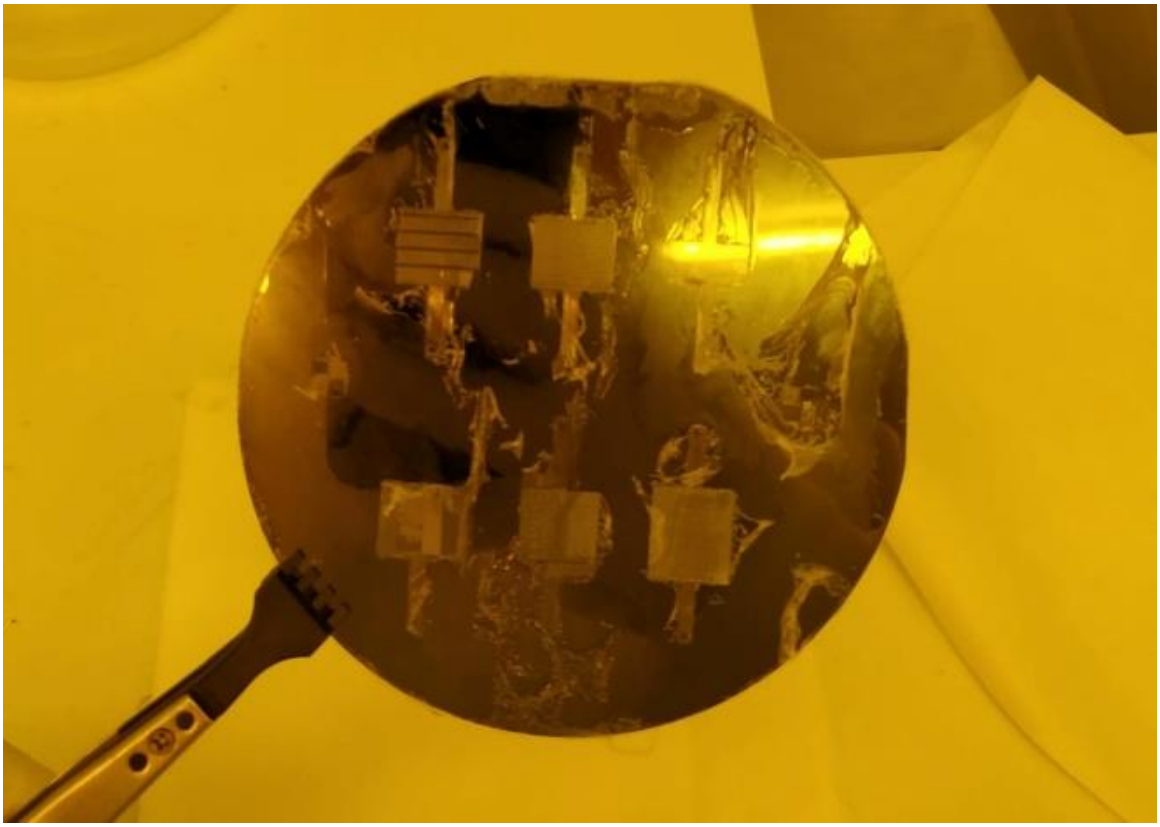

Figure 4.17: Image showing a wafer exposed to a dose lower than the minimum threshold to polymerize the interface between layers.

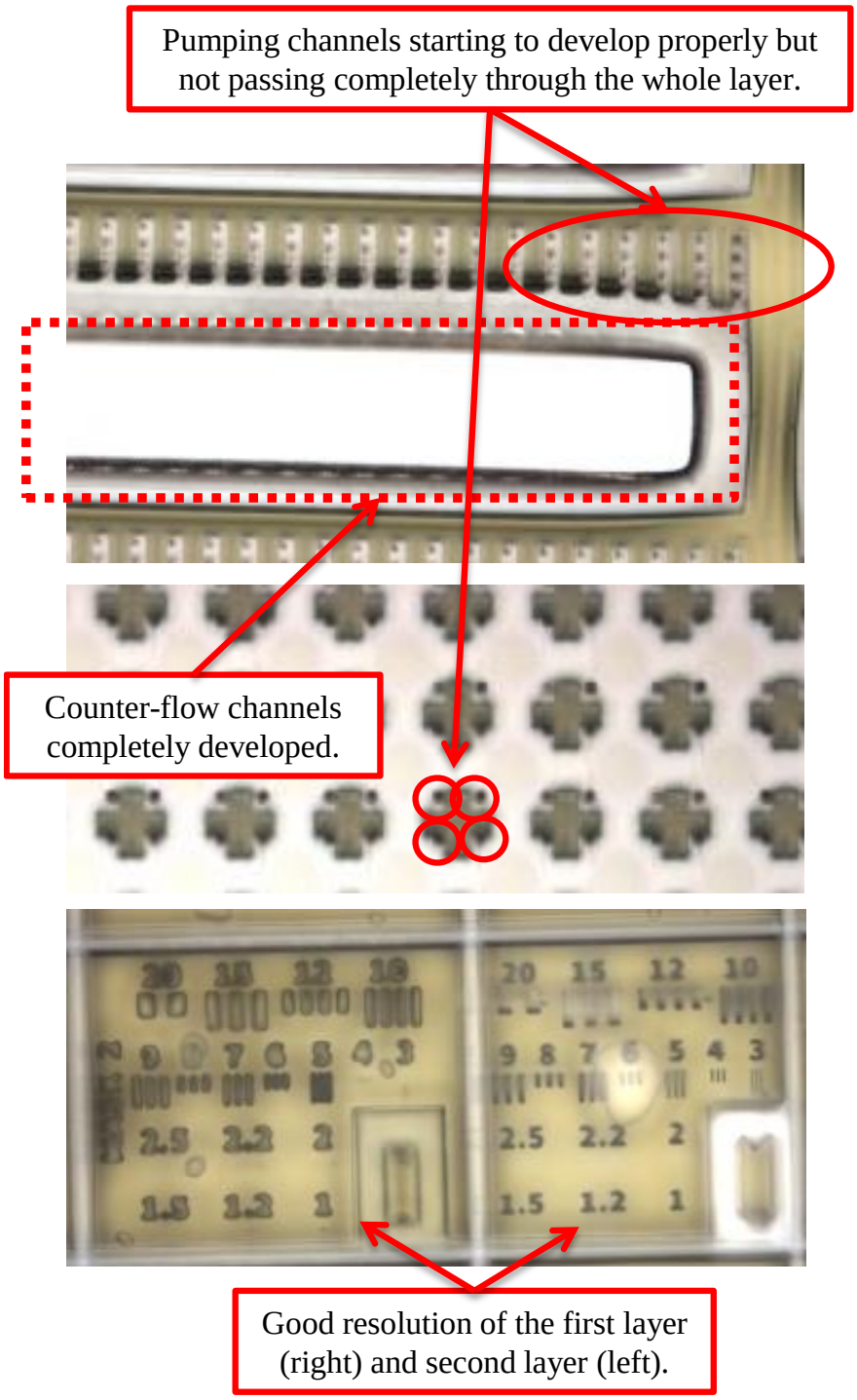

Figure 4.18: Optical microscope images of SIP3465 wafer showing a good resolution for the second layer (bottom) and a representative area of samples C (top) and E (middle). However, although the resolution mark (bottom) shows a good profile for the 10 µm bars of the second layer, the pumping channels are still not completely developed (top and middle) as it can be observed by their dark color, indicating that the channels are closed. The counter-flow channels are properly formed this time (top). (150 mJ cm^{-2} and PEB of 3.5 min)

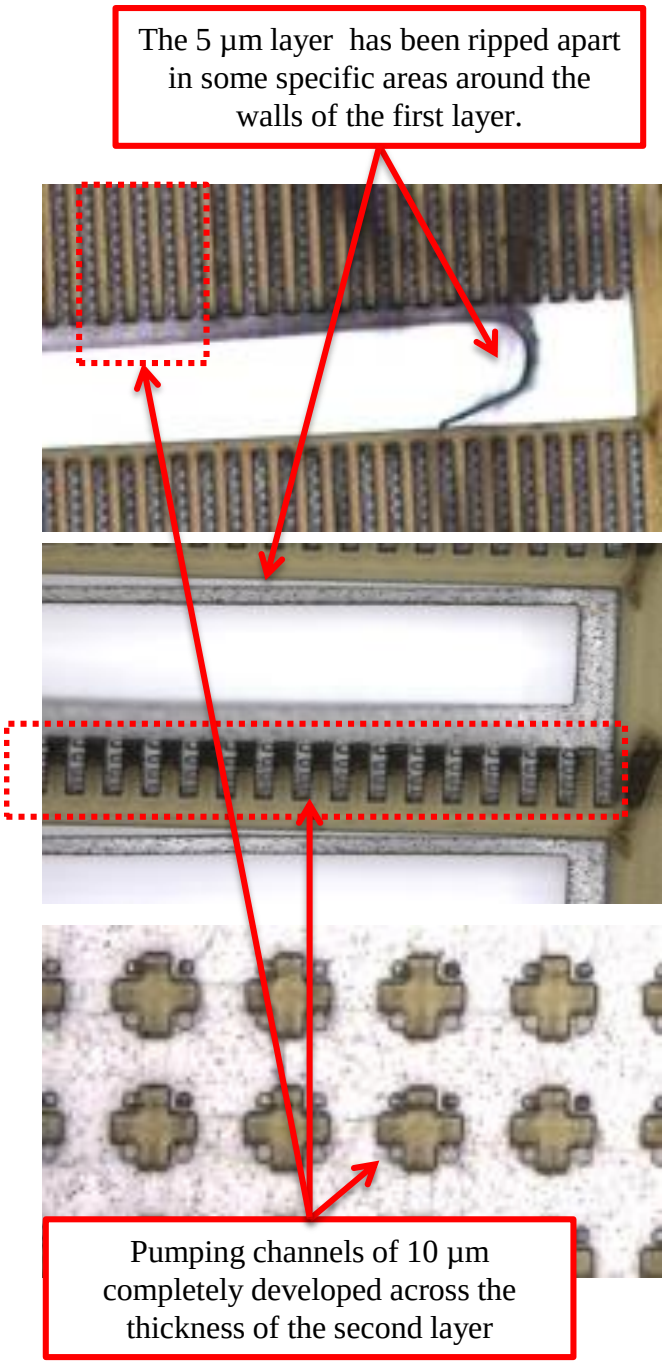

Figure 4.19: Optical microscope images of SIP3385 wafer showing the pumping channels completely developed in representative areas of samples D (top), C (middle) and F (bottom). Also it can be observed how the 5 µm DF is ripped apart from the previous layer in some specific locations. (100 mJ cm^{-2} and PEB of 2.5 min)

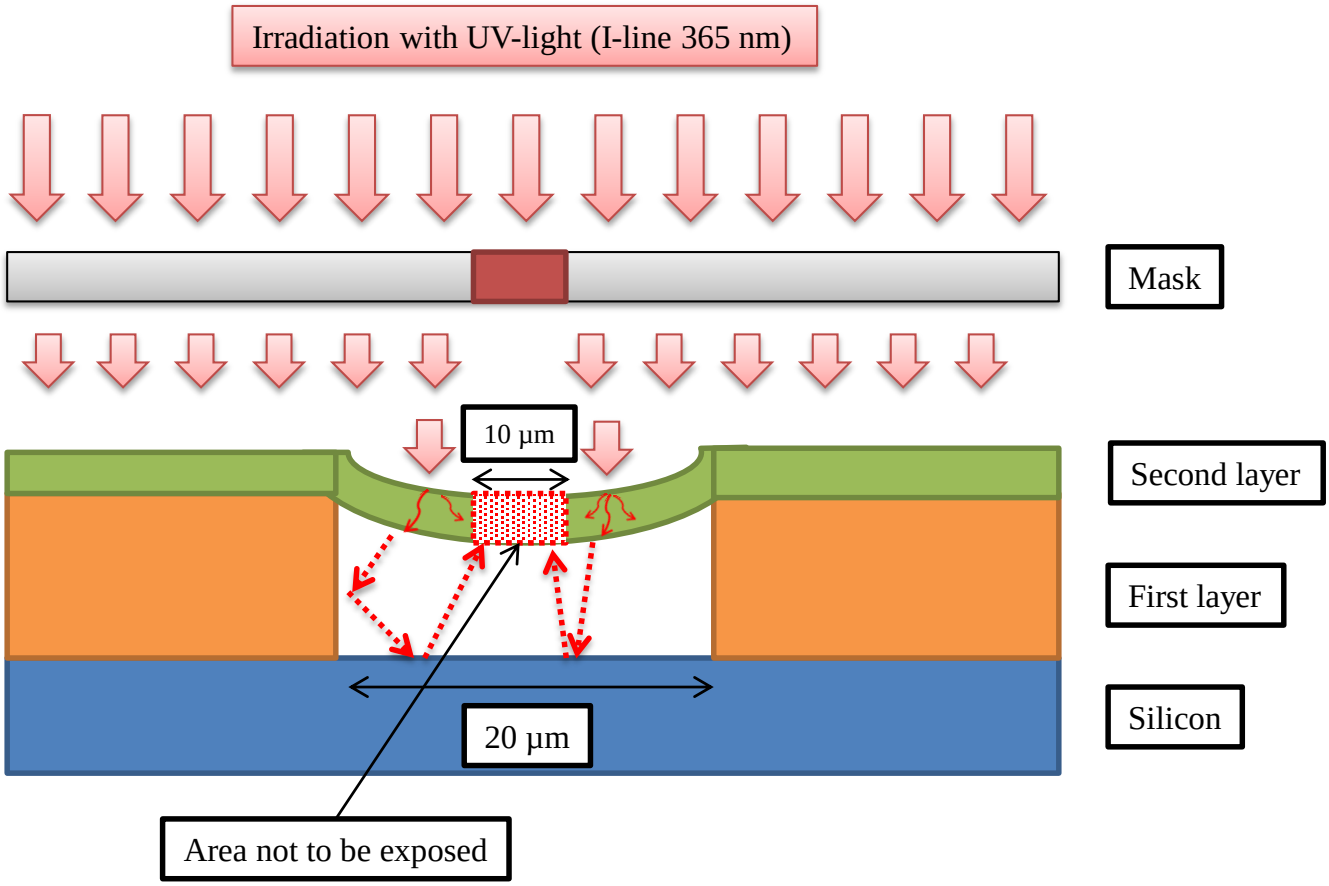

Figure 4.20: Proposed physical mechanism responsible for the over polymerization of the pumping channels even when the exposure dose is low. The light is refracted in the second layer and then reflected on the walls of the first layer and the silicon substrate, reaching the area that was not supposed to be exposed from the bottom side of layer.

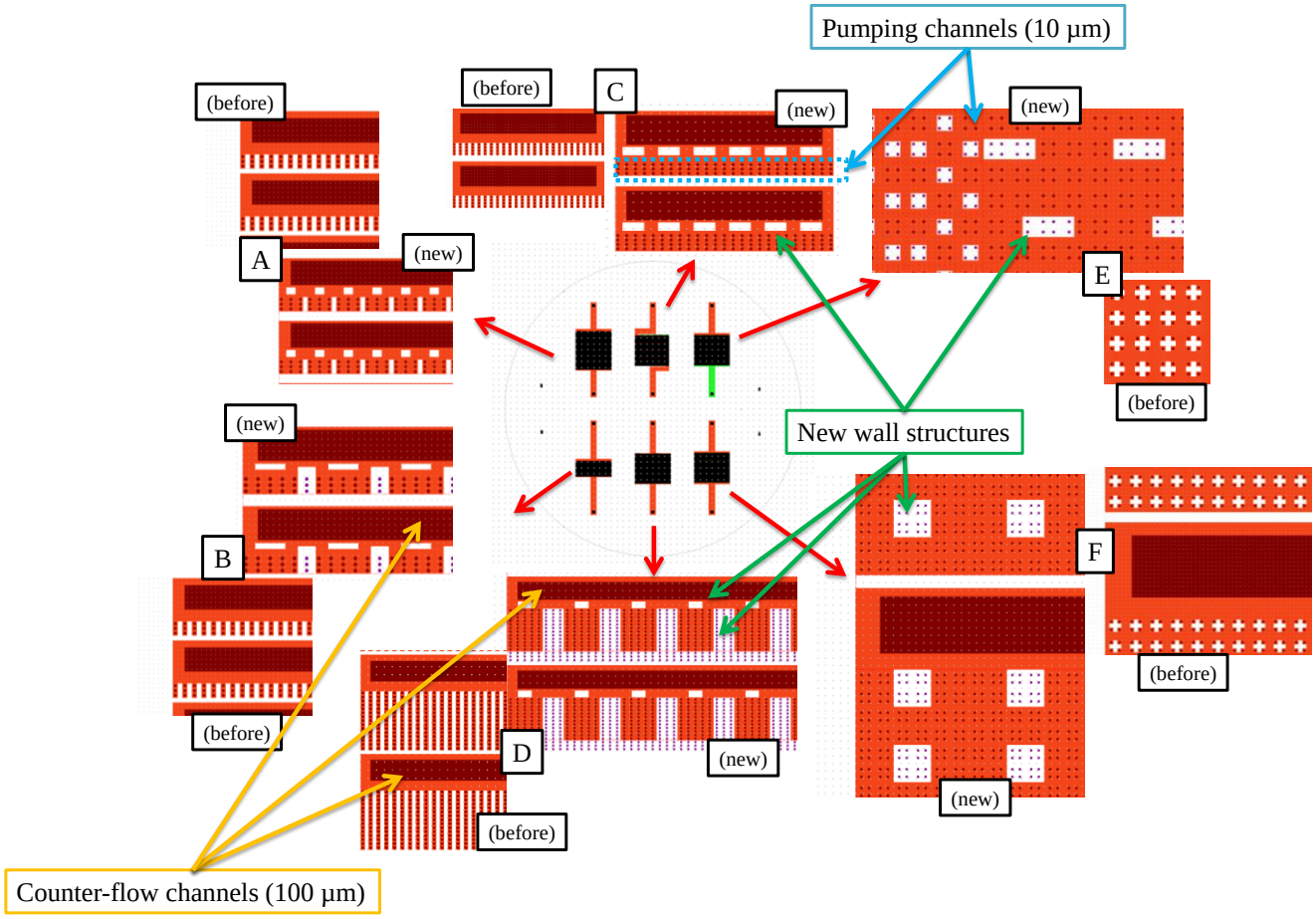

Figure 4.21: New mask with a different arrangement of the first layer (orange) to evaluate the role of the distance between walls of the first layer and channels of the second layer (dark brown). Since the photoresist is negative, the white areas will be exposed and polymerized, resulting into the walls and support structures of the first layer with various distances between them. Since only the mask of the first layer has been modified, some channels of the second layer are over the new wall structures and will be not functional.

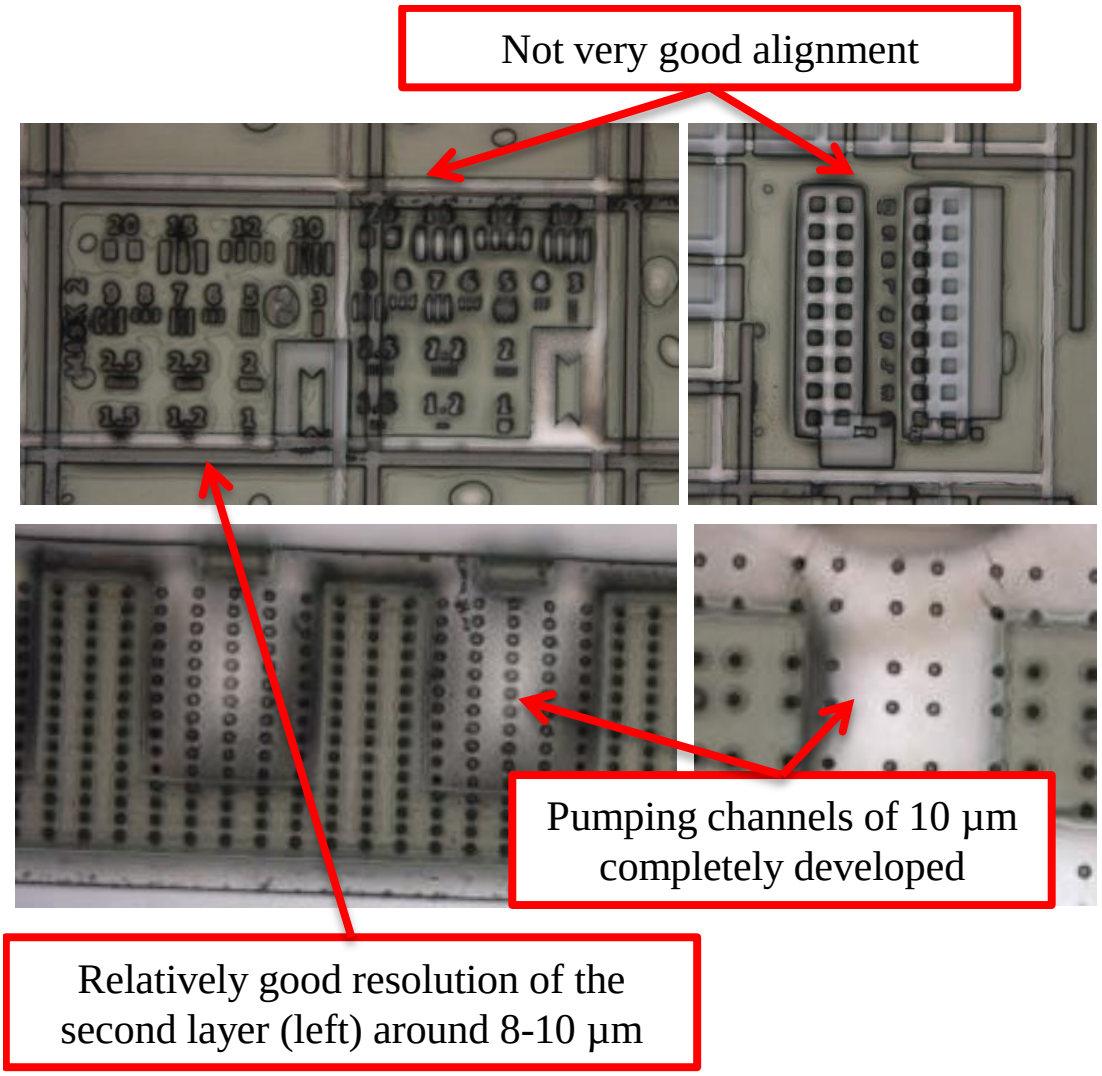

Figure 4.22: Optical microscope images of the wafer SIP3651 showing a relatively good resolution (top left) and a good profile of the pumping channels completely developed, with some deviation in the alignment (top right). Representative areas of samples D (bottom left) and F (bottom right) show the pumping channels completely developed through the thickness of the DF layer with a clear defined profile. (120 mJ cm^{-2} and PEB 3.5 of min)

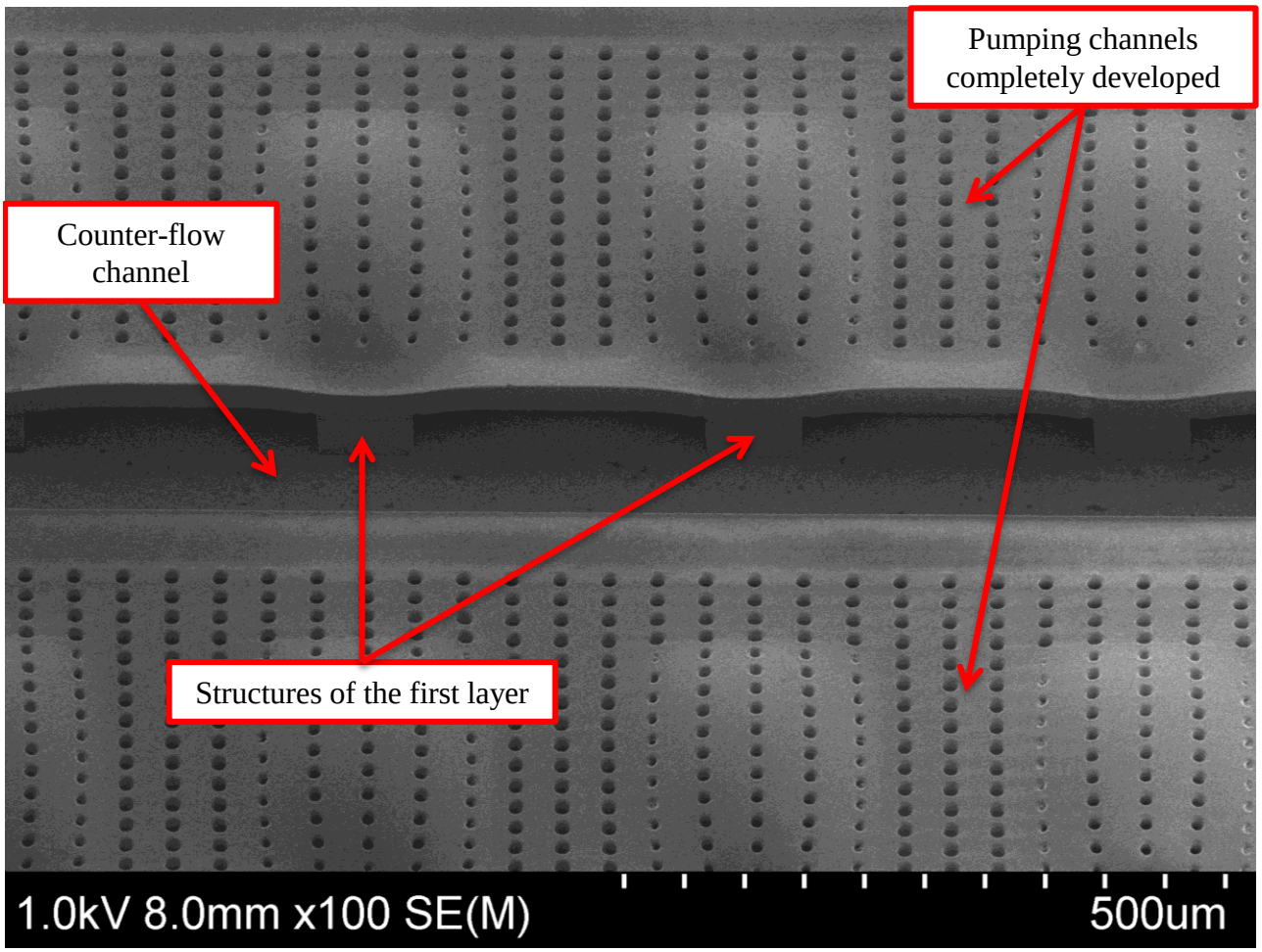

Figure 4.23: SEM image of the wafer SIP3651 showing the pumping channels completely developed through the thickness of the second layer over a representative area of sample D. (120 mJ cm^{-2} and PEB 3.5 of min)

Chapter 5

Thermal transpiration experiments

The experimental work, performed at ICA, Toulouse, in the course of the present Ph.D. thesis, related to thermal transpiration flow through long circular tubes as well as through orthogonal tapered channels is described. The well-known constant volume technique [114], [115] is applied. The existing setup has been slightly modified by adding a new housing system in order to allow the rapid and easy replacement of the tapered channel samples. The new housing system also displays a low leak rate. In addition, a newly acquired differential pressure sensor has been installed in the experimental setup providing better accuracy in the measurements of the pressure difference. The thermal transpiration flow experiments in the long glass tube have been performed as part of a broader ongoing project between ICA and UTH related to the estimation of the coefficients of the Cercignani-Lampis boundary condition model. Thermal transpiration experiments have been carried out on tapered channels fabricated by lamination of two DF layers (first layer for the channels and second layer for the sealing of the channels including their inlet and outlet) over a glass substrate following the process introduced in Chapter 4. Preliminary experimental results with the tapered channels suggest the existence of the diode effect between the converging and diverging directions of the flow in the tapered channel.

5.1 Thermal transpiration flow experiment on tube

Thermal transpiration flow experiments have been performed in a long glass tube with two different gases, namely, helium and nitrogen, to measure the maximum difference of pressure generated by the thermal transpiration flow at different initial pressures. Also, the corresponding maximum mass flow rates at the beginning of the experiment have been measured using the constant volume technique.

5.1.1 Initial experimental apparatus

The initial experimental setup for the glass tube consisted of a test section with the tube, three valves, two capacitance diaphragm gauges (CDG), three thermocouples, a vacuum pump and the pressurized gas tanks to fill the setup (Figure 5.1). The setup is basically a closed circuit in which the test section and a valve (V-A) separate the circuit in two volumes, cold side volume V_C and hot side volume V_H, containing a capacitance diaphragm gauge each, CDG_C and CDG_H, respectively. Then, valve V-B connects the closed circuit with the vacuum pump to make vacuum inside the system while valve V-C connects it with the pressurized tank to fill the setup with a particular gas species. The vacuum pump is an Oerlikon Turbolab80 turbormolecular vacuum pump capable of keeping the system at pressures below 1 Pa, while the pressurized tanks are used to fill the closed circuit of the setup with a specific gas species. All connections in the system are provided by standard ISO KF16 flanges.

The variation of pressure in the closed circuit is monitored by two INFICON capacitance diaphragm gauges, which are connected to the cold (CDG_C) and hot (CDG_H) volumes. The full scale of the pressure gauges is 1333.22 Pa with a resolution 0.015 % of the full scale and a precision of 0.2 % of the reading. The ideal operating temperature of these CDGs is 25 ºC. In the setup there is only a small area around the hot end of the test section where the temperature is high. If CDG_H was placed close to the hot end of the test section, parasite thermal transpiration flows could appear. However, by locating CDG_H far from this area, the temperature of the whole sensor is uniform and can be considered close to the room temperature (295 K), avoiding any possible parasite thermal transpiration flow inside the gauge fittings.

5.1.2 Test section

The test section consists of a long glass tube in which the thermal transpiration flow is taking place due to thermal gradient generated by a heating resistance wire. The tube is glued to the KF16 flanges by a high thermal conductivity adhesive to facilitate a uniform temperature distribution at the ends of the tube. The heating resistance consists of a constantan wire coiled around the KF16 flange at one end of the tube (hot side), covered by thermal paste and a silicone based insulator to provide a uniform heating and avoid heat losses as shown in Figure 5.2. In the same figure, the arrangement of the thermocouple T-2 measuring the temperature at the outside of the hot end of the tube it is also be observed. The hot temperature can be regulated by tuning

the intensity of the current through the wire. Due to the low thermal conductivity of glass, cooling by means of natural convection is enough to generate a significant temperature difference $T_H - T_C$ between the hot and cold sides of the tube.

The three type K thermocouples are arranged in the setup to provide measurements of temperature at different points of the test section. Thermocouple T-1 is placed at the cold end of the glass tube, surrounded by a silicone based insulator and a thermal paste with high conductivity similarly to the thermocouple T-2 shown in Figure 5.2. Thermocouple T-2 measures the temperature at the hot end of the tube where the heating wire is situated (Figure 5.2). The combination of the insulator and the thermal paste in both cases helps to properly measure a uniform temperature. Thermocouple T-3 is introduced inside the system using a thermocouple feedthrough ISO KF – NW16KF single pair. This thermocouple is put in contact with the hot end of the tube, from the inside of the experimental setup, and it is in direct contact with the inner wall of the tube. This provides a more accurate measurement of temperature T_H at the hot end of the tube. Although T-1 is put at the outside of the tube, it is observed that this point is kept at room temperature even when the heating is activated. Therefore, it was not necessary to include a thermocouple inside the tube at the cold side since it would provide very similar information than the one place on the outer wall. This remark is also supported by heat transfer simulations.

The radius, R, of the tube is measured by an optical 3D Alicona Infinite Focus Measurement System by taking a close picture of the inner diameter of the tube on both sides, and then performing a series of measurements of the radius. Table 5.1 shows the average radius, standard deviation and the minimum and maximum values of three different measurements. The effective length, measured with a standard caliper, in which the temperature gradient is imposed is $L = 72.29\,\text{mm}$.

5.1.3 Experimental procedure

The experimental procedure for the thermal transpiration flow consists on measuring the maximal pressure difference $\Delta P_{\max}$ generated by the same temperature difference ΔT at different inlet pressures P_{in}. The procedure for each of the measurements of the thermal transpiration flow experiments includes the following steps:

1) Vacuuming the system: at the beginning of the experiment, V-A and V-B are open while V-C is kept closed. The vacuum pump is activated and the system is evacuated reaching pressures below 1 Pa. This vacuuming is kept for a long time to limit outgassing and completely empty the setup from any gas species. This vacuum can be kept up to several days if the system has been opened to atmospheric environment. Also, vacuum-pumping and gas-filling are performed several times by closing V-B and opening V-C to fill the system with the gas species of the experiment and to wash the inner surfaces of the setup from other gas species.
2) Heating of the test section: to generate the thermal gradient in the tube an electrical current is provided to the heating wire resistance. The heating of the tube is performed in several steps to moderate the thermal stress on the glass tube and the connections. The difference of temperature targeted between the hot side and the cold side of the tube is $\Delta T = T_C - T_H = 80\,\mathrm{K}$.
3) Filling the system: by having V-B closed and V-A and V-C open, the whole circuit of the experimental setup is filled with a particular gas species, in this experiments either helium or nitrogen. Once the desired pressure at which the experiment will take place is reached, V-C is closed and V-A is left opened. A certain time is required to reach the thermal equilibrium in the system. During this period, a thermal transpiration flow is already taking place from the cold to the hot side of the tube, but since V-A is opened, the circuit is also opened and the pressures measured by CDG_C and CDG_H are the same.
4) Leakage measurement: once the thermal equilibrium is reached in the system, the pressure in the system starts to increase in a linear manner due to leakage. This leakage has to be quantified to properly post-process the data acquired from the experiment. This leakage is measured while V-A is open and it measures the leakage combined from the whole circuit. Therefore, it is assumed that the leakage is the same in the cold side volume and the hot side volume. Several leakage measurements have been performed for a long time (more than 1 hour) as well as before every thermal transpiration experiment (around 5 minutes). All of them showed a leakage rate of the order of $6\times10^{-4}\,\mathrm{Pa\ s^{-1}}$.
5) Measurement of the thermal transpiration flow: once the thermal equilibrium has been reached and certain time has passed to quantify the leakage, the measurement of the thermal transpiration flow is launched by closing V-A at time t_0. Before closing valve V-

A, pressure P_0 at both sides is the same. Then, after V-A is closed, pressures in the cold and hot sides start to vary until they reach stable values, P_C and P_H respectively. A typical example of this thermal transpiration flow measurement is shown in Figure 5.3 and can be divided in three distinctive stages: i) initial equilibrium state, ii) transient flow and iii) final equilibrium state. The beginning of the measurement starts with the leakage measurement for some minutes as described in the previous step (4). During this stage, valve V-A is open and a thermal transpiration is taking place from the cold to the hot side of the tube in an initial thermodynamic equilibrium. Once valve V-A is closed, the transient flow stage starts. Due to the thermal transpiration flow, the pressure from the cold side decreases while the pressure from the hot side increases. This pressure disequilibrium starts to generate a Poiseuille flow (pressure driven flow) from the hot side to the cold side in the inner part of the tube. This Poiseuille flow increases as the difference of pressures between the cold and the hot sides increases. Finally, at the final equilibrium stage, the thermal transpiration flow and the Poiseuille flow rates are equal, resulting on a zero net mass flow rate. At this point, the pressures in the cold and hot sides reach a stable value and the pressure difference generated is constant. This maximal pressure difference ΔP_{max} is the thermomolecular pressure difference (TPD). It is noted that the variation of pressure is larger in the cold side than in the hot side due to the difference of volumes between the two sides (the hot side volume being larger than the cold side volume).

5.1.4 Constant volume time dependent technique

Since the mass flow rates in gas microflows are typically very small (less than 10^{-10} kg s^{-1}), different techniques are often required to indirectly extract this value. The constant volume technique [114], [115], implemented in this work, correlates the gas mass flowing through the inlet and outlet of a channel to the variation of pressure in time of the cold side volume and the hot side volume.

Differentiating the ideal gas law and taking into account that the thermodynamic variations are relatively small with the volumes being constant, yields the following relationship of the mass variation in the tube:

$$\frac{dP}{P} = \frac{dm}{m} + \frac{dT}{T} \qquad (5.53)$$

Then, the mass variation inside any of the volumes V (at the cold side or hot side) can be expressed in terms of the other thermodynamic parameters as

$$dm = \frac{V}{R_g T} dP \left(1 - \frac{dT/T}{dP/P} \right) \qquad (5.54)$$

In order to be able to use the constant volume technique and to calculate the stationary mass flow rate in an isothermal constant volume, it is assumed that the relative temperature variation is negligible compared to the relative pressure variation, i.e.

$$\frac{dT/T}{dP/P} \ll 1 \qquad (5.55)$$

It is noted that the temperature in the cold side and hot side volumes are approximately the room temperature with very little variation. Only a very small area in the test section is non-isothermal.

Using the mass conservation law, the variation of mass of the cold and hot side volumes correspond to the mass flow rate in the tube of the test section. It is then possible to measure the mass flow rate at a precise instant with the following expression

$$\dot{m} = \frac{V}{R_g T} \left| \frac{dP}{dt} \right| \quad (5.56)$$

where dP/dt is the pressure variation measured.

It is important to note that in order to properly calculate a steady mass flow rate entering or leaving one of the volumes, it is necessary to have a linear pressure variation with time. Then, the calculated mass flow rate can be considered quasi steady and therefore independent from time. However, the methodology is intrinsically correlated to a non-steady evolution with time of the mass flow rate that enters or leaves the volumes. Hence, the mass flow rate through the duration of each experiment starts at a maximum and asymptotically tends to the final equilibrium in which the net mass flow rate in the tube is zero. Consequently, in order to calculate a steady mass flow rate, it is necessary to choose a specific time interval that is short enough to remain close to a steady flow. This specific time interval in which the mass flow rate is steady, fully developed and not perturbed is given at the beginning of the experiment t_0 as explained in [104], [116].

To adequately calculate the mass flow rate from the pressure variation of the experiments, the derivative of the pressure variation in time is required. Therefore, the pressure variation measured with the CDGs can be fitted by an exponential function

$$P_C(t) = P_{Cf} + (P_0 - P_{Cf})e^{-t/\tau} \qquad (5.57)$$

$$P_H(t) = P_{Hf} - (P_{Hf} - P_0)e^{-t/\tau} \qquad (5.58)$$

where P_{Cf} and P_{Hf} are the pressures at the final equilibrium state in the cold and hot sides respectively and the fitting parameter τ is the characteristic time constant of one experiment. Then, a single experiment behavior depends entirely on the initial state of rarefaction of the gas, the temperatures and the gas nature. The characteristic time constant also quantifies the amount of time needed to reach the equilibrium using the previous expression. For example, it is easy to calculate the time $t_{95\%}$ required to reach 95 % of the final pressure increase in the hot reservoir, i.e. $P_H(t_{95\%}) - P_0 = 0.95[P_{Hf} - P_0]$, as $t_{95\%} = -\ln(0.05)\tau$. At time $t = \tau$, only 63.2 % of the final equilibrium pressure variation is reached.

Finally, the mass flow rates leaving the cold reservoir and entering the hot one are

$$\dot{m}_C = -\frac{V_C}{R_g T_C}\left|\frac{dP_C(t)}{dt}\right\|_{t_0} \qquad (5.59)$$

$$\dot{m}_H = \frac{V_H}{R_g T_H}\left|\frac{dP_H(t)}{dt}\right\|_{t_0} \qquad (5.60)$$

respectively at the initial time of the experiment. Since the mass variation at the cold and hot sides has to be the same to comply with the mass conservation law, $\dot{m}_C$ and $\dot{m}_H$ are equal. This mass flow rate corresponds to the maximum mass flow rate produced by the thermal transpiration flow before the pressure gradient in the channel starts to develop a Poiseuille flow opposite to the thermal transpiration one.

5.1.5 Results of the thermal transpiration experiments on a glass tube

The generated TPD, $\Delta P_{\max}$, characterizing the thermal transpiration flow has been measured following the procedure already described at different inlet pressures and for two gases (helium and nitrogen). The reference gas rarefaction parameter is

$$\delta_0 = \frac{RP_0}{\mu(T_0)\upsilon(T_0)}\ , \qquad (5.61)$$

where P_0 is the pressure before valve V-A is closed and the system in thermal equilibrium, while the viscosity and the most probable molecular speed are at mean temperature T_0. The pressure range for these measurements has been $P_0 = 25-1000$ Pa corresponding to a range of the gas rarefaction parameter $\delta_0 \approx 0.25-10$ and $\delta_0 \approx 0.75-30$ for helium and nitrogen, respectively.

Results for the pressure difference

The results obtained for the thermal transpiration flow experiments for helium and nitrogen are shown in Figure 5.4 in terms of δ_0 (top) and P_0 (bottom). They are compared with the numerical results calculated with the code developed for circular channels using the Shakhov model subject to diffuse boundary conditions on fully developed flows. The results obtained for both helium and nitrogen are in very good agreement with the theoretical ones obtained with the kinetic code, suggesting that the diffuse boundary condition provides realistic results for this tube in the setup with an accommodation coefficient very close to unity. A peak of the performance $\Delta P_{\max}$ is observed around $\delta_0 = 3$ with pressure difference developed by helium being larger than the one developed by nitrogen as it is expected [104]. Additionally, Figure 5.5 shows the good temperature stability reached through all the experimental campaign for the glass tube with a consistent $\Delta T = 80 \pm 0.5$ K for all the data points acquired, with an average value of 79.97 K and a standard deviation of 0.17 K. In addition to the thermal paste and the insulator around the heating wire, in order to avoid temperature oscillations due to the natural convection of air inside the room, a box was designed and fabricated in Plexiglas to enclose the setup.

Results for the mass flow rate

The mass flow rate calculated from the fitting of the pressure variation is presented in Figure 5.6 for both helium and nitrogen in terms of the initial pressure P_0. Similarly to the results for the pressure difference, the mass flow rate calculated from the exponential fitting are in good agreement with the theoretical results. As it is expected, the mass flow rate of nitrogen is larger

than the one from helium. All the exponential fittings have a deviation lower than 2.5% from the raw data.

5.2 Experiments on tapered channels

Thermal transpiration flow experiments have been performed in one fabricated sample of the tapered channels following a similar experimental procedure as in the long tube, but with some adjustments of the setup. In particular, a differential pressure sensor has been introduced in the setup and the test section has been modified to include the housing with the tapered channel sample. The thermal transpiration flow experiments have been performed only for helium suggesting the existence of a diode behavior when comparing the converging and diverging flow directions of the channel. Based on the gained experience and knowledge additional experimental work with flows through tapered channels is required in the future, utilizing the proposed improvements, in order to further validate and analyze the present preliminary results.

5.2.1 Experimental apparatus

The setup is very similar to the one with the glass tube. However, now a differential pressure sensor (DPS) has been installed as shown in Figure 5.7. This DPS has been connected to the cold side and the hot side of the close circuit with two valves, V-D and V-E respectively, in order to be able to isolate the device when required. Also, T-3 is not used anymore since the test section has been changed and it is not possible to access the end of the samples anymore. Hence, now only two thermocouples are present to measure the temperatures in the setup. The characteristic length of the tapered channels is smaller than the one of the glass tube and therefore, the peak at which the maximal performance of ΔP_{max} appears should be observed at larger pressures. To acquire measurements in that range, the CDGs had to be changed and now instead of a full scale of 1333.22 Pa (10 Torr), the full scale is 13332.2 Pa (100 Torr) with the consequent decrease of the accuracy in the measurement.

The DPS is a differential pressure transducer MKS Baratron type 226A with a full scale of 26.66 Pa (0.2 Torr) and a resolution of 0.5 % of the full scale. This type of sensor consists of a diaphragm separating the device in two parts: the measure side and the reference side of the sensor. Then, the sensor is able to measure the difference of pressure (not the absolute pressure)

between the two sides as a result of the deformation of this diaphragm. In the setup the measure side is connected to the hot side while the reference side is connected to the cold side, resulting in a measurement of the difference of pressure $\Delta P = P_H - P_C$ between the hot and cold sides. This measurement is essentially the same as the one provided by the difference between CDG_H and CDG_C, but more accurate due to the technical specifications of the DPS.

The DPS is very sensitive and can provide very accurate measurements; however, the diaphragm connecting the measure side and the reference side is very delicate. The maximum overpressure limit recommended is 120 % of the full scale in both directions (positive and negative pressures), meaning that over this difference of pressure the integrity of the diaphragm is compromised. To facilitate the use of the DPS, when the positive overpressure (higher pressure on the measure side than on the reference side) reaches 120 % of the full scale the diaphragm is stopped by a plate inside the device to avoid its damage. However, when the overpressure is negative (higher pressure on the reference side than on the measure side), there is no internal protection and if the negative overpressure keeps increasing the diaphragm might be damaged. Since the full scale of the device is so low, this limit of the difference of pressure is only around 32 Pa, meaning that very small overpressures might damage the device. For this reason a couple of manual valves, V-D and V-E, have been installed to be able to always keep a lower pressure on the reference side of the sensor and avoid this negative overpressure.

5.2.2 Test section

With the new tapered channel samples the test section is modified to include a new housing system that connects the tapered channel to the setup, including a new heating and cooling approach with Peltier modules (thermoelectrical modules). A scheme of the housing is shown in Figure 5.8; it includes the arrangement of the sample inside the device with all the components. The housing has been 3D printed with a standard polymer similar to PEEK (polyetheretherketone) capable of withstanding temperatures up to 150 ºC without any change in the structure. The housing consists of two parts, one that holds the sample and the other one that connects the inlet and outlet of the channel to the setup through a couple of PEEK tubes. This part with the PEEK tubes also includes O-rings to seal the inlet and outlet and avoid leakage. The part holding the sample includes the heating and cooling systems provided by Peltier modules, as well as two metal pieces to conduct the heat from the Peltier modules to the sample bottom.

Also, these metal pieces incorporate an access for thermocouples T-1 and T-2 to measure the temperature on cold and hot sides, respectively, of the bottom part of the glass substrate.

The Peltier modules are able to either provide heating or cooling depending on the direction of the electrical current provided. Hence, they can be used for heating or cooling just by inverting the electrical connection to the power supply. The Peltier modules are glued to the metal pieces with a high thermal conductivity adhesive to improve the heat conductance through the metal to the sample. The maximum intensity current and voltage that should be provided to the Peltier modules are 3.2 A and 8.8 V respectively. Also, the maximum temperature for a continuous operation is 150 ºC. However, when the Peltier is used for heating and temperatures between 100-120 ºC is reached on the hot plate of the Peltier module, the welded electrical connections has been detached and the module has been damaged. A couple of modules have been tried without however, resolving the problem. Therefore, the same heating system from the long tube setup with the constantan resistance wire coiled around the metal piece of the hot side has been used, while cooling has been provided by a Peltier module on the other metal piece.Since thermocouples T-1 and T-2 do not measure the temperature in the channel but in the bottom part of the glass substrate, heat transfer simulations have been performed to estimate the temperatures on the channel walls. With $T\text{-}1 - T\text{-}2 = 40$ K measured by the thermocouples (T-1=333 K and T-2=373 K) an approximate temperature difference of $\Delta T = T_H - T_C = 17.43$ K was calculated as shown in Figure 5.9.

The sample with the tapered channel has an area of 2×2 cm^2 with a channel length $L = 7$ mm and a constant depth $W = 200$ μm. The maximum and minimum tapered dimensions are $H_{\max} = 90$ μm and $H_{\min} = 9$ μm respectively, while the average tapered dimension is $H_m = 50$ μm, resulting in an inclination parameter $\alpha = 10$.

5.2.3 Modification of the experimental procedure

The experimental procedure is essentially the same as for the glass tube. Few adjustments have been made to guarantee that the pressure in the reference side (cold side of the setup) of the DPS is always lower than in the measure side (hot side of the setup). Therefore, whenever the setup is going to be vacuumed (V-B open), since the reference side is closer to the vacuum pump than the measure side, by just having both valves V-D and V-E open (with V-A also open and V-

C closed), the reference side decreases the pressure faster than the measure side. Then, when the setup is to be filled with the gas species by opening V-C (with V-A open and V-B closed), V-D is closed and V-E is opened to fill in first the measure side while keeping a lower pressure on the reference side in order to avoid an overpressure from the reference side. Once the setup has been filled (except for the reference side of the DPS) with the gas species up to the required pressure for the experiment, V-D can be opened to equilibrate the pressures. Then, at this moment in which V-A, V-D and V-E are open (with V-B and V-C closed), the pressure in the system is the same, with the DPS providing a zero Pa reading and the two CDGs providing the same pressure measurement. Once the thermal transpiration flow experiment is launched, the evolution of the pressure from the cold side and the hot side is similar to the one shown in Figure 5.4. However, when observing the evolution of the difference of pressure provided by the DPS and the CDGs, as in Figure 5.10, the advantage of the DPS for the measurement of this pressure difference when comparing the amplitude of the signal. The precision of the measurement of the DPS is much higher and provides directly the quantity to measure, while the measurement from the CDGs is less accurate and results from two different measurements. Consequently, the values provided by the DPS are the ones that have been considered in the measurements.

5.2.4 Thermal transpiration experiments in tapered channel samples

The experimental campaign for the tapered channel samples has been limited due to several reasons (manufacturing delays, small number of available of samples, limited resources). In addition, due to the lower, than expected, temperature difference between the cold and hot ends of the channel and the reduced mass flow rate, each measurement requires at least 2 hours. This long experimental time makes very difficult to keep steady conditions in the setup and as a result the measurement accuracy is reduced.

The measurements of the generated $\Delta P_{\max}$ that characterizes the thermal transpiration flow have been performed for the converging and diverging directions of the channel. The reference rarefaction parameter is calculated now from the average tapered dimension H_m as

$$\delta_0 = \frac{H_m P_0}{\mu(T_0)\upsilon(T_0)} \qquad (5.62)$$

where the characteristic length is the average tapered dimension Hm, P_0 is the initial pressure before closing valve V-A to launch the experiment and T_0 is the mean temperature between the inlet and outlet. The pressure range in the performed experiments performed is $P_0 = 100 - 7200$ Pa, corresponding to gas rarefaction parameter $\delta_0 \approx 0.1 - 7$. Following the present work, more measurements may be performed, implementing the discussed improvements of the setup, to adequately characterize the tapered channel sample.

Temperature measurements

Observing the stability of the temperature difference in Figure 5.11, it is evident that the variation of temperatures over the experiments is larger than for the tube experiments on the tube with an average temperature of 39.94 K, a standard deviation of 0.93 K and with approximately all measured values within the interval $\Delta T = 40 \pm 2$ K. With the installation of the DPS, the Plexiglas box that covered the setup had to be removed because it does not fit in the whole experimental apparatus. Therefore, the natural convection of air inside the room, mainly due to the air conditioning system, causes the temperature oscillation in the setup. Also, due to the longer time of the experiments, instabilities from the power supply can be observed. Even if the temperature perturbations are not large, their influence in the experimental procedure can be observed in Figure 5.12. During the transient flow stage it is difficult to notice the influence of the slight temperature fluctuation in the room. However, when the final equilibrium state is reached, the difference of pressure clearly follows the temperature oscillation. For the pressure difference measurements only the beginning and final states are of interest; while for the calculation of the mass flow rate any perturbation in the transitional state is significant. A new box to protect the setup from the air convection in the room is planned to be installed to improve future measurements.

Results for the pressure difference

The experimental values of the maximum pressure difference ΔP_{max} in terms of δ_0 for both the converging and diverging directions are presented in Figure 5.13 and compared to the numerical results obtained with the kinetic code. The numerical simulations of the thermal

transpiration flow have been made considering the temperature difference calculated through the heat transfer simulations. The agreement between the numerical and experimental results is rather good for the majority of the data points, with less than 10% deviation. However, a few data present a larger dispersion (see colored data points) with deviations up to 35% from the numerical results, most probably due to the temperature oscillation in the setup.

Since the temperature difference is small, the difference in performance in terms of ΔP_{max} between the converging and diverging directions is negligible. Therefore, both the numerical and experimental results show similar values for the converging and diverging directions of the flow without revealing any significant diode behavior. However, it was noticed that although the final pressure difference is about the same, the experiments on the converging direction require longer times to reach the final equilibrium state, providing some evidence on the presence of the diode effect.

Results for the mass flow rate

Performing the experiments with tapered channels at similar initial pressures, it is observed that the flow in the diverging direction reaches the final equilibrium state faster than in the converging direction even though the resulting difference of pressure generated is about the same. This is consistently observed in most of the experiments. The fitting to the exponential function showed that, generally, the characteristic time (Figure 5.14) in the converging direction is larger than in the diverging direction, suggesting that the mass flow rate in the diverging direction is larger than in the converging one. The mass flow rates are calculated following the same process, as in the glass tube. In Figure 5.15 the experimental mass flow rates in converging and diverging channels, along with the corresponding numerical ones, are presented. It can be observed that the numerical mass flow rates in the diverging direction are slightly larger than in the converging direction (up to 10 %). The experimental mass flow rates also seem to be larger in the diverging direction than in the converging direction (around 10-45%) for similar initial pressures. However, it is very important to note that the scattering of results is quite significant for both the diverging and converging directions. Therefore, although the preliminary results suggest the existence of a diode behavior, these results should be treated very carefully and further experimental investigation is needed.

Due to the required long time to run each experiment and the difficulty to keep stable conditions during this period, the scattering in the pressure measurements makes difficult a good fit of all the points. In fact, in Figures 5.14 and 5.15, only the values extracted from adequate fittings (less than 8% deviation from the data points to the fitted exponential function) are kept. That is the reason for having less data in the mass flow rate calculation (Figure 5.15) than for the pressure difference (Figure 5.12). The values of the mass flow rate are very sensitive to small details in the experimental procedure such as the time required to close valve V-A, the associated small overpressure in the cold side due to this abrupt closing and the time selected for calculating the mass flow rate. could the sensitivity of the mass flow rates can be improved in the future by installing a valve that will be closed without disturbing the pressures and will be electronically controlled in the setup, to improve the repeatability of each measurement. Even with the addition of the new valve, due to the very low mass flow rates in the tapered channels, the assessment of a good experimental procedure will be challenging.

To increase the mass flow rates, either channels of different geometry may be used or the temperature difference between the inlet and outlet may be increased in order to have larger mass flow rates and reduce the duration of each single experiment. It is one of the perspectives to fabricate new channels with different geometry to generate larger mass flow rates and have a larger diode effect that can be more easily detected. To increase the temperature difference, it is planned that future samples integrate the heating elements inside the channel as a part of the microfabrication process. This way, larger temperature gradients should be achieved and the power consumption will be reduced. Finally, in order to reduce the time of the experiment, the volumes of the hot and cold sides may be reduced. This idea, however, is hardly implementable since it would require the complete change of the setup structure.

5.3 Summary

Experimental work to characterize the thermal transpiration flow in a long glass tube and tapered channels has been performed by providing the maximal difference of pressure at the final equilibrium state and the maximal mass flow rate calculated at the beginning of the experiment. The experimental results for the tube are in very good agreement with the numerical ones both for helium and nitrogen. On the contrary, the experimental results for the tapered channel exhibited much larger deviations due to the longer running time required for each single

experiment and the associated difficulties to keep a stable environment during the experiment. However, encouraging preliminary results have been obtained that suggest the existence of the diode effect for thermal transpiration flows. The results should be treated carefully and further investigation should be performed to accurately describe the physical behavior of the tapered channel as a thermal driven diode.

The experimental setup has been modified to include a differential pressure sensor to improve the accuracy of the measurements. Also, it has been proposed to include a covering box for the setup with the tapered channels to reduce external perturbations due to natural convection of air in the room. Another possible improvement for refining the experimental procedure and the calculation of the mass flow rate could be to include an electronically activated valve to better control the closing of valve V-A, which was a critical point.

It has also been proposed to fabricate new tapered channel samples with different geometry to achieve increased mass flow rate and stronger diode behavior, in order to reduce the duration of the experiments and to be able to better measure a difference of performance between converging and diverging directions. Additionally, to increase the temperature difference it is planned to include the heating elements inside the channels in the fabrication process.

Finally, the experimental work on tapered channels should be continued with the improvements mentioned above in order to accurately characterize the thermal transpiration flow. New samples with converging-diverging diode geometries are of great interest to fundamentally demonstrate the thermally driven diode effect and its possible applications for gas separation and gas sensor technologies.

Table 5.1: Measurement of the radius of the long glass microtube with the Alicona system.

	R (µm)
Mean	249.5298
Std. Deviation	0.4162
Min. value	249.0158
Max. value	249.8125

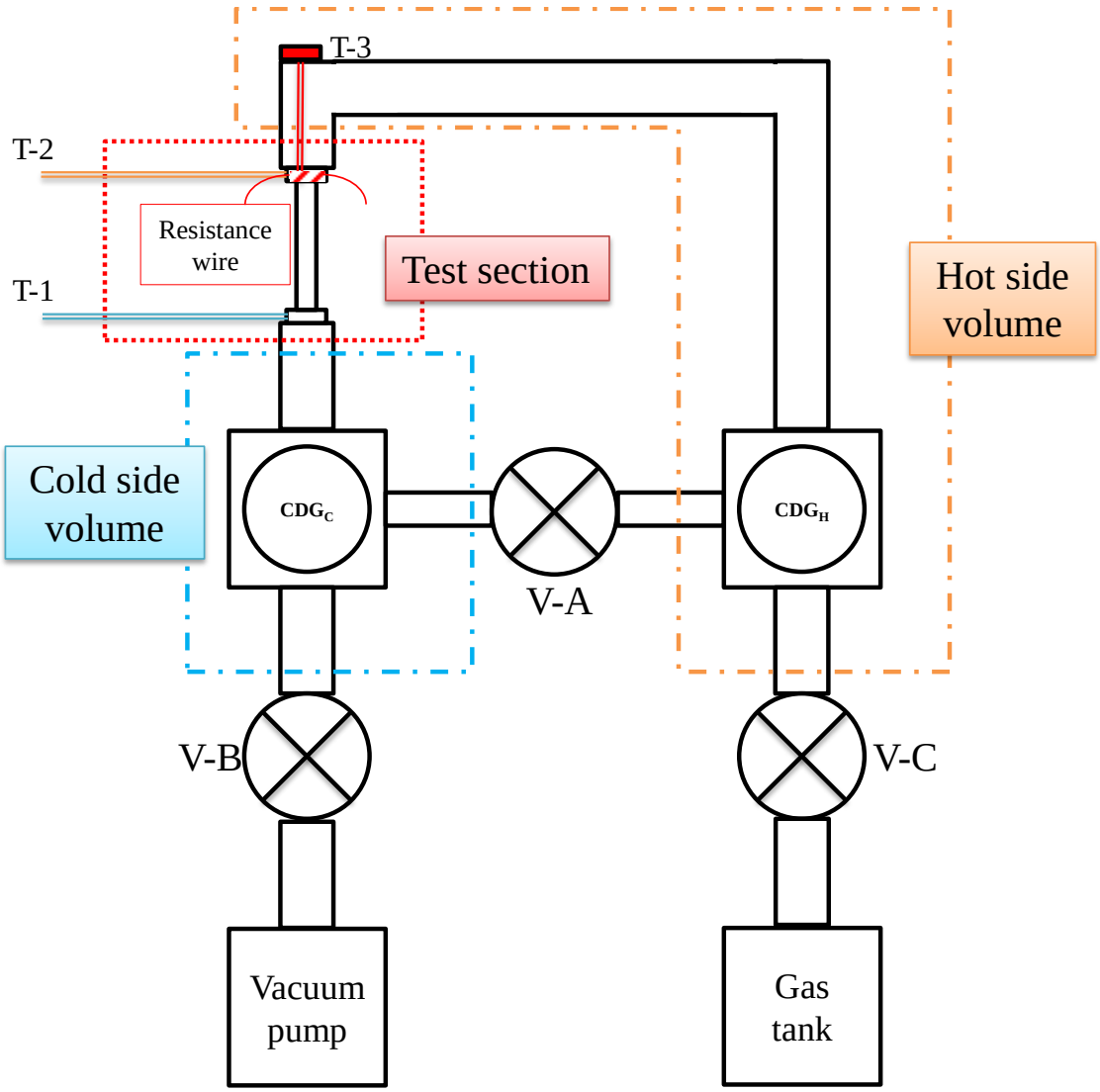

Figure 5.1: Scheme of the original setup including a test section with the tube and heating wire, three valves (V-A, V-B, V-C), two capacitance diaphragm gauges (CDG_C, CDG_H), three thermocouples (T-1, T-2, T-3), a vacuum pump and the pressurized gas tanks to fill the setup.

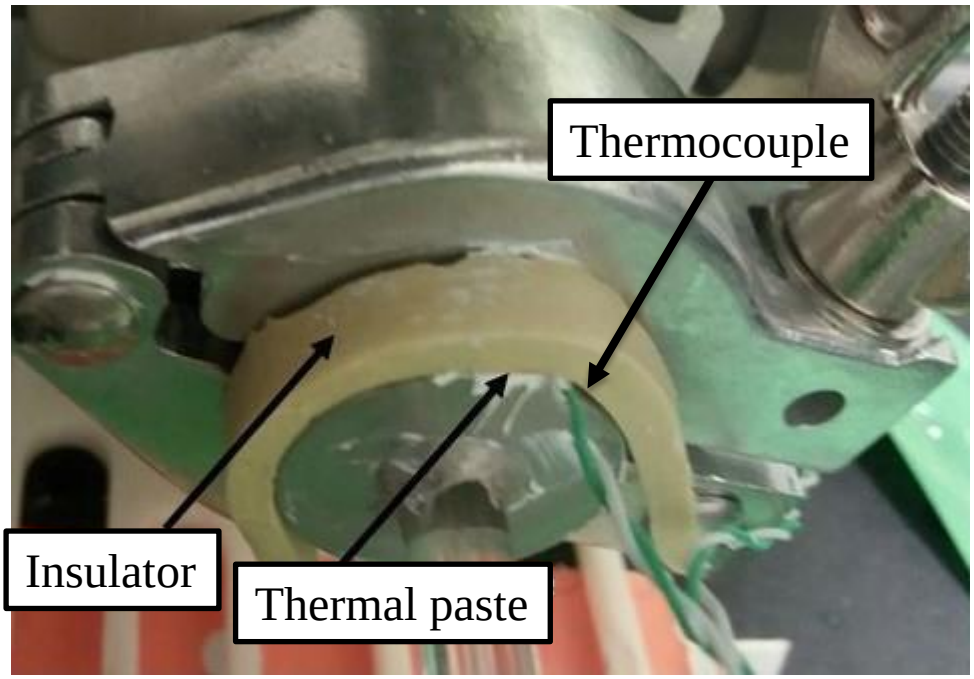

Figure 5.2: Hot end of the tube displaying the thermal paste and insulator around the heating resistance wire and the thermocouple T-2.

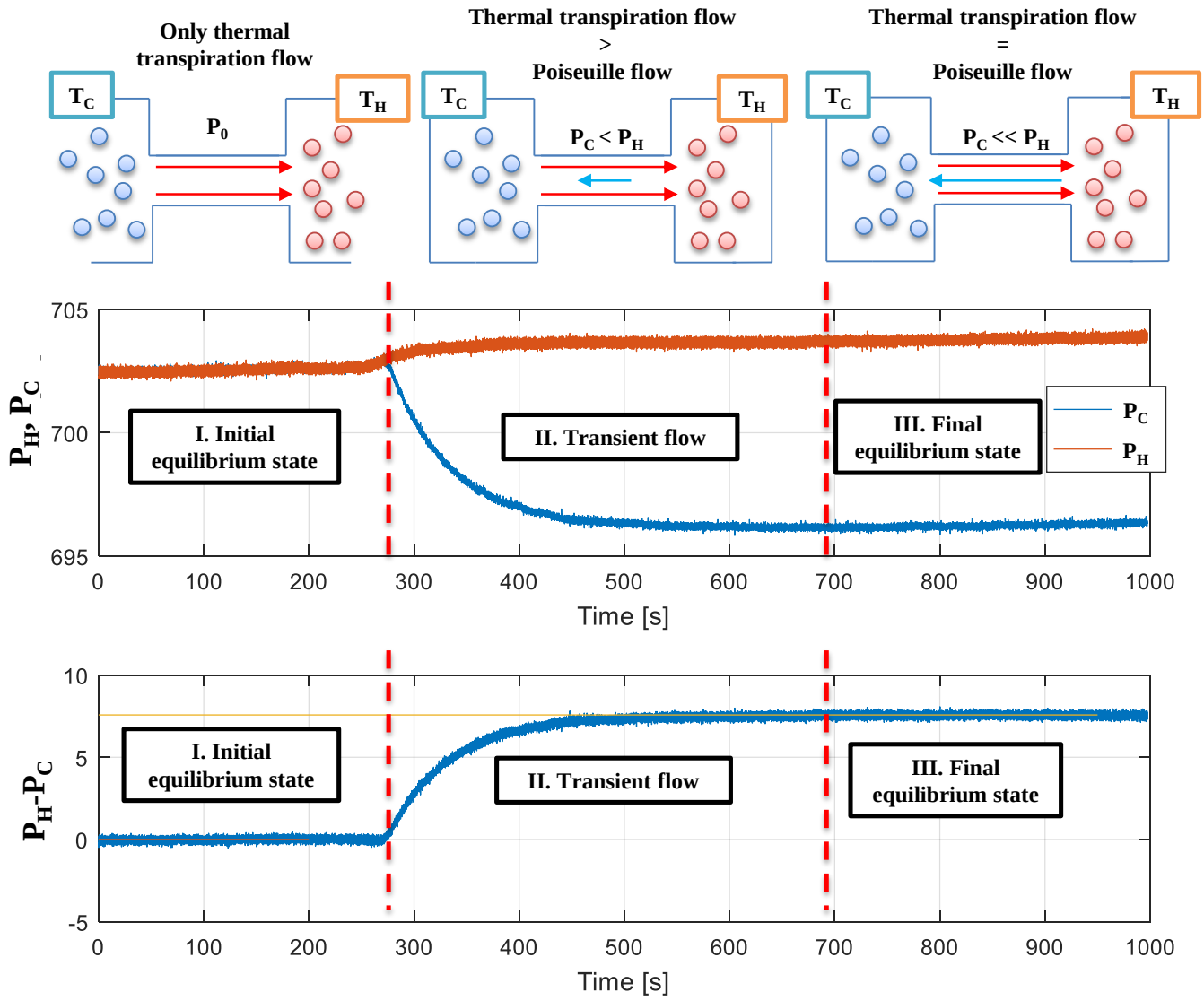

Figure 5.3: Example of a thermal transpiration experiment denoting the three main stages, i) initial equilibrium state, ii) transient flow and iii) final equilibrium state, and showing the transition from an open configuration to the closed configuration when the valve V-A is closed.

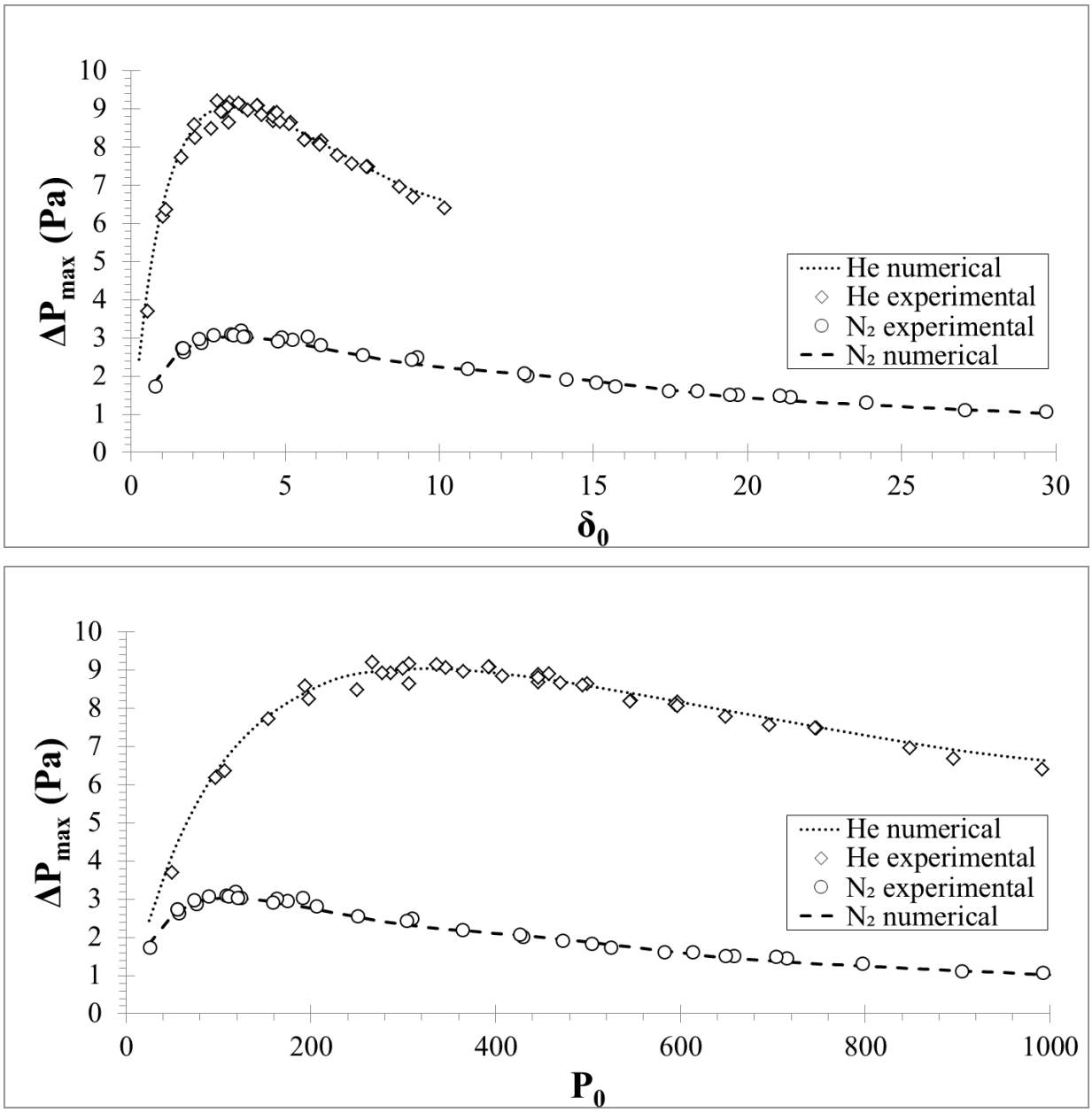

Figure 5.4: Experimental and numerical results for final difference of pressure generated in thermal transpiration flow experiments. The results are shown for both gases, helium (diamond) and nitrogen (circle), in terms of the reference rarefaction parameter (top) and the initial pressure (bottom).

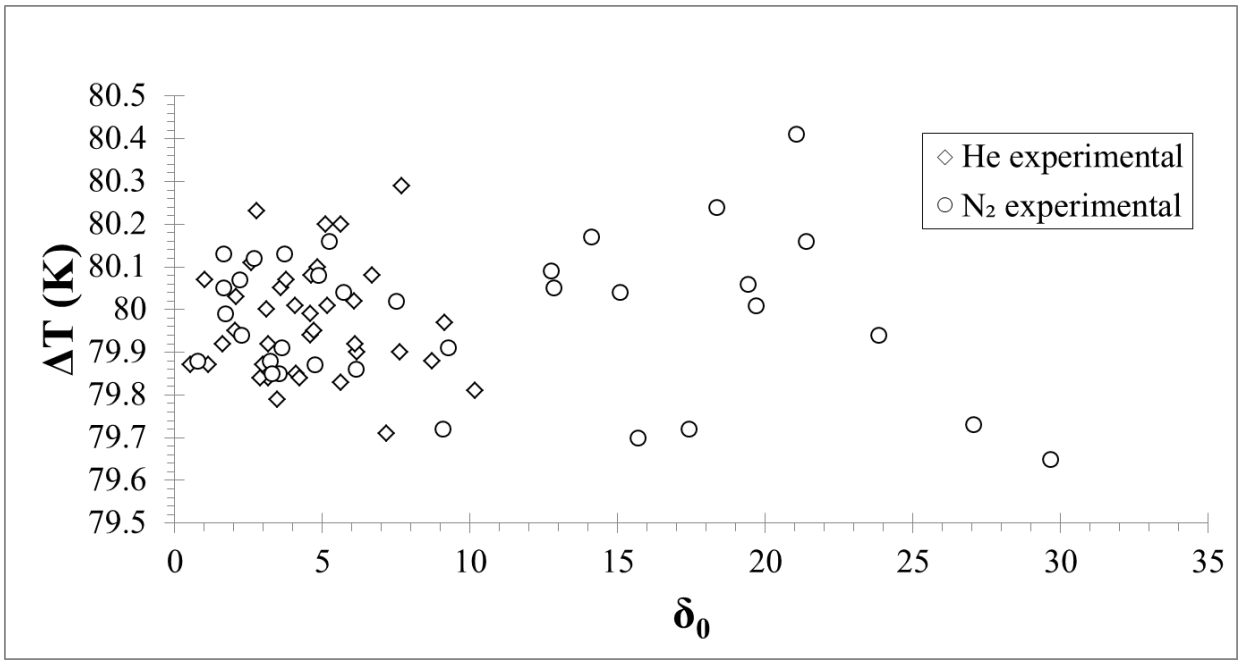

Figure 5.5: Stability of the temperature difference through all the experiments performed in the glass tube.

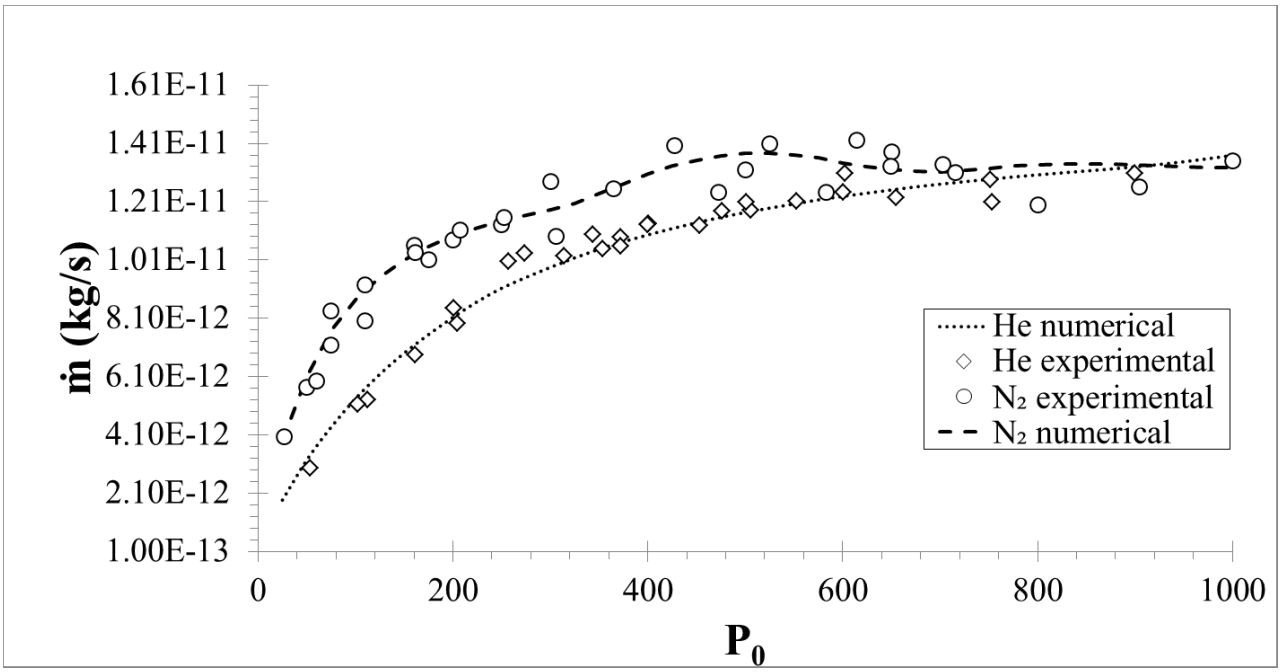

Figure 5.6: Numerical and experimental results of the mass flow rate calculated from the variation of pressure data using the constant volume time dependent methodology for helium (diamond) and nitrogen (circle) in terms of the initial pressure.

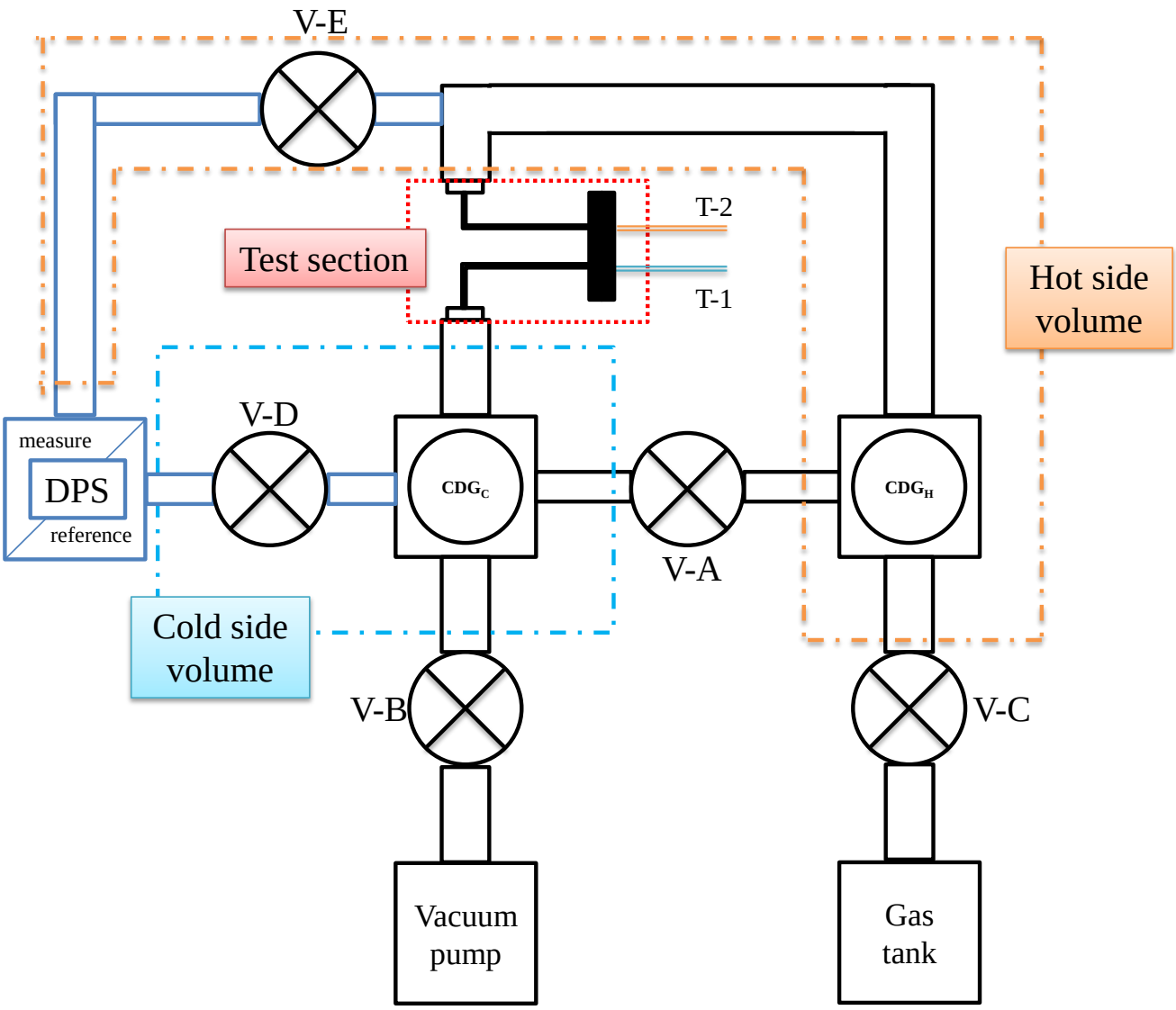

Figure 5.7: Scheme of the modified experimental setup including a test section with the tapered channel, five valves (V-A, V-B, V-C, V-D, V-E), two capacitance diaphragm gauges (CDG_C, CDG_H), a differential pressure sensor (DPS), two thermocouples (T-1, T-2), a vacuum pump and the pressurized gas tanks to fill the setup.

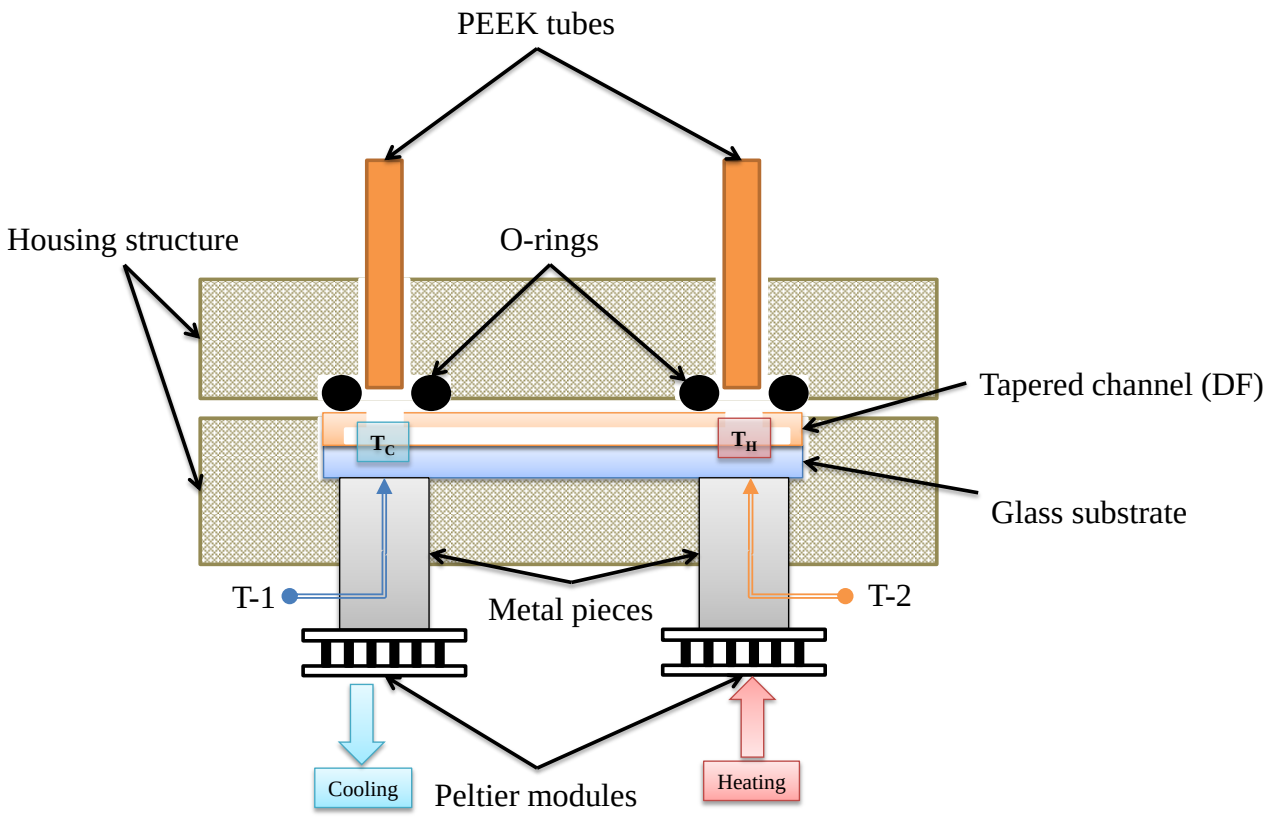

Figure 5.8: Scheme of the housing system designed to hold the samples and to provide external cooling and heating from two Peltier modules. It is noted that the temperatures measured by T-1 and T-2 are not the cold and hot temperatures in the channel, but the temperatures on the bottom side of the glass substrate.

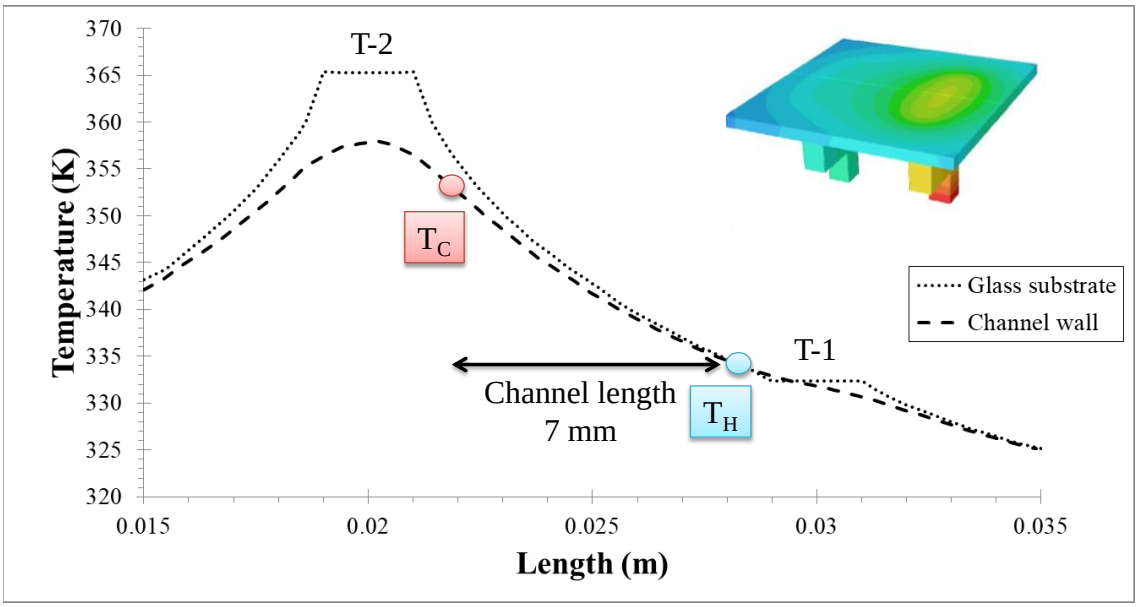

Figure 5.9: Heat transfer simulation showing the temperature in the center line of the bottom of glass substrate and the average of the temperatures in the channel walls when the temperatures measured in the glass substrate and the metal part in contact with it are T-1=333 K and T-2=373 K. The image shows the sample supported over the metal pieces (the housing is hidden to show the sample) with the hottest and coolest point corresponding to the surface in contact with the heating (resistance wire) and cooling (Peltier module) elements.

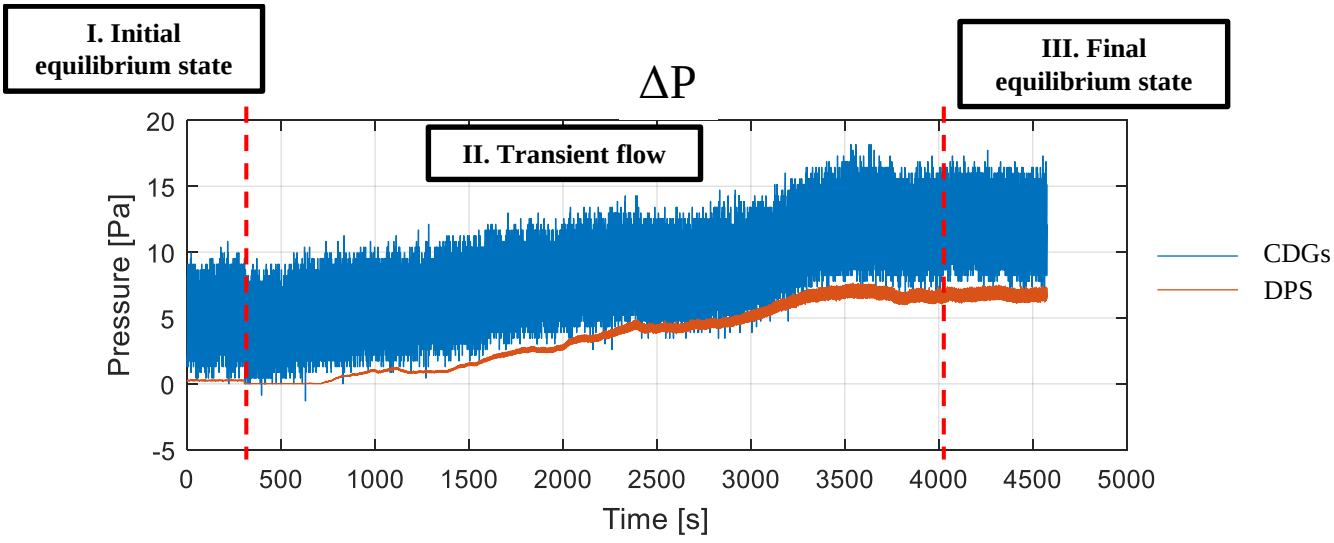

Figure 5.10: Comparison between the pressure difference measured by the differential pressure sensor (brown) and the capacitance diaphragm gauges (blue), showing the better accuracy and resolution of the differential pressure sensor.

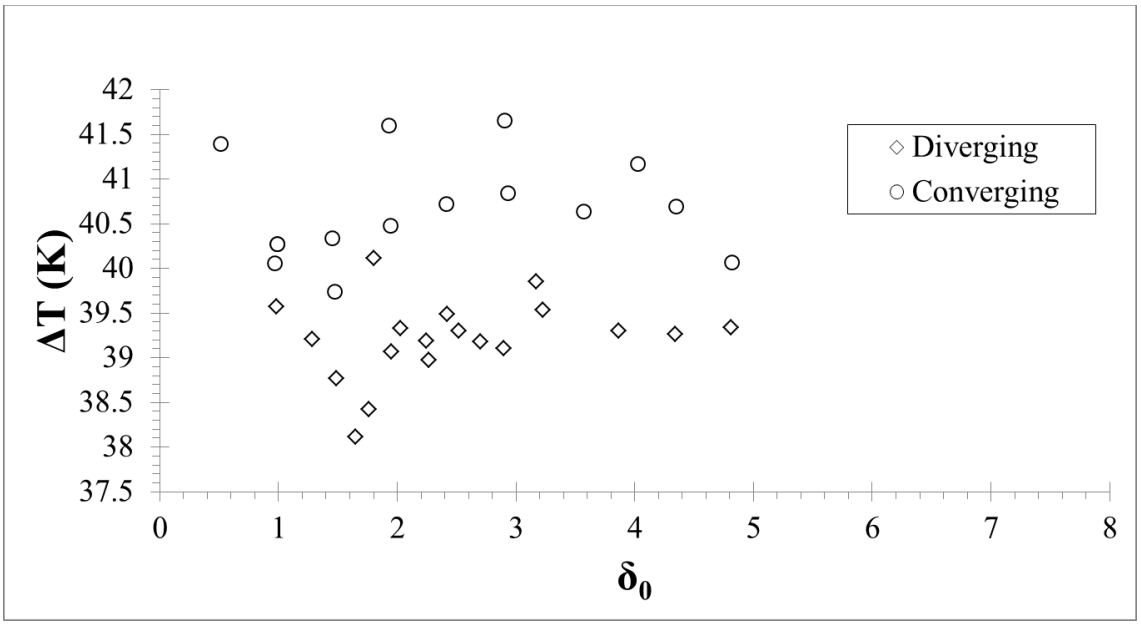

Figure 5.11: Measurements of the temperature difference for all the experimental data acquired for the tapered channel.

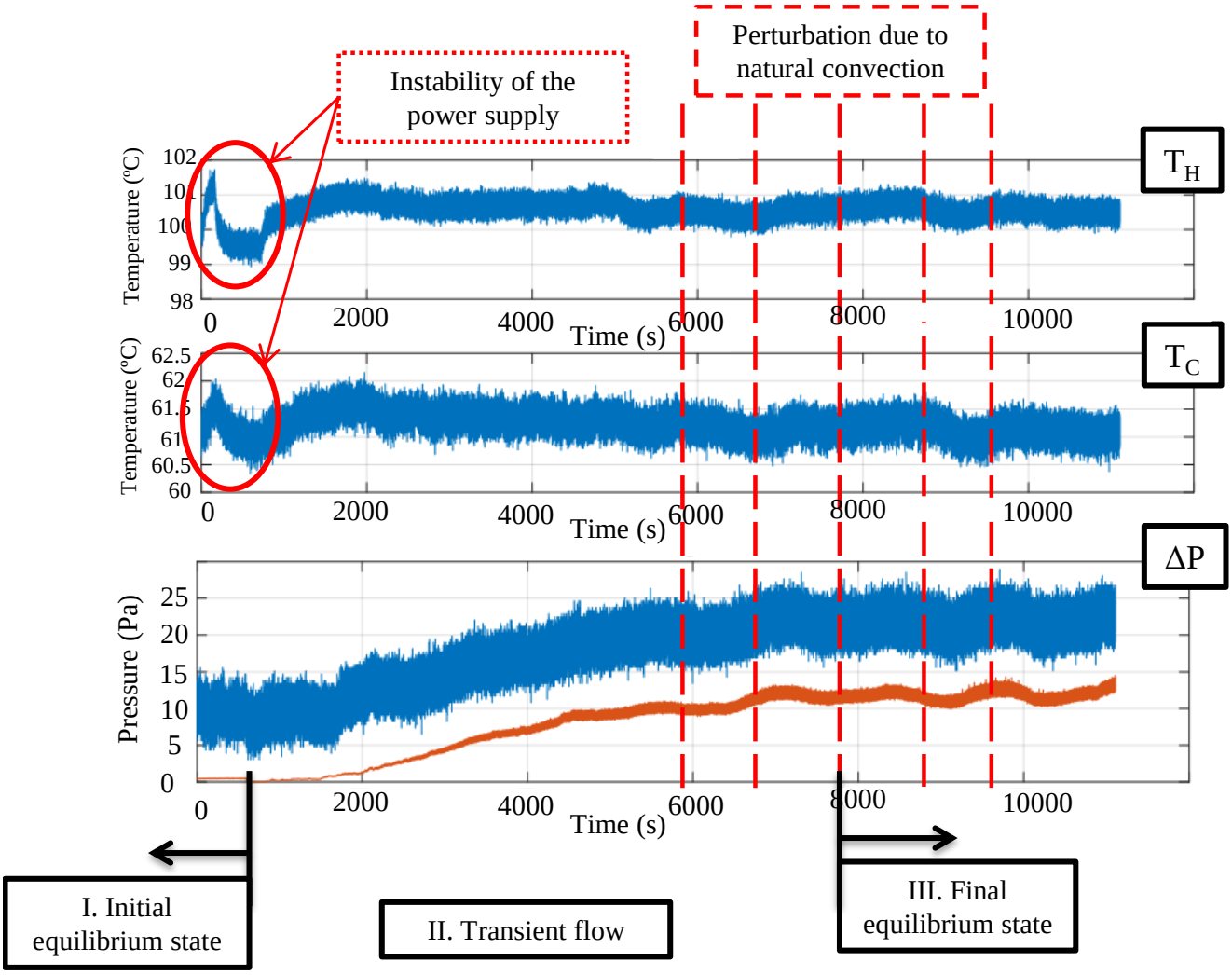

Figure 5.12: Representative experiment showing the instabilities registered in the temperature due to the power supply and the natural convection of air in the room due to the air conditioning system.

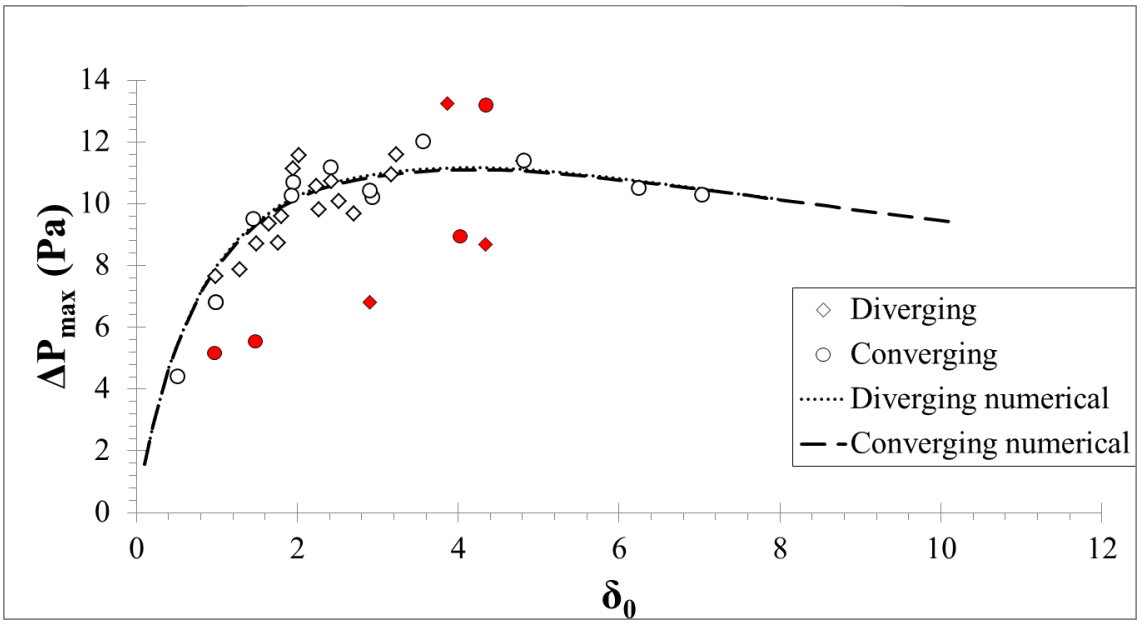

Figure 5.13: Numerical and experimental results of the pressure difference generated in the tapered channel sample for both directions of the flow, diverging (diamond) and converging (circle), in terms of the reference rarefaction parameter. The colored data points represent the experimental measurements that deviate more than 10 % from the numerical results.

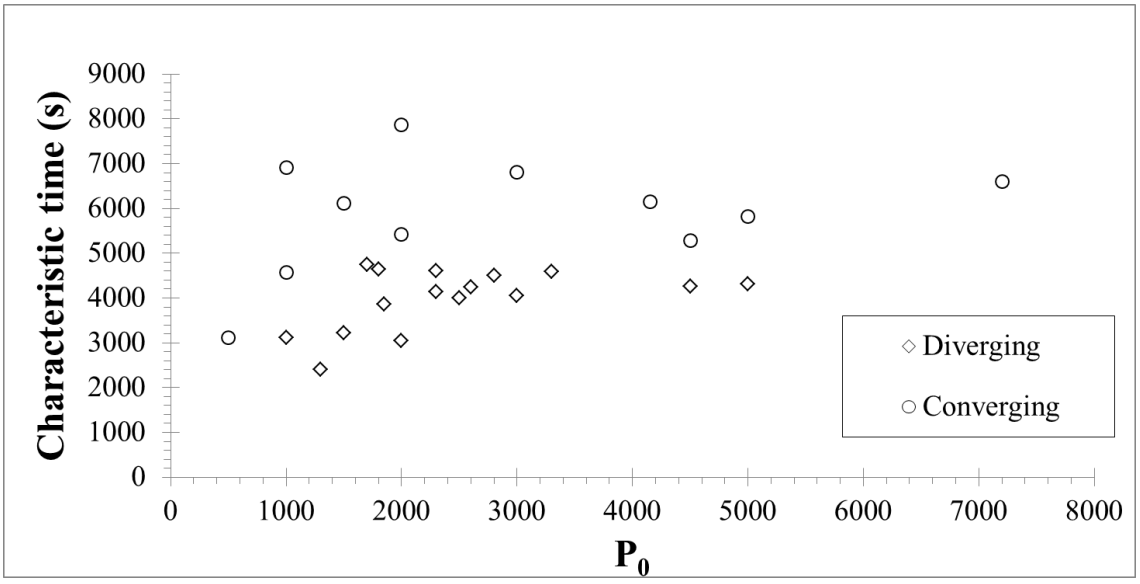

Figure 5.14: Characteristic time constant for each single experiment provided by the exponential fitting function to the pressure variation with time for the tapered channel in both directions, diverging (diamond) and converging (circle), in terms of the initial pressure of the experiment.

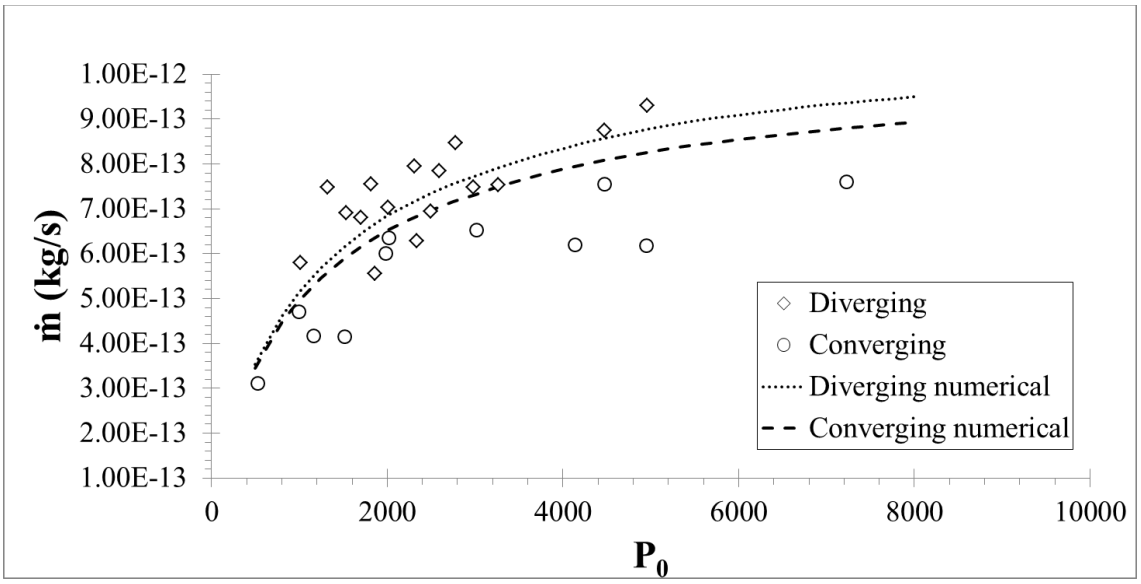

Figure 5.15: Numerical and experimental results of the mass flow rate calculated from the variation of pressure data using the constant volume time dependent methodology for the tapered channel in both directions, diverging (diamond) and converging (circle), in terms of the initial pressure of the experiment.

Chapter 6

Concluding remarks

The present Ph.D. work includes computational and experimental investigations, as well as the development and implementation of reliable fabrication techniques in one-stage and multi-stage Knudsen-type gas pumping micro devices. Gas flows through microchannels of both constant and variable (tapered) cross sections subject to pressure and temperature gradients have been considered. The so-called diode effect has been thoroughly investigated. The Ph.D. thesis was co-supervised by Prof. Stephane Colin of the National Institute of Applied Sciences (INSA) in Toulouse, France and by Prof. Dimitris Valougeorgis of the University of Thessaly (UTH) in Volos, Greece.

The theoretical/computational investigation was based on linear kinetic theory and is valid in the whole range of the Knudsen number. Useful guidelines concerning the tentative micropump designs have been obtained. The experimental work has been performed at the Clément Ader Institute (ICA); it was based on the constant volume time dependent methodology, for single microchannels with constant and variable cross sections. In the former case, very good agreement with corresponding computational results has been obtained. In the latter case, due to certain measurement uncertainties, only qualitative remarks have been provided. The manufacturing work has been performed at LAAS and collaborating CNRS laboratories. Following extensive efforts, the standard manufacturing LAAS procedure has been accordingly modified and successfully implemented to fabricate single tapered channels, which have been used in the experimental work. This novel fabrication methodology along with the computational and experimental findings will be applied in the short future in the development of multistage micropumps.

The main results and contributions of the present Ph.D. thesis are given in Section 6.1, followed by some remarks concerning future work in Section 6.2.

6.1 Summary and major contributions

Overall, the major contributions of the presented research can be summarized as follows:

- Two kinetic codes have been developed to characterize the performance of multi-stage systems with microchannels of rectangular tapered and circular cross sections. The codes are based on the linear Shakhov kinetic model subject to purely diffused boundary conditions combined with the infinite capillary theory.

- A parametric study of multi-stage Knudsen pumps consisting of various combinations of converging, diverging and uniform cross section channels has been performed, characterizing the performance of the following four different assemblies: converging-uniform, diverging-uniform, converging-diverging and uniform-uniform. The mass flow rate and pressure difference generated by each assembly has been provided, as well as the characteristic curves of the pump at different operating pressure in terms of the inclination parameter of the tapered walls and the number of stages of the assembly.

- A further investigation regarding the particular converging-diverging assembly has been performed to characterize the blocking pressure at which the pressure difference generated by the converging and diverging channels are equal (the resulting pressure difference and mass flow rate in the assembly are zero). This way, a thermal driven diode can be developed in which, depending on the operating pressure of the device, the flow can be in either converging or diverging direction without inverting the thermal gradient. The parametric investigation of this thermal driven diode has been performed by studying the influence of the size of the channels, the temperature and the gas species with the associated blocking pressure. It has been shown that the blocking pressure can be regulated by varying the temperature difference. More importantly, it has been demonstrated that the blocking pressure is different for each particular gas species, indicating that this thermal driven diode, based on converging and diverging channels, can be used for gas separation technological applications.

- A novel Knudsen pump design has been proposed with an architecture based on channels drilled across the thickness of a substrate (rather than etched along the substrate), connecting

two reservoirs at different uniform temperatures located at the top and bottom sides of the device. The arrangement of multiple parallel channels at each pumping stage combined with an adequate number of stages facilitates the development of tailor-made devices for specific performance applications. The proposed channel arrangement design provides a compacted structure with the cold and hot sides of the device spatially separated, facilitating the overall temperature. Three different modules have been studied in which the first two ones target either large mass flow rate or large pressure difference. The third module corresponds to the combination of the previous two target applications with moderate mass flow rate and pressure head. A parametric study of these modules has been performed providing the mass flow rate and the pressure difference generated by the thermal transpiration flow along with the pump characteristic curves in terms of the operating pressure, number of parallel pumping channels and stages.

- A manufacturing process has been proposed for the fabrication of Knudsen pumps consisting on the multi-level lamination of dry film photoresist layers with different patterns to fabricate 3D structures. The proposed manufacturing process can be used for fabricating the tapered channels assemblies, as well as the proposed modular Knudsen pump design. It is noted that the dry film photoresist material provides an improved thermal behavior compared to silicon devices due to its much lower thermal conductivity which is similar to glass. The manufacturing of some tapered channel has been completed with precise and accurate geometry.

- The standard manufacturing procedure developed at LAAS, based on dry film photoresist layer, displays a good resolution for single layer devices as in the case of the fabricated tapered channels. However, it has been seen that following this procedure in the fabricating of multi-layered devices the resolution attained has not been adequately accurate and fabrication of the channels of the modular Knudsen pump has failed. Consequently, the standard procedure has been modified. An approximate threshold dose for the polymerization of the interface between layers has been provided for different thicknesses of the dry film photoresist. Also, the proper manufacturing parameters for the fabrication of the modular

Knudsen pump design proposed have been identified allowing the fabrication of a device according to the specified guidelines.

- Thermal transpiration experiments in a long glass tube have been completed for two gases, namely helium and nitrogen, providing the measured difference of pressure generated by the thermal transpiration flow and the associated mass flow rate calculated using the constant volume time dependent methodology. The results obtained are in very good agreement with the numerical ones provided by the kinetic code.

- Preliminary experimental work for thermal transpiration flow in tapered channels has provided some results for the converging and diverging directions of the flow. No noticeable difference between the measured pressure difference in the converging and diverging directions has been observed. However, the observed longer times required in the converging experiments, compared to the diverging one, to reach quasi-steady conditions along with the characteristic times extracted from data fitting and the estimated mass flow rates using the constant volume time dependent methodology, indicate that the mass flow rate in the converging direction is lower than in the diverging direction.

6.2 Future work

The outcome of the present research is very significant, encouraging a continuation of present work in modeling, manufacturing and experiments to further improve the technological knowledge in the field and to fabricate promising gas microfluidics devices such as modular Knudsen pumps or thermal driven diodes for gas separation applications. In this research line the following steps are proposed:

- Simulations of thermal transpiration gas mixture flows in converging-diverging assemblies, assessing the flow blocking capabilities with various gas species, to further analyze the diode effect for gas separation, may be performed.

- A wide study to better characterize the polymerization of the dry film photoresist may be performed to accurately define the threshold dose to achieve the targeted resolution. In the

same study, a better characterization of the achievable resolution for multi-layer processes depending on the parameters of the manufacturing process will also be acquired.

- The proposed mechanism of refraction and reflection in multi-layer processes may be further investigated to demonstrate that it is the cause for the over polymerization of the samples in this work. First a characterization of the reflection and refraction of the dry film photoresist layer is required both before and after being exposed. Then, simulations of the exposure dose due to this mechanism in the areas that should not be exposed shall be performed to compare with the samples already manufactured.

- The fabrication of the modular Knudsen pump design, following the guidelines provided to improve the manufacturing process, may be completed.

- New tapered channel samples with internal heating elements included, following the lift-off process introduced in this work, may be manufactured. The new tapered channel samples should have an optimized geometry for characterizing the diode effect in order to increase the mass flow rate and to reduce the duration of the experiments. Multi-stage converging-diverging samples may also be included to investigate the blocking pressure behavior both for single gas and gas mixtures experiments.

- A better thermal isolation of the experimental setup is the key issue to guarantee a proper thermal stability and the quality of the results. Therefore it must be considerably improved. A new box to better isolate the setup from the natural convection in the room has been prepared. Also, once the internal heating elements in the new samples are introduced, it will be easier to isolate the test section to improve the thermal stability. The introduction of an electronically regulated valve can also help to improve the results obtained by achieving a more uniform and repeatable set of initial values through the experiments.

Appendices

Appendix A: Database of kinetic coefficients for tapered channels

The linearized Shakhov model equation for fully developed pressure- and temperature-driven flows in both tapered channels subject to purely diffuse boundary conditions has been computationally solved to deduce kinetic coefficients G_P and G_T for several values of the gas rarefaction parameter $\delta \in \left[1\times10^{-3}, 80\right]$ and a wide range of the local tapered channel aspect ratio $H(z)/W \in \left[0.01, 1\right]$. They have been obtained based on the discrete velocity method. Comparable results are also available in the literature [25], [27], [117] and they are presented here, in Table A.1-4, mainly for completeness, since they are implemented (linearly interpolated) in the solution of Equation (3.1) in order to compute the mass flow rate and the associated pressure distribution along the channel. Furthermore, for values of $\delta > 80$, which are associated with high inlet pressures, the kinetic coefficient G_P is obtained by linearly extrapolating the values from Table A.1 and Table A.2. This way, the kinetic coefficient G_P for values of $\delta > 80$ (hydrodynamic and slip regimes) can be expressed as $G_P = G_{P_h} + G_{P_{slip}}$, where G_{P_h} corresponds to the reduced mass flow rate in the hydrodynamic regime and $G_{P_{slip}}$ is the slip flow regime correction. The values obtained from the linear extrapolation of the kinetic database, which are in good agreement with previous results obtained in the literature [27], [117], are presented in Table A.5. On the other hand, the kinetic coefficient G_T for values of $\delta > 80$ is calculated as $G_T = \sigma_T / \delta$, where $\sigma_T = 1.175$ is the thermal slip coefficient.

Table A.1: Kinetic coefficients G_P for the pressure driven flow, in terms of the gas rarefaction parameter δ and the local tapered channel aspect ratio $H(z)/W \in [0.7,1]$.

	G_P						
δ	H(z)/W=1	H(z)/W=0.95	H(z)/W=0.9	H(z)/W=0.85	H(z)/W=0.8	H(z)/W=0.75	H(z)/W=0.7
0	0.838626	0.86028	0.88339	0.90816	0.93478	0.96351	0.99464
0.001	0.836952	0.85852	0.88154	0.9062	0.93271	0.9613	0.99229
0.01	0.828096	0.84927	0.87186	0.89604	0.922	0.94998	0.98027
0.02	0.821605	0.84251	0.8648	0.88864	0.91423	0.94179	0.97159
0.04	0.812205	0.83274	0.85463	0.87802	0.9031	0.93008	0.95923
0.05	0.808506	0.82891	0.85065	0.87387	0.89876	0.92553	0.95443
0.08	0.799721	0.81982	0.84122	0.86407	0.88854	0.91482	0.94317
0.1	0.795165	0.815124	0.836365	0.859033	0.8833	0.909346	0.937418
0.2	0.78058	0.800167	0.820989	0.843176	0.86688	0.892284	0.919589
0.4	0.769282	0.788822	0.809566	0.831632	0.85516	0.880306	0.907249
0.5	0.767668	0.787328	0.808188	0.830366	0.854	0.879224	0.906225
0.8	0.770313	0.79057	0.812043	0.834842	0.85909	0.884924	0.912493
1	0.775653	0.79641	0.81841	0.84175	0.86655	0.89294	0.92107
1.5	0.795238	0.81743	0.84092	0.86581	0.89221	0.92025	0.95004
2	0.819627	0.84336	0.86848	0.89507	0.92323	0.95309	0.98474
4	0.935202	0.96556	0.99762	1.0315	1.06728	1.10504	1.14485
5	0.997683	1.03146	1.06713	1.10479	1.14452	1.18639	1.23046
8	1.192656	1.2369	1.28359	1.33282	1.38465	1.43913	1.49626
10	1.326112	1.37743	1.43157	1.48861	1.54862	1.61162	1.67759
20	2.009863	2.09697	2.18876	2.28533	2.38671	2.49285	2.60363
30	2.704174	2.82727	2.95695	3.09329	3.23631	3.3859	3.54184
40	3.402165	3.56131	3.72893	3.90511	4.08984	4.28297	4.48417
50	4.101873	4.29709	4.50267	4.71872	4.9452	5.1819	5.4284
80	6.205355	6.5088	6.82832	7.16404	7.5158	7.88332	8.26583

Table A.2: Kinetic coefficients G_P for the pressure driven flow, in terms of the gas rarefaction parameter δ and the local tapered channel aspect ratio $H(z)/W \in [0.01, 0.6]$.

	G_P						
δ	H(z)/W=0.6	H(z)/W=0.5	H(z)/W=0.4	H(z)/W=0.25	H(z)/W=0.1	H(z)/W=0.05	H(z)/W=0.01
0	1.06572	1.15223	1.26129	1.50004	1.9857	2.3575	2.818
0.001	1.06298	1.14897	1.25724	1.49364	1.9704	2.3289	2.7663
0.01	1.04922	1.13278	1.23742	1.46311	1.9004	2.2039	2.5514
0.02	1.03934	1.12121	1.22333	1.44155	1.8522	2.1211	2.4157
0.04	1.02532	1.10488	1.20351	1.41136	1.7855	2.0106	2.2422
0.05	1.0199	1.09858	1.19588	1.39975	1.7601	1.9697	2.1801
0.08	1.00723	1.0839	1.17811	1.37262	1.701	1.8768	2.0436
0.1	1.000791	1.07645	1.16909	1.35877	1.6709	1.8308	1.9782
0.2	0.980931	1.05351	1.14115	1.31481	1.5744	1.6888	1.7862
0.4	0.967393	1.03769	1.12097	1.2788	1.4887	1.569	1.6342
0.5	0.96635	1.03629	1.11853	1.2718	1.4677	1.54	1.5983
0.8	0.973524	1.04372	1.1248	1.27015	1.4418	1.5017	1.5497
1	0.98313	1.05408	1.13528	1.27804	1.4411	1.497	1.5418
1.5	1.01537	1.08917	1.17212	1.31296	1.4659	1.5174	1.5587
2	1.05383	1.13119	1.21701	1.35938	1.5099	1.5603	1.6007
4	1.23074	1.32487	1.42629	1.58732	1.7516	1.8063	1.8502
5	1.3252	1.42838	1.53866	1.71205	1.8879	1.9466	1.9935
8	1.61826	1.74962	1.88815	2.10284	2.3192	2.3913	2.4491
10	1.8181	1.96871	2.1268	2.37069	2.6161	2.6979	2.7634
20	2.83812	3.08711	3.34599	3.74217	4.139813	4.27237	4.378409
30	3.87119	4.21979	4.58113	5.13282	5.686175	5.87065	6.018222
40	4.90866	5.35723	5.82151	6.52958	7.2396	7.4763	7.665643
50	5.94814	6.49684	7.06424	7.92905	8.796113	9.08513	9.316362
80	9.07156	9.92097	10.79814	12.13388	14.27627	13.91924	14.27627

Table A.3: Kinetic coefficients G_T for the pressure driven flow, in terms of the gas rarefaction parameter δ and the local tapered channel aspect ratio $H(z)/W \in [0.7,1]$.

	G_T						
δ	**H(z)/W=1**	**H(z)/W=0.95**	**H(z)/W=0.9**	**H(z)/W=0.85**	**H(z)/W=0.8**	**H(z)/W=0.75**	**H(z)/W=0.7**
0	0.4193	0.43014	0.4417	0.45408	0.46739	0.48175	0.49732
0.001	0.4175	0.42827	0.43973	0.452	0.46519	0.47942	0.49483
0.01	0.4078	0.41806	0.42903	0.44077	0.45335	0.4669	0.48155
0.02	0.4003	0.41023	0.42085	0.43219	0.44434	0.45739	0.47148
0.04	0.3888	0.39834	0.40844	0.41921	0.43073	0.44307	0.45635
0.05	0.3841	0.39345	0.40335	0.41389	0.42515	0.43721	0.45017
0.08	0.3723	0.3812	0.39059	0.40058	0.41123	0.4226	0.43479
0.1	0.3658	0.37439	0.38352	0.39321	0.40353	0.41453	0.42631
0.2	0.3412	0.34898	0.35714	0.36576	0.3749	0.38459	0.39489
0.4	0.3103	0.31693	0.32394	0.3313	0.33904	0.34718	0.35575
0.5	0.2989	0.3052	0.3118	0.31871	0.32596	0.33355	0.34151
0.8	0.2727	0.27815	0.28382	0.28971	0.29585	0.30222	0.30883
1	0.2591	0.26415	0.26934	0.27472	0.28029	0.28605	0.29199
1.5	0.2325	0.23669	0.24096	0.24535	0.24985	0.25446	0.25916
2	0.2121	0.21561	0.21921	0.22287	0.2266	0.23038	0.2342
4	0.1587	0.16068	0.16268	0.16468	0.16668	0.16866	0.17063
5	0.141	0.14259	0.14415	0.1457	0.14724	0.14876	0.15026
8	0.1054	0.10626	0.1071	0.10792	0.10873	0.10953	0.11031
10	0.0901	0.09065	0.09125	0.09183	0.09241	0.09297	0.09353
20	0.05175	0.05194	0.05212	0.0523	0.05248	0.05266	0.05284
30	0.03622	0.03631	0.0364	0.03649	0.03657	0.03666	0.03675
40	0.02785	0.0279	0.02795	0.02801	0.02806	0.02811	0.02816
50	0.02262	0.02265	0.02269	0.02272	0.02276	0.02279	0.02282
80	0.01447	0.01448	0.01449	0.01451	0.01452	0.01454	0.01455

Table A.4: Kinetic coefficients G_P for the pressure driven flow, in terms of the gas rarefaction parameter δ and the local tapered channel aspect ratio $H(z)/W \in [0.01, 0.6]$.

	G_T						
δ	H(z)/W=0.6	H(z)/W=0.5	H(z)/W=0.4	H(z)/W=0.25	H(z)/W=0.1	H(z)/W=0.05	H(z)/W=0.01
0	0.53286	0.57612	0.63065	0.75002	0.9928	1.1788	1.409
0.001	0.52997	0.57268	0.6264	0.74342	0.9777	1.1512	1.3603
0.01	0.5148	0.55492	0.60485	0.71111	0.9087	1.0351	1.1704
0.02	0.50336	0.54162	0.58886	0.68761	0.8614	0.9611	1.0588
0.04	0.48626	0.52185	0.56526	0.65355	0.7965	0.8659	0.9254
0.05	0.4793	0.51384	0.55575	0.64002	0.7717	0.8315	0.88
0.08	0.46204	0.49406	0.53238	0.60717	0.7141	0.755	0.7843
0.1	0.45255	0.48322	0.51964	0.58952	0.6845	0.7177	0.7401
0.2	0.41757	0.4435	0.47335	0.52681	0.587	0.6029	0.6126
0.4	0.37428	0.39482	0.41741	0.45422	0.4879	0.4957	0.5012
0.5	0.3586	0.3773	0.39751	0.42931	0.4567	0.4633	0.4681
0.8	0.32276	0.33754	0.35283	0.37514	0.393	0.3978	0.4015
1	0.30438	0.3173	0.33039	0.34886	0.3635	0.3677	0.371
1.5	0.26875	0.27844	0.28787	0.30059	0.311	0.3143	0.3169
2	0.24189	0.24947	0.25669	0.26627	0.2745	0.2772	0.2793
4	0.17445	0.17807	0.18145	0.18609	0.1905	0.192	0.1932
5	0.15316	0.1559	0.15847	0.16208	0.1656	0.1668	0.1677
8	0.11182	0.11327	0.11465	0.11667	0.1187	0.1193	0.1199
10	0.09461	0.09565	0.09666	0.09815	0.0996	0.1001	0.1005
20	0.05319	0.05353	0.05387	0.05437	0.05488	0.05505	0.05518
30	0.03692	0.03709	0.03726	0.03751	0.03776	0.03784	0.03791
40	0.02826	0.02836	0.02846	0.02861	0.02876	0.02881	0.02885
50	0.02289	0.02296	0.02302	0.02312	0.02322	0.02325	0.02328
80	0.01458	0.0146	0.01463	0.01467	0.01471	0.01472	0.01473

Table A.5: Coefficients for the calculation of *Gp* in terms of the aspect ratio *H(z)/W* for values of *δ>80*.

	$G_P = G_{P_h} + G_{P_{slip}}$	
Aspect ratio	G_{P_h} / δ	$G_{P_{slip}}$
H(z)/W=1	0.070116	0.596071
H(z)/W=0,95	0.073724	0.610907
H(z)/W=0,9	0.077522	0.626587
H(z)/W=0,85	0.081511	0.643187
H(z)/W=0,8	0.085687	0.660867
H(z)/W=0,75	0.090047	0.679533
H(z)/W=0,7	0.094581	0.69935
H(z)/W=0,6	0.104114	0.74244
H(z)/W=0,5	0.114138	0.789957
H(z)/W=0,4	0.124463	0.841073
H(z)/W=0,25	0.140161	0.921
H(z)/W=0,1	0.156005	0.99585
H(z)/W=0.05	0.161137	1.02828
H(z)/W=0.01	0.16533	1.049848

Appendix B: Database of kinetic coefficients for circular channels

The linearized Shakhov model equation for fully developed pressure- and temperature-driven flows in a channel subject to purely diffuse boundary conditions has been computationally solved to deduce kinetic coefficients G_P and G_T for several values of the gas rarefaction parameter $\delta \in \left[5\times10^{-4}, 50\right]$. They have been obtained based on the discrete velocity method. These results are also available in the literature [26], [85], [96] and they are presented here, in Table B1, mainly for completeness, since they are implemented (linearly interpolated) in the solution of Equation (1) in order to compute the mass flow rate and the associated pressure distribution along the channel. Furthermore, for values of $\delta > 50$, which are associated with high inlet pressures, the kinetic coefficients are analytically obtained by the corresponding slip solutions as $G_P = \delta/4 + \sigma_P$ and $G_T = \sigma_T/\delta$, where the viscous and thermal slip coefficients are $\sigma_P = 1.018$ and $\sigma_T = 1.175$, respectively [85].

Table B.1: Kinetic coefficients G_P and G_T for the pressure- and temperature-driven flows, respectively, in terms of the gas rarefaction parameter δ.

δ	**0.0005**	**0.001**	**0.005**	**0.01**	**0.02**	**0.03**	**0.04**	**0.05**
G_P	1.5023	1.5008	1.4904	1.4800	1.4636	1.4514	1.4418	1.4339
G_T	0.7502	0.7486	0.7366	0.7243	0.7042	0.6884	0.6752	0.6637
δ	**0.06**	**0.07**	**0.08**	**0.09**	**0.1**	**0.2**	**0.3**	**0.4**
G_P	1.4273	1.4217	1.4168	1.4127	1.4101	1.3911	1.3876	1.3920
G_T	0.6536	0.6444	0.6359	0.6281	0.6210	0.5675	0.5303	0.5015
δ	**0.5**	**0.6**	**0.7**	**0.8**	**0.9**	**1.0**	**1.2**	**1.4**
G_P	1.4011	1.4130	1.4270	1.4425	1.4592	1.4758	1.5158	1.5550
G_T	0.4779	0.4576	0.4367	0.4237	0.4092	0.3959	0.3721	0.3514
δ	**1.6**	**1.8**	**2.0**	**3.0**	**4.0**	**5.0**	**6.0**	**7.0**
G_P	1.5956	1.6373	1.6799	1.9014	2.1315	2.3666	2.6049	2.8455
G_T	0.3330	0.3165	0.3016	0.2439	0.2042	0.1752	0.1531	0.1359
δ	**8.0**	**9.0**	**10.0**	**20.0**	**30.0**	**40.0**	**50.0**	
G_P	3.0878	3.3314	3.5749	6.0492	8.5392	11.0360	13.4950	
G_T	0.1220	0.1106	0.1014	0.05426	0.03685	0.02785	0.02212	

References

[1] Y. Sone, “Flows Induced by Temperature Fields in a Rarefied Gas and their Ghost Effect on the Behavior of a Gas in the Continuum Limit,” *Annu. Rev. Fluid Mech.*, vol. 32, no. 1, pp. 779–811, Jan. 2000.

[2] Y. Sone, *Molecular gas dynamics : theory, techniques, and applications*. Birkhäuser, 2007.

[3] O. Reynolds, “XVIII. On certain dimensional properties of matter in the gaseous state,” *Philos. Trans. R. Soc. London, Ser. A*, vol. 170, pp. 727–845, Jan. 1879.

[4] J. C. Maxwell, “On stresses in rarefied gases arising from inequalities of temperature,” *Proc. R. Soc. London*, vol. 27, no. 185–189, pp. 304–308, Jan. 1878.

[5] M. Knudsen, “Eine Revision der Gleichgewichtsbedingung der Gase. Thermische Molekularströmung,” *Ann. Phys.*, vol. 336, no. 1, pp. 205–229, 1909.

[6] M. Knudsen, “Thermischer Molekulardruck der Gase in Röhren,” *Ann. Phys.*, vol. 338, no. 16, pp. 1435–1448, Jan. 1910.

[7] S. Weber and G. Schmidt, “Commun. Leiden. Rapp. et Commun.,” in *7e Congre. intern du Froid*, 1936, p. 246c,72.

[8] A. Van Itterbeek and E. De Grande, “Measurements on the thermomolecular pressure difference for hydrogen and deuterium gas at low temperatures,” *Physica*, vol. 13, no. 6–7, pp. 289–304, Aug. 1947.

[9] J. M. Los and R. R. Fergusson, “Measurements of thermomolecular pressure differences on argon and nitrogen,” *Trans. Faraday Soc.*, vol. 48, no. 0, p. 730, Jan. 1952.

[10] S. C. Liang, “Some Measurements of Thermal Transpiration,” *J. Appl. Phys.*, vol. 22, no. 2, pp. 148–153, Feb. 1951.

[11] S. C. Liang, “On the Calculation of Thermal Transpiration,” *J. Phys. Chem.*, vol. 57, no. 9, pp. 910–911, Sep. 1953.

[12] M. J. Bennett and F. C. Tompkins, “Thermal transpiration: application of Liang’s equation,” *Trans. Faraday Soc.*, vol. 53, no. 0, p. 185, Jan. 1957.

[13] T. Takaishi and Y. Sensui, “Thermal transpiration effect of hydrogen, rare gases and methane,” *Trans. Faraday Soc.*, vol. 59, no. 0, p. 2503, Jan. 1963.

[14] H. H. Podgurski and F. N. Davis, “Thermal transpiration at low pressure. The vapor pressure of xenon below 90°K,” *J. Phys. Chem.*, vol. 65, no. 8, pp. 1343–1348, Aug. 1961.

[15] T. Edmonds and J. P. Hobson, “A Study of Thermal Transpiration Using Ultrahigh-Vacuum Techniques,” *J. Vac. Sci. Technol.*, vol. 2, no. 4, pp. 182–197, Jul. 1965.

[16] R. A. Watkins, W. L. Taylor, and W. J. Haubach, “Thermomolecular Pressure Difference Measurements for Precision Helium−3 and Helium−4 Vapor-Pressure Thermometry,” *J. Chem. Phys.*, vol. 46, no. 3, pp. 1007–1018, Feb. 1967.

[17] Y. Sone and K. Yamamoto, “Flow of Rarefied Gas through a Circular Pipe,” *Phys. Fluids*, vol. 11, no. 8, p. 1672, Aug. 1968.

[18] S. K. Loyalka, “Thermal Transpiration in a Cylindrical Tube,” *Phys. Fluids*, vol. 12, no. 11, p. 2301, Sep. 1969.

[19] B. K. Annis, “Thermal Creep in Gases,” *J. Chem. Phys.*, vol. 57, no. 7, pp. 2898–2905, Oct. 1972.

[20] S. K. Loyalka and J. W. C. Jr., “Thermal Creep Slip with Arbitrary Accommodation at the

Surface," *Phys. Fluids*, vol. 14, no. 8, p. 1656, Aug. 1971.
[21] B. T. Porodnov, A. N. Kulev, and F. T. Tuchvetov, "Thermal transpiration in a circular capillary with a small temperature difference," *J. Fluid Mech.*, vol. 88, no. 4, pp. 609–622, Oct. 1978.
[22] J. G. Méolans and I. A. Graur, "Continuum analytical modelling of thermal creep," *Eur. J. Mech. - B/Fluids*, vol. 27, no. 6, pp. 785–809, Nov. 2008.
[23] J. Chen, "Numerical and experimental analysis of flows generated by temperature fields in rarefied gas : application to the design of Knudsen micropumps," INSA Toulouse, 2016.
[24] F. Sharipov, "Rarefied gas flow through a long tube at arbitrary pressure and temperature drops," *J. Vac. Sci. Technol. A Vacuum, Surfaces, Film.*, vol. 15, no. 4, pp. 2434–2436, Jul. 1997.
[25] F. Sharipov, "Non-isothermal gas flow through rectangular microchannels," *J. Micromech. Microeng.*, vol. 9, no. 4, pp. 394–401, Dec. 1999.
[26] F. Sharipov and G. Bertoldo, "Rarefied gas flow through a long tube of variable radius," *J. Vac. Sci. Technol., A*, vol. 23, no. 3, pp. 531–533, May 2005.
[27] I. Graur and M. T. Ho, "Rarefied gas flow through a long rectangular channel of variable cross section," *Vacuum*, vol. 101, pp. 328–332, Mar. 2014.
[28] I. Graur and F. Sharipov, "Non-isothermal flow of rarefied gas through a long pipe with elliptic cross section," *Microfluid. Nanofluid.*, vol. 6, no. 2, pp. 267–275, Feb. 2009.
[29] K. Ritos, Y. Lihnaropoulos, S. Naris, and D. Valougeorgis, "Pressure- and Temperature-Driven Flow Through Triangular and Trapezoidal Microchannels," *Heat Transf. Eng.*, vol. 32, no. 13–14, pp. 1101–1107, Nov. 2011.
[30] G. A. Bird, *Molecular gas dynamics and the direct simulation of gas flows*. Clarendon Press, 1994.
[31] N. D. Masters and W. Ye, "Octant flux splitting information preservation DSMC method for thermally driven flows," *J. Comput. Phys.*, vol. 226, no. 2, pp. 2044–2062, Oct. 2007.
[32] H. Akhlaghi and E. Roohi, "Mass flow rate prediction of pressure–temperature-driven gas flows through micro/nanoscale channels," *Contin. Mech. Thermodyn.*, vol. 26, no. 1, pp. 67–78, Jan. 2014.
[33] F. Sharipov and D. Kalempa, "Gaseous mixture flow through a long tube at arbitrary Knudsen numbers," *J. Vac. Sci. Technol. A Vacuum, Surfaces, Film.*, vol. 20, no. 3, pp. 814–822, May 2002.
[34] S. Naris, D. Valougeorgis, D. Kalempa, and F. Sharipov, "Flow of gaseous mixtures through rectangular microchannels driven by pressure, temperature, and concentration gradients," *Phys. Fluids*, vol. 17, no. 10, p. 100607, 2005.
[35] A. Yakunchikov and V. Kosyanchuk, "Numerical investigation of gas separation in the system of filaments with different temperatures," *Int. J. Heat Mass Transf.*, vol. 138, pp. 144–151, Aug. 2019.
[36] K. Aoki, L. Mieussens, S. Takata, P. Degond, M. Nishioka, and S. Takata, "Numerical Simulation of a Knudsen Pump Using the Effect of Curvature of the Channel," 2007.
[37] K. Aoki, P. Degond, L. Mieussens, S. Takata, and H. Yoshida, "A Diffusion Model for Rarefied Flows in Curved Channels," *Multiscale Model. Simul.*, vol. 6, no. 4, pp. 1281–1316, Jan. 2008.
[38] V. Leontidis, J. Chen, L. Baldas, and S. Colin, "Numerical design of a Knudsen pump with curved channels operating in the slip flow regime," *Heat Mass Transf.*, vol. 50, no. 8, pp. 1065–1080, Aug. 2014.

[39] D. M. Bond, V. Wheatley, and M. Goldsworthy, "Numerical investigation of curved channel Knudsen pump performance," *Int. J. Heat Mass Transf.*, vol. 76, pp. 1–15, Sep. 2014.

[40] D. M. Bond, V. Wheatley, and M. Goldsworthy, "Numerical investigation into the performance of alternative Knudsen pump designs," *Int. J. Heat Mass Transf.*, vol. 93, pp. 1038–1058, Feb. 2016.

[41] J. Chen *et al.*, "Investigation of temperature-driven flow between ratchet surfaces," in *Proceedings of the 2nd European Conference on Non-equilibrium Gas Flows – NEGF15*, 2015, pp. 101–109.

[42] J. Chen, S. Stefanov, L. Baldas, S. Colin, and S. K. Stefanov, "Analysis of flow induced by temperature fields in ratchet-like microchannels by Direct Simulation Monte Carlo," *Int. J. Heat Mass Transf.*, vol. 99, pp. 672–680, 2016.

[43] G. Tatsios, G. Lopez Quesada, M. Rojas-Cardenas, L. Baldas, S. Colin, and D. Valougeorgis, "Computational investigation and parametrization of the pumping effect in temperature-driven flows through long tapered channels," *Microfluid. Nanofluid.*, vol. 21, no. 5, p. 99, May 2017.

[44] G. Pham-Van-Diep, P. Keeley, and E. P. Muntz, "A micromechanical Knudsen compressor," *19th Symp. Rarefied Gas Dynaimics*, vol. 1, no. Oxford University Press, pp. 715–721, 1995.

[45] S. E. Vargo, E. P. Muntz, and W. C. Tang, "The MEMS Kndusen compressor as a vacuum pump for space exploration applications," in *2nd International Conference on Integrated Micro/Nanotechnology for Space Applications Pasadena*, 1999, p. 11.

[46] S. E. Vargo, "Initial results from the first MEMS fabricated thermal transpiration-driven vacuum pump," in *AIP Conference Proceedings*, 2001, vol. 585, pp. 502–509.

[47] M. Young, "Characterization and Optimization of a Radiantly Driven Multi-Stage Knudsen Compressor," in *AIP Conference Proceedings*, 2005, vol. 762, pp. 174–179.

[48] Y.-L. Han and E. P. Muntz, "Experimental investigation of micro-mesoscale Knudsen compressor performance at low pressures," *J. Vac. Sci. Technol. B Microelectron. Nanom. Struct.*, vol. 25, no. 3, p. 703, 2007.

[49] Y. L. Han, M. Young, E. P. Muntz, and G. Shiflett, "Knudsen Compressor Performance at Low Pressures," in *AIP Conference Proceedings*, 2005, pp. 162–167.

[50] N. K. Gupta and Y. B. Gianchandani, "Thermal transpiration in zeolites: A mechanism for motionless gas pumps," *Appl. Phys. Lett.*, vol. 93, no. 19, p. 193511, Nov. 2008.

[51] N. K. Gupta and Y. B. Gianchandani, "A high-flow Knudsen pump using a polymer membrane: Performance at and below atmospheric pressures," in *2010 IEEE 23rd International Conference on Micro Electro Mechanical Systems (MEMS)*, 2010, pp. 1095–1098.

[52] N. K. Gupta and Y. B. Gianchandani, "Porous ceramics for multistage Knudsen micropumps-modeling approach and experimental evaluation," *J. Micromech. Microeng.*, vol. 21, no. 9, p. 095029, Sep. 2011.

[53] K. Pharas and S. McNamara, "Knudsen pump driven by a thermoelectric material," *J. Micromechanics Microengineering*, vol. 20, no. 12, p. 125032, Dec. 2010.

[54] H. Sugimoto and Y. Sone, "Vacuum Pump without a Moving Part and its Performance," in *AIP Conference Proceedings*, 2003, pp. 1041–1048.

[55] S. McNamara and Y. B. Gianchandani, "On-chip vacuum generated by a micromachined Knudsen pump," *J. Microelectromech. Syst.*, vol. 14, no. 4, pp. 741–746, Aug. 2005.

[56] N. K. Gupta, S. An, and Y. B. Gianchandani, "A Si-micromachined 48-stage Knudsen pump for on-chip vacuum," *J. Micromech. Microeng.*, vol. 22, p. 8, 2012.

[57] S. An, N. K. Gupta, and Y. B. Gianchandani, "A Si-Micromachined 162-Stage Two-Part Knudsen Pump for On-Chip Vacuum," *J. Microelectromech. Syst.*, vol. 23, no. 2, pp. 406–416, Apr. 2014.

[58] Y. Qin, S. An, and Y. B. Gianchandani, "Arrayed architectures for multi-stage Si-micromachined high-flow Knudsen pumps," *J. Micromech. Microeng.*, vol. 25, no. 11, p. 115026, Nov. 2015.

[59] H. Kim, A. A. Astle, K. Najafi, L. P. Bernal, and P. D. Washabaugh, "An Integrated Electrostatic Peristaltic 18-Stage Gas Micropump With Active Microvalves," *J. Microelectromechanical Syst.*, vol. 24, no. 1, pp. 192–206, Feb. 2015.

[60] N. Van Toan, N. Inomata, N. H. Trung, and T. Ono, "Knudsen pump produced via silicon deep RIE, thermal oxidation, and anodic bonding processes for on-chip vacuum pumping," *J. Micromechanics Microengineering*, vol. 28, no. 5, p. 055001, May 2018.

[61] P. Zeng, K. Wang, J. Ahn, and P. D. Ronney, "Thermal Transpiration Based Pumping and Power Generation Devices," *J. Therm. Sci. Technol.*, vol. 8, no. 2, pp. 370–379, 2013.

[62] K. Kugimoto, Y. Hirota, and Y. Kizaki, "Motionless heat pump – A new application of thermal transpiration," 2016, p. 080004.

[63] K. Kugimoto, Y. Hirota, T. Yamauchi, H. Yamaguchi, and T. Niimi, "A novel heat pump system using a multi-stage Knudsen compressor," *Int. J. Heat Mass Transf.*, vol. 127, pp. 84–91, Dec. 2018.

[64] K. Kugimoto, Y. Hirota, T. Yamauchi, H. Yamaguchi, and T. Niimi, "Design and demonstration of Knudsen heat pump without moving parts free from electricity," *Appl. Energy*, vol. 250, no. November 2018, pp. 1260–1269, 2019.

[65] Y. Qin and Y. B. Gianchandani, "A fully electronic microfabricated gas chromatograph with complementary capacitive detectors for indoor pollutants," *Microsystems Nanoeng.*, vol. 2, no. 1, p. 15049, Dec. 2016.

[66] Yutao Qin and Y. B. Gianchandani, "iGC1: An Integrated Fluidic System for Gas Chromatography Including Knudsen Pump, Preconcentrator, Column, and Detector Microfabricated by a Three-Mask Process," *J. Microelectromechanical Syst.*, vol. 23, no. 4, pp. 980–990, Aug. 2014.

[67] Q. Cheng, Y. Qin, and Y. B. Gianchandani, "A bidirectional Knudsen pump with superior thermal management for micro-gas chromatography applications," in *2017 IEEE 30th International Conference on Micro Electro Mechanical Systems (MEMS)*, 2017, pp. 167–170.

[68] S. Nakaye, H. Sugimoto, N. K. Gupta, and Y. B. Gianchandani, "Thermally enhanced membrane gas separation," *Eur. J. Mech. - B/Fluids*, vol. 49, pp. 36–49, Jan. 2015.

[69] S. Nakaye and H. Sugimoto, "Demonstration of a gas separator composed of Knudsen pumps," *Vacuum*, vol. 125, pp. 154–164, Mar. 2016.

[70] K. Aoki, S. Takata, and K. Kugimoto, "Diffusion Approximation for the Knudsen Compressor Composed of Circular Tubes," in *AIP Conference Proceedings*, 2008, pp. 953–958.

[71] D. Bernoulli, *Hydrodynamica, sive de viribus et motibus fluidorum commentarii*. 1738.

[72] J. Herapath, *Mathematical physics: or, The mathematical principles of natural philosophy: with a development of the causes of heat, gaseous elasticity, gravitation, and other great phenomena of nature*. 1847.

[73] J. P. Joule, “On the Mechanical Equivalent of Heat and on the Constitution of Elastic Fluids,” in *18th Meeting BAAS*, 1848.
[74] R. Clausius, “XI. On the nature of the motion which we call heat,” *London, Edinburgh, Dublin Philos. Mag. J. Sci.*, vol. 14, no. 91, pp. 108–127, Aug. 1857.
[75] T. Graham, “XVII. On the molecular mobility of gases,” *Philos. Trans. R. Soc. London*, vol. 153, pp. 385–405, Jan. 1863.
[76] J. Maxwell, “On the Dynamical Theory of Gases,” *Philos. Trans. R. Soc. London, Vol. 157, pp. 49-88*, vol. 157, pp. 49–88, 1867.
[77] J. Maxwell, “VII. On stresses in rarified gases arising from inequalities of temperature,” *Philos. Trans. R. Soc. London*, vol. 170, pp. 231–256, Jan. 1879.
[78] L. Boltzmann, “Weitere Studien über das Wörmegleichgewicht unter Gasmolekülen,” *Sitzungsberichte Akad. Wiss., Vienna, part II*, vol. 66, pp. 275–370, 1872.
[79] C. Shen, *Rarefied Gas Dynamics*. Berlin, Heidelberg: Springer Berlin Heidelberg, 2005.
[80] J. H. Ferziger and H. G. Kaper, *Mathematical theory of transport processes in gases*. North-Holland Pub. Co, 1972.
[81] G. A. Bird, “Monte Carlo Simulation of Gas Flows,” *Annu. Rev. Fluid Mech.*, vol. 10, no. 1, pp. 11–31, Jan. 1978.
[82] K. Koura and H. Matsumoto, “Variable soft sphere molecular model for inverse-power-law or Lennard-Jones potential,” *Phys. Fluids A Fluid Dyn.*, vol. 3, no. 10, pp. 2459–2465, Oct. 1991.
[83] S. Colin, “Single-Phase Gas Flow in Microchannels,” in *Heat Transfer and Fluid Flow in Minichannels and Microchannels*, Elsevier, 2014, pp. 11–102.
[84] M. Gad-el-Hak, *The MEMS handbook*. CRC/Taylor & Francis, 2001.
[85] F. Sharipov and V. Seleznev, “Data on Internal Rarefied Gas Flows,” *J. Phys. Chem. Ref. Data*, vol. 27, no. 3, pp. 657–706, May 1998.
[86] P. L. Bhatnagar, E. P. Gross, and M. Krook, “A Model for Collision Processes in Gases. I. Small Amplitude Processes in Charged and Neutral One-Component Systems,” *Phys. Rev.*, vol. 94, no. 3, pp. 511–525, May 1954.
[87] P. Welander, “On the temperature jump in rarefied gas,” *Ark. Fys.*, vol. 7, 1954.
[88] E. M. Shakhov, “Generalization of the Krook kinetic relaxation equation,” *Fluid Dyn.*, vol. 3, no. 5, pp. 95–96, 1972.
[89] P. Bassanini, C. Cercignani, and C. D. Pagani, “Influence of the accommodation coefficient on the heat transfer in a rarefied gas,” *Int. J. Heat Mass Transf.*, vol. 11, no. 9, pp. 1359–1369, 1968.
[90] J. R. Thomas, T. S. Chang, and C. E. Siewert, “Heat transfer between parallel plates with arbitrary surface accommodation,” *Phys. Fluids*, vol. 16, no. 12, p. 2116, Jul. 1973.
[91] C. Cercignani and M. Lampis, “Kinetic models for gas-surface interactions,” *Transp. Theory Stat. Phys.*, vol. 1, no. 2, pp. 101–114, Jan. 1971.
[92] S. K. Dadzie and J. G. Méolans, “Anisotropic scattering kernel: Generalized and modified Maxwell boundary conditions,” *J. Math. Phys.*, vol. 45, no. 5, pp. 1804–1819, May 2004.
[93] S. Pantazis and D. Valougeorgis, “Rarefied gas flow through a cylindrical tube due to a small pressure difference,” *Eur. J. Mech. - B/Fluids*, vol. 38, pp. 114–127, Mar. 2013.
[94] S. Naris, C. Tantos, and D. Valougeorgis, “Kinetic modeling of a tapered Holweck pump,” *Vaccum*, vol. 109, pp. 341–348, 2014.
[95] L. Mieussens, “A survey of deterministic solvers for rarefied flows,” 2014, pp. 943–951.
[96] F. Sharipov, “Rarefied gas flow through a long tube at any temperature ratio,” *J. Vac. Sci.*

Technol., A, vol. 14, no. 4, pp. 2627–2635, Jul. 1996.
[97] V. Leontidis, J. Chen, L. Baldas, and S. Colin, "Numerical design of a Knudsen pump with curved channels operating in the slip flow regime," *Heat Mass Transf.*, vol. 50, no. 8, pp. 1065–1080, 2014.
[98] L. Szalmás, T. Veltzke, and J. Thöming, "Analysis of the diodic effect of flows of rarefied gases in tapered rectangular channels," *Vacuum*, vol. 120, pp. 147–154, Oct. 2015.
[99] I. Graur, J. G. Méolans, P. Perrier, J. Thöming, and T. Veltzke, "A physical explanation of the gas flow diode effect," *Microfluid. Nanofluid.*, vol. 20, no. 10, p. 145, Oct. 2016.
[100] H. Yamaguchi, M. Rojas-Cárdenas, P. Perrier, I. Graur, and T. Niimi, "Thermal transpiration flow through a single rectangular channel," *J. Fluid Mech.*, vol. 744, pp. 169–182, Apr. 2014.
[101] M. Rojas Cardenas, I. Graur, P. Perrier, and J. G. Meolans, "Thermal transpiration flow: A circular cross-section microtube submitted to a temperature gradient," *Phys. Fluids*, vol. 23, no. 3, 2011.
[102] S. Pantazis, D. Valougeorgis, and F. Sharipov, "End corrections for rarefied gas flows through circular tubes of finite length," *Vacuum*, vol. 101, pp. 306–312, Mar. 2014.
[103] D. Valougeorgis, N. Vasileiadis, and V. Titarev, "Validity range of linear kinetic modeling in rarefied pressure driven single gas flows through circular capillaries," *Eur. J. Mech. B. Fluids*, vol. 64, pp. 2–7, Jul. 2017.
[104] M. Rojas-Cárdenas, P. Perrier, I. Graur, and J. G. Méolans, "Time-dependent experimental analysis of a thermal transpiration rarefied gas flow," *Phys. Fluids*, vol. 25, p. 72001, 2013.
[105] M. Rojas Cárdenas, "Temperature Gradient Induced Rarefied Gas Flow," no. September, 2012.
[106] PRIME Faraday Partnership, *An Introduction to MEMS (Micro-electromechanical Systems)*. 2002.
[107] S. Queste, R. Salut, S. Clatot, J. Y. Rauch, and C. G. Khan Malek, "Manufacture of microfluidic glass chips by deep plasma etching, femtosecond laser ablation, and anodic bonding," *Microsyst. Technol.*, vol. 16, no. 8–9, pp. 1485–1493, 2010.
[108] S. Pandey *et al.*, "Low cost lift-off process optimization for MEMS applications," 2016, p. 020105.
[109] C. Iliescu, H. Taylor, M. Avram, J. Miao, and S. Franssila, "A practical guide for the fabrication of microfluidic devices using glass and silicon," *Biomicrofluidics*, vol. 6, no. 1, p. 016505, Mar. 2012.
[110] A. Accardo, R. Courson, R. Riesco, V. Raimbault, and L. Malaquin, "Direct laser fabrication of meso-scale 2D and 3D architectures with micrometric feature resolution," *Addit. Manuf.*, vol. 22, pp. 440–446, Aug. 2018.
[111] R. Courson *et al.*, "Low-cost multilevel microchannel lab on chip: DF-1000 series dry film photoresist as a promising enabler," *RSC Adv.*, vol. 4, no. 97, pp. 54847–54853, 2014.
[112] M. Fouet, R. Manczak, R. Courson, C. Blatche, K. Reybier, and A.-M. Gue, "Multilevel (3D) microfluidic technology for an innovative magnetic cell separation and counting platform," in *18th International Conference on Miniaturized Systems for Chemistry and Life Sciences, MicroTAS 2014*, 2014, pp. 440–442.
[113] S. Abada *et al.*, "Comparative study of soft thermal printing and lamination of dry thick photoresist films for the uniform fabrication of polymer MOEMS on small-sized

samples," *J. Micromechanics Microengineering*, vol. 27, no. 5, 2017.
[114] S. Colin, P. Lalonde, and R. Caen, "Validation of a Second-Order Slip Flow Model in Rectangular Microchannels," *Heat Transf. Eng.*, vol. 25, no. 3, pp. 23–30, 2010.
[115] P. Perrier, I. A. Graur, T. Ewart, and J. G. Méolans, "Mass flow rate measurements in microtubes: From hydrodynamic to near free molecular regime," *Phys. Fluids*, vol. 23, no. 4, p. 042004, Apr. 2011.
[116] E. Silva *et al.*, "A time-dependent method for the measurement of mass flow rate of gases in microchannels," *Int. J. Heat Mass Transf.*, vol. 120, pp. 422–434, 2018.
[117] F. Sharipov, "Rarefied gas flow through a long rectangular channel," *J. Vac. Sci. Technol. A Vacuum, Surfaces, Film.*, 1999.